

Spin Dynamics in Transition Metal Compounds: Towards Nuclear-Spin-Free Molecular Quantum Bits

Von der Fakultät Chemie der Universität Stuttgart
zur Erlangung der Würde eines Doktors der Naturwissenschaften
(Dr. rer. nat.) genehmigte Abhandlung

Vorgelegt von

Anna Katharina Bader

geboren am 21.04.1988 in Stuttgart-Bad Cannstatt

Hauptberichter: Prof. Dr. Joris van Slageren

Mitberichter: Prof. Dr. Michael Hunger

Prüfungsvorsitzender: Prof. Dr. Dietrich Gudat

Tag der mündlichen Prüfung: 13.12.2016

Institut für Physikalische Chemie der Universität Stuttgart

2016

Erklärung über die Eigenständigkeit der Dissertation

Hiermit versichere ich, dass ich die vorliegende Arbeit mit dem Titel „Spin Dynamics in Transition Metal Compounds: Towards Nuclear-Spin-Free Molecular Quantum Bits“ selbständig verfasst und keine anderen als die angegebenen Quellen und Hilfsmittel verwendet habe; aus fremden Quellen entnommene Passagen und Gedanken sind als solche kenntlich gemacht.

Declaration of Authorship

I hereby certify that the dissertation entitled “Spin Dynamics in Transition Metal Compounds: Towards Nuclear-Spin-Free Molecular Quantum Bits” is entirely my own work except where otherwise indicated. Passages and ideas from other sources have been clearly indicated.

Ort/Location, Datum/Date

Katharina Bader

Contents

Erklärung über die Eigenständigkeit der Dissertation	1
Declaration of Authorship	1
Contents	2
List of Abbreviations and Symbols	6
Zusammenfassung	12
Summary	19
1 Introduction	25
1.1 General Introduction	25
1.2 Aims and Objectives	27
1.3 Investigated Systems and Experiments	27
1.4 Organization of the Thesis	30
2 Theoretical Background and Experimental Techniques	31
2.1 Introduction to EPR	31
2.2 Electron Spin Relaxation Theory	37
2.2.1 Classical Relaxation Theory	37
2.2.2 Semi-Classical Relaxation Theory	40
2.2.3 Spin-Spin Relaxation Theory	46
2.2.4 Thermodynamic Spin-Lattice Relaxation Theory	51
2.2.5 Summary Electron Spin Relaxation Theory	54
2.3 Influences on Spin Dynamics	55
2.3.1 Physical Influences	55
2.3.2 Chemical Influences	60

2.4	EPR Spectroscopy: Experimental Techniques	63
2.4.1	CW EPR	63
2.4.2	Pulsed EPR	64
3	Results & Discussion.....	72
3.1	Chemical Influences on Electron Spin Relaxation	72
3.1.1	Spin Dynamics in Compounds with O-Donor Ligands.....	73
3.1.2	Spin Dynamics in Compounds with N-Donor Ligands.....	92
3.1.3	Spin Dynamics in Compounds with S-Donor Ligands.....	104
3.2	Physical Influences on Electron Spin Relaxation.....	131
3.2.1	Magnetic Field Dependence of Spin Dynamics.....	132
3.2.2	Temperature Dependence of Spin Dynamics	140
3.2.3	Frequency Dependence of Spin Dynamics.....	147
3.2.4	Couplings to Nuclear Spins	157
3.2.5	Summary regarding Physical Influences on Electron Spin Relaxation.....	167
4	Conclusion.....	170
5	Experimental Section.....	173
5.1	Syntheses	173
5.1.1	General Remarks on Syntheses and Characterization Methods	173
5.1.2	Cu(Otfacac) ₂ , Cu-Otfacac	173
5.1.3	Cu(Ohfac) ₂ , Cu-Ohfac	174
5.1.4	Cu(Ofod) ₂ , Cu-Ofod	174
5.1.5	Cu(Obzac) ₂ , Cu-Obzac	174
5.1.6	Cu(Odbm) ₂ , Cu-Odbm	175
5.1.7	Pd(Odbm) ₂ , Pd-Odbm	175

5.1.8	$(d_{20}\text{-PPh}_4)\text{Br}$	176
5.1.9	$(d_{20}\text{-AsPh}_4)\text{Br}$	176
5.1.10	$(\text{PPh}_4)_2[\text{Cu}(\text{Smnt})_2]$, $\text{Cu-Smnt}^{\text{P}}$	176
5.1.11	$(\text{PPh}_4)_2[\text{Ni}(\text{Smnt})_2]$, $\text{Ni-Smnt}^{\text{P}}$	177
5.1.12	$(\text{PPh}_4)[\text{Ni}(\text{Smnt})_2]$, $\text{Ni-Smnt}_{\text{para}}^{\text{P}}$	177
5.1.13	$(d_{20}\text{-PPh}_4)_2[\text{Cu}(\text{Smnt})_2]$, $\text{Cu-Smnt}^{\text{P/d}}$	177
5.1.14	$(d_{20}\text{-PPh}_4)_2[\text{Ni}(\text{Smnt})_2]$, $\text{Ni-Smnt}^{\text{P/d}}$	178
5.1.15	$(d_{20}\text{-PPh}_4)[\text{Ni}(\text{Smnt})_2]$, $\text{Ni-Smnt}_{\text{para}}^{\text{P/d}}$	178
5.1.16	$(d_{20}\text{-AsPh}_4)_2[\text{Cu}(\text{Smnt})_2]$, $\text{Cu-Smnt}^{\text{As/d}}$	178
5.1.17	$(d_{20}\text{-AsPh}_4)_2[\text{Ni}(\text{Smnt})_2]$, $\text{Ni-Smnt}^{\text{As/d}}$	179
5.1.18	$\text{Na}_2[\text{Cu}(\text{Smnt})_2] \cdot \text{D}_2\text{O}$, $\text{Cu-Smnt}^{\text{Na}}$	179
5.1.19	$\text{Na}_2[\text{Ni}(\text{Smnt})_2] \cdot \text{D}_2\text{O}$, $\text{Ni-Smnt}^{\text{Na}}$	180
5.1.20	K_2Sdto	180
5.1.21	$(\text{PPh}_4)_2[\text{Cu}(\text{Sdto})_2]$, $\text{Cu-Sdto}^{\text{P}}$	180
5.1.22	$(\text{PPh}_4)_2[\text{Ni}(\text{Sdto})_2]$, $\text{Ni-Sdto}^{\text{P}}$	181
5.1.23	$(d_{20}\text{-PPh}_4)_2[\text{Cu}(\text{Sdto})_2]$, $\text{Cu-Sdto}^{\text{P/d}}$	181
5.1.24	$(d_{20}\text{-PPh}_4)_2[\text{Ni}(\text{Sdto})_2]$, $\text{Ni-Sdto}^{\text{P/d}}$	182
5.1.25	$(d_{20}\text{-AsPh}_4)_2[\text{Cu}(\text{Sdto})_2]$, $\text{Cu-Sdto}^{\text{As/d}}$	182
5.1.26	$(d_{20}\text{-AsPh}_4)_2[\text{Ni}(\text{Sdto})_2]$, $\text{Ni-Sdto}^{\text{As/d}}$	182
5.1.27	Synthesis of doped powders.....	183
5.2	EPR Measurements.....	183
5.2.1	Sample Preparation	183
5.2.2	Spectrometers	183
5.2.3	Experiment Design and Data Analysis	185

6	Appendix.....	186
6.1	Supplementary Information to Spin Dynamics in Compounds with O-Donor Ligands	186
6.2	Supplementary Information to Spin Dynamics in Compounds with N-Donor Ligands	191
6.3	Supplementary Information to Spin Dynamics in Compounds with S-Donor Ligands	194
6.4	Supplementary Information to Orientation Dependence of Spin Dynamics	205
6.5	Supplementary Information to Temperature Dependence of Spin Dynamics	209
6.6	Supplementary Information to Frequency Dependence of Spin Dynamics	212
6.7	Supplementary Information to Couplings to Nuclear Spins	217
7	References	218
8	Acknowledgements	229

List of Abbreviations and Symbols

	Abbreviations
CPMG	Carr-Purcell-Meiboom-Gill
CW	continuous wave
DCM	dichloromethane
DEER	double electron-electron resonance
DET	diethylether
el.	electron(ic)
ENDOR	electron-nuclear double resonance
EPR	electron paramagnetic resonance
ESD	electron spin diffusion
ESE	electron spin echo
ESEEM	electron spin echo envelope modulation
<i>et al.</i>	et alii
f	fast
FFT	fast Fourier transformation
FWHM	full width at half maximum
G	Gaussian
HF	hyperfine interaction
ID	instantaneous diffusion
L	Lorentzian
MO	molecular orbital
MQB	molecular quantum bit
MW	microwave
NMR	nuclear magnetic resonance
Npc	phthalocyaninate
NSD	nuclear spin diffusion

nuc.	nuclear
Oacac	acetylacetonate
qubit	quantum bit
RF	radiofrequency
s	slow
SD	spectral diffusion
Sdto	1,2-dithiooxalate
SHF	superhyperfine interaction
SOC	spin-orbit coupling
SOMO	singly occupied molecular orbital
Smnt	maleonitrile-1,2-dithiolate

Symbols

\mathbf{A}	hyperfine coupling tensor
A_f	prefactor for fast component in exponential fits
A_s	prefactor for slow component in exponential fits
\vec{B}_0	static magnetic field
\vec{B}_1	magnetic field component of electromagnetic wave
$B_q(t)$	time dependent magnetic field along q-direction
$\langle B_x^2 \rangle$	mean square of magnetic field fluctuations along x-direction
c	coefficient; concentration
$E_{el.Zeeman}$	electron spin Zeeman energies
$f(\omega_s)$	lineshape function
g	g -factor, Landé-factor
\mathbf{g}	g -tensor
g_N	nuclear g -factor
G	Gaussian linewidth of Voigtian convolution
$G(\tau)$	auto-correlation function
h	Planck constant

\hbar	reduced Planck constant
\hat{H}_0	(static) Hamiltonian including electronic- and nuclear Zeeman effect and hyperfine coupling
\hat{H}_{DD}	Hamiltonian for spin-only electron-nuclear dipole-dipole interaction
$\hat{H}_{el,Zeeman}$	Hamiltonian for electron spin Zeeman interaction
$\hat{H}_{el,Zeeman,L}$	Hamiltonian for el. Zeeman interaction incl. orbital angular momentum
\hat{H}_{HF}	Hamiltonian for hyperfine interaction
$\hat{H}_{nuc,Zeeman}$	Hamiltonian for nuclear spin Zeeman interaction
\hat{H}_s	Hamiltonian for the spin system
\hat{H}_{SOC}	Hamiltonian for spin-orbit coupling
$\hat{H}(t)$	time-dependent Hamiltonian
i	number of unpaired electrons; number of groups of nuclei
I	total nuclear spin quantum number; intensity
\hat{I}	total nuclear spin vector operator
$J(\omega)$	spectral density
k	stretch parameter
k_B	Boltzmann constant
L	Lorentzian linewidth of Voigtian convolution
\hat{L}	orbital angular momentum vector operator
m_e	electron mass
M_I	total magnetic nuclear spin quantum number
M_s	total magnetic electron spin quantum number
m_s	magnetic electron spin quantum number
\vec{M}	magnetization
M_z	z-component of magnetization
N	population of a state; number of resonance lines; number of spins
n_i	number of equivalent nuclei of group i
n_k	number of existing phonons in k^{th} vibronic state
r	distance

R	gas constant
R_{auto}	leakage rate or auto relaxation rate constant
R_{cross}	cross-relaxation rate
R_T	transition rate
$R_{\alpha\alpha'\beta\beta'}$	relaxation matrix elements
S	total electron spin quantum number
\vec{S}	total electron spin
\hat{s}_i	electron spin operator
S_z	z-component of total electron spin
T	temperature
t	time
T_1	spin-lattice or longitudinal relaxation time
$T_{1,n}$	nuclear spin-lattice relaxation time
$T_{1\rho}$	rotating-frame relaxation time
T_2	spin-spin or transverse relaxation time
\mathbf{T}_{DD}	dipolar coupling tensor
T_f	mean spin flip time
T_{ID}	instantaneous diffusion time
T_M	phase memory time
T_{nm}	average nuclear spin flip-flop time
T_{NSD}	nuclear spin diffusion time
t_p	pulse length
\vec{T}	torque
V	volume
\hat{V}	perturbation operator
W	transition probability

Greek symbols

$ \alpha\rangle$	spin state with $m_s = +1/2$
$ \beta\rangle$	spin state with $m_s = -1/2$
γ_e	gyromagnetic ratio of electron spin
Δ	difference
ΔB_{exc}	excitation bandwidth
ΔB_{lwpp}	simulation parameter for Voigtian convolution line broadening, given as peak-to-peak linewidths [$G L$]
ΔB_{Strain}	simulation parameter for orientation dependent line broadening, given as Gaussian peak-to-peak linewidth [$Strain_{\perp} Strain_{\parallel}$]
$\Delta\omega_{dip}$	dipolar line broadening
ε_n	time dependent strain
$\varepsilon(t)$	effect of microwave field on spins
θ	angle
θ_D	Debye temperature
λ	spin-orbit coupling constant
μ_N	nuclear magneton
$\vec{\mu}$	magnetic moment
μ_B	Bohr magneton
ν	oscillation frequency
ν_D	Debye frequency
ν_L	Larmor frequency
ν_{MW}	microwave frequency
v_s	velocity of sound
\hat{v}	crystal field perturbation operator
π	180°-pulse
$\pi/2$	90°-pulse
π_{nut}	nutation pulse
π_{RF}	radio frequency pulse

π_{sat}	saturation pulse
ρ	density
ρ_β	population of $ \beta\rangle$ -state
ρ_p	density of phonon states at a certain temperature
$\hat{\rho}$	density matrix operator
τ	time delay
τ_c	correlation time
τ_{fix}	fixed time delay
Φ	basis function
φ_n	Eigenfunctions of phonon system
ψ	wave function
$\psi_{el.spin}$	electron spin wave function
$\psi_{el,nuc spin}$	product wave function for electron- and nuclear spin
ω_1	(angular) Rabi frequency
$\omega_{flipflop}$	(angular) flip-flop frequency
ω_L	(angular) Larmor frequency
ω_L^n	(angular) nuclear Larmor frequency
ω_{MW}	(angular) microwave frequency
ω_{nut}	(angular) nutation frequency
ω_{offset}	(angular) offset frequency

Other Symbols

\parallel	parallel
\perp	perpendicular

Zusammenfassung

Thema dieser Dissertation ist die Untersuchung von Einflussfaktoren auf Elektronenspindynamik in Übergangsmetallkomplexen mit Hilfe von systematischen Untersuchungen mittels gepulster Elektronenspinresonanz-Spektroskopie (ESR). Das übergeordnete Ziel hierbei war die Identifizierung und Klassifizierung dieser Faktoren, um allgemeine Designprinzipien für die Synthese neuer molekularer Quantenbits (MQBs) aufzustellen. MQBs können möglicherweise als Bausteine für Recheneinheiten in einem Quantencomputer dienen. Die Entwicklung eines Quantencomputers würde unseren Alltag grundsätzlich verändern, denn aufgrund einer komplett neuen Hardware-Architektur ist Quanten-Datenverarbeitung deutlich effizienter als klassische elektronische Datenverarbeitung. Bislang ungelöste Aufgaben, wie die verlässliche Simulation von Quanten-Systemen oder eine abhörsichere Datenübermittlung wären mit einem Quantencomputer realisierbar. Der Hauptunterschied zwischen einem klassischen und einem Quantenbit (Qubit) ist, dass letzteres auch in kohärenten Überlagerungszuständen der Eigenzustände $|0\rangle$ und $|1\rangle$ vorliegen kann. Die Zeit in welcher dieser Überlagerungszustand stabil ist, wird Kohärenzzeit genannt. Für MQBs kann die Kohärenzzeit anhand der Phasengedächtniszeit abgeschätzt werden, welche mit Hilfe von gepulsten ESR-Experimenten bestimmt werden kann. Entsprechend den DiVincenzo-Kriterien für Qubits muss die Phasengedächtniszeit mindestens 10 000-mal länger sein als die Dauer einer Qubit-Operation. Diese entspricht der zeitlichen Länge des Mikrowellenpulses in gepulsten ESR-Experimenten, welche beispielsweise etwa 20 ns bei Q-Band-Frequenz beträgt. Aus dem Quotienten der Phasengedächtniszeit und der Pulslänge kann ein Qubit-Gütefaktor berechnet werden, welcher oft als Bewertungskriterium für Qubits zur Rate gezogen wird.

Die Untersuchung von Einflussfaktoren auf Elektronenspindynamik in dieser Arbeit wurde in zwei Themenkomplexe eingeteilt, welche sich zum einen mit den chemischen und zum anderen mit den physikalischen Faktoren beschäftigen. Chemische Einflüsse wurden mit Hilfe von gepulster Q-Band ESR-Spektroskopie bei 7 K untersucht. Hierbei wurden drei Arten von Verbindungen unter den gleichen Bedingungen untersucht, um eine Vergleichbarkeit der Messergebnisse

sicherzustellen. Neben Elektronen-Spin-Echo- (ESE) detektierten ESR-Spektren wurden Inversion Recovery- und Hahn-Echo-Experimente aufgenommen, aus welchen Spin-Gitter-Relaxations- und Phasengedächtniszeiten bestimmt wurden. Im ersten Teil der Studie von chemischen Einflussfaktoren auf Elektronenspindynamik wurden Verbindungen mit O-Donor-Liganden, namentlich β -diketonato-Kupfer(II)-Komplexe, untersucht. In den ESE-detektierten ESR-Spektren gab es Hinweise auf zwei paramagnetische Spezies in gefrorenen Lösungen der Verbindungen. Vermutlich handelt es sich hierbei um die betrachtete Koordinationsverbindung sowie eine Solvent-Addukt-Spezies des Komplexes. Die Elektronenspindynamik-Experimente zeigten biexponentielle Kurven, hervorgerufen durch einen schnellen und einen langsamen Relaxationsprozess. Hierbei konnte der schnelle Prozess nicht eindeutig zugeordnet werden, jedoch wurde der langsame Prozess der Relaxation der jeweiligen untersuchten Verbindung zugeschrieben. Es wurde beobachtet, dass eine höhere Beweglichkeit (oder geringere Rigidität) in den Liganden und in der Lösungsmittel-Matrix zu kürzeren Spin-Gitter-Relaxations- und Phasengedächtniszeiten führt. Außerdem wurden Kernspins als weitere Quelle starken Einflusses auf die Spin-Spin-Relaxation identifiziert. Hierbei wurde ein besonders starker kohärenzzerstörender Einfluss durch Methylgruppen festgestellt. Die längste Phasengedächtniszeit in dieser Messreihe ($48 \pm 2 \mu\text{s}$) wurde für **Cu-Odbm** im kernspinfreien Lösungsmittel CS_2 (0.001 M gefrorene Lösung) gefunden. Im Gegensatz zu den Proben in gefrorener Lösung wurde im dotierten Pulver **Cu-Odbm_{0.001%}** nur eine paramagnetische Spezies in den ESE-detektierten ESR-Spektren sowie jeweils ein Relaxationsprozess für Spin-Gitter- und Spin-Spin-Relaxation beobachtet. Die Spin-Gitter-Relaxationszeit von **Cu-Odbm_{0.001%}** von $18.3 \pm 0.1 \text{ ms}$ ist ungefähr siebenmal länger als in gefrorener Lösung, was auf eine höhere Rigidität im dotierten Pulver zurückgeführt wird. Diese Vermutung wird durch einen Vergleich der dominanten Dephasierungsprozesse im dotierten Pulver und gefrorener Lösung bestätigt: für das Pulver wurde Kernspindiffusion als dominanter Prozess gefunden, wohingegen physikalische Bewegung von magnetischen Kernen in den gefrorenen Lösungen dominiert. Es wurden Gütefaktoren von bis zu 2500 für die Verbindungen mit O-Donor-Liganden gefunden. In gefrorener Lösung sind die paramagnetischen Spezies und die Relaxationsprozesse nicht klar definiert, was künftig verbessert werden kann. Die hohe Beweglichkeit von Liganden und Umgebung der paramagnetischen Spezies wurde als stärkster kohärenzbeschränkender Faktor in den untersuchten Verbindungen mit

O-Donor-Liganden identifiziert. Längere Relaxationszeiten sollten daher möglich sein, wenn mehr konformationelle Rigidität in den Liganden vorliegt. Dies könnte zum Beispiel durch Einbringen von π -Konjugation oder höherer Zähigkeit die Liganden erreicht werden.

Im zweiten Teil der Studie von chemischen Einflussfaktoren auf Elektronenspindynamik wurden Verbindungen mit N-Donor-Liganden untersucht. Hierfür wurden Phthalocyanin-Derivate (Npc) in Kombination mit Cu^{2+} und anderen Übergangsmetallen ausgewählt. Für diese paramagnetischen Spezies konnten wohldefinierte ESE-detektierte ESR-Spektren aufgenommen werden. Die Relaxationskurven sind überwiegend biexponentiell und auch hier konnte der schnelle Prozess nicht eindeutig zugeordnet werden. Ein Austausch der peripheren Substituenten des Liganden in **Cu-Npc** hat keinen Einfluss auf Spin-Gitterrelaxation. Eine außergewöhnlich lange Spin-Gitter-Relaxationszeit von 2.4 ± 0.3 s wurde für **VO-Npc** gefunden, welche auf die Kombination einer stabilen Koordinationsgeometrie, die Rigidität des Liganden und der geringe Spin-Bahn-Kopplung in dieser Verbindung zurückgeführt wurde. Durch den Vergleich der Elektronenspindynamik in Verbindungen mit N-Donor-Liganden und unterschiedlichen Zentralionen konnte die Geometrie des SOMOs im Vergleich zur Ausrichtung des Liganden als starker Einflussfaktor auf die Elektronenspinrelaxation identifiziert werden. Je größer die Überlappung zwischen dem SOMO und der Umgebung, desto schneller ist die Relaxation. Elektronen in Orbitalen, welche senkrecht zum Phthalocyanin-Ring ausgerichtet sind, werden stärker durch Fluktuationen in der Umgebung beeinflusst als solche in Orbitalen, welche in der Ringebene liegen. Zusammenfassend wurden lange Phasengedächtniszeiten von bis zu 43 ± 1 μs gefunden, welche Gütefaktoren von ca. 2000 ergeben. Diese Werte sind unter den höchsten berichteten für Übergangsmetallkomplexe in gefrorenen Lösungen.^[1-2] Des Weiteren wurde für **Cu-Npc^{Cl}** nur eine langsame Phasengedächtniszeit gefunden. Das Fehlen eines schnellen Spin-Spin-Relaxationsprozesses ist vorteilhaft für Qubit-Anwendungen, da so eine hohe Kontrolle über das Qubit-System gewährleistet ist. Insgesamt sind die untersuchten Verbindungen mit N-Donor-Liganden chemisch sehr robust und können mittels Molekularstrahlepitaxie prozessiert werden, was für MQB-Anwendungen relevant ist. Der beschränkende Einfluss in den untersuchten Verbindungen mit N-Donor-Liganden in gefrorener Lösung sind vermutlich die Deuterium-Kernspins des Lösungsmittels. Wenn diese entfernt werden, sollten Kohärenzzeiten im Sekunden-Bereich möglich sein, da die gefundenen Spin-Gitter-Relaxationszeiten sehr lang sind. Eine

lösungsmittelfreie Alternative ist die Synthese von diamagnetischen Analoga der Verbindungen, z.B. **Zn-Npc**, und der Herstellung von dotierten Pulvern. Für eine weitere Charakterisierung der kohärenzbeschränkenden Einflüsse muss die Messreihe erweitert werden. Zukünftige Arbeit sollte die Untersuchung von dotierten Pulvern, deuterierten Spezies, Einkristallen und monomolekularen Schichten umfassen.

Im dritten und letzten Teil der Studie von chemischen Einflussfaktoren auf Elektronenspindynamik wurden Verbindungen mit S-Donor-Liganden untersucht. Hier wurden vornehmlich Kupfer(II)-Dithiolenkomplexe in gefrorenen Lösungen und dotierten Pulvern untersucht. Im Fall der Spin-Gitter-Relaxation wurde die konformationelle Rigidität des Liganden als größter Einflussfaktor identifiziert. Des Weiteren stellen die Rigidität der Qubit-umgebenden Matrix und der Grad der dreidimensionalen Ordnung, sprich die Kristallstruktur, weitere wichtige Einflüsse auf die Spin-Gitter-Relaxation dar. Der Grad an Ordnung und die Rigidität des MQBs und seiner Umgebungen sind auch wichtige Einflüsse für die Phasengedächtniszeit. Der stärkste Einfluss ist hier jedoch durch die Anzahl von Kernspins und ihr Abstand zum ungepaarten Elektron gegeben. Für **Cu-Smnt^{P/d}_{0.01%}** wurde eine Phasengedächtniszeit von $68 \pm 3 \mu\text{s}$ bei 7 K gefunden, was bislang den höchsten berichteten Wert für MQBs in dotierten Pulvern darstellt. Des Weiteren wurden in diesem Teilprojekt die ersten Kohärenzmessungen an einem Ni³⁺-basierten potentiellen MQB durchgeführt, namentlich **Ni-Smnt^{P/d}_{para.}**. Zusammenfassend konnte in diesem Teilprojekt die Komplexität des Zusammenspiels von Einflussfaktoren auf Elektronenspinrelaxation gezeigt werden. Einzelne Messungen können zu Fehlinterpretationen der Effekte auf Elektronenspindynamik führen. Für eine Identifizierung und Beurteilung verschiedener Einflussfaktoren und deren relativer Stärke bedarf es mehrdimensionaler Messungen. Künftige Arbeiten zur Elektronenspindynamik in Verbindungen mit S-Donor-Liganden könnte die Untersuchung von monomolekularen Lagen beinhalten. Ein Übergang von sehr großen Ensembles an MQBs zu einzelnen Molekülen könnte von fundamentalen Änderungen in der Spindynamik begleitet sein, was tiefere Einblicke in Relaxationsmechanismen und -prozesse im Allgemeinen ermöglichen könnte.

Für eine detaillierte Untersuchung der physikalischen Einflussfaktoren auf Spindynamik wurde **Cu-Smnt^{P/d}_{0.01%}** als Zielverbindung ausgewählt. Diese Verbindung wurde im vorangegangenen Teilprojekt als potentielles MQB mit einer der längsten Kohärenzzeiten identifiziert, welche in

dieser Arbeit vorgestellt werden. In der Studie physikalischer Einflussfaktoren wurde zunächst der Einfluss der Magnetfeldposition auf Spindynamik bei konstanter Mikrowellenfrequenz untersucht. Hierzu wurden sowohl Inversion-Recovery- und Hahn-Echo-Experimente als auch zweidimensionale ESE-detektierte ESR-Spektren zur Rate gezogen. Die Spin-Gitter-Relaxationszeit wurde als magnetfeldunabhängig charakterisiert, was der geringen Anisotropie des g -Tensors des Systems zugeschrieben wird. Im Gegensatz dazu wurden unterschiedliche Phasengedächtniszeiten für verschiedene Ausrichtungen des Komplexes zum externen Magnetfeld beobachtet. Dabei wurde eine Korrelation zwischen struktureller Rigidität von Komplex bzw. Kristallstruktur und Phasengedächtniszeit vermutet: Es wurden tendenziell längere Phasengedächtniszeiten gefunden für Magnetfeldpositionen, welche einer Anregung des Komplexmoleküls in Orientierungen mit potentiell höherer konformationeller Rigidität entsprechen.

In einem zweiten Schritt der Studie wurde der Einfluss der experimentellen Temperatur auf die Spindynamik bei Q-Band und konstanter Magnetfeldposition untersucht. Hier wurden abnehmende Spin-Gitter-Relaxationszeiten mit zunehmender Temperatur gefunden, mit Werten zwischen 87 ms bei 7 K und 0.5 μ s bei Zimmertemperatur. Die Modellierung der Temperaturabhängigkeit zeigte einen Raman-Prozess als dominanten Spin-Gitter-Relaxationsprozess. Für die Phasengedächtniszeit von **Cu-Smmt**^{P/4}_{0.01%} wurden Werte zwischen 68 μ s bei 7 K und 0.6 μ s bei Zimmertemperatur gefunden, welche unter den höchsten bislang berichteten Werten für MQBs sind.^[1-6] Als dominanter Dephasierungsprozess wurde bei Temperaturen unter 100 K die Kernspindiffusion gefunden. Bei höheren Temperaturen sind die Spin-Gitter-Relaxation und physikalische Bewegung magnetischer Kernspins die beschränkenden Einflüsse auf die Phasengedächtniszeit.

Im nächsten Schritt wurde eine detaillierte Studie der Mikrowellenfrequenzabhängigkeit der Spindynamik im Bereich von 3.7–240 GHz durchgeführt. Hier wurden Spin-Gitter-Relaxationszeiten zwischen 1.1–218 ms (langsamer Prozess) gefunden. Die Spin-Gitter-Relaxation ist schneller bei höheren Frequenzen, was durch höhere Phononenzustandsdichten und damit einhergehend höheren Übergangswahrscheinlichkeiten bei höheren Frequenzen verursacht wird. Durch Modellieren der Frequenzabhängigkeit der Spin-Gitter-Relaxationszeiten konnte eine Kombination von einem direkten und einem Raman-Prozess gefunden werden. Die gemessenen

Phasengedächtniszeiten decken Werte zwischen 19–70 μs ab (langsamer Prozess), wobei keine eindeutige Frequenzabhängigkeit beobachtet werden konnte. Bei 120 GHz wurde eine fundamentale Änderung der Spindynamik beobachtet: hier wurde im Gegensatz zu den anderen untersuchten Frequenzen eine nicht-exponentielle Hahn-Echo-Zerfallskurve detektiert. Ein erweitertes Fit-Modell^[7] ermöglichte die Extraktion einer charakteristischen Kernspindiffusionszeit von $109 \pm 1 \mu\text{s}$ und einer Elektronenspin-Phasengedächtniszeit von $68.5 \pm 0.6 \mu\text{s}$. Über 120 GHz wird die Phasengedächtniszeit vermutlich durch die elektronische Spin-Gitter-Relaxation beschränkt. Die Spindynamik bei sehr hohen Frequenzen (120 GHz und mehr) wird zu diesem Zeitpunkt noch nicht vollständig verstanden und die präsentierte Messreihe zeigt die Notwendigkeit weiterer systematischer Studien und neuer theoretischer Ansätze.

Im letzten Teil der Studie wurden die Kopplungen zwischen Elektronen- und Kernspins in **Cu-Smnt**^{P/d}_{0.01%} untersucht. ESEEM-Effekte wurden bei S-, X- und Q-Band Frequenzen (3.7, 9.7, 36.1 GHz) gefunden. Die Modulationen wurden schwachen Kopplungen zwischen dem Elektronenspin und ²H- sowie ¹⁴N-Kernspins zugeschrieben. Diese schwachen Kopplungen wurden in den vorhergehenden Untersuchungen als hauptsächliche kohärenzzerstörende Einflussfaktoren identifiziert. Deshalb wurden CPMG-Experimente bei Q- und W-Band durchgeführt, um störende kernspindinduzierte Fluktuationen von der Elektronenspinrelaxation zu entkoppeln. Es wurden bis zu dreimal längere Phasengedächtniszeiten in den CPMG-Experimenten im Vergleich zu Standard-Hahn-Echo-Messungen gefunden. Die zugehörigen Spin-Gitter-Relaxationszeiten sind trotzdem noch um Größenordnungen länger, was zeigt, dass es daneben noch weitere dominante Einflüsse auf die Phasengedächtniszeit im untersuchten System gibt. Im Verlauf der vorhergegangenen Untersuchungen wurden die strukturelle Rigidität und dreidimensionale Ordnung als solche identifiziert. Diese Faktoren müssen eliminiert werden, um neue MQBs mit längeren Kohärenzzeiten zu entwickeln.

Davies-ENDOR-Experimente bei Q-Band zeigten eine starke Hyperfeinkopplung zwischen dem Elektronenspin und den ^{63,65}Cu-Kernspins in **Cu-Smnt**^{P/d}_{0.01%}. Diese Kopplungen wurden für erste einfache Qubit-Operationen und Kohärenztransfer-Experimente genutzt. Es konnten Rabi-Oszillationen für **Cu-Smnt**^P_{0.001%} detektiert werden, was zeigt, dass sogar das protonierte Derivat der Zielverbindung grundsätzlich als MQB einsetzbar ist. Für **Cu-Smnt**^{P/d}_{0.01%} wurden außerdem transiente Kernspin-Nutationen detektiert, was die grundlegende Einsetzbarkeit der Verbindung

in Kohärenztransfer-Experimenten zwischen Elektronen- und Kernspin-Ensemble beweist. Mit diesen beiden Experimenten konnte die Möglichkeit der Verwendung von **Cu-Smnt^{P/d}_{0.01%}** sowohl in der Quanten-Datenverarbeitung als auch in der Quanten-Datenspeicherung gezeigt werden.

Zusammenfassend werden in dieser Dissertation systematische gepulste ESR-Studien an potentiellen MQBs präsentiert, anhand derer die dominanten Einflussfaktoren auf Spindynamik identifiziert werden konnten. Durch systematische Auswahl der Verbindungen konnten sehr lange Spin-Gitter-Relaxations- und Phasengedächtniszeiten detektiert werden, welche vergleichbar mit den Rekordwerten der einschlägigen Literatur sind. Es wird gezeigt, dass einzelne Messungen meist nur einen oder einige wenige von vielen relevanten Aspekten enthüllen. Systematische Studien sind daher unabdingbar für die Einstufung verschiedener Einflussfaktoren auf Elektronenspindynamik.

Zukünftige Arbeit beinhaltet die Untersuchung potentieller MQBs und insbesondere **Cu-Smnt^{P/d}_{0.01%}** in monomolekularen Lagen oder Quanten-Schaltkreisen, wofür erste Schritte schon durchgeführt wurden.^[8] Im Hinblick auf die theoretische Beschreibung der Spindynamik von MQBs werden neue Modelle und Formalismen benötigt. Auch hierfür wurden erste Schritte bereits gemacht,^[9] welche hoffentlich Wegbereiter für ein quantitatives Verständnis der Elektronenspinrelaxation in MQBs sind.

Summary

This thesis deals with the investigation of factors influencing electron spin dynamics in transition metal coordination compounds by the means of systematic pulsed EPR studies. The aim here was to identify and classify these factors in order to find design principles for new molecular qubits (MQBs). MQBs are potential building units of a quantum computer. The development of a quantum computer would change the world that we live in, as it would allow much more efficient information processing by the means of completely new hardware architecture. This could enable breakthroughs in so far unsolved problems, such as the reliable simulation of quantum systems or tap-proof data transmission. The main difference between a classical and a quantum bit is that the latter can exist in coherent superpositions of the eigenstates $|0\rangle$ and $|1\rangle$. The time during which this superposition is stable is called coherence time. For MQBs, the coherence time can be approximated by the phase memory time, which can be investigated by the means of pulsed EPR experiments. According to the DiVincenzo criteria, which need to be fulfilled by qubits, the phase memory time must be at least 10 000 times longer than the duration of a qubit manipulation. In pulsed EPR experiments, this corresponds to the length of a MW-pulse, which is typically around 20 ns at commonly used Q-band frequencies. The figure of merit is the ratio of the phase memory time and the qubit manipulation time and serves here as qubit assessment parameter.

The investigation of factors influencing electron spin relaxation was divided into two main sections in this thesis, discussing chemical and physical influences respectively. Chemical influences on electron spin relaxation were investigated by the means of pulsed Q-band EPR measurements at 7 K. Three classes of compounds were studied, all under similar experimental conditions to provide comparability of the results. Electron spin echo (ESE) detected EPR spectra were recorded and inversion recovery and Hahn echo experiments were performed for the determination of spin-lattice relaxation and phase memory times. In the first part of the investigation of chemical influences on electron spin relaxation, the spin dynamics in compounds with O-donor ligands, β -diketonato-copper(II)-complexes, were studied. Indications of two paramagnetic species were found in the ESE-detected EPR spectra of frozen solution samples,

which are presumably the complex of interest and a solvent adduct species. Biexponential relaxation characteristics were observed, where a definitive assignment of the origin of the fast process was not possible. The slow process is assigned to the species of interest. Higher mobility in the ligands and the solvent matrix was observed to lead to shorter spin-lattice relaxation and phase memory times. For the phase memory time, also the present nuclear spins heavily impact spin-spin relaxation. Methyl groups were found to act strongly dephasing. The longest phase memory times in this measurement series (up to $48 \pm 2 \mu\text{s}$) were found for **Cu-Odbm** in the nuclear-spin-free solvent CS_2 (0.001 M frozen solution). In the doped powder **Cu-Odbm**_{0.001%} only one paramagnetic species was found in the ESE-detected EPR spectra and monoexponential relaxation characteristics were found in contrast to the frozen solution samples. The spin-lattice relaxation time of $18.3 \pm 0.1 \text{ ms}$ in **Cu-Odbm**_{0.001%} is ca. seven times longer than in the frozen solution samples, probably related to a higher rigidity in the doped powder. This is confirmed by the fact that the dominant dephasing process in the doped powder is nuclear spin diffusion, whereas in frozen solution physical motion of magnetic nuclei is dominant. In conclusion, figures of merit of up to 2500 were found for the investigated compounds with O-donor ligands. However, the paramagnetic species and relaxation processes are not well-defined in the frozen solution samples, which can be improved in the future. In general, the lability of ligand and surrounding proved to be a main coherence limiting factor in the investigated compounds with O-donor ligands. Introducing more conformational rigidity in the ligand, e.g. by π -conjugation or higher ligand-denticity should thus enable longer relaxation times.

In the second part of the investigation of chemical influences on electron spin relaxation, the spin dynamics in compounds with N-donor ligands was studied. Here phthalocyanine (Npc) and derivatives were chosen as target ligands in combination with Cu^{2+} and others as central ions. Well-defined ESE-detected EPR spectra were observed for these paramagnetic species. In most cases, biexponential relaxation characteristics were found in the spin dynamics experiments. Again, a definitive assignment of the fast relaxation process was not possible. Alterations of the peripheral ligand substituents in the **Cu-Npc** compounds do not affect spin-lattice relaxation. An extraordinarily long spin-lattice relaxation time of $2.4 \pm 0.3 \text{ s}$ was found for **VO-Npc**, which was traced to the combination of a stable coordination geometry, rigidity of the ligand and a low SOC. From the variation of the central ion in the investigated compounds with N-donor ligands,

the nature of the SOMO was found to crucially influence electron spin relaxation. The higher the overlap between the environment and the SOMO, the faster is the relaxation. Electrons in orbitals perpendicular to the phthalocyanine ring are more exposed to environmental fluctuations compared to those in orbitals in the ring plane. In conclusion, long phase memory times of up to $43 \pm 1 \mu\text{s}$ leading to figures of merit of ca. 2000 were found, which are among the highest reported ones for transition metal complexes in frozen solutions.^[1-2] Furthermore, for **Cu-Npc^{Cl}** solely a slow spin-spin relaxation time was observed. The lack of a fast relaxation process is beneficial for qubit applications, providing high controllability of the qubit system. The investigated compounds with N-donor ligands are furthermore chemically robust and processable by molecular beam deposition, which makes them interesting for MQB applications. The limiting influences on coherence in the investigated compounds with N-ligands in frozen solutions are presumably the deuterium nuclear spins in the solvent. If these could be removed, engineering of MQBs with coherence times in the range of seconds would be possible, because the spin-lattice relaxation is very long. One solution to this problem is the synthesis of diamagnetic analogues of the compounds, such as **Zn-Npc** for example, and the preparation of doped powders. To identify further limiting processes, an extension of the measurement series is necessary. Thus, future work should involve investigation of doped powders, deuterated species, single crystals and molecular monolayers.

In the third and last part of the investigation of chemical influences on electron spin relaxation, the spin dynamics in compounds with S-donor ligands were studied. Copper(II)-dithiolene complexes in frozen solution and doped powders were the main target compounds. For spin-lattice relaxation, again the conformational rigidity of the ligands was found as main limiting factor. Furthermore, the rigidity of the qubit-surrounding matrix and the degree of three-dimensional ordering, i.e. the crystal structure, were found to be important influences on spin-lattice relaxation. The degree of ordering and rigidity of the MQB and its surrounding were also found to be strong influences on phase memory times. Even stronger, number and distance of nuclear spins influence dephasing. Unprecedented phase memory times in a doped powder MQB of $68 \pm 3 \mu\text{s}$ were found for **Cu-Smnt^{P/d}_{0.01%}** at 7 K. Furthermore, the first coherence measurements of a potential Ni³⁺-based MQB were performed with **Ni-Smnt^{P/d}_{para}**. Summarizing, the complexity of the interplay of influences on electron spin dynamics was shown in this

subproject. Individual measurements can be misleading for the interpretation of effects on electron spin dynamics. Identifying and rating various factors influencing spin-lattice relaxation and phase memory times requires systematic investigations. Future work in the investigation of spin dynamics in compounds with S-ligands could involve the investigation of molecular monolayers. A transition from bulk material to single molecules could be accompanied by fundamental changes in spin dynamics, giving more information on the nature of the processes in general.

Cu-Smnt^{P/d}_{0.01%} was the target compound for a uniquely extensive investigation of the influence of physical parameters on spin dynamics. The compound was selected as it proved to be a potential MQB with one of the longest coherence times in the investigation of chemical influences on electron spin relaxation. First, the influence of the magnetic field position at fixed MW frequency on electron spin dynamics was investigated by the means of Hahn echo experiments and two-dimensional ESE detected EPR spectra. The found spin-lattice relaxation times were independent from the applied magnetic field, which was attributed to the low anisotropy of the g -tensor of the system. In contrast, phase memory times were sensitive to the orientation of the complex towards the external magnetic field. Here a correlation between structural rigidity of the complex and the crystal structure and the detected phase memory times was suggested. For magnetic field positions corresponding to excitation of the molecule in orientations, where potentially higher conformational rigidity is present, in general longer phase memory times were found.

In a second step of the study, the influence of experimental temperature on electron spin dynamics was investigated at Q-band and a fixed magnetic field position. Decreasing spin-lattice relaxation times for increasing temperatures were found with values between 87 ms at 7 K and 0.5 μ s at room temperature. Modeling of the temperature dependence revealed a Raman process as dominant process in spin-lattice relaxation. For the phase memory time of **Cu-Smnt^{P/d}_{0.01%}** values between 68 μ s at 7 K and 0.6 μ s at room temperature were found, which are among the highest reported values for MQBs.^[1-6] The dominant dephasing processes were found to be nuclear spin diffusion below 100 K and limitation by spin-lattice relaxation and physical motion of magnetic nuclei at higher temperatures.

A detailed frequency dependent electron spin dynamics study was performed between 3.7 and 240 GHz for **Cu-Smnt**^{P/d}_{0.01%}. Spin-lattice relaxation times between 1.1–218 ms (slow process) were found. Spin-lattice relaxation is faster at higher frequencies, which is attributed to higher phonon densities and therefore higher transition probabilities at higher MW frequencies. A combination of a direct and a Raman process was identified was found by modeling the frequency dependence of spin-lattice relaxation. The detected phase memory times range between 19 μ s and 70 μ s (slow process), where no clear frequency dependence was observed. A fundamental change in spin dynamics was observed at 120 GHz, where in contrast to the other investigated frequencies a non-exponential Hahn echo decay curve was found. An augmented fit model^[7] yielded in the identification of the nuclear spin diffusion characteristic time of $109 \pm 1 \mu$ s and an electron spin phase memory time of $68.5 \pm 0.6 \mu$ s. At higher frequencies, the phase memory time is probably limited by the electronic spin-lattice relaxation. The spin dynamics at very high frequencies (120 GHz and more) are not fully understood at this point and the presented measurement series displays the need for more systematic studies and new theoretical models.

Finally, the couplings between electron and nuclear spins in **Cu-Smnt**^{P/d}_{0.01%} were investigated. ESEEM effects were found at S-, X- and Q-band frequencies (3.7, 9.7, 36.1 GHz). The modulations were attributed to weak couplings between the electron spin to ²H- and ¹⁴N-nuclear spins. These weak couplings were identified as one of the main coherence destroying sources in the previous experiments. CPMG-experiments at Q- and W-band were performed in order to eliminate those, leading to an increase by a factor of three in the phase memory times compared to standard Hahn echo decay experiments. The corresponding spin-lattice relaxation times are still orders of magnitude longer, displaying that other dominant influences on spin-spin relaxation are present in the system. In the course of the investigation in this thesis, these were identified to be mainly structural rigidity and three-dimensional ordering. In order to design MQBs with longer coherence times, these factors need to be eliminated.

Davies-ENDOR experiments at Q-band showed strong hyperfine coupling between the electron spin and ^{63,65}Cu nuclear spins in **Cu-Smnt**^{P/d}_{0.01%}. These couplings were exploited in first simple qubit manipulations and coherence transfer experiments. Rabi oscillations were detected for **Cu-Smnt**^P_{0.001%}, showing that even the protonated analogue of the target compound is in principle eligible as MQB. Nuclear spin transient nutations were performed with **Cu-Smnt**^{P/d}_{0.01%} as proof-

of-principle for coherence transfer between the electron and nuclear spin valve. With this experiment the potential applicability of **Cu-Smnt^{P/d}_{0.01%}** not only in quantum information processing, but also in quantum information storage scaffolds is demonstrated.

In conclusion, this thesis shows systematic pulsed EPR studies on potential MQBs, identifying the most dominant factors influencing electron spin dynamics. By systematic selection of the compounds, very long spin-lattice and phase memory times were found which are comparable to the record values for MQBs present in literature. It is shown, that individual measurements show mostly just one or only a few of several aspects to be considered. Systematic studies are helpful for rating various influences on electron spin dynamics.

Future work includes the investigation of potential MQBs and especially **Cu-Smnt^{P/d}_{0.01%}** in molecular monolayers or in quantum circuits, for which first steps were already performed.^[8]

Concerning theory, new models and formalisms are necessary to describe the relaxation mechanisms and processes in MQBs more precisely. Here also first steps were performed,^[9] hopefully paving the way for a quantitative understanding of electron spin relaxation in MQBs in the future.

1 Introduction

1.1 General Introduction

Since the very first days of computation heralded by Turing's machine and Zuse's Z1 in the early thirties of the last century, there has been a growing and still ongoing demand for faster, safer computation accompanied by smaller device dimensions. In the age of digital natives, the current technology is reaching limitations set by the fundamental physics behind classical computation. For example the further increase of magnetic data storage densities in classical devices is limited by the minimum domain size of magnetic particles which can maintain a stable magnetization. Similarly, a further speeding up of computation requires completely new working principles of data processing, because certain problems cannot be handled by a classical computer. In physical chemistry the reliable simulation of quantum mechanical behavior of complicated systems is not possible with current technology.^[10] Besides the needs for novel data processing methods, the improvement of encryption algorithms and secure information transmission is required by individual citizens and national administrations alike. A quantum computer could solve all these problems by employing a completely different working principle compared to current hard- and software. In contrast to classical bits, the smallest processing units of quantum computers (quantum bits or qubits) can not only be in the states $|0\rangle$ and $|1\rangle$, but also in arbitrary superpositions of these two states. Entanglement of N qubits leads to a 2^N -dimensional space of superposition states in which the quantum register can be simultaneously. In contrast, N classical bits form a register of N states, and a classical computer can be in only one of these at a certain point of time. These fundamental differences lead to the fact that quantum computers can solve certain computational problems much more efficiently compared to classical computers. Famous examples for that are the search of entries in large databases^[11] or the prime factorization of large numbers.^[12] Quantum cryptography offers a further advance as teleportation of entangled qubits would not allow unnoticed information tapping in contrast to state of the art classical encryption.

Qubits can in principle be implemented in any physical two-level system, as long as the DiVincenzo criteria are fulfilled.^[13] *Inter alia*, these state that the system must consist of well characterized, scalable qubits which can be initialized easily and efficiently. Another important criterion is the life time of the coherent superposition state (coherence time), which needs to be at least 10 000 times longer than the duration of an individual operation. Often the figure of merit, defined as the ratio of the coherence time and required operation time, is used as a quality measure for qubits. So far, a number of physical systems have been proposed for the implementation of qubits, including ion traps,^[14] superconducting circuits^[15] and electron spins.^[16] The last approach has the advantage that electron spins are relatively well protected from external influences and therefore do not dephase as rapidly as charge based qubits for example. An excellent realization of electron spin based qubits are Molecular Qubits (MQBs), which are paramagnetic coordination compounds.* The properties of MQBs can be synthetically tailored at will by employing the powerful, vast toolbox of synthetic chemistry.^[17] The term MQB is introduced to discriminate from purely inorganic electron spin qubits, such as nitrogen vacancy defect centers in diamond,^[18] Si:P^[19] or erbium(III)-doped CaWO₃.^[20] In such systems, the qubit distribution is largely random and poorly controllable. In contrast, MQBs can be arranged in ordered arrays, e.g. by molecular beam epitaxy or surface self-assembly, which creates spatially selective addressable qubits.^[21-22] Generally, in electron spin based qubits the coherence time can be approximated with the phase memory time of the electron spins, which can be detected conveniently by the well-established technique of pulsed electron paramagnetic resonance (EPR) spectroscopy. Before this project, only insufficiently short coherence times of a few microseconds have been published for MQBs,^[3-4] apart from very few exceptions.^[1-2] The data on influences on decoherence in these compounds is sparse and even textbook paragraphs dedicated to this topic are based on only a few exemplary studies.^[23] In order to find suitable MQBs, new design principles based on a detailed understanding of the influences on electron spin relaxation are needed.

* The term MQBs denotes any molecular paramagnetic species, which can be coordination compounds or organic radicals. Organic radicals are not studied in this thesis, because there is no g -value anisotropy. Differences of g -values in different qubits are needed to create selective addressability, which is another DiVincenzo-criterion.

1.2 Aims and Objectives

The aim of this thesis was to identify and classify factors influencing electron spin relaxation by systematic pulsed EPR studies in order to find new design principles for rational synthesis of MQBs with long phase memory times. A first objective of this dissertation was a careful literature research on existing MQBs and chemical factors influencing spin-lattice and spin-spin relaxation. Based on this knowledge, compounds for a systematic in-depth pulsed EPR investigation were chosen. These compounds will be introduced in the following paragraph. Subsequently, an extensive investigation of spin-lattice and spin-spin relaxation times of the selected compounds was performed. The comparison of pulsed EPR-measurements under the same physical conditions allowed a weighing of chemical influences upon spin dynamics. The investigation involved variations of central ions, ligands, counter ions as well as various sample matrices (disordered environment, i.e. glassy solution, versus structured environment, i.e. microcrystalline doped powders). Finally, the compound revealing the best qubit properties in the screening was selected for a detailed investigation of the impact of physical measurement conditions on electron spin relaxation behavior. To this end the magnetic field value, temperature, measurement frequency and pulse sequences were all varied to elucidate the relaxation mechanisms and processes in the selected target compound.

1.3 Investigated Systems and Experiments

This thesis focusses on electron spin relaxation processes in one-qubit systems consisting of mononuclear transition metal coordination compounds. There are only few systematic studies of influences on electron spin dynamics in general, so we chose to investigate simple MQB building blocks. Simple systems can be well described by theory, which should allow deeper insight into the complicated interplay of influences on electron spin relaxation processes.

Figure 1 graphically summarizes the compounds investigated in this dissertation. In the following, the selection criteria for the qubit building blocks (central ion, ligands, counter ions and matrix) will be outlined.

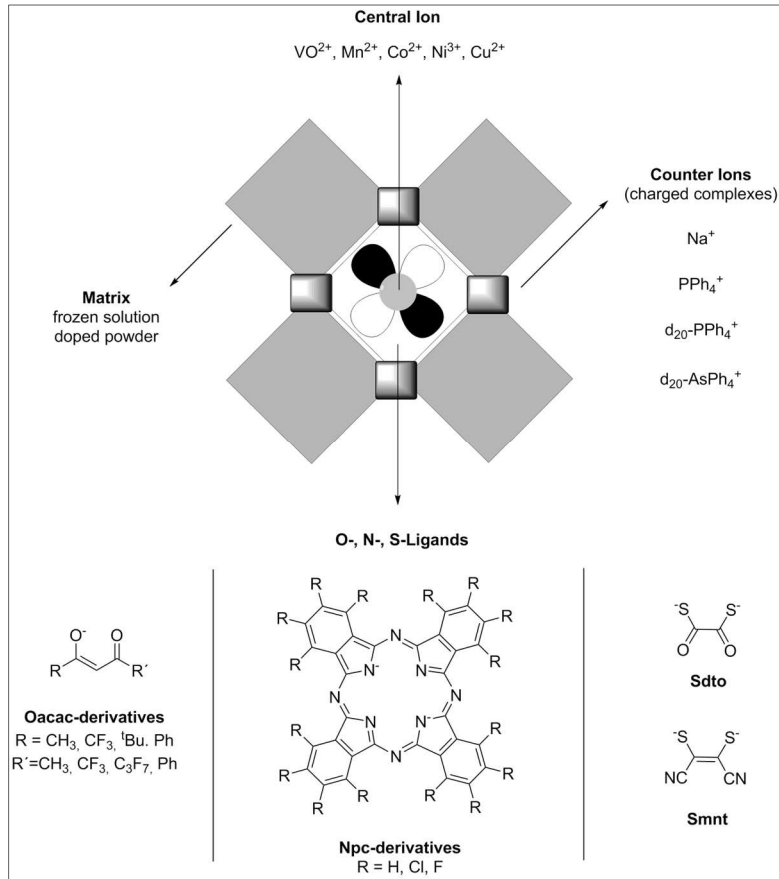


Figure 1: Overview investigated compounds. Ligands are abbreviated as Oacac (acetylacetonate), Npc (phthalocyanine), Sdto (1,2-dithiooxalate) and Smnt (maleonitrile-1,2-dithiolate).

The employed metal ion determines the magnitude of spin-orbit coupling (SOC), which in turn strongly influences spin-lattice relaxation (section 2.3.2). For example, decreasing spin-lattice relaxation times and increasing temperature dependencies of spin-lattice relaxation were found for increasing spin-orbit couplings.^[24-25] Hence low spin-orbit coupling values are favorable and therefore first-row transition metal ions were employed in this thesis. The oxidation state and crystal field of the selected transition metal ion determine the spin of the compound. For $S > 1/2$ a scattering processes in spin-lattice relaxation gain dramatically in efficiency (section 2.2.4), hence longer relaxation times are expected for $S = 1/2$ compounds. We chose to investigate VO²⁺, Mn²⁺, Co²⁺, Ni³⁺ and Cu²⁺ as central ions. This should allow the investigation of the influence of spin-orbit coupling for mainly, but not exclusively $S = 1/2$ compounds.

The coordination environment is another major influence on electron spin relaxation. Square-planar and octahedral coordination geometries are more rigid and therefore enable longer relaxation times compared to tetrahedral and other geometries.^[26] Different ligands possess

various vibrational modes which modulate spin-orbit coupling.^[24] Also the mobility of groups in the surrounding of the electron spin affects relaxation.^[25, 27] In all cases of investigated compounds in this thesis, square-planar, homoleptic coordination environments were chosen. Three groups of compounds were studied; namely those with N-, O- and S-donor ligands. The comparison of results from these three compound-groups should show influences on relaxation by altering the ligating atoms.

The influence of nuclear spins on electron spin relaxation is ambivalent. The critical parameter here is the coupling between the nuclear- and the electron spin. Weakly (dipolar) coupled nuclear spins in the qubit's environment are major contributors to decoherence in paramagnetically dilute conditions.^[28-30] Especially protons have a strong effect on dephasing due to their large magnetic moments compared to most other nuclei. Methyl groups can additionally decrease phase memory times because they are able to rotate via tunneling processes even at very low temperatures (section 2.3.2).^[3] In contrast to weakly coupled nuclear spins in the qubit's surrounding, a strongly (hyperfine) coupled nuclear spin, e.g. of the transition metal ion carrying the unpaired electron spin itself, was reported to have no discrete influence on dephasing under standard measurement conditions (i.e. as long as the applied field is large compared to the coupling).^[24-25, 31-32] Therefore, coordination complexes with nuclear spin-free ligands and counter ions in magnetically dilute environments are very promising qubits (nuclear spin-free MQBs).[†]

The chosen ligands for this dissertation are derivatives of acetylacetonate (Oacac), variously substituted phthalocyanines (Npc), maleonitrile-1,2-dithiolate (Smnt) and 1,2-dithiooxalate (Sdto). This range of ligands enables the comparison of compounds with a broad variety in ligand rigidity as well as number, nature and position of contained nuclear spins. Similarly, the employment of protonated and per-deuterated counter ions and other allows the investigation of the impact of number and kind of nuclear spins and variations in the crystal structure in the solid state on electron spin relaxation.

An investigation of the compounds in various matrices was carried out to probe the effect of the matrix surrounding of the complexes on electron spin dynamics. A disordered, glassy surrounding

[†] Elements with mainly $I = 0$ -isotopes (e.g. C, O, S) are regarded as nuclear spin-free within this thesis and in relevant literature. In addition, these elements can be isotopically purified in case of necessity.

was examined in dilute frozen solutions employing different solvents at concentrations of typically $< 0.001 \text{ mol}\cdot\text{l}^{-1}$. Here nuclear-spin-free and nuclear-spin-containing solvents were contrasted. Furthermore doped powders were examined, providing an ordered, rigid microcrystalline qubit arrangement. Paramagnetic species were doped at low concentrations (typically $\leq 0.01 \text{ mol}\%$) into an isostructural diamagnetic host lattice. For all compounds, spectra and relaxation measurements were recorded at one selected measurement frequency and temperature (7 K, Q-band: 35 GHz).

In addition to the above named chemical influences on relaxation, physical parameters also have important impact on spin dynamics. Effects known from literature and the underlying theoretical framework will be discussed in detail in chapter 2. In the present dissertation, the effects of physical parameters on electron spin relaxation were also probed. For this purpose, one target compound was chosen to perform experiments under a broad range of various conditions. Relaxation was studied from 1.5 K up to room temperature, the microwave frequency in the pulsed EPR experiments was varied from 2.7–330 GHz and also the orientation excited in pulsed measurements was varied. In addition to standard pulse sequences, also various advanced measurements were performed, such as ENDOR-, CPMG- and nutation experiments.

1.4 Organization of the Thesis

After the general introduction to the subject, aims and objectives in this first chapter, important theoretical principles will be presented in Chapter 2. A general introduction to EPR will be given, and electron spin relaxation theory as well as influences on spin dynamics will be covered in depth. Furthermore the employed experimental techniques will be presented. The Results and Discussion section in Chapter 3 is divided into sections on chemical and physical influences on electron spin relaxation, respectively. After a Conclusion in Chapter 4, the Experimental Section in Chapter 5 gives details on syntheses, measurements and data analysis.

2 Theoretical Background and Experimental Techniques

In this chapter, a general introduction to EPR and electron spin relaxation as well as influences on spin dynamics will be given, all focusing on solid state phenomena. For section 2.1, mainly the textbook of Schweiger and Jeschke^[23] and an EPR-lecture of Van Slageren^[33] served as helpful guidelines. The theoretical foundations discussed in section 2.2.1 are extensively explained in the book by Atherton^[34] and the NMR textbook by Levitt.^[35] For sections 2.2.2-2.2.3, the text books of Kevan and Schwartz,^[36] Schweiger and Jeschke^[23] and Kittel^[37] provided valuable resources and a book section by Eaton and Eaton^[3] contains a recommendable summary on mechanisms and influences of electron spin relaxation. In addition, the textbooks of Abragam and Bleaney^[38] as well as Misra^[39] were used for section 2.3. Furthermore, numerous journal papers were used as resources; they are cited at the relevant positions in the text.

2.1 Introduction to EPR

Electron paramagnetic resonance spectroscopy is a powerful tool for determining electronic and geometric structures as well as distances in species with at least one unpaired electron spin. Time-domain EPR allows furthermore the elucidation of chemical and molecular dynamics. The basic foundations of EPR are similar to those of nuclear magnetic resonance (NMR). However the development of instrumentation and methodology of EPR occurred mostly separately. Due to the lack of suitable, inexpensive experimental components for microwave bridges and electronics, the pioneering work of Mims in the 1960s only slowly gained broader interest. Nevertheless, today commercial EPR spectrometers are available at one to three digit Gigahertz operating frequencies. Furthermore a vast variety of elaborate pulse techniques such as ENDOR and DEER have become standard measurements in chemistry, biology, physics and also application-related fields such as materials and environmental science.

For a basic EPR experiment, a static magnetic field \vec{B}_0 must be applied to the paramagnetic sample. Spin transitions can then be induced by microwave radiation with a suitable frequency, which is discussed below.

The magnetic moment of an electron $\vec{\mu}$ is defined as

$$\vec{\mu} = -g \frac{e\hbar}{2m_e} \vec{S} = -g\mu_B \vec{S} \quad (1)$$

with the Landé-factor (or g -factor) g , the charge e and the mass m_e of an electron, the reduced Planck constant \hbar , the electron spin \vec{S} and the Bohr magneton μ_B . From equation (1), the gyromagnetic ratio γ_e of the electron spin can be derived:

$$\gamma_e = -\frac{|\vec{\mu}|}{\hbar|\vec{S}|} = -\frac{ge}{2m_e} = -\frac{g\mu_B}{\hbar} \quad (2)$$

The total spin \vec{S} of compounds with i unpaired electrons each possessing a spin of $\vec{s}_i = 1/2$ is given by:

$$\vec{S} = \sum_i \vec{s}_i \quad (3)$$

$$|\vec{S}| = \hbar\sqrt{S(S+1)} \quad (4)$$

where S is the total spin quantum number. Switching on an external, static magnetic field \vec{B}_0 fixes a preferential axis in space (conventionally, the direction of \vec{B}_0 is set to z) and the degeneracy of the $(2S+1)$ levels distinguished by the magnetic spin quantum number M_s is lifted (Zeeman effect). In other words, applying an external magnetic field leads to a fixing of the quantization axis of \vec{S} in space and the spin aligns towards \vec{B}_0 with the following projections on the z -axis, depending on the spin quantum number:

$$S_z = \hbar M_s \quad (5)$$

$$M_s = 0, \pm 1, \dots, \pm S \quad (6)$$

Due to the non-collinearity of $\vec{\mu}$ and \vec{B}_0 , the aligned electron spin experiences a torque \vec{T} :

$$\vec{T} = \vec{\mu} \times \vec{B}_0 \quad (7)$$

Effectively, the magnetic moment of the spin precesses around the external static magnetic field, where the precession frequency is called Larmor frequency ω_L :

$$\omega_L = 2\pi\nu_L = \frac{g\mu_B B_0}{\hbar} \quad (8)$$

Electromagnetic waves can induce spin state transitions in paramagnetic compounds in a static magnetic field, if the frequency of the irradiation matches the Larmor frequency. In order to calculate these transition energies, the Schrödinger equation for this problem has to be solved. Here the electron spin wave functions need to be considered:

$$|\psi_{el.spin} \rangle = |SM_s \rangle \quad (9)$$

Furthermore a Hamiltonian considering the treated electron-spin Zeeman interaction is needed:

$$\hat{H}_{el,Zeeman} = \mu_B \vec{B}_0 \mathbf{g} \hat{S} \quad (10)$$

The principal axis of \mathbf{g} are usually assumed to be aligned with the molecular coordinate frame. An isotropic \mathbf{g} -tensor is characterized by $g_{xx} = g_{yy} = g_{zz}$, an axial one by $g_{xx} = g_{yy} = g_{\perp} \neq g_{zz} = g_{\parallel}$ and a rhombic \mathbf{g} -tensor by $g_{xx} \neq g_{yy} \neq g_{zz}$. The differences in the expected EPR spectra are depicted in Figure 2.

The value of the free-electron g -factor is 2.0023 but in actual compounds deviations occur due to spin-orbit coupling. If a degenerate electronic ground state exists, an orbital angular momentum can be present. In most organic radicals and transition metal complexes, the orbital angular momentum is quenched in the electronic ground state. However, spin-orbit coupling can account for a mixing of excited states and the ground state, resulting in orbital angular momentum.

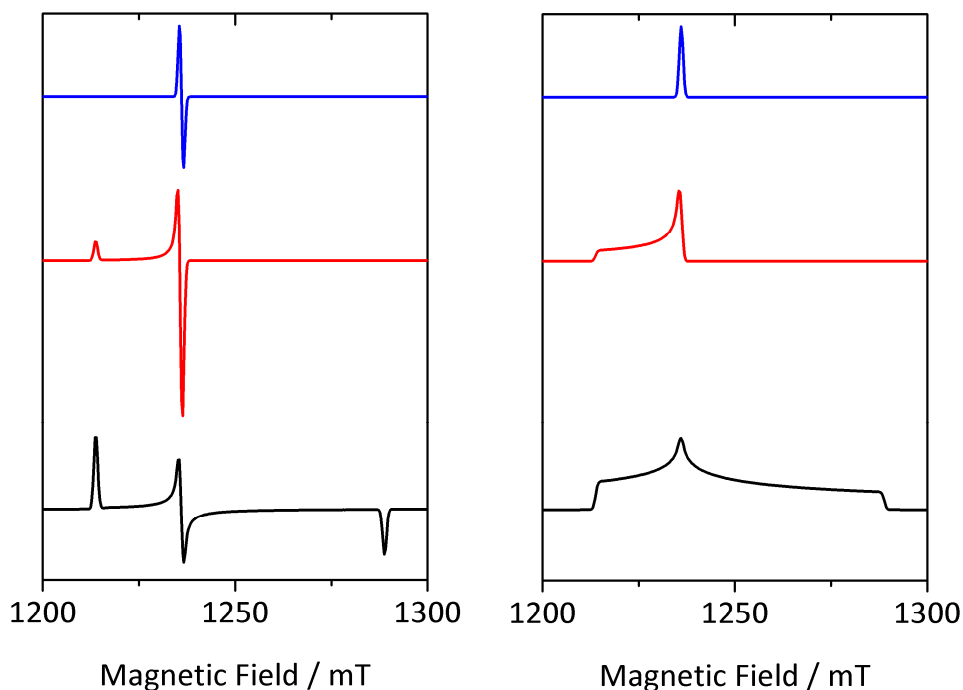


Figure 2: Visualization of various \mathbf{g} -tensor forms. From top to bottom, isotropic, axial and rhombic \mathbf{g} -tensors were simulated. The left panel shows the first derivative of the absorption, which is usually detected in cw EPR due to field modulation. The right panel the absorption spectra, as typically detected in pulsed EPR. Simulation parameters were $\mathcal{G}_{isotropic} = [2.023]$, $\mathcal{G}_{axial} = [g_{\perp} \ g_{\parallel}] = [2.023 \ 2.060]$ and $\mathcal{G}_{rhombic} = [g_{xx} \ g_{yy} \ g_{zz}] = [1.940 \ 2.023 \ 2.06]$ and in all cases a homogenous linewidth of 1 mT, microwave frequency of 35 GHz was assumed.

Covalency of coordination bonds generally decreases of spin-orbit coupling. The corresponding spin-orbit coupling Hamiltonian for both scenarios is:

$$\hat{H}_{SOC} = \lambda \hat{L} \hat{S} \quad (11)$$

with the orbital angular momentum operator \hat{L} and the spin-orbit coupling constant λ .

The usage of the electron spin Zeeman Hamiltonian in equation (10) is adequate for $L = 0$. The corresponding eigenvalue equation for this problem with the external magnetic field in z -direction leads to the following electron spin Zeeman energies:

$$E_{el.Zeeman} = M_s g \mu_B B_0 \quad (12)$$

Due to the conservation of angular momentum, a photon can only induce transitions according to the selection rule

$$\Delta M_s = \pm 1 \quad (13)$$

The corresponding transition energy is:

$$\Delta E_{el.Zeeman} = g \mu_B B_0 \quad (14)$$

If the resonance condition

$$\Delta E_{el.Zeeman} = h \nu_{MW} \quad (15)$$

is fulfilled, a change of spin state is induced. In the case of electron spins, for convectional magnetic field strengths typically microwave (MW) energies are required. Among other factors, the intensities of resonance lines are proportional to the population differences between the relevant states, determined by the Boltzmann distribution. For $M_s = \pm 1/2$ states, the population ratio is:

$$\frac{N_{1/2}}{N_{-1/2}} = \exp\left(-\frac{g \mu_B B_0}{k_B T}\right) \quad (16)$$

with the Boltzmann constant k_B and the temperature T . This ratio is very small for 1000 mT and room temperature (0.999) but still quite large compared to the NMR-population difference at the same field (0.99999), showing the higher sensitivity of EPR. Furthermore one can see from Equation (16) that lower temperatures will lead to higher population differences, i.e. larger signal intensities. Lower temperatures are also favorable because they lead to slower spin dynamics, as we will see later on.

EPR resonance lines can exhibit homogeneous or inhomogeneous broadening. The linewidth is usually given as the full width at half maximum (FWHM) of a Lorentzian resonance line. If a set

of spins has the same Hamiltonian parameters and is exposed to the same time average of local magnetic fields, the lineshape for each individual spin is the same. In effect the spin packet shows a homogeneously broadened line which can be described by a Lorentzian function. In the absence of MW power saturation this homogeneous linewidth is proportional to the inverse of the phase memory time. The origin of homogeneous line-broadening is the energy-time uncertainty, as energy levels are blurred by the finite excited state lifetime.

Inhomogeneous line broadenings arise due to distributions in Larmor frequencies, which lead to the existence of several spin packets. Usually a Gaussian lineshape is obtained due to a Gaussian distribution of parameters. These parameter distributions could be due to inhomogeneity of the external static magnetic field, unresolved interactions such as hyperfine- (see in the following), dipolar- or exchange interactions with other magnetic centers as well as anisotropic interactions (e.g. electron Zeeman-, hyperfine interaction) in randomly distributed solid state systems.

So far only contributions to the Hamiltonian from the electron Zeeman interaction were considered. In most cases, this approximation is not precise enough to reproduce experimental results. Often nuclear spins are present in the investigated systems and must be considered for correct determination of energy levels. Nuclear spins also experience a Zeeman effect in an external magnetic field and can undergo a (super)hyperfine interaction with an electron spin (SHF, HF). The nuclear Zeeman effect can be treated analogously to the electron Zeeman effect and leads to similar equations (see further below). The hyperfine interaction between one type of electron- and one type of nuclear spin can be described in general by the following Hamiltonian:

$$\hat{H}_{HF} = \hat{I} \mathbf{A} \hat{S} \quad (17)$$

with the hyperfine coupling tensor \mathbf{A} and the nuclear spin operator \hat{I} . The hyperfine interaction consists of the isotropic or Fermi contact interaction and the electron-nuclear dipole-dipole coupling, so \hat{H}_{HF} can also be written as the sum of these two components. The spin-only electron-nuclear dipole-dipole interaction Hamiltonian \hat{H}_{DD} is

$$\hat{H}_{DD} = \hat{I} \mathbf{T}_{DD} \hat{S} \quad (18)$$

where \mathbf{T}_{DD} designates the dipolar coupling tensor. Considering a point-dipole and an isotropic g -value, the diagonal dipolar coupling tensor \mathbf{T}_{DD}^d is approximated by:^[40]

$$\mathbf{T}_{DD}^d = \frac{g_e \mu_B g_N \mu_N}{hr^3} \begin{pmatrix} -1 & & \\ & -1 & \\ & & 2 \end{pmatrix} \quad (19)$$

where r describes the distance between the electron-spin point dipole and the coupling nucleus. For rough calculations this equation is also valid for small g -anisotropies.

The Hamiltonian for the magnetic field in z-direction regarding the electron- and nuclear Zeeman effect (nuc,Zeeman) as well as a hyperfine coupling according to equation (17) is:

$$\hat{H}_{0,z} = \hat{H}_{el,Zeeman} + \hat{H}_{nuc,Zeeman} + \hat{H}_{HF} = \mu_B \vec{B}_0 \mathbf{g} \hat{S} - \mu_N \vec{B}_0 \mathbf{g}_N \hat{I} + \hat{I} \mathbf{A} \hat{S} \quad (20)$$

with the nuclear g -tensor \mathbf{g}_N and the nuclear magneton μ_N . This Hamiltonian can be applied to the product wave functions:

$$|\psi_{el,nuc\ spin} \rangle = |SM_s IM_I \rangle \quad (21)$$

with the nuclear spin quantum number I and the magnetic nuclear spin quantum number M_I . The effect of the Hamiltonian in equation (20) is a further splitting of energy levels according to the energy eigenvalues

$$E_{0,z} = M_S \mathbf{g} \mu_B B_0 - M_I \mathbf{g}_N \mu_N B_0 + \mathbf{A} M_S M_I \quad (22)$$

which is illustrated in Figure 3. For $A \ll g \mu_B B_0$, only transitions with $\Delta M_s = \pm 1$, $\Delta M_I = 0$ are allowed.

The number of lines N in the hyperfine split EPR signal can be calculated according to:

$$N = \prod_i (2n_i I_i + 1) \quad (23)$$

where i denotes groups of n_i equivalent nuclei with the nuclear spin quantum number I_i . The intensity distribution within a hyperfine multiplet for $S = 1/2$ follows Pascal's triangle, where the row of the triangle is given by n_i . Similarly to g -tensors, the hyperfine interaction can be anisotropic, which can be observed in randomly oriented solid state systems. So \mathbf{A} can also be isotropic, axial or rhombic. Nuclear spins with a nuclear spin quantum number $I > 1/2$ furthermore possess quadrupole moments which can also alter the energy levels of the system. Usually these quadrupole interactions are weak and mostly only resolved in systems with very sharp lines, such as single crystals.

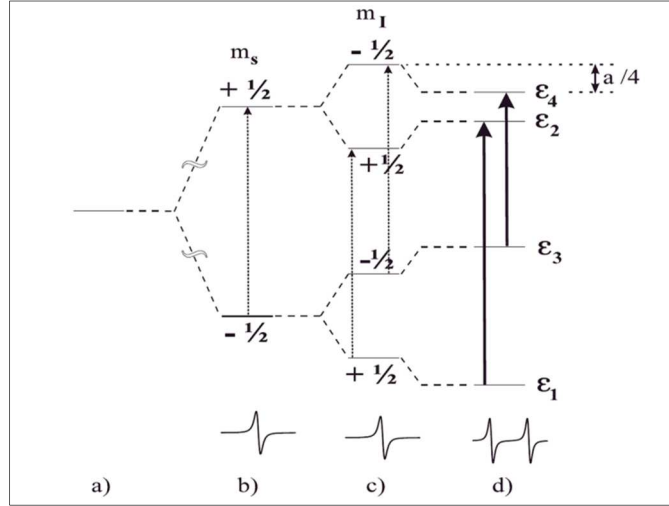


Figure 3: Schematic energy level diagram.^[41] a) Energy levels for an $S = 1/2$ system without external magnetic field. b) Energy levels for an $S = 1/2$ system in an external magnetic field considering the electron spin Zeeman effect, bottom: corresponding EPR response. c) Energy levels for an $S = 1/2, I = 1/2$ -system in an external magnetic field considering electron- and nuclear spin Zeeman effect, bottom: corresponding EPR response. d) Energy levels for an $S = 1/2, I = 1/2$ -system in an external magnetic field considering electron- and nuclear spin Zeeman effect as well as hyperfine coupling, bottom: corresponding EPR response.

For $S > 1/2$ systems further effects can be present in EPR such as zero-field splitting or exchange coupling. In this thesis, mostly $S = 1/2$ -systems were investigated, so these effects are not treated in detail here. Finally dipole-dipole couplings among electron spins and between electron- and nuclear spins can lead to spectral changes. The former was avoided in the performed experiments by investigating only paramagnetically dilute samples. The latter interaction is usually too small to be resolved in standard EPR experiments, but can be observed in more sophisticated experiments such as ENDOR or ESEEM (see later).

2.2 Electron Spin Relaxation Theory

2.2.1 Classical Relaxation Theory

Standard EPR experiments do not detect single spins but a macroscopic magnetization \vec{M} . In thermal equilibrium, the magnetization of N spins in a volume V is defined as

$$\vec{M}_0 = \frac{1}{V} \sum_{i=1}^N \vec{\mu}_i \quad (24)$$

In thermal equilibrium, the magnetization has a positive component along z . The x - and y -components are both zero, because the individual spins precess with a homogeneous distribution of phases, i.e. the transverse components cancel each other out. So in thermal equilibrium, the

magnetization is constant and a torque perpendicular to \vec{M} is present. We can write for the equation of motion of the magnetization:

$$\frac{d\vec{M}}{dt} = \gamma \vec{M} \times \vec{B}_0 \quad (25)$$

This induces a precession of the magnetization around the z -axis with Larmor frequency as introduced in equation (8). If the system is not in thermal equilibrium, relaxation effects have to be considered in addition to this precession. The phenomenological Bloch equations take this into account with the longitudinal (or spin-lattice-) relaxation time T_1 and the transverse (or spin-spin-) relaxation time T_2 :

$$\begin{aligned} \frac{dM_x}{dt} &= \gamma B_0 M_y - \frac{M_x}{T_2} \\ \frac{dM_y}{dt} &= -\gamma B_0 M_x - \frac{M_y}{T_2} \\ \frac{dM_z}{dt} &= \frac{M_0 - M_z}{T_1} \end{aligned} \quad (26)$$

The longitudinal relaxation describes the returning of the longitudinal magnetization component to its thermal equilibrium value involving an energy exchange with the surrounding lattice, whereas transverse relaxation describes the entropy gain by dephasing of the spins.

Irradiation with microwave radiation, where the magnetic field component \vec{B}_1 of the microwave is perpendicular to \vec{B}_0 leads to a tilting of the magnetization. For a circularly polarized microwave, the oscillating magnetic field component \vec{B}_1 as a function of time t can be described with:

$$\begin{aligned} B_{1,x}(t) &= B_1 \cos(\omega_{MW}t) \\ B_{1,y}(t) &= B_1 \sin(\omega_{MW}t) \\ B_{1,z}(t) &= 0 \end{aligned} \quad (27)$$

In here, B_1 describes the amplitude of the magnetic component of the electromagnetic radiation. The Bloch equations in an external static magnetic field and with applied MW radiation introducing a time-dependent magnetic field are:

$$\begin{aligned} \frac{dM_x}{dt} &= \gamma(B_0 M_y - B_1 \sin \omega_{MW}t M_z) - \frac{M_x}{T_2} \\ \frac{dM_y}{dt} &= \gamma(B_1 \cos \omega_{MW}t M_z - B_0 M_x) - \frac{M_y}{T_2} \\ \frac{dM_z}{dt} &= \gamma(B_1 \sin \omega_{MW}t M_x - B_1 \cos \omega_{MW}t M_y) + \frac{M_0 - M_z}{T_1} \end{aligned} \quad (28)$$

Equations (28) can be simplified by introducing a right-hand sense rotating coordinate frame which rotates with ω_{MW} about the z-axis of the former one (laboratory frame). \vec{B}_1 will be time-independent in this rotating frame (coordinates x', y' and $z' = z$). The Bloch equations in the rotating frame considering a static magnetic field, an oscillating magnetic field introduced by the MW irradiation as well as relaxation effects are:

$$\begin{aligned}\frac{dM_{x'}}{dt} &= -\omega_{offset}M_{y'} - \frac{M_{x'}}{T_2} \\ \frac{dM_{y'}}{dt} &= \omega_{offset}M_{x'} + \gamma B_1 M_{z'} - \frac{M_{y'}}{T_2} \\ \frac{dM_{z'}}{dt} &= -\gamma B_1 M_{y'} + \frac{M_0 - M_{z'}}{T_1}\end{aligned}\quad (29)$$

Here an offset frequency $\omega_{offset} = \omega_L - \omega_{MW}$ between the Larmor frequency ω_L and the microwave frequency ω_{MW} is taken into account. The solutions of the Bloch equations (29) without MW irradiation ($B_1 = 0$) and for $t > 0$ are:

$$\begin{aligned}M_{x'} &= M_0 \exp(-t/T_2) \\ M_{y'} &= 0 \\ M_{z'} &= M_0[1 - \exp(-t/T_1)]\end{aligned}\quad (30)$$

In pulsed EPR, signals are usually recorded employing quadrature-detection, which corresponds to a phase-sensitive detection in the rotating frame. Therefore, a back-transformation to the laboratory coordinate frame is usually not required. In real experiments, not the pure spin-spin relaxation time T_2 is detected, but rather the phase memory time T_M . The latter is shorter than the former and contains additional influences (see below).

For relaxation under microwave irradiation, the full Bloch equations (29), i.e. equations of motion for the magnetization vector under microwave irradiation and in a static magnetic field, must be considered. The superposition of a precession with ω_{offset} around z' and the precession about \vec{B}_1 with the Rabi frequency ω_1 results in a nutation of the magnetization vector about an effective field which is tilted away from z' by

$$\theta = \arctan\left(\frac{\omega_1}{\omega_{offset}}\right)\quad (31)$$

and the nutation frequency is

$$\omega_{nut} = \sqrt{\omega_{offset}^2 + \omega_1^2}\quad (32)$$

From equation (31) it is obvious that the angle θ vanishes in the resonance case ($\omega_{MW} = \omega_L$) and the solutions of equations (29) then describe a precession of the magnetization around \vec{B}_1 . If the microwave irradiation is stopped, the system relaxes into the thermal equilibrium state, as previously described.

2.2.2 *Semi-Classical Relaxation Theory*

The previously introduced classical relaxation theory within the framework of the phenomenological Bloch equations is valid for a description of macroscopic magnetization relaxation processes. For a more precise description and quantitative calculations, the quantum mechanical nature of the individual spins needs to be considered and a more elaborate theoretical treatment is necessary. One approach for this is the description of relaxation processes with a semi-classical relaxation theory. Here magnetic field fluctuations are considered to be the origin of relaxation and the Bloch equations are expressed by the means of density matrices. The density matrix formalism is a widely used tool in statistical quantum mechanics. It allows the calculation of ensemble averages without knowing the wave functions of the system. The ensemble average for an arbitrary operation \hat{O} is defined as

$$\langle \bar{O} \rangle = \langle \overline{\psi | \hat{O} | \psi} \rangle = \sum_{k,j} \overline{c_k c_j^*} \langle \Phi_j | \hat{O} | \Phi_k \rangle = \sum_{k,j} \overline{c_k c_j^*} \langle \Phi_j | \hat{O} | \Phi_k \rangle \quad (33)$$

here the wave function ψ has been expanded in terms of coefficients c and basis functions Φ , other symbols and notations have their usual meanings. The equation can be solved independently from the basis functions with the help of the density matrix ρ and the density matrix operator $\hat{\rho}$:

$$\rho = \langle k | \hat{\rho} | j \rangle = \overline{c_k c_j^*} \quad (34)$$

The diagonal elements of the density matrix indicate the fractional populations of the states. For an orthogonal set of basis functions, the ensemble average can be rewritten as

$$\langle \bar{O} \rangle = \sum_{k,j} \langle k | \hat{\rho} | j \rangle \langle \Phi_j | \hat{O} | \Phi_k \rangle = \text{Trace} \{ \hat{\rho} \hat{O} \} \quad (35)$$

In order to find $\hat{\rho}$, the Liouville-von Neumann equation (or equation of motion of the density matrix operator) needs to be solved:

$$\frac{d\rho}{dt} = \frac{i}{\hbar} [\hat{\rho}, \hat{H}] \quad (36)$$

For relaxation problems, only time-dependent contributions in equation (36) to the Hamiltonian have to be considered. For an $S = 1/2$ -system in a static magnetic field, relaxation is assumed to be caused by magnetic field fluctuations and the corresponding Hamiltonian is:

$$\hat{H} = g\mu_B B_0 \hat{S}_z + g\mu_B \sum_q B_q(t) \hat{S}_q \quad (37)$$

where $q = x, y$ or z . A quantum mechanical calculation of the magnetic field fluctuations $B_q(t)$ is difficult and only possible for systems with well-known eigenstates. For simplification, correlation functions for these fluctuations are calculated classically (semi-classical relaxation theory). In order to do so, one needs to think about the relevance of possible fluctuations for spin relaxation. Here the time-scale of the fluctuation is crucial: processes which are much faster or much slower than the relaxation time have no effect on spin relaxation. Processes on the spectral timescale (which is the inverse of the width of the spectrum in terms of frequencies) only affect the spectral lineshape, but have no effect on spin relaxation. Magnetic field fluctuation processes with rates comparable to the Larmor frequency influence relaxation.[‡] For $S > 1/2$ -systems also electric quadrupole couplings need to be considered. The origins of magnetic field fluctuations on the Larmor timescale in solids are thermal motional processes such as local rotations, molecular vibrations and librations. The latter are small angle vibrations with main direction perpendicular to the corresponding bond, typically only around $\pm 15^\circ$. If the fluctuation frequency matches the transition energy of the spin system, a spin flip is induced.

Within this theoretical approach, the magnetic field fluctuations are assumed to be spin-independent and to emanate from an external source. For simplicity, only 1D-fluctuations are considered. The relaxing spins experience small, individual transverse field fluctuations which are unrelated to each other but have the same general timescale and amplitude. So an auto-correlation function $G(\tau)$ can be set up, defining the rate of field fluctuations.

$$G(\tau) = \langle B_x(t) B_x(t + \tau) \rangle \quad (38)$$

The time τ defines the point of comparison to the time point t for the fluctuations. The fluctuating fields are assumed to be independent from t (stationary assumption) and zero in average, the magnitude of the fluctuations is defined by the mean square of the fluctuating field,

[‡] Processes on the experimental timescale in pulsed EPR-experiments also have a strong influence on electron spin relaxation. This is not considered in the semi-classical relaxation theory, but will be covered in the following sections.

which is non-zero. For large τ the auto-correlation function tends towards zero. The auto-correlation function can be approximated by a simple exponential and the mean square of field fluctuations along the x-direction $\langle B_x^2 \rangle$:

$$G(\tau) = \langle B_x^2 \rangle \exp\left(-\frac{|\tau|}{\tau_c}\right) \quad (39)$$

The correlation time τ_c indicates the average time between signal changes of the randomly fluctuating field. The correlation time depends on physical parameters such as the temperature of the system.

Fourier-transformation of equation (39) leads to the spectral density $J(\omega)$:

$$J(\omega) = 2 \int_0^\infty G(\tau) \exp(-i\omega\tau) d\tau = 2 \langle B_x^2 \rangle \frac{\tau_c}{1+\omega^2\tau_c^2} \quad (40)$$

which describes the transition probability at the frequency ω . Note that short correlation times or in other words rapid fluctuations lead to broad spectral densities and vice versa. Quantum mechanically speaking, a fluctuating field transfers a spin in state $|\alpha\rangle$ at the time t into a superposition state of $|\alpha\rangle$ and $|\beta\rangle$ at the time $t + \tau$. The notation follows the usual conventions: $|\alpha\rangle$ assigns a spin with $m_s = +1/2$ and $|\beta\rangle$ one with $m_s = -1/2$.

By finding now an expression for the transition probabilities W_\pm considering the thermal equilibrium populations:

$$W_\pm = W \left(1 \pm \frac{1}{2} \frac{\hbar\gamma B_0}{k_B T}\right) \quad (41)$$

with the mean transition probability W :

$$W = \frac{1}{4} \gamma^2 J(\omega_L) = \frac{1}{2} \gamma^2 \langle B_x^2 \rangle \frac{\tau_c}{1+\omega_L^2\tau_c^2} \quad (42)$$

the rate of population change can be written as

$$\frac{d}{dt} \rho_\alpha = -W_- \rho_\alpha + W_+ \rho_\beta \quad (43)$$

and similarly for $\frac{d}{dt} \rho_\beta$. This is needed, as for relaxation a time derivation of the magnetization

$$M_z = \left(\frac{\hbar\gamma B_0}{k_B T}\right)^{-1} (\rho_\alpha - \rho_\beta) \quad (44)$$

has to be calculated. The outcome of that is

$$M_z(t) = M_z(0) [1 - \exp(-2W\tau)] \quad (45)$$

By comparison of exponents of equations (45) and (30), bottom, it can be seen that

$$T_1^{-1} = 2W = \gamma^2 \langle B_x^2 \rangle \tau_c / [1 + (\omega_L \tau_c)^2] \quad (46)$$

The influence of varying mean squares of the fluctuating fields on spin-lattice relaxation time is visualized in Figure 4.

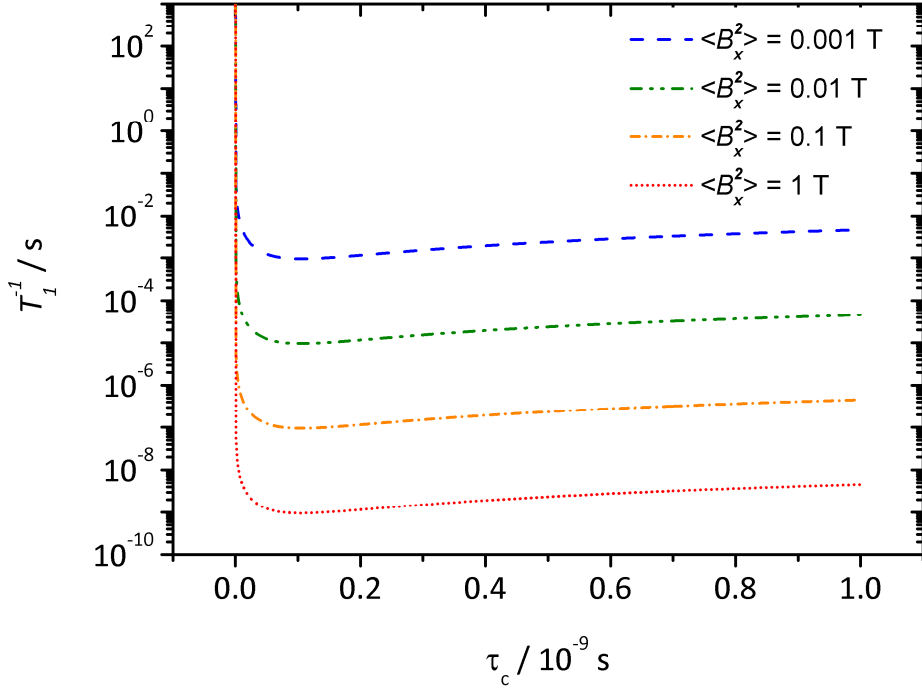


Figure 4: Graphical representation of equation (46). An $S = 1/2$ -system with $g = 2$ and a Larmor frequency of 9.47 GHz was used for the visualization and fluctuating magnetic fields as indicated in the legend.

Equation (46) describes relaxation of spins due to randomly fluctuating fields. So far the influence of other spins, e.g. nuclear spins, was neglected. Other nuclear and electron spins influence the fluctuating fields and vice versa. In a weakly dipolar coupled spin system of two types of electron spins 1 and 2, relaxation pathways via zero-, single- and double quantum transitions (W_0, W_1, W_2) are possible, as depicted in Figure 5.

An equation of motion considering all these relaxation possibilities is the Solomon equation:

$$\frac{d}{dt} \begin{pmatrix} \langle \hat{S}_{1z} \rangle \\ \langle \hat{S}_{2z} \rangle \end{pmatrix} = \begin{pmatrix} -R_{auto} & R_{cross} \\ R_{cross} & -R_{auto} \end{pmatrix} \begin{pmatrix} \langle \hat{S}_{1z} \rangle - \langle \hat{S}_{1z} \rangle^{eq} \\ \langle \hat{S}_{2z} \rangle - \langle \hat{S}_{2z} \rangle^{eq} \end{pmatrix} \quad (47)$$

where R_{auto} describes the leakage rate or auto relaxation rate constant:

$$R_{auto} = W_0 + 2W_1 + W_2 \quad (48)$$

and R_{cross} denotes the cross-relaxation rate:

$$R_{cross} = W_0 - W_2 \quad (49)$$

A solution considering spectral density descriptions of transition probabilities leads to analytical expressions for longitudinal and transverse relaxation rates. This dipole-dipole relaxation scheme only considers one-dimensional field fluctuations.

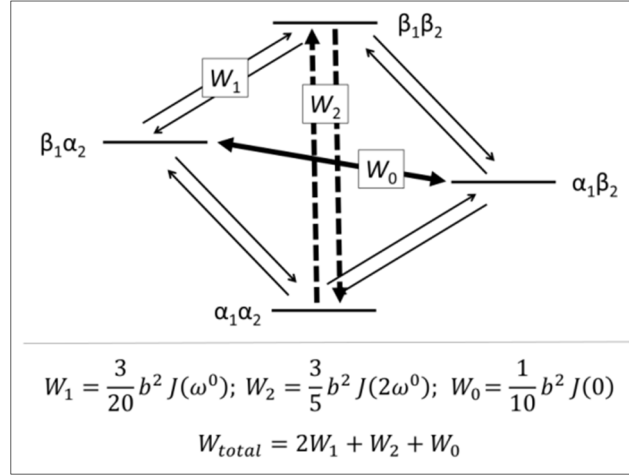


Figure 5: Possible relaxation pathways in a weakly dipolar coupled spin system of spins 1 and 2. Bottom lines indicate corresponding transition probabilities for individual paths and total relaxation probability W_{total} .

For a full, three-dimensional description the Redfield equation has to be considered:

$$\frac{d\rho_{\alpha\alpha'}(t)}{dt} = \frac{i}{\hbar} [\rho(t), \hat{H}_0] + \sum_{\beta\beta'} R_{\alpha\alpha'\beta\beta'} \{ \rho_{\beta\beta'}(t) - \rho_{\beta\beta'}^0 \} \quad (50)$$

Here an expanded Hamiltonian is applied:

$$\hat{H} = \hat{H}_0 + \hat{H}(t) + \varepsilon(t) \quad (51)$$

including contributions of the lattice in the static Hamiltonian \hat{H}_0 , time-dependent contributions $\hat{H}(t)$ and the effect $\varepsilon(t)$ of the microwave field on the spins. In the Redfield equation, $R_{\alpha\alpha'\beta\beta'}$ are the elements of the relaxation matrix of two spins with the states denoted by α and α' , β and β' , while $\rho_{\beta\beta'}^0$ represents the thermal equilibrium values of the density matrix elements. Equation (50) is valid within the limitation $\omega_L^2 \tau_c^2 \ll 1$.

Under exclusion of the microwave field from the analysis and assuming the absence of a correlation between the components of the fluctuating fields, solving the Redfield equation yields for the spin-lattice relaxation time

$$\frac{1}{T_1} = \left(\frac{g\mu_B}{\hbar}\right)^2 (\langle B_x^2 \rangle + \langle B_y^2 \rangle) \frac{\tau_c}{1 + \omega_L^2 \tau_c^2} \quad (52)$$

and for the spin-spin relaxation time

$$\frac{1}{T_2} = \left(\frac{g\mu_B}{\hbar}\right)^2 \langle B_z^2 \rangle \tau_c \quad (53)$$

From (52) and (53) it can be seen, that components of the fluctuating field which are perpendicular to \vec{B}_0 and fluctuate at ω_0 induce spin-state transitions while fluctuations parallel to \vec{B}_0 lead to dephasing of the spins.

Outside the Redfield limit ($\omega_L^2 \tau_c^2 \ll 1$; for slow oscillations, high frequencies), T_2' is obtained:

$$\frac{1}{T_2'} = \frac{1}{T_2} + \frac{1}{2T_1} = \left(\frac{g\mu_B}{\hbar}\right)^2 \left[\langle B_z^2 \rangle \tau_c + \frac{1}{2}(\langle B_x^2 \rangle + \langle B_y^2 \rangle) \frac{\tau_c}{1+\omega_L^2 \tau_c^2} \right] \quad (54)$$

showing that besides spin-spin relaxation, also spin-lattice relaxation is a limiting factor towards the phase memory time. Figure 6 shows increasing relaxation times for decreasing τ , until they become equal in the extreme narrowing limit, where the mean square of all components of the fluctuation field is assumed to be equal to $\langle B^2 \rangle$:

$$\frac{1}{T_1} = 2 \left(\frac{g\mu_B}{\hbar}\right)^2 \langle B^2 \rangle \tau_c = \frac{1}{T_2} \quad (55)$$

If microwave irradiation is present, the spins have other dynamics than described in equations (52)-(55). Relaxation in the rotating frame considers this; here the x' -direction (propagation direction of the microwave) acts as quantization axis and dressed electron spin states have to be considered. The rotating-frame relaxation $T_{1\rho}$ is determined by ω_1 (and not by ω_L) and is close to the spin-lattice relaxation of the system:

$$\frac{T_2}{2} < T_{1\rho} \leq T_1 \quad (56)$$

Even for simple systems, rotating-frame relaxation is a difficult subject and an active area of research.

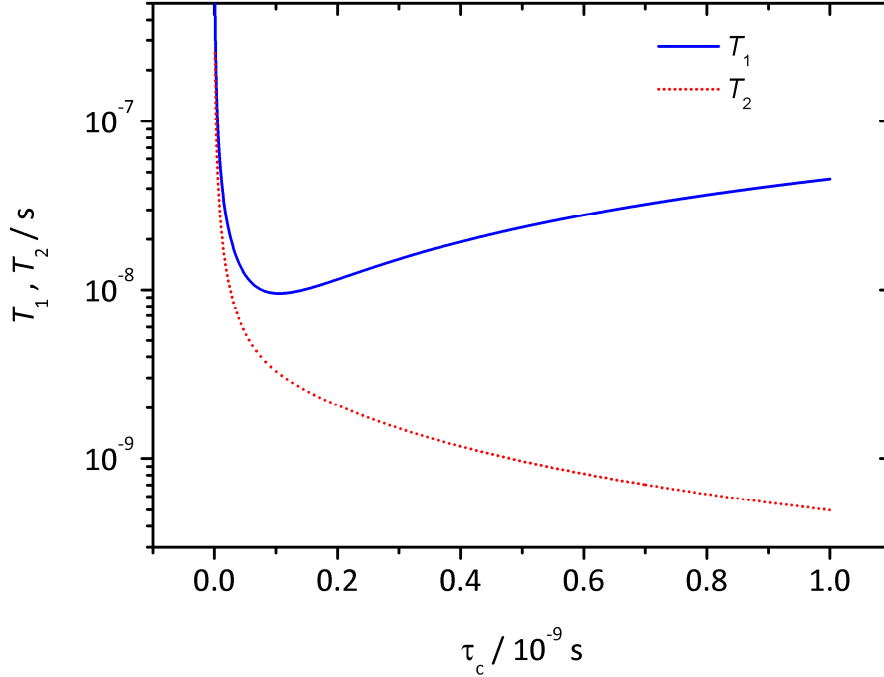


Figure 6: Graphical representation of equations (52)-(53). An $S = 1/2$ - system with $g = 2$ and a Larmor frequency of 9.47 GHz and $\langle B_x^2 \rangle = 0.1$ T was used for the visualization.

2.2.3 Spin-Spin Relaxation Theory

Spin-spin relaxation theory is established on the semi-classical relaxation theory based on the fluctuating field approach introduced in the previous section. Prior to a discussion of spin-spin relaxation theory, the different effects of fluctuating magnetic field on spin-lattice and spin-spin relaxation should be pointed out once again. Magnetic field components perpendicular to the static magnetic field, which fluctuate at Larmor frequency lead to spin state changes, i.e. spin-lattice relaxation. This involves an energy transfer between the spin system and the lattice. If this energy exchange is very fast, spin-lattice relaxation will limit spin-spin relaxation. However, very often spin-lattice relaxation is much slower than spin-spin relaxation and therefore a separate discussion of spin-spin relaxation theory is important. Spin-Spin relaxation is induced by magnetic fields which fluctuate parallel to the static magnetic field. These fluctuations cause a blurring of the energy levels or in other words, variations of the Larmor frequency, which lead to dephasing of the spins. For fluctuation frequencies which are comparable to the Larmor frequency, a theoretical description according to the previously introduced semi-classical relaxation theory applies. Besides these bath-fluctuations, other processes on the timescale of the experiments employed for detecting electron spin relaxation times (section 2.4.2) have to be considered. By the means of pulsed EPR, spin-spin relaxation times are usually detected by monitoring the spin echo decay. Typically, the experimental timescale in pulsed EPR is typically around a few hundred nanoseconds up to some microseconds, whereas the inverse Larmor frequency is in the range of some hundred picoseconds at applied static magnetic fields of a few hundred millitesla. On the longer experimental timescale, various diffusion processes can lead to dephasing of electron spins. Spin-lattice relaxation can also be influenced by these diffusion processes. Experimentally, a vast variety of spin echo decay shapes can be observed, depending on the active diffusion processes. These will be reviewed in the subsequent paragraphs.

For a classification of relaxation inducing diffusion processes, A- and B-spins are distinguished. For transition metal compounds, the excitation bandwidth (see section 2.4.2) is usually smaller than the spectral width. A-spins represent the excited spins, whereas spins outside the excitation window are called B-spins. Diffusion processes can be divided into A-A interactions (instantaneous diffusion) and A-B interactions (spectral diffusion, cross relaxation and spin

diffusion). Due to these various types of dephasing processes, a vast variety of echo decay shapes can be experimentally detected as mentioned above. Furthermore, various time constants can be observed. The terminology strongly depends on the consulted literature, in here the following will be used: the pure spin-spin relaxation time will be denominated T_2 , whereas the inverse width of a dipolar broadened spin-packet is $(\Delta\omega_{dip})^{-1}$. T_f is used for the mean electron spin-spin flip time and T_M describes the experimentally determined dephasing time (phase memory time). The pure spin-spin relaxation time T_2 cannot be detected experimentally. For low concentrations of spins, the relation of experimentally detectable spin-spin relaxation times usually is:

$$(\Delta\omega_{dip})^{-1} < T_M < T_f \quad (57)$$

Instantaneous Diffusion

Instantaneous diffusion is an A-A interaction. If dipolar coupled A-spins are excited by a MW pulse, also the coupling is influenced, due to its anisotropic nature. A MW pulse therefore leads to an instantaneous change of the local field (at the position) of an A-spin. As a result, the accumulated phases during de- and refocusing are inequivalent. Two cases can be distinguished here, in the case of a complete excitation of the EPR resonance line; the experimental echo decay shape $I(2\tau)$ is:

$$I(2\tau) = I(0) \exp\left(-2\tau c \frac{\pi}{9\sqrt{3}} \frac{\mu_0 g_1 g_2 \mu_B^2}{\hbar} \sin^2(\beta_{MW}/2)\right) = I(0) \exp(-2\tau/T_{ID}) \quad (58)$$

where I is the echo intensity, τ is the inter-pulse distance of the pulsed EPR experiment, c is the concentration of the A-spins, g_1 and g_2 the g -values of the observed and excited spins respectively (i.e. of the A-spins before and after the MW pulse), β_{MW} the flip angle of the MW-pulse and T_{ID} the instantaneous diffusion time. For incomplete excitation, additionally a lineshape function $f(\omega_s)$ is considered:

$$I(2\tau) = I(0) \exp\left[-2\tau c \frac{\pi}{9\sqrt{3}} \frac{\mu_0 g^2 \mu_B^2}{\hbar} \int \sin^2\left(\frac{\beta_{MW}}{2}\right) f(\omega_s) d\omega_s\right] \quad (59)$$

The integration accounts for an averaging over Larmor frequency distributions associated with the EPR-linewidth. For a constant flip angle, T_{ID} is proportional to the pulse length as long as the excitation bandwidth is much smaller than the spectral width. If non-instantaneous diffusion contributions are present, an additional exponential factor $\exp(-2\tau/T_2)$ has to be considered in equation (59). As dipolar coupling among the A spins is prerequisite for instantaneous diffusion, this process can only be observed above a certain threshold concentration of electron spins.

Spectral Diffusion

For low concentrations of the paramagnetic species and/or high temperatures, the A-B interaction of spectral diffusion (SD) is often the dominant spin-spin relaxation process: If a B-spin flips during the echo observation of A-spins, local field jumps are experienced by the A-spins. This leads to a time-dependent frequency-shift of A-spins which causes irreversible dephasing. A special case of spectral diffusion is cross-relaxation, here a B-spin flip induces an A-spin flop. The magnetization transfer from B- to A-spins leads to a loss of spin echo intensity and therefore it is visible as apparent spin-spin relaxation process. In both cases, spin-lattice relaxation of B-spins is the source of dephasing. In the theoretical modeling, distances and time fluctuations of all B-spins with respect to A-spins are considered. For the B-spins, random distributions over the lattice are assumed. Various models are available employing different averaging methods for these B-spin distributions. Table 1 provides an overview of different spectral diffusion models. The linewidth $\Delta\omega_{dip}$ indicates here the broadening due to dipolar A-B-interactions.

Nuclear Spin Diffusion

Another important and often dominant A-B interaction is nuclear spin diffusion (NSD). Here nuclear spins (B-spins) perform flip-flop processes among themselves which induce magnetic field fluctuations at the location of the A-spins via dipolar coupling. This problem can be treated with similar models as spectral diffusion. As the matrix nuclei represent concentrated systems in most cases, a different averaging over the spin positions is necessary compared to the models applied for spectral diffusion. Furthermore it should be mentioned, that within a certain radius around the electron spin, the nuclear spins experience a strong (dipolar) coupling to the electron spin. This coupling shifts the nuclear Larmor frequency and therefore flip-flop processes are inhibited within that radius. Usually this so called diffusion barrier has a radius of 3-6 Å. Although very rare, it is also possible that nuclear spin diffusion happens only within this diffusion barrier, if the coupling between electron- and nuclear spins is weaker inside than outside the diffusion radius.

The Mims model for NSD is valid for dipolar couplings between A- and B-spins which are of the same order of magnitude as the difference of their resonance frequencies. The rate of spin diffusion $1/T_{SpinDiffusion}$ depends on the distance r_{AB} between A- and B-spins as:

$$1/T_{SpinDiffusion} \propto r_{AB}^{-6} \quad (60)$$

Table 1: Overview models for spectral diffusion dominated Hahn echo decay.

echo decay function	limitations, definitions	comments, references
$I(2\tau) = I(0) \exp \left[-2b\tau \left(\frac{\tau}{\tau_c} \right)^k \right]$	valid for $\tau < \tau_c$ $k \geq \frac{1}{2}$, $b \approx \Delta\omega_{dip}$	general echo decay Milov, <i>J. Exptl. Theoret. Phys.</i> 1972 ^[42]
$I(2\tau) \approx I(0) \exp \left[-K' \left(\frac{2\tau^3}{3\tau_c} \right)^{1/2} \right]$	valid for $\tau < \tau_c$ $K' = \frac{16\pi\sqrt{\pi}}{27} \sqrt{S_B(S_B + 1)} \gamma_A \gamma_B \hbar C_B$	Gaussian model by Mims good for large S , Gaussian distribution of B-spins Mims, <i>Phys. Rev.</i> 1968 ^[43]
$I(2\tau) = \exp \left[- \left(\frac{2\tau}{T_M} \right)^k \right]$	valid for $\tau < \tau_c$ $k = 3/2$ for $\tau \ll T$ and $k = 1/2$ for $\tau \gg T$ $T_M = 1.9(R\Delta\omega_{dip}^2)^{-1/3}$ $\Delta\omega_{dip}^{S_B=1/2} = 2.53\gamma_A g_B \mu_B N_B$	Gauss-Markovian model by Mims B-spins as Gaussian random variables with Markovian correlation function Mims, <i>Phys. Rev.</i> 1961 ^[44]
$I(2\tau) = \exp \left[- \left(\frac{2\tau}{T_M} \right)^2 \right]$	valid for $\tau < \tau_c$ and $\tau \ll T_1^B$ $T_M = 1.4(R\Delta\omega_{dip})^{-\frac{1}{2}}$	Sudden-jump model by Klauder & Anderson: good for small S , flips of B-spins described by Poisson process Klauder, <i>Phys. Rev.</i> 1962 ^[45]
$I(2\tau) \approx I(0) \exp(-2\Delta\omega_{1/2}\tau)$	valid for $\tau/\tau_c \approx 1$	model by Hartmann & Hu Hu, <i>Phys. Rev.</i> 1974 ^[46]
$I(2\tau) = I(0) \exp \left[- \frac{4\pi}{27} \frac{\mu_0 g_A g_B \mu_B^2}{\hbar} C_B \sqrt{2S_B(S_B + 1) T_1^B} \tau^{1/2} \right]$	-	Salikhov-model allows determination of T_1^B (spin-lattice relaxation time of B-spins) Salikhov, <i>Fiz. Tverd. Tela</i> 1972 ^[47]

As there are often various types of B-spins present, most likely a distribution of flip-flop rates will be encountered. For a model cubic lattice distribution of the nuclear spins with a concentration c_n , the phase memory time can be approximated by:

$$\frac{1}{T_m} = \frac{0.37\mu_0(g_e\mu_B)^{\frac{1}{2}}(g_n\mu_n)^{\frac{3}{2}}[I(I+1)]^{1/4}c_n}{4\pi\hbar} \quad (61)$$

In the case of dominant nuclear spin diffusion, the echo decay function with $2 \leq k \leq 3$ is:

$$V(2\tau) \approx V_0 \exp[-2\tau^k] \quad (62)$$

Electron Spin Diffusion

Finally, also electronic B-spins can induce spin diffusion (electron spin diffusion, ESD). Electronic B-spins can *e.g.* be represented by various paramagnetic species in the sample or by one species in different lattice environments. The theoretical treatment is very similar to nuclear spin diffusion and the rate of electron spin diffusion depends on the distance $r_{A,B}$ between A- and B-electron spins in the same way as given in equation (60).

Summary Spin-Spin Relaxation Theory

Summarizing it should be noted that in all theoretical spin-spin relaxation approaches a uniform distribution of spins in the matrix is assumed which is certainly not the case in reality. This makes it difficult to compare theoretical and experimental results. Furthermore in most cases there are not only one but several contributions to dephasing. The contributions can in some cases be distinguished *e.g.* by varying concentration, amplitude of the MW field and temperature in comparative measurements. In all cases, this involves extensive data collection and careful analysis. Often there is a dominant diffusion process, which determines the observed echo decay shape. As a guideline for dilute paramagnetic transition metal complexes, most typically mono-, bi- and stretched exponential echo decay curves are found. From a mono- or biexponential decay, T_M can be extracted by fitting the curve with the following formula

$$I(2\tau) = I(0) + A_f \exp(-2\tau/T_{M,f}) + A_s \exp(-2\tau/T_{M,s}) \quad (63)$$

The indices f and m describe fast and slow processes of relaxation respectively. Biexponential decay curves are often caused by spectral diffusion, here the fast process is commonly attributed to dephasing induced by spectral diffusion and the slow process is connected with the actual spin-spin relaxation. Another very commonly detected echo decay shape is a stretched exponential:

$$I(2\tau) = I(0) + A_s \exp(-2\tau/T_{M,s})^k \quad (64)$$

where the stretch parameter k indicates the dominant dephasing process. If the inverse rate of the dominant dephasing process is of the same order of magnitude as the interpulse distance τ , the stretch parameter is $k \approx 0.5$. For physical motion of magnetic nuclei as main dephasing process, the stretch parameter is $k \approx 1 - 1.5$. Nuclear spin diffusion can be considered the dominant dephasing process for $k \approx 2 - 2.5$. In the slow motion regime, nuclear spin diffusion or nuclear spin induced spectral diffusion can lead to $k \approx 3$.

2.2.4 Thermodynamic Spin-Lattice Relaxation Theory

The diffusion processes discussed in the previous section can also have an influence on spin-lattice relaxation. In general, magnetic field fluctuations perpendicular to the external magnetic field can influence spin-lattice relaxation. Here, a microscopic model is available for the energy exchange between the spin system and the lattice. This process can be described with a thermodynamic theory by the means of the so-called phonon approach, which was derived for crystalline solids of ions but is also widely applied for molecular, disordered systems.^[3, 48-50]

Phonons are quanta of collective lattice vibrations. The surrounding of the observed paramagnetic species is denoted the lattice, which is assumed to be in thermal equilibrium with the surrounding of the sample (the bath). The phonons present at a certain temperature lead to oscillating electric fields which modulate the crystal field splitting of the paramagnetic species among others. This modulation is translated into an oscillating magnetic field by spin-orbit coupling. As discussed previously, this induces electron spin transitions. Within the phonon approach, different relaxation processes are considered, as explained in the following text. Important assumptions for the thermodynamic description of relaxation are that the phonon wavelengths are long compared to the lattice dimensions (so called acoustic phonons) and the lattice is well described by the Debye model. This model can be used to describe the heat capacity in solid matter for coupled oscillators. The normal modes of these oscillators are considered to be quantized with the energy eigenvalues:

$$E_k = \left(n_k + \frac{1}{2}\right) h\nu_k \quad (65)$$

here the fundamental energy describes the phonon energy and the state assigned by $k = 0, 1, 2, \dots$

represents n_k phonons of this particular energy being present. According to Bose-Einstein statistics, the average thermal energy of such phonons is:

$$\langle E_k \rangle = \frac{h\nu_k}{\exp(h\nu_k/k_B T) - 1} \quad (66)$$

In general, the internal energy of solid matter in the Debye model is:

$$U = \frac{9}{8}R\theta_D + 9RT \left(\frac{T}{\theta_D}\right)^3 \int_0^{\theta_D/T} \frac{(h\nu/k_B T)^3}{\exp(h\nu/k_B T) - 1} d(h\nu/k_B T) \quad (67)$$

with the gas constant R , the oscillation frequency ν and the Debye temperature θ_D :

$$\theta_D = \frac{h\nu_D}{k_B} \quad (68)$$

where ν_D assigns the cutoff or Debye frequency, or the maximum phonon frequency, with a wavelength defined by half of the smallest lattice dimension. The cutoff frequency originates from the maximum number of $3N$ vibrational states in a three-dimensional network of N coupled oscillators. Effective Debye temperatures of molecular solids are typically around 20-150 K.^[3] The density of phonon states ρ_p at a certain temperature is given by:

$$\rho_p = \frac{2V\nu^2}{v_s^3} \quad (69)$$

with the velocity of sound v_s . With that, the Debye frequency for N primitive unit cells can be rewritten as:

$$\nu_D^3 = \frac{3v_s^3 N}{4V} \quad (70)$$

Fundamentally, the phonon approach uses a perturbation ansatz of a time-dependent perturbation \hat{V} :

$$\hat{V} = \sum_n \frac{\partial \hat{H}_s}{\partial \varepsilon_n} \varepsilon_n + \sum_{n,m} \frac{\partial^2 \hat{H}_s}{\partial \varepsilon_n \partial \varepsilon_m} \varepsilon_n \varepsilon_m = \hat{v}' \varepsilon_n + \hat{v}'' \varepsilon_n \varepsilon_m \quad (71)$$

In this perturbation operator, a Hamiltonian affecting just the spin system \hat{H}_s is regarded. The perturbation is introduced by the crystal field perturbation operators \hat{v}' and \hat{v}'' as well as a strain ε_n . The latter describes the time-dependent relative displacement from the equilibrium position of a nucleus n (or m) with respect to the nucleus belonging to the unpaired electron. Depending on the relaxation process, perturbation theory with time-dependent perturbations up to first or second order has to be considered. The system can be described by a product function

$$\psi_{system} = \psi_s \varphi_n \quad (72)$$

which contains the eigenfunctions $\psi_s = c_1\alpha + c_2\beta$ of the spin sub-system as well as φ_n , the eigenfunctions of the phonon system with n phonons.

The simplest possible spin-lattice relaxation pathway is the direct process. Here the returning of an excited spin to its ground state involves the formation of a phonon with the corresponding energy. With first order crystal field perturbation and time-dependent perturbation to first order, the transition probability W for this case can be expressed as:

$$W = \frac{4\pi^2}{h} |\langle \beta | \hat{v}' | \alpha \rangle|^2 |\langle n+1 | \varepsilon | n \rangle|^2 \quad (73)$$

and the transition rate is defined by the product of transition probability and phonon density:

$$R_T = W \rho_p \quad (74)$$

For $kT \gg h\nu$, the temperature dependence of the spin-lattice relaxation rate is described by:

$$T_1^{-1} = \frac{4\pi\nu^3 |\langle \alpha | \hat{v}' | \beta \rangle|^2}{v_s^5 \rho} (2k_B T / h\nu) \quad (75)$$

Here ρ denotes the density of the solid, and it is evident that there is a linear proportionality between the spin-lattice relaxation rate and the temperature for the direct process.

In addition, relaxation processes involving more than one phonon have to be considered. One of these is the Raman process. In the first order Raman process, a nonlinear mixing of two phonons produce perturbations of the electron spin, if the spin transition energy corresponds to the difference frequency of the phonons. Application of second order perturbation theory with time-dependent perturbation theory up to first order leads to the following temperature dependence of spin-lattice relaxation rate:

$$T_1^{-1} = |\langle \alpha | \hat{v}'' | \beta \rangle|^2 \frac{9\hbar}{8\pi^3 v_s^{10} \rho^2} \left(\frac{k_B T}{\hbar} \right)^{7+d} \int_0^{h\nu_D/k_B T} \frac{x^{6+d} \exp(x)}{(\exp(x) - 1)^2} dx \quad (76)$$

The integral over lattice vibrations is called ‘‘transport integral’’, where $x = h\nu_k/k_B T$ and several numerical approximations are tabulated for various lattices. The exponent $d = 0$ for non-Kramers systems (integer spin) and $d = \pm 2$ for Kramers systems (half-integer spin). A second order Raman process can be described with first order crystal field perturbation and second order time-dependent perturbation. Here a phonon is absorbed by the excited spin which in turn is lifted to a virtual energy level, followed by relaxation to the ground state involving the generation of a phonon. The energy difference of the absorbed and emitted phonon corresponds to the energy

difference of the electron spin states. The proportionality of spin-lattice relaxation rate and temperature for this second order process is the same as in equation (76). Both Raman processes are important for higher temperatures where high numbers of phonons are present.

Last but not least, for $S > 1/2$ -systems, a scattering process of relaxation can be realized via an excitation to a real spin state and this is called the Orbach process. If this process is operative, a significant increase in T_1^{-1} results. For $T \gg \frac{\hbar\omega_L}{k_B}$ the maximum phonon density can be found for $\omega_{max} \gg \omega_L$. The temperature dependence is given by:

$$T_1^{-1} \propto \frac{\Delta E^3}{\rho v_s^5} \left[\exp\left(\frac{\Delta E}{k_B T}\right) - 1 \right]^{-1} \quad (77)$$

Here, ΔE describes the energy separation between the electronic ground- and first excited state.

For very high temperatures, the Orbach process also leads to a linear dependence $T_1^{-1} \propto T$.

In conclusion, the theoretical description for spin-lattice relaxation theory can be carried out either with the phonon approach or with the previously discussed field-fluctuation approach. As general guideline, atomic motions are better described by correlation functions, if the inverse lifetime of the phonons approaches the EPR frequency or when motions in the sample become very anharmonic. In the latter case, the phonon model is not useful as the Debye approximation cannot be applied any longer.^[36]

2.2.5 Summary Electron Spin Relaxation Theory

Figure 7 summarizes relaxation types, mechanisms and processes for $S = 1/2$ -systems.

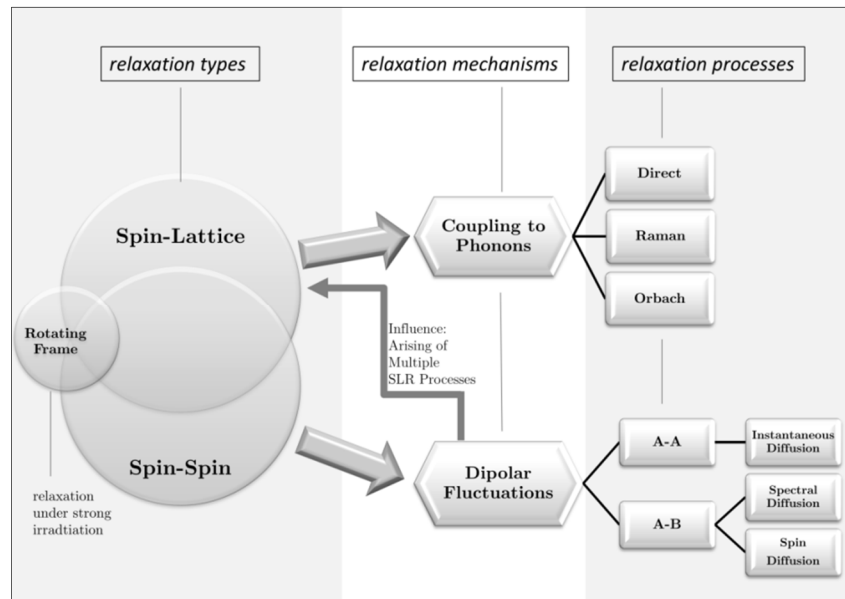


Figure 7: Overview electron spin relaxation types, mechanisms and processes.

Note that spin-lattice relaxation always represents an upper limit for spin-spin relaxation. Dipolar fluctuations leading to various spin-spin relaxation processes can also influence spin-lattice relaxation to various extents. For strong influences they can give rise to multiple spin-lattice relaxation processes. Especially spectral diffusion is often present in spin-lattice relaxation of transition metal spectra with broad, overlapping resonance lines.

2.3 Influences on Spin Dynamics

2.3.1 *Physical Influences*

Orientation of the molecular g -tensor towards the magnetic field

In this thesis, only disordered solid state systems (doped powders, frozen solutions) were investigated. The spectra of such systems always represent a sum over all possible orientations of the g -tensor with respect to the external static magnetic field. Nevertheless, also in disordered systems the g -components can be distinguished, as long as the difference between the components is large enough and/or the line-width small enough to resolve the resonance lines.

In general, anisotropic contributions in the Hamiltonian can lead to an orientation dependence of the spin-lattice relaxation time, where orientations exhibiting stronger disturbances on the electron spin Hamiltonian usually lead to shorter spin-lattice relaxation times.^[23] Furthermore with increasing strength of the modulation of spin-orbit coupling through internal vibrations, which are orientation selective, the electron spin relaxation rates increase. The number of available lattice modes also influences T_1 : fewer modes lead to slower spin dynamics. In anisotropic systems, the number of available modes varies with orientation.

For spin-spin relaxation it has been reported, that a dependence of the relaxation rate on magnetic field orientation at constant MW frequency is possible. T_M appears to be generally longer for higher field parts of broad transition metal spectra.^[23] The dependence of phase memory time on physical parameters is not well understood yet, so this is only an empirical statement. Also the following discussion on influences on spin-spin relaxation will be more qualitative compared to the quantitative concepts of spin-lattice relaxation dependencies.

Temperature

As introduced in section 2.2.4, spin-lattice relaxation can occur via different processes, which can be distinguished by the temperature dependence of T_1 . Table 2 gives an overview of proportionalities for direct, Raman and Orbach process.

Table 2: Temperature dependence of spin-lattice relaxation rates for direct, Raman and Orbach process.

Process \rightarrow	direct process		Raman process		Orbach process
Ion type \rightarrow	non-Kramers	Kramers	non-Kramers	Kramers	non-/ Kramers
$T \gg \frac{h\nu_L}{k_B}$	$T_1^{-1} \propto T$	$T_1^{-1} \propto T$	$T_1^{-1} \propto T^7$	$T_1^{-1} \propto T^9$ (2 nd order)	$T_1^{-1} \propto (\Delta E)^3 \exp\left(-\frac{\Delta E}{k_B T}\right)$ with $h\nu_L \ll \Delta E < h\theta_D$
$T \ll \frac{h\nu_L}{k_B}$	temp. indep.	temp. indep.	$T_1^{-1} \propto T^7$	$T_1^{-1} \propto T^7$ (1 st order, low T)	

In general, the direct process is dominant at low temperatures, whereas two-phonon processes gain importance with higher temperatures due to the larger number of phonons available. For very low temperatures, a phonon bottleneck can be active rather than the direct process. In the phonon-bottleneck case, the heat dissipation of spin relaxation energy into the lattice is confined to a small fraction of effective phonons and heat redistribution to the rest of the lattice and also heat dissipation to the bath require extra time. The presence of a phonon bottleneck can be recognized by a temperature dependence of $T_1^{-1} \propto T^2$. For $S > 1/2$ also a tunneling process is possible, here the temperature dependence has a proportionality similar to the direct process with $T_1^{-1} \propto T$.

Hoffmann *et al.* summarized procedures for fitting experimental $T_1^{-1}(T)$ -curves,^[48] which will be reproduced here in brevity by just naming the most important limiting cases without derivation.

Considering the processes introduced in Table 2, experimental temperature dependencies of spin-lattice relaxation for Kramers ions and in the high temperature limit can be fit with:

$$T_1^{-1} = a + bT + cT^9 I_8(\theta_D/T) + d \exp(-\Delta/kT) \quad (78)$$

where a is a background term, b , c and d are factors and the other parameters have their usual meaning (as introduced previously). The term $I_8(\theta_D/T)$ represents the transport integral for Kramers ions, compare equation (76). The integral has no general analytical solution, but various

approximations for different limiting cases exist. For very low temperatures (i.e. $T < 0.05 \theta_D$), the Raman process described by $cT^9 I_8(\theta_D/T)$ in equation (84) can be replaced by

$$T_{1,Raman}^{-1} = 8! cT^9 \quad (79)$$

For very high temperatures (i.e. $T > \theta_D$), a quadratic temperature dependence is observed:

$$T_{1,Raman}^{-1} = \frac{c}{7} \theta_D^7 T^2 \quad (80)$$

For temperatures between the two named high and low temperature limiting cases, an effective temperature is applied:

$$T_{1,Raman}^{-1} \propto T^n \quad (81)$$

where n usually varies from ca. 2.5–6.^[48-50]

For a fit of the whole temperature range, equation (84) can be used with a phenomenological expression for the transport integral:

$$\ln I_8(\theta_D/T) = -12.6355 + 7.10213x - 0 - 13101x^2 - 0.2813x^3 \quad (82)$$

where $x = \ln(\theta_D/T)$. Note that this phenomenological expression is valid only for $(\theta_D/T) = 0.4 - 18$. With the help of equation (81), the Debye temperature of the investigated species can be found. Alternatively, Debye temperatures can be extracted from heat capacity measurements.^[51] Strictly speaking all this is only valid for ionic crystals within the Debye theory, but in practice the presented procedures are also applied for molecular crystals.^[48-50]

Also for spin-spin relaxation, the dominance of dephasing processes changes with varying temperature. At low temperatures, matrices are rigid due to limited thermally activated movements and dephasing is often dominated by spin diffusion (nuclear and electron spin diffusion). For dominant nuclear spin diffusion and assuming that the spin flip-flop rate is only dependent on the number of pairs being available for flip-flop processes, the temperature dependence of the phase memory time can be modeled according to:

$$T_M^{-2} = \frac{A}{(1+e^{T_{Zeeman}/T})(1+e^{T_{Zeeman}/T})} \Gamma_{res} \quad (83)$$

where A is a parameter, T_{Zeeman} corresponds to the Zeeman energy of the system in Kelvin and Γ_{res} is a residual relaxation rate.^[52-53] This residual relaxation rate can be experimentally detected under strongly polarizing conditions, i.e. large magnetic fields and very low temperatures.

With increasing temperatures, the matrix becomes more agile. If tumbling of matrix nuclei is possible, phase memory time will show a local maximum at intermediate temperatures as the

mean spin-flip time of matrix nuclei is increased (and therefore the contribution to electron spin dephasing is decreased) by this effect. At high temperatures, non-rigid matrices and time-dependent anisotropic interactions are present, which lead to additional dephasing and the phase memory time will decrease with increasing temperature.

MW Frequency

Thermally activated processes such as vibrational effects on SOC, relaxation via modulation of g - or A - anisotropy are generally frequency-dependent. The phonon density varies strongly with frequency. From equation (69) it can be seen, that higher phonon densities are available for higher MW frequencies, leading to higher transition probabilities (equation (74)) and therefore shorter spin-lattice relaxation times. As in the case of the temperature dependence, different SLR processes show distinct frequency dependences as shown in Table 3.

Table 3: Frequency dependence of spin-lattice relaxation rates for direct, Raman and Orbach process.

direct process	Raman process	Orbach process
$T_1^{-1} \propto \nu_{MW}^4, B_0^4$ (<i>Kramers ions</i>)	$T_1^{-1} \propto \nu_{MW}^2, B_0^2$ (Kramers ions, very low T)	independent of ν_{MW}, B_0
$T_1^{-1} \propto \nu_{MW}^2, B_0^2$ (non-Kramers)	all other cases: independent of ν_{MW}, B_0	(except possible alteration of ΔE)

For spin-spin-relaxation, the beforehand mentioned reduction in spectral diffusion at higher frequencies needs to be considered. Furthermore, dynamic effects contributing to dephasing show complex dependencies on the MW frequency.^[23] For example, the dynamics of nuclear spins strongly depends on MW frequency, which will be discussed in the following paragraph.

Nuclear Spin Dynamics

Nuclear spins can influence electron spins via weak and strong couplings, leading to various effects, which can be distinguished into static and dynamic effects. Strong couplings lead to static effects like hyperfine couplings, which can be observed in EPR- or ENDOR-spectra (electron nuclear double resonance, see section 2.4.2). These effects have no influence on spin dynamics, as long as the hyperfine splitting is small compared to the applied external field. Weak couplings usually lead to dynamic effects, such as electron spin dephasing due to nuclear spin flips and flipflops. For rigid matrices and the in absence of instantaneous diffusion, nuclear spin diffusion is the main dephasing process at low temperatures besides spectral diffusion, so a closer look at nuclear spin dynamics can provide valuable information for electron spin relaxation. Spin-lattice

relaxation of nuclear spins is in the range of hours under typical EPR measurement conditions, so nuclear-spin-induced spectral diffusion is usually not relevant for electron spin dynamics. Far more important are nuclear spin flip-flops caused by dipolar interactions. Typical flip-flop frequencies are in the kHz-range, i.e. the flip-flop timescale is in the millisecond range.^[54] The flip-flop rate is frequency dependent and can be quenched under strong nuclear polarization ($h\nu_{MW} \gg k_B T$). This condition is for example fulfilled at milli-Kelvin temperatures at X- and Q-band, or more generally at high MW frequencies and low temperatures. Overall, the analytical form of the electron spin echo decay experiment depends on the MW frequency, on the measurement temperature and also on the timescale of the experiment.

Theoretical analysis of nuclear spin diffusion for $I = 1/2$ provides information on the electron spin echo decay shape as neatly presented by de Sousa *et al.*^[54] In general, the Larmor frequency of an electron spin changes by Δ_{nm} during a flip-flop event of nuclear spins n and m :

$$\Delta_{nm} = \frac{|A_n - A_m|}{2} \quad (84)$$

Where A_n, A_m are the coupling constants between nuclear spins n, m and the electron spin. The average nuclear spin flip-flop time is denoted with T_{nm} . Furthermore the correlation time τ_c of the effect of the nuclear spin bath on the electron spins needs to be considered. Essentially, two limiting cases can be considered exhibiting different electron spin echo decay shapes. In the fast flip-flop limit: $T_{nm}^{-1} \gg \Delta_{nm}$, $T_M \gg \tau_c$, many fast flip-flops of nuclear spins occur during the electronic spin dephasing. Effectively, the nuclear spins do not form an echo on this timescale. The fast limit also called motional narrowing regime and the electron spin echo decay shape is:

$$I(2\tau) \propto \exp(-2\tau) \quad (85)$$

In the slow flip-flop limit: $T_{nm}^{-1} \ll \Delta_{nm}$, $T_M \ll \tau_c$ less than one flip-flop on average occurs during the electronic phase memory time experiment. The nuclear spins contribute to the electron spin echo decay and a Gaussian echo decay shape is expected:

$$I(2\tau) \propto \exp(-2\tau^3) \quad (86)$$

Nuclear spin induced spectral diffusion is only important for high nuclear spin polarizations as discussed above. Assuming a common spin-lattice relaxation time for all non-resonant (nuclear) spins $T_{1,n}$, the central (electron) spin Zeeman frequency evolves with Gaussian or Lorentzian probabilities due to spin flips of non-resonant spins (= spectral diffusion). Again two limiting time domains can be distinguished. For $\tau \gg T_{1,n}$ motional narrowing occurs. Like above, spectral

diffusion is suppressed by fast flip-flops of nuclear spins. Depending on Gaussian (G) or Lorentzian (L) probability distribution, the following electron spin echo decay shapes are expected, where δ is a line-width parameter:

$$\begin{aligned} G: \quad I(2\tau) &\propto \exp(-T_{1,n}\delta^2\tau) \\ L: \quad I(2\tau) &\propto \exp(-\delta\tau) \end{aligned} \tag{87}$$

For $\tau \ll T_{1,n}$, nuclear spin induced spectral diffusion is observed. Depending on Gaussian (G) or Lorentzian (L) probability distribution of the flip-flop processes, again two different electron spin echo decay shapes are expected:

$$\begin{aligned} G: \quad I(2\tau) &\propto \exp(-(T_{1,n})^{-1}\delta^2\tau^3/3) \\ L: \quad I(2\tau) &\propto \exp(-(T_{1,n})^{-1}\delta\tau^2) \end{aligned} \tag{88}$$

In conclusion, also nuclear spin dynamics is influenced by a complex interplay of possible impact factors and care should be taken in electron spin echo decay analysis, considering all relevant effects.

2.3.2 Chemical Influences

In this thesis, the term ‘‘chemical influences’’ describes the effect of chosen transition metal ion and oxidation state, of ligands, counter ions, coordination geometry, crystal structure and of the sample matrix (doped powder, dilute solution) on electron spin dynamics. These chemical influences were already introduced in section 1.3, but a more comprehensive survey of established and more recent literature shall be given in here.

In paramagnetically concentrated samples, instantaneous diffusion will be the dominant dephasing process, as introduced in section 2.2.3. In this thesis, mainly paramagnetically dilute samples were studied in order to explore sample-specific, concentration-independent influences on electron spin dynamics. Furthermore mainly $S = 1/2$ -systems were investigated, on the one hand for longer expected relaxation times due to the absence of Orbach processes in spin-lattice relaxation and on the other hand for employing relatively simple systems with the aim to establish quantitative understanding.

Starting from the core of the MQB, the first building block to choose is the employed transition metal ion. As previously mentioned, the extent of spin-orbit coupling is determined by the ion impacts spin-lattice relaxation. Du *et al.* investigated VO^{2+} -, Cu^{2+} - and Ag^{2+} -porphyrins at X-

band in frozen solutions and doped powders.^[24] They found stronger temperature dependencies of T_1 for increasing SOC-constants. Furthermore they found an orientation dependence of spin-lattice relaxation with smaller T_1 in the porphyrin plane compared to the perpendicular direction, which was ascribed to a larger number of vibrational modes in the ring plane. Summarizing they state that higher mobility of the ligand leads to shorter relaxation times and that SOC is a dominant factor in spin-lattice relaxation, whereas hyperfine coupling to nuclear spins of the metal center seems to have no influence on electron spin dynamics. Similar results were found previously by Konda *et al.* for substituted nitridochromium(V)-porphyrins^[55] and Husted *et al.* for various oxo-molybdenato porphyrin complexes.^[31] Also Zhou *et al.* came to these conclusions for a range of $S = 1/2$ organic radicals and transition metal complexes, in addition they found larger impact of motions in the surrounding of the unpaired spin for increasing g -anisotropies i.e. increasing deviation from the free-electron g -value.^[25] As deviations from $g = 2.0023$ are caused by SOC, this is just another but relevant formulation of the statement above. Graham *et al.* recently published a systematic study of influences of spin-orbit coupling and total spin quantum number on electron spin dynamics in transition metal (Cr, Fe, Ru, Os) complexes with simple ligands (CN^- , C_2O_2^-).^[56] No effect of SOC and S on dephasing was found and nuclear spin dephasing was found to be the main dephasing process.

The choice of ligand and central ion determines the coordination geometry of the compound, which also influences spin dynamics. Fielding *et al.* investigated various copper(II) complexes in glassy solutions by the means of pulsed X-band EPR spectroscopy, among them a series of Cu(II)N_4 -pyrrolate-imine complexes offering a range of tetrahedral distortions.^[26] In this comprehensive study, relaxation rates were faster in more flexible molecules compared to more rigid ones for similar first coordination spheres. Spin-lattice relaxation was up to six times faster in pseudo-tetrahedral complexes compared to square planar ones. Nevertheless, they did not find a direct correlation between dihedral angles and T_1 -values. Accordingly, they judged the coordination geometry to be an important- but not the sole influence on spin-lattice relaxation.

The choice of ligand furthermore contributes to the total number of (anisotropic) vibrational modes being available. Vibrational modes influence spin-lattice relaxation via modulations of spin-orbit coupling as described previously.^[24]

Ligand substitution can also influence conformation and structure of a complex which in turn influences electron spin dynamics. Wedge *et al.* performed a systematic study on Cr₇Ni derivatives, a polynuclear molecular nanomagnets with an $S = 1/2$ ground state.^[30] By varying bridging ligand and counter ions, they found that the conformational rigidity as well as the absolute number of nuclear spins being present in the sample have major influence on electron spin dynamics. In terms of nuclear spins, especially dynamic processes, e.g. tunneling rotation movements of methyl groups were found to act strong dephasing sources. They also found a lower dephasing effect with higher steric hindrance of the methyl groups. Deuteration of the solvent led to longer phase memory times in samples where nuclear spin diffusion was the major dephasing process. The work was continued by Kaminski *et al.* who studied the effect of ligand H-atom substitution by deuterium and halogens on dephasing.^[57] They stated that electron spin dephasing is not only governed by the size of the magnetic moment of contained nuclear spins, but also depends on the mass of the nuclei and on changes in molecular morphology upon ligand substitution. Interestingly, they found an increase in phase memory time for exchanging H by the magnetically similar F-atoms. The increase was attributed to structural changes upon strongly altering the electronegativity of ligand substituents.

Generally phase memory times are expected to increase if solvents, ligands and/or counter ions are deuterated, if nuclear spin diffusion is a major dephasing process.^[3, 28-30] The presence of methyl groups is usually associated with low phase memory times, as these mobile groups can perform various movements even at very low temperatures such as vibrations, librations, rotations (classical rotations or via quantum mechanical tunneling) for example.^[3]

In conclusion, ideal MQB candidates are transition metal compounds where the central ion exhibits a low spin orbit coupling and low spin quantum number, the ligand should be rigid, nuclear spin-free and form an octahedral or related coordination geometry and the surrounding matrix should also be nuclear spin-free and rigid. The consequent application of these design principles has led to record phase memory times of up to 0.7 ms in frozen solution.^[2] However, the small number of comprehensive, systematic studies (see references above) makes it hard to judge the relative importance of the named individual design principles for qubits. Most of the limited number of reported electron-spin relaxation studies deals with frozen solutions. Very little is known about coherence in more ordered solid state systems such as doped powders, single

crystals or thin layers.^[21-22] Eventually devices for real quantum computers will be developed, where MQBs will probably be present in ordered arrays of molecularly flat layers. To achieve this, a more quantitative and elaborate understanding of electron spin dynamics in similar environments needs to be developed with the help systematic pulsed EPR studies and theoretical calculations.

2.4 EPR Spectroscopy: Experimental Techniques

2.4.1 CW EPR

In order to record continuous wave (CW) EPR spectra, usually a constant microwave frequency is employed while the magnetic field is swept to bring the sample into resonance. Electron spin transition energies generally correspond to microwave frequencies, which are traditionally divided into bands. MW-bands used for experiments within this dissertation are collected in Table 4. For consistency, the frequencies 120 and 240 GHz are also assigned to band-letters, although this is not commonly done. As the splitting of g -components scales with the employed magnetic field and the hyperfine interaction in turn is field-independent, often spectra better resolved at higher frequencies. Furthermore spectra are simplified at higher frequencies, as there no formally forbidden transitions are observed. Also at a fixed temperature, for higher frequencies higher signal intensities are expected due to larger population differences.

Table 4: Selected MW-frequency bands and corresponding magnetic field ranges for expected resonance of an $S = 1/2$ system with $g = 2$.

Band	Frequency range / GHz	magnetic field range / T
S	2.6-3.95	0.09-0.14
X	8.2-12.4	0.29-0.44
Q	33-50	1.18-1.79
W	75-100	2.7-3.6
F	90-140	3.2-5.0
Y	170-260	6.1-9.3

In a CW-EPR spectrometer, microwaves are generated commonly by Gunn diodes and guided via wave guides through a circulator into the cavity or resonator, where the sample is mounted. The sample is located in between the poles of an electro- or superconducting magnet. After interaction with the sample, the microwave is guided back through the circulator to a detection diode.

Microwave irradiation bypassed through a reference arm to the detector and a phase shifter is adjusted to match the phase of the sample signal. Improvement of signal intensity is commonly performed by modulation of the static magnetic field. As the signal is finally detected in terms of difference voltages, a derivative shaped signal is recorded instead of the absorption spectrum (compare Figure 2).

2.4.2 Pulsed EPR

Pulsed EPR spectrometers work similarly to CW devices with some distinct differences. First of all, instead of continuous MW irradiation, short high power pulses are required (at X-band in the two digit ns-range and with power of some kW). For their creation, the generated MW radiation is again split into a reference- and a measurement arm. In the measurement arm, the MW is guided through a pulse channel, usually consisting of amplifiers, phase shifters and switches. Modern pulsed EPR spectrometers have multiple phase channels (e.g. four) bundled in a pulse forming unit, allowing sophisticated phase cycles in pulsed experiments. The generated MW pulses are usually further power amplified, mostly by the means of a travelling wave tube amplifier. Also the detection scheme is quite different in pulsed compared to CW EPR. The detected signals are very weak, whereas the incident MW pulses are strong in power, so a sophisticated timing pattern of amplifiers and protection switches needs to be employed. The amplified signal is detected in a quadrature detection scheme, allowing simultaneous detection of x' - and y' -components of the magnetization in the rotating frame as indicated in section 2.2.1. Here, usually an absorption signal is detected in contrast to CW EPR, because no field modulation can be employed. In homebuilt spectrometers the pulse generation and detection units often differ from the described scheme, but the general working principle is the same.^[58]

In addition to spectrometer specific parameters such as the quality factor of the resonator, the excitation bandwidth ΔB_{exc} of a MW pulse is mainly determined by the MW bandwidth. The excitation bandwidth can be expressed in terms of the pulse length t_p :

$$\Delta B_{exc} = 1.6 B_1 = \frac{1.6}{2\gamma_e t_p} \quad (89)$$

From equation (89) it can be seen, that longer MW pulses lead to smaller excitation bandwidths, therefore long pulses are more selectively than short ones. Commonly, long, selective pulses are

termed „soft“, whereas short, unselective ones are „hard“. For fixed MW power, the pulse length determines the tip angle of the magnetization. Most importantly, 90° ($\pi/2$ -) and 180° (π -) pulses are used in various combinations with different interpulse distances, leading to spin echoes which are integrated yielding the detected signal. Every combination of two pulses generates an echo, so also pulse echoes can occur and disturb the spin-echo detection. The formation of pulse echoes can be prevented by the means of phase cycling, which means sending pulses with different phases ($+x, -x, +y, -y$ – depending on the number of available pulse channels).

In the following some standard pulse sequences will be described which are widely used not only in this dissertation but also in the EPR community. More sophisticated and specially designed experiments will be introduced in chapter 3 at the relevant positions.

One simple, widely used two-pulse sequence is the Hahn echo (Table 5). Here a 90° pulse is followed by a variable time τ , after which a 180° -pulse is applied. This generates a spin echo after another time τ . For the electron spin echo (ESE) detection of EPR spectra, the Hahn echo is applied with a fixed interpulse distance τ while sweeping the magnetic field. The echo will be present as soon as the resonance condition is fulfilled. An execution of the Hahn echo sequence with a fixed resonant magnetic field and a variable time τ will lead to an exponential or similar decay of the echo intensity, from which the phase memory time can be extracted according to section 2.2.3.

Table 5: Overview standard pulse sequences in pulsed EPR spectroscopy (explanation of parameters see text).

Notation	pulse sequence	Determination of...
Hahn echo	$\pi/2 - \tau - \pi - \tau - echo$	T_M
CMPG	$\pi/2 - \tau - (\pi - \tau - echo - \tau)_n$	T_M w/o time dependent dephasing processes
Inversion recovery	$\pi - \tau - \pi/2 - \tau_{fix} - \pi - \tau_{fix} - echo$	T_1
Stimulated echo	$\frac{\pi}{2} - \tau_{fix} - \frac{\pi}{2} - \tau - \frac{\pi}{2} - \tau_{fix} - echo$	T_1
Saturation recovery	$\pi_{sat} - \tau - \pi/2 - \tau_{fix} - \pi - \tau_{fix} - echo$	T_1 w/o contribution of spectral diffusion
Nutation experiment	$\pi_{nut} - \tau_{nut} - \pi/2 - \tau_{fix} - \pi - \tau_{fix} - echo$	qubit viability, $T_{1\rho}$

The influence of nuclear spins leads to an additional dephasing in many cases. Time-dependent contributions such as nuclear spin diffusion can effectively be filtered out by employing the Carr-Purcell-Meiboom-Gill (CPMG) sequence. The experiment starts like the Hahn echo sequence with the generation of an echo by a 90° - 180° -pulse combination. After the time interval 2τ after

the last pulse, another 180° -pulse is applied and this $2\tau - \pi$ -subsequence is repeated n times. A transient is detected and by plotting the echo intensity over the interpulse distance, usually an echo decay curve with exponential shape is obtained. Some fluctuations are cancelled out by the refocusing procedure. Furthermore, the CPMG sequence improves the signal-to-noise ratio by \sqrt{n} for n applied refocusing pulses compared to a Hahn echo experiment with n points in τ . Phase memory times extracted from CPMG are expected to be much longer than Hahn echo detected ones, if e.g. nuclear spin diffusion is a limiting process in the latter.

For the determination of spin-lattice relaxation various pulse sequences can be applied. Commonly, an inversion recovery sequence is applied (Table 5). Here an inversion pulse (180° and large bandwidth) inverts the population. The readout of the returning of the spin population to its equilibrium state is performed by a Hahn echo sequence with fixed interpulse distances τ_{fix} after varying times τ . As the short, intense inversion pulse excites the maximum number of spins, inversion recovery is very well suited for weak signals. Especially for incomplete excitation of resonance lines, the sequence is quite sensitive towards spectral and electron/nuclear spin diffusion. So very often, the recovery curve follows a biexponential form:

$$I(\tau) = I(0) + A_f \exp(-\tau/T_{1,f}) + A_s \exp(-2\tau/T_{1,s}) \quad (90)$$

where the fast process is usually assigned to the spectral diffusion and the slow process to the actual spin-lattice relaxation.^[3, 59]

For perfect 90° -pulses, the stimulated echo represents an alternative to inversion recovery. Here an initial 90° -pulse is followed by a fixed time interval τ_{fix} then another 90° -pulse followed by a variable interpulse distance τ is applied followed by a final third 90° -pulse. After another τ_{fix} , a spin echo is formed. In reality, imperfect pulses are present and T_1 extracted from the stimulated echo experiment is often much shorter than the actual spin-lattice relaxation time. Spectral diffusion also strongly influences this experiment.

The spectral diffusion contribution in spin-lattice relaxation can be avoided with the saturation recovery sequence. In principle, it is the same as inversion recovery, but here the first pulse needs to be very long ($t_p \gg T_1$). During this first long saturation pulse π_{sat} , the nutation of the magnetization slowly decays until finally reaching a steady state. In other words, all spin packets which can be reached through spectral diffusion will be saturated. The generation of the long

required pulses often comes along with overheating of the MW bridge, so this experiment cannot be performed on all EPR spectrometers.

Transient nutation can be detected with a variable length nutation pulse π_{nut} which generates coherent spin state superpositions or in other words tips the magnetization with variable angles. After a fixed time interval τ_{nut} , a Hahn echo readout sequence is performed. The decaying oscillation gives information on optimal 90/180°-pulse length as well as on the relaxation time in the rotating frame. This experiment is commonly performed to prove viability of coherent manipulations of spins.

In addition to dynamic and spectral properties of the probed electron spin also interactions with nuclear spins can be studied with various experiments. For a model $S = 1/2$, $I = 1/2$ -system in an external magnetic field, a schematic level energy diagram can be drawn as shown in Figure 8.

The EPR transitions and corresponding experiments were discussed previously. Here the hyperfine transitions are focused and the most important pulse sequences are summarized in Table 6 and will be discussed in the following. First the allowed NMR-transitions will be discussed, which are spin flip transitions of the nuclear spin without change of the electron spin state. NMR-transitions can be detected by the means of EPR in an electron-nuclear double resonance (ENDOR) experiment.

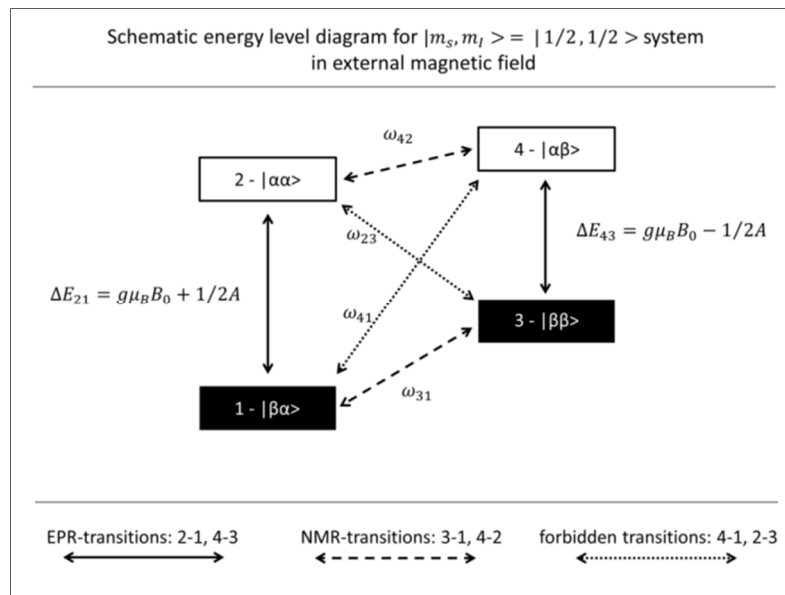


Figure 8: Schematic energy level diagram for hyperfine coupled electron and nuclear spin in an external magnetic field and possible transitions.

Table 6: Overview standard sequences for detection of interactions between nuclear and electron spins in pulsed EPR spectroscopy (explanation of parameters see text).

Notation	pulse sequence
Davies-ENDOR	$\pi_{MW} - \underset{\substack{ \\ \pi_{RF}}}{T} - \pi_{MW}/2 - \tau - \pi_{MW} - \tau - echo$
Mims-ENDOR	$\pi_{MW}/2 - \tau - \pi_{MW}/2 - \underset{\substack{ \\ \pi_{RF}}}{T} - \pi_{MW}/2 - \tau - echo$
2p-ESEEM	see Hahn echo, Table 5
3p-ESEEM	see stimulated echo, Table 5
Nuclear Nutation	Davies-ENDOR with constant ν_{RF} , where power, phase or length of π_{RF} is varied

In cw ENDOR, generally an EPR-transition is partially saturated followed by a polarization transfer to the nuclear spin manifold and ESE readout. As radiofrequency (RF) irradiation is necessary in ENDOR-experiments, special equipment is required (RF generator and amplifier, RF pulse unit and ENDOR-coils at the resonator). Basically, ENDOR measurements can be performed with pulsed and cw-EPR. The former has some advantages e.g. larger acquisition temperature range compared to cw-ENDOR. The latter is often restricted by relaxation effects, or covered by artifacts due to the simultaneous excitation and detection. As the linewidth is determined by nuclear spin dynamics, which are much slower compared to electron spin dynamics, the resolution of hyperfine couplings in ENDOR-experiments is much larger than in EPR-spectra. The number and spectral position of resonance lines in ENDOR-spectra not only depends on the spin quantum numbers as described in section 2.2.1, but also on the size of the hyperfine coupling. Two limiting cases can be distinguished: nuclear Larmor frequencies ω_L^n smaller than half of the hyperfine coupling constant are within the so called strong-coupling- or low field regime and the other case $\omega_L^n \gg A/2$ is assigned as weak coupling or high field limit. In the weak coupling limit, signals appear centered at the nuclear Larmor frequency and split by the hyperfine coupling constant. Strong couplings in turn are visible as signals centered around half of the hyperfine coupling constant and split two times the nuclear Larmor frequency. As the hyperfine coupling tensor is anisotropic in many cases, ENDOR spectra are often rich in features and not trivial to interpret. Two pulse sequences are mainly used: Davies- and Mims-ENDOR. In Davies-ENDOR (Table 6), a selective MW π -pulse at a fixed static magnetic field inverts the

polarization of an EPR transition, for example ΔE_{21} in Figure 8. Then a selective radiofrequency (RF) π -pulse is applied, which will change the polarization of an NMR-transition, e.g. ω_{42} in Figure 8, if the RF pulse matches a nuclear resonance frequency. After the mixing period, a Hahn echo sequence is applied for readout. In the resonance case, a reduction of the electron spin echo intensity will be visible, as part of the EPR-polarization was transferred to the nuclear spin manifold. These circumstances are sketched in Figure 9. All interpulse distances are fixed in the Davies-ENDOR-sequence and the RF-frequency is swept. The nuclear resonances will appear at positions determined by their hyperfine coupling constant or nuclear Larmor frequency, depending on the limiting case as indicated above.

The length of the selective first MW π -pulse can suppress small hyperfine couplings, so Davies-ENDOR is no good choice for couplings $A < 5$ MHz. For these small couplings Mims-ENDOR can be performed as an alternative. Here a stimulated echo sequence with non-selective MW pulses is applied with an RF π -pulse after the second MW $\pi/2$ -pulse. Like in Davies-ENDOR, all time delays are fixed and the echo intensity is measured as a function of RF frequency. In the Mims sequence, an RF π -pulse mixes electron- and nuclear spin polarizations and the effect is read out by a stimulated echo.

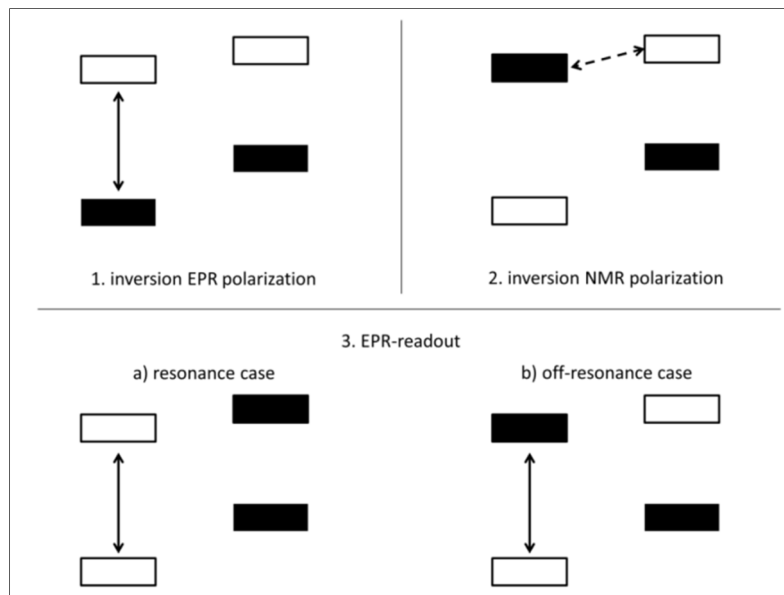


Figure 9: Sketch of polarization transfer between electron- and nuclear spin manifold during Davies-ENDOR-experiment. Specification and further explanation see Figure 8 and text.

Mims-ENDOR exhibits blind spots for:

$$\tau = \frac{2n\pi}{a_{iso}} \quad (91)$$

where $n = 0, 1, 2, \dots$ and a_{iso} is the isotropic hyperfine coupling constant, the experiment should always be performed for several τ -values in order to record all relevant signals.

Information on weakly coupling nuclei can also be derived from electron spin echo envelope modulation (ESEEM) spectra. The simplest pulse sequence here is 2-pulse ESEEM, which is the same as the Hahn echo experiment. The expected exponential decay can be modulated with nuclear Larmor frequencies (and their differences and sums), which can be extracted by data processing involving Fourier-transformation. The modulation originates from excitation of the formally forbidden transitions involving a change of nuclear and electron spin orientation (Figure 8: ω_{41}, ω_{23}). The probability of this process is non-zero if hyperfine coupling is anisotropic or if quadrupole couplings are present. The modulation intensity for an $S = 1/2, I = 1/2$ -system is given by:

$$I_{mod}(\tau) = 1 - \frac{k}{4} [2 - 2 \cos(\omega_{42}\tau) - 2 \cos(\omega_{31}\tau) + \cos((\omega_{42} - \omega_{31})\tau) + \cos((\omega_{42} + \omega_{31})\tau)] \quad (92)$$

with the modulation depth parameter k :

$$k = \frac{9}{4} \left(\frac{\mu_0}{4\pi} \right)^2 \left(\frac{g\mu_B}{B_0} \right)^2 \frac{\sin^2 2\theta}{r^6} \quad (93)$$

where r describes the distance and θ the angle between electron and nuclear spin. The total echo intensity is then in the simplest case described by a product of an exponential decay and the modulation intensity according to formula (92). Advantageously, the 2-pulse ESEEM is technically easier to record and does not show blind spots as Mims-ENDOR. On the other hand, no hyperfine coupling constants can be determined from this simple technique and the limiting factor here is the electronic T_M , whereas ENDOR is limited on the orders of magnitude longer nuclear T_M^{nuc} or the electronic T_1 . Similarly to 2-pulse ESEEM, the echo decay curve of a 3-pulse experiment can feature a modulation in the stimulated echo experiment. Here the limiting parameter is the electronic T_1 which leads usually to a better resolution compared to 2-pulse ESEEM. The modulation intensity in a 3-pulse ESEEM experiment is:

$$\begin{aligned}
I_{mod,3p}(T, \tau) = & 1 \\
& - \frac{k}{4} \{ [1 - \cos(\omega_{31}\tau)][1 - (\cos \omega_{42}(\tau + T))] \\
& + [1 - \cos(\omega_{42}\tau)][1 - (\cos \omega_{31}(\tau + T))] \}
\end{aligned} \tag{94}$$

with the modulation depth parameter k as defined above. The modulation intensity is generally lower compared to 2-pulse ESEEM. It can be directly seen from equation (94) that the modulation does have blind spots here, so as in Mims-ENDOR, the measurement of 3-pulse ESEEM should always be performed with various τ -values. Conveniently, this is done by a so-called 2D experiment: various 3-pulse ESEEM experiments with various τ -values are recorded and presented in a two dimensional contour level plot.

The coupling between an electronic qubit and a nuclear spin can be exploited to transfer coherence from the electronic to the nuclear spin valve, as for example introduced for the ^{31}P nuclear spin in Si.^[60] Due to the much slower dynamics of nuclear spins, they are perfectly suited as a quantum memory utilizing such coherence transfer scaffolds. Measuring the transient nutation of the nuclear spin is a first viability check for qubits in this direction. Nuclear spin transient nutations can be detected by the means of EPR with a modified Davies-ENDOR-sequence. Here, the RF is fixed in order to selectively probe a certain electron-nuclear spin coupling. The power, phase or length of RF-pulse is varied, which leads then to a nutating nuclear spin.

3 Results & Discussion

In this section, the results of a range of systematic pulsed EPR investigations for the purpose of identifying and classifying influences on electron spin relaxation are presented and discussed.

In the first subsection, chemical influences on spin dynamics will be focused. Three classes of compounds were investigated to this end under the same physical conditions. Changes in ESE-detected EPR spectra and spin-lattice- as well as spin-spin relaxation measurements with varying components of the MQBs, such as central ion, ligand substitution and matrix were investigated in depth. The compound showing the best MQB-properties in the first subsection was then employed as target compound in the investigation of physical influences on electron spin relaxation, presented in the second subsection. Here experimental parameters, such as the temperature, MW-frequency or pulse sequence were varied in order to explore accompanied changes in spin dynamics. Selected compounds, experiments and theoretical models for interpretation of the empirical study are presented in detail in the following.

3.1 Chemical Influences on Electron Spin Relaxation

Systematic studies of electron spin relaxation and especially of the factors that influence on spin-spin relaxation are sparse and the vast majority of spin dynamics studies are single-experiment relaxation measurements.^[2-3, 24-26, 28-29, 30, 31, 55, 57] In the following, a number of systematic investigations of chemical influences on electron spin dynamics will be presented. Numerous chemical aspects are known to influence electron spin relaxation in coordination compounds, such as the central transition metal ion and the employed ligands and solvents (compare section 1.3 and 2.3.2). The aim here is to contribute to a deeper understanding of various fundamental electron spin relaxation processes by disentangling the complex interplay of chemical influences on spin dynamics and assess the contribution of each of these. A quantitative understanding of relaxation processes and influences will further establish design criteria for the rational synthesis of improved MQBs.

The investigations presented in the following sections deal with three series of complexes, all of which are homoleptic, mainly square-planar $S = 1/2$ transition metal coordination compounds. These compounds were selected according to the knowledge gained through literature research on known factors that lead to long coherence times (section 1.3 and 2.3.2). The three sections are divided according to the ligating atoms in the coordination compounds. First the results for compounds with O-donor ligands will be discussed, where β -diketonates (Oacac = acetylacetonate and others) were employed as ligands. Next, complexes with N-donor ligands will be focused on, where phthalocyanine (Npc) coordination compounds were investigated. S-donor ligands are the third group of compounds, where maleonitrile-1,2-dithiolato(Smnt)- and 1,2-dithiooxalato(Sdto)-complexes were investigated.

All pulsed EPR measurements presented in this Section were performed in Stuttgart with a homebuilt pulsed Q-band EPR-spectrometer^[58] (see Experimental Section for details). The MW frequency was 35.000 GHz unless specified differently. The measurements were performed at 7 K, which was the lowest stable temperature in the utilized cryostat (details: see 5.2.1).

3.1.1 Spin Dynamics in Compounds with O-Donor Ligands

In this section, the results of spin dynamics investigations of coordination compounds with acetylacetonate-type ligands (O-donor ligands) will be presented and discussed. The key objective for this part of the investigations was to understand how variations in the qubit periphery impact spin relaxation, with special interest for the influence of protons and methyl groups in both ligand and solvent. Copper(II)-acetylacetonate complexes with a core structure as shown in Figure 10 were selected as target compounds. The selection criteria will be presented in the following.

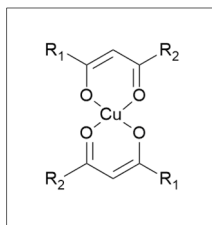


Figure 10: Core structure of investigated compounds with O-donor ligands. R_1 and R_2 denote residues which can be equal (symmetrically substituted complexes) or different (asymmetrically substituted complexes).

Coordination compounds with β -diketonate ligands are very well investigated systems due to their interesting properties and possible application as water splitting catalysts.^[61] A broad range of synthetically facilely and furthermore cheaply accessible acetylacetonate(Oacac)-type complexes is known.^[62] In general, the complexes of Oacac-type ligands and bivalent transition metal ions are robust and stable under ambient conditions. Oacac-type ligands usually provide a square-planar coordination environment for bivalent metal ions, which is favorable for enabling slow electron spin relaxation.^[26] Hence, coordination compounds with Oacac-type ligands conveniently allow for the investigation of the consequences of variations in the ligand- and qubit periphery, while maintaining the same square-planar core structure. This is important, as changes in the coordination geometry also influence electron spin relaxation (see 2.3.2). Moreover, the Oacac-type core structure is conformational quite rigid and possesses only one proton as source of nuclear spin induced dephasing, which should in principle lead to favorable coherence times. One potential drawback of some square-planar coordination compounds with Oacac-type ligands is their affinity to axial donor-ligands leading to pronounced hygroscopicity.^[63-64] In some cases, axially coordinated water molecules can be removed under reduced pressure or by sublimation of the compounds; in other cases this is not possible.^[65-66] The sublimability of charge neutral complexes themselves further enables the arrangement of the potential MQBs in thin layers of ordered arrays. Especially Oacac-complexes can be easily sublimed and have been proposed in this context as qubits recently.^[22] A comparative study including one complex with an Oacac-derivative ligand was performed by Fielding *et al.*, investigating the influence of the ligand on spin-lattice relaxation time.^[67] To the best of our knowledge, no similar investigations of the influences on spin dephasing have been published so far.

The first part of the study of influences on spin dynamics in compounds with O-donor ligands comprises a comparison of electron spin relaxation behavior in copper(II)-complexes with various Oacac-type ligands. The selected compounds are shown in Figure 11. Cu^{2+} was chosen as central metal ion because it forms stable, $S = 1/2$ complexes with the selected ligands. The employed ligands are acetylacetonate (Oacac), trifluoroacetylacetonate (Otfac), hexafluoroacetylacetonate (Ohfac), 6,6,7,7,8,8,8-heptafluoro-2,2-dimethyl-3,5-octanedione (Ofod), benzoylacetonate (Obzac) and dibenzoylacetonate (Odbm).

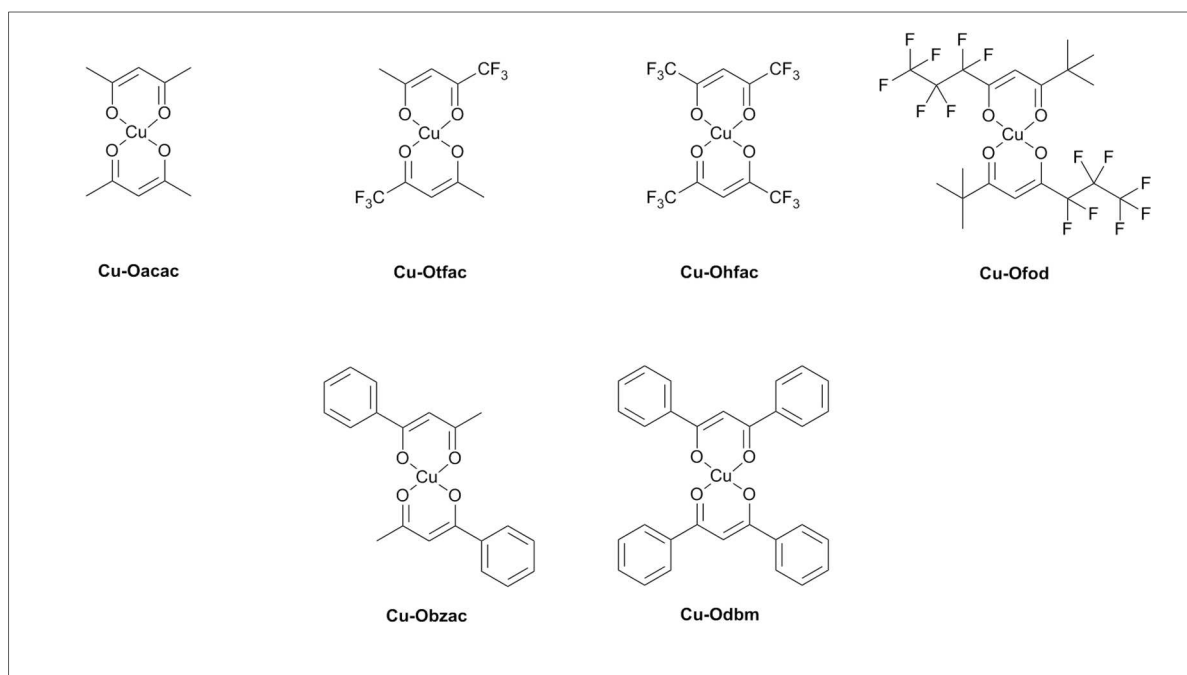


Figure 11: Investigated compounds with O-donor ligands.

The ligands were chosen to probe the impact of variations in the ligand periphery on electron spin relaxation while maintaining the core structure, as introduced above. First the influence of methyl- and trifluoromethyl-groups on electron spin dynamics was of interest. The dephasing tunneling rotations of the former are far less active for the latter and therefore an increase in phase memory times is expected for an exchange of CH₃ by CF₃ groups.^[3, 57, 68] Furthermore, the absolute number of protons being present in the ligand was investigated. Protons are known as highly efficient source of dephasing due to the large magnetic moment of their nuclear spin. Exchange of protons for nuclei with smaller magnetic moments such as deuterons or complete removal of nuclear spins is known to result in longer phase memory times.^[3, 28-30] Furthermore the influence substituent rigidity was probed. Lower mobility of chemical groups in compounds leads to a decrease in spin-lattice-relaxation and phase memory rates^[24-27] and very long T_1 and T_M times have been associated with rigid ligand- and matrix structures.^[69-70] All of the introduced compounds with O-donor ligands were investigated in 0.001 M solutions in 1:1 CD₂Cl₂/CS₂. The selection criteria for this solvent were good solubility towards the investigated compounds and presence of a low number of magnetic nuclei. Furthermore, the mixture 1:1 CD₂Cl₂/CS₂ forms solvent glasses in the solid state (checked visually during freezing). Glassy solutions are important in EPR-studies, as in case of (partly) crystallization of a solvent, local concentration variations of

the probed compound will be present.^[3] A homogeneous distribution of the paramagnetic molecules in the solvent matrix with a determined concentration is crucial, as intermolecular interactions leading to instantaneous diffusion and other relaxation processes are only absent for sufficiently dilute concentrations (e.g. 0.001 M here) of the probed material. Furthermore, varying local environments can lead to a distribution in static and dynamic EPR parameters.

In the second part of the study, the influence of the chosen solvent on electron spin relaxation was probed. Cu²⁺-Oacac-type complexes are known to form solvent adducts, which can be observed as different paramagnetic species in EPR experiments.^[71] In order to probe the effect of solvent adducts on spin relaxation, one compound from the ligand-dependence study was selected and investigated in various solvent matrices, namely CH₂Cl₂, CHCl₃, CD₂Cl₂, CDCl₃, CS₂ and 1:1 CD₂Cl₂/CS₂. These solvents were selected because they are similar to the initially used 1:1-mixture of CD₂Cl₂/CS₂. They all provide good solubility towards all investigated compounds and allow a study of the impact on relaxation by changing the kind and number of magnetic nuclei (H, D, Cl) contained in the solvent molecules. The concentration of the samples was also 0.001 M, as above.

The third and last part of the study consisted of a comparison between the glassy matrices of the investigated frozen solutions and a microcrystalline qubit matrix in a doped powder for one of the systems investigated in the first and second part. As stated above, the rigidity of ligand and matrix can have substantial influence on electron spin relaxation. Higher mobility of chemical groups leads to faster relaxation in general (see section 2.2). Furthermore, in a doped powder a higher degree of three-dimensional ordering is present. The absence of distributions in static and dynamic EPR parameters can result in lower local field inhomogeneities and less fluctuations, leading to longer relaxation times. For the doped powder sample, a diamagnetic host with a similar coordination environment to that of the paramagnetic species of interest was selected. A low concentration of the paramagnetic compound (0.001 %) ensured the absence of instantaneous diffusion in the relaxation measurements.

The remainder of the section is organized as follows. First, the ESE-detected EPR spectra will be introduced, followed by the spin dynamics measurements. In both cases, the discussion is structured according to the influences of ligands, solvents and matrices. First test measurements on the EPR behavior of compounds with O-donor ligands were performed in the B.Sc.-projects of

Maurice Conrad and Michael Tran.^[72-73] The syntheses of the investigated compounds and the measurements presented in this section as well as preliminary data analysis were performed by Samuel Lenz during his M.Sc.-project.^[74] **Cu-Oacac** was purchased and the other compounds were synthesized according to literature procedures (Section 5.1).^[75-77] Details on sample preparation, collection and evaluation of data can be found in the Experimental Section (5.2).

ESE-Detected EPR Spectra of Compounds with O-Donor Ligands

Electron spin echo (ESE) detected EPR spectra of all compounds with O-donor ligands (Figure 11) were recorded in 0.001 M solution (1:1 CD₂Cl₂/CS₂) and the results are shown in Figure 12. For the solvent-dependent study, **Cu-Odbm** was chosen as target compound, based on the results of the ligand dependent spin dynamics study. The spectra of **Cu-Odbm** in 0.001 M solution of different solvents are displayed in Figure 13. Finally, **Cu-Odbm** in a doped powder was investigated. The powder **Cu-Odbm**_{0.001%} contains 0.001 mol-% **Cu-Odbm** in the diamagnetic host **Pd-Odbm**, which provides a similar coordination environment as the dopant.^[78-79] The ESE-detected EPR spectrum of **Cu-Odbm**_{0.001%} is shown in Figure 14.

In all spectra, two pronounced features are visible with resolved fine structure in some cases. The magnetic field positions of the spectral features are comparable in all cases (overall spectral range: ca. 1060-1250 mT). Asterisks in the spectra indicate the magnetic field values at which spin dynamics measurements were carried out, as discussed later on. The observed shapes and magnetic field positions of the spectra are very typical for square-planar Cu²⁺ coordination compounds.^[26] The spectra were simulated with the Matlab-toolbox EasySpin,^[80] employing a Hamiltonian incorporating electronic- and nuclear Zeeman-, as well as hyperfine interaction, see equation (20). The corresponding simulation parameters can be found in Table 7–Table 9. In most cases, the spectral shape is reproduced by an axial g - and A -tensor of an $S = 1/2$, $I = 3/2$ -spin system. At lower magnetic fields, the parallel component $g_{\parallel} = g_{zz}$ is visible with lower intensities compared to the perpendicular component $g_{\perp} = g_{xx} = g_{yy}$ at higher fields. Both g -components are quite similar for all investigated compounds with values of $g_{\parallel} = 2.26$ – 2.32 and $g_{\perp} = 2.050$ – 2.064 . The partially resolved fine-structure of the signals is assigned to a hyperfine-coupling of the unpaired electron with the copper nuclear spin of $I = 3/2$ for both naturally occurring isotopes (⁶³Cu, ⁶⁵Cu).

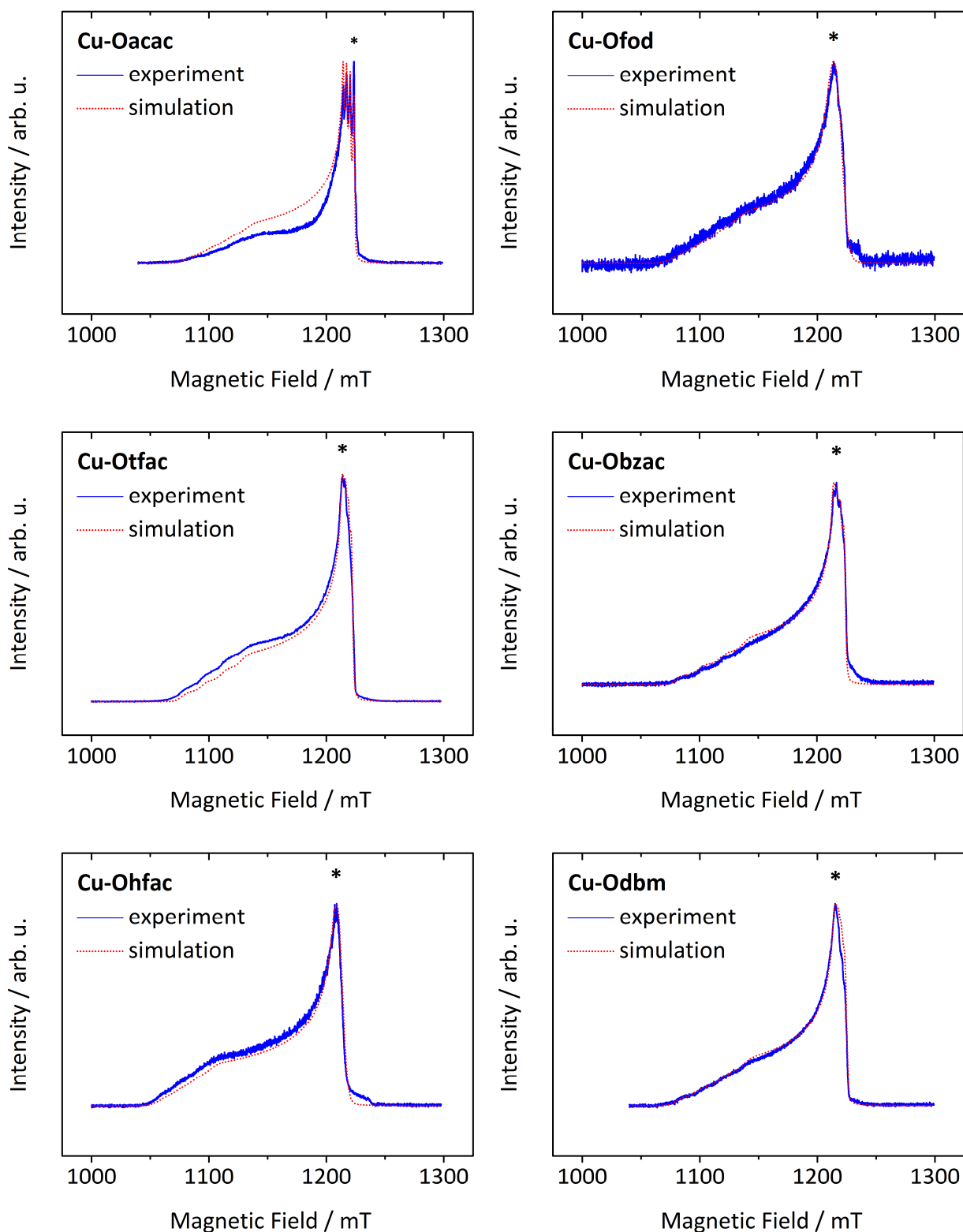


Figure 12: ESE-detected EPR spectra of investigated compounds with O-donor ligands in 0.001 M solution (1:1 $\text{CD}_2\text{Cl}_2/\text{CS}_2$) recorded at Q-band (35.000 GHz in all cases) and 7 K. Blue, solid lines represent experimental data and red, dotted lines indicate corresponding simulations. Simulation parameters can be found in Table 7. The asterisks indicate field positions for spin dynamics measurements.

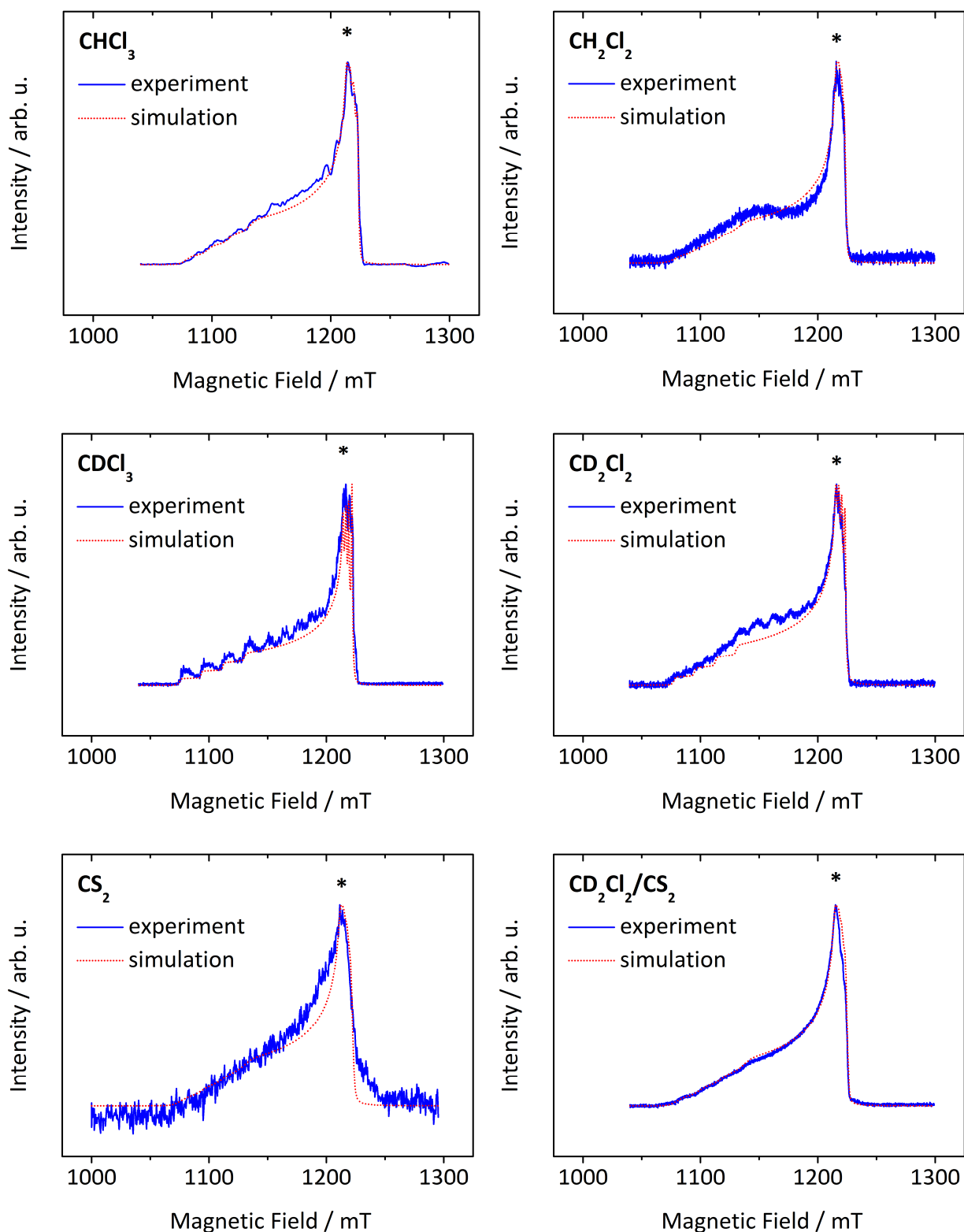


Figure 13: ESE-detected EPR spectra of Cu-Odbm in different solvents (0.001 M) recorded at Q-band (35.000 GHz in all cases) and 7 K. Blue, solid lines represent experimental data and red, dotted lines indicate corresponding simulations. Simulation parameters can be found in Table 8. The asterisks indicate field positions for spin dynamics measurements.

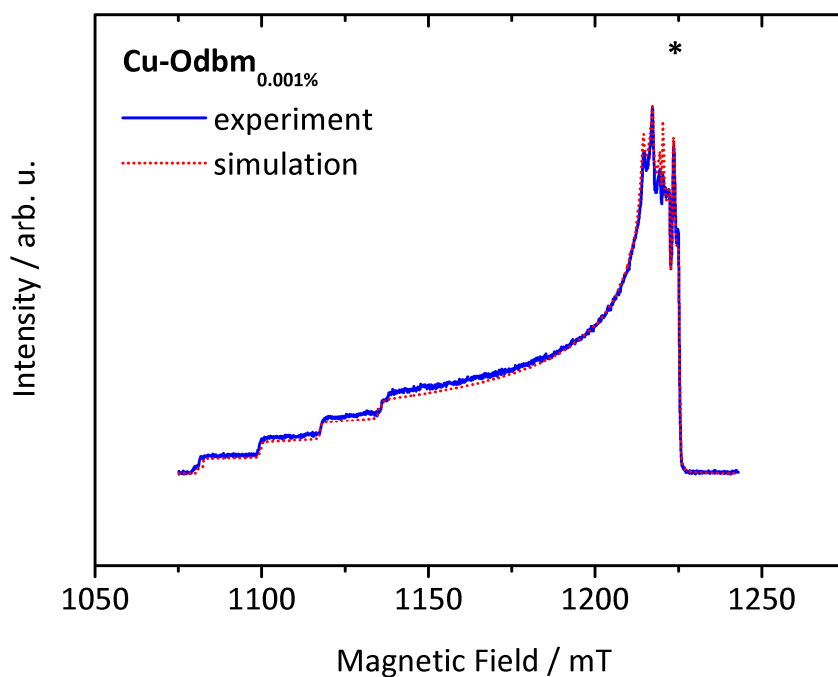


Figure 14: ESE-detected EPR spectra of **Cu-Odbm_{0.001%}** recorded at Q-band (35.000 GHz) and 7 K. Blue, solid line represents experimental data and red, dotted line indicates corresponding simulation. Simulation parameters can be found in Table 9. The asterisk indicates field positions for spin dynamics measurements.

Table 7: Simulation parameters for ESE-detected EPR spectra (Figure 12) of investigated compounds with O-donor ligands in 0.001 M solution (1:1 CD₂Cl₂/CS₂) recorded at Q-band (35.000 GHz in all cases) and 7 K.

compound	g_{\parallel}	g_{\perp}	A_{\parallel} / MHz	A_{\perp} / MHz	ΔB_{lwpp} / mT	ΔB_{Strain} / MHz
Cu-Oacac	2.26 ± 0.01	2.050 ± 0.001	520 ± 50	85 ± 5	[0 0.4]	[15 410]
Cu-Otfac	2.266 ± 0.005	2.052 ± 0.005	520 ± 20	70 ± 10	[0 0.4]	[55 300]
Cu-Ohfac	2.32 ± 0.01	2.064 ± 0.005	500 ± 20	-	[0 0.4]	[250 400]
Cu-Ofod	2.27 ± 0.01	2.055 ± 0.005	550 ± 20	-	[0 0.4]	[300 500]
Cu-Obzac	2.255 ± 0.005	2.051 ± 0.005	580 ± 20	80 ± 10	[0 0.4]	[65 300]
Cu-Odbm	2.255 ± 0.005	2.050 ± 0.005	580 ± 20	80 ± 10	[0 0.4]	[80 400]

Table 8: Simulation parameters for ESE-detected EPR spectra (Figure 13) of **Cu-Odbm** in different solvents (0.001 M) recorded at Q-band (35.000 GHz in all cases) and 7 K.

solvent	g_{\parallel}	g_{\perp}	A_{\parallel} / MHz	A_{\perp} / MHz	ΔB_{lwpp} / mT	ΔB_{Strain} / MHz
CH ₂ Cl ₂	2.262 ± 0.005	2.050 ± 0.001	550 ± 20	60 ± 10	[0 0.4]	[60 400]
CHCl ₃	2.262 ± 0.005	2.052 ± 0.001	550 ± 20	80 ± 10	[0 0.4]	[60 300]
CD ₂ Cl ₂	2.265 ± 0.005	2.050 ± 0.005	550 ± 40	70 ± 10	[0.6 0.6]	-
CDCl ₃	2.267 ± 0.005	2.052 ± 0.005	570 ± 40	70 ± 10	[0 0.4]	-
CS ₂	2.262 ± 0.005	2.053 ± 0.005	550 ± 20	80 ± 10	[0 0.4]	[80 550]
1:1 CD ₂ Cl ₂ /CS ₂	2.255 ± 0.005	2.050 ± 0.005	580 ± 20	80 ± 10	[0 0.4]	[80 400]

Table 9: Simulation parameters for ESE-detected EPR spectra (Figure 14) of **Cu-Odbm**_{0.001%} (doped powder) recorded at Q-band (35.000 GHz) and 7 K.

g_{zz}	g_{yy}	g_{xx}	A_{zz} / MHz	A_{yy} / MHz	A_{xx} / MHz	$\Delta B_{l_{wpp}} / \text{mT}$
2.225 ± 0.005	2.051 ± 0.001	2.047 ± 0.001	550 ± 10	76 ± 10	85 ± 10	[0 0.2]

An axial hyperfine coupling tensor was applied in most simulations, where the principal axes were assumed to be collinear with the g -tensors principal axes. The axial and perpendicular A -components each show similar values for the investigated compounds with $A_{\parallel} = 500\text{--}580$ MHz and $A_{\perp} = 70\text{--}85$ MHz. All determined values for g - and A -components are in good agreement with literature values for these compounds in frozen solutions^[64, 71, 81-83] or for **Cu-Odbm** in a **Pd-Odbm** host, respectively.^[84] The line-broadening was simulated with a Lorentzian peak-to-peak linewidth of 0.4 mT in most cases ($\Delta B_{l_{wpp}}$), which suggests a lifetime broadening. Additionally, a strain was included for the majority of the frozen solution samples in the simulation (ΔB_{Strain}), which accounts for orientation dependent Gaussian line broadenings due to unresolved hyperfine couplings. The intensities of the simulations do not always reproduce the intensities of the experimental data and in some cases additional signals are visible, which will be discussed further below.

The ligand dependence of simulation parameters for EPR-spectra of the investigated compounds with O-donor ligands in frozen solution is very weak. The perpendicular g - and A -components are virtually identical within the error margins. The parallel components of the both tensors vary slightly. This leads to the conclusion that the peripheral ligand substituents in the molecular plane have negligible influence on the ESE-detected EPR spectra of the compounds. Furthermore, differences between the intensities of experiments and simulations are visible in some spectra. This effect is very pronounced in **Cu-Oacac**. The intensities perfectly match in this case, if a minor second spin system is incorporated (not shown, ratio 1 : 0.2 for main and minor system). As this does not improve the parameters of the main spin system and only leads to a loss in significance of those, the additional system is not regarded in the simulations shown here. A possible origin of a second paramagnetic species in the samples is the formation of solvent adducts. As stated above, compounds with Oacac-ligands and derivatives are known to show a high affinity towards axial donor ligands.^[63-64] However, the named intensity differences could also be artifacts. The S/N -ratio is very low in some cases which make a clear assignment difficult

(e.g. spectra of **Cu-Ofod**, Figure 12). Further investigations are necessary for a more detailed interpretation.

The values for g - and A -components for **Cu-Odbm** in the investigated solvents are identical within the error margins (Table 8). The appearance of minor, but pronounced additional signals in some samples (e.g. in CD_2Cl_2) leads again to the conclusion that additional paramagnetic species are present as minor components. However, it is not expected that a solvent adduct would show highly pronounced differences in g -components compared to the pure system, which are visible e.g. for **Cu-Odbm** in CD_2Cl_2 (Figure 13), so also artefacts could be responsible for the additional signals.

In contrast to the measurements in frozen solutions, an $S = 1/2$, $I = 3/2$ -spin system with rhombic g - and A -tensors was applied in the simulation for doped powder sample **Cu-Odbm**_{0.001%} (simulation parameters: Table 9). The difference between the xx - and yy -components of the tensors are small, which evidences a small rhombic distortion of a square planar complex. The components of g and A are similar to those determined for the frozen solution samples. A Lorentzian peak-to-peak linewidth of 0.2 mT reproduces the experimental lineshape sufficiently well. In contrast to the frozen solution measurements, no strain needs to be included to reproduce the lineshapes. This is assigned to the lower linewidth in the doped powder, which leads to a higher resolution of the resonance lines. The higher degree of ordering in the defined three dimensional structure of the microcrystalline powder seems advantageous at this point of the investigation: a more defined structure leads to better separation of signals and a clearer interpretation of experimental data.

Results of Electron Spin Relaxation Measurements of Compounds with O-Donor Ligands

For all compounds with O-donor ligands, relaxation measurements were performed. For the determination of the spin-lattice relaxation times, inversion recovery experiments were performed with the magnetic field set to the value of the most intense line in the corresponding ESE detected EPR-spectra, as indicated by the asterisks in Figure 12–Figure 14. For the determination of the phase memory times, Hahn echo experiment were carried out with the magnetic field set to the same position as in inversion recovery experiments. Examples for the experimental results of spin dynamics measurements are shown in Figure 15. Figure 15a shows

the inversion recovery and Hahn echo experiments for **Cu-Oacac** in 0.001 M CD₂Cl₂/CS₂ (1:1) at 1218.4 mT. Panel b) of Figure 15 shows the corresponding experiments for the doped powder sample **Cu-Odbm**_{0.001%} at 1217.8 mT. The corresponding measurement results for the other compounds with O-donor ligands can be found in the Appendix (Supplementary Figure 1–Supplementary Figure 10). Spin-lattice relaxation times and phase memory times were extracted by fitting the experimental inversion recovery and Hahn echo decay curves, respectively. In most cases, biexponential fit functions according to equations (63) and (90) were applied. The results of these fits can be found in Table 10–Table 12 (spin-lattice relaxation times) and Table 13–Table 15 (phase memory times).[§] The extracted fast spin-lattice relaxation times are $T_{1,f} = 0.5\text{--}4.4$ ms and the slow spin-lattice relaxation times are $T_{1,s} = 2.4\text{--}18.3$ ms. The values of $T_{1,s}$ are common spin-lattice relaxation times for Cu²⁺-complexes in frozen solution.^[3, 26] The fast phase memory times are $T_{M,f} = 1.7\text{--}5.0$ μs and the slow phase memory times are $T_{M,s} = 6.9\text{--}48$ μs. In general, these values for $T_{M,s}$ times are long with respect to phase memory times of most transition metal complexes in frozen solutions, typically ranging around some hundred nanoseconds up to one microsecond.^[3]

The biexponential nature of relaxation can have various origins. Typically, the slow process is assigned to the actual relaxation of the investigated species and the fast process to a faster relaxing paramagnetic species^[23, 59] or spectral diffusion. The occurrence of spectral diffusion is highly probable for broad transition metal spectra.^[3] Also cluster formation of the paramagnetic species in the frozen solution is possible. Furthermore the existence of different paramagnetic species due to solvent adduct formation^[71] is likely, as this was already suspected on the basis of the ESE detected EPR spectra. Nevertheless, it is difficult to distinguish between the proposed origins of the biexponential relaxation behavior from these data sets and all may be true simultaneously. The origin of the fast relaxation processes cannot be established beyond doubt, therefore only qualitative rather than quantitative conclusions can be drawn from this dataset.

[§] Indicated errors are standard deviations of the fit functions. However, the experimental error for relaxation measurements with the employed homebuilt EPR spectrometer^[58] is in general around 10 % (see Experimental Section 5.2).

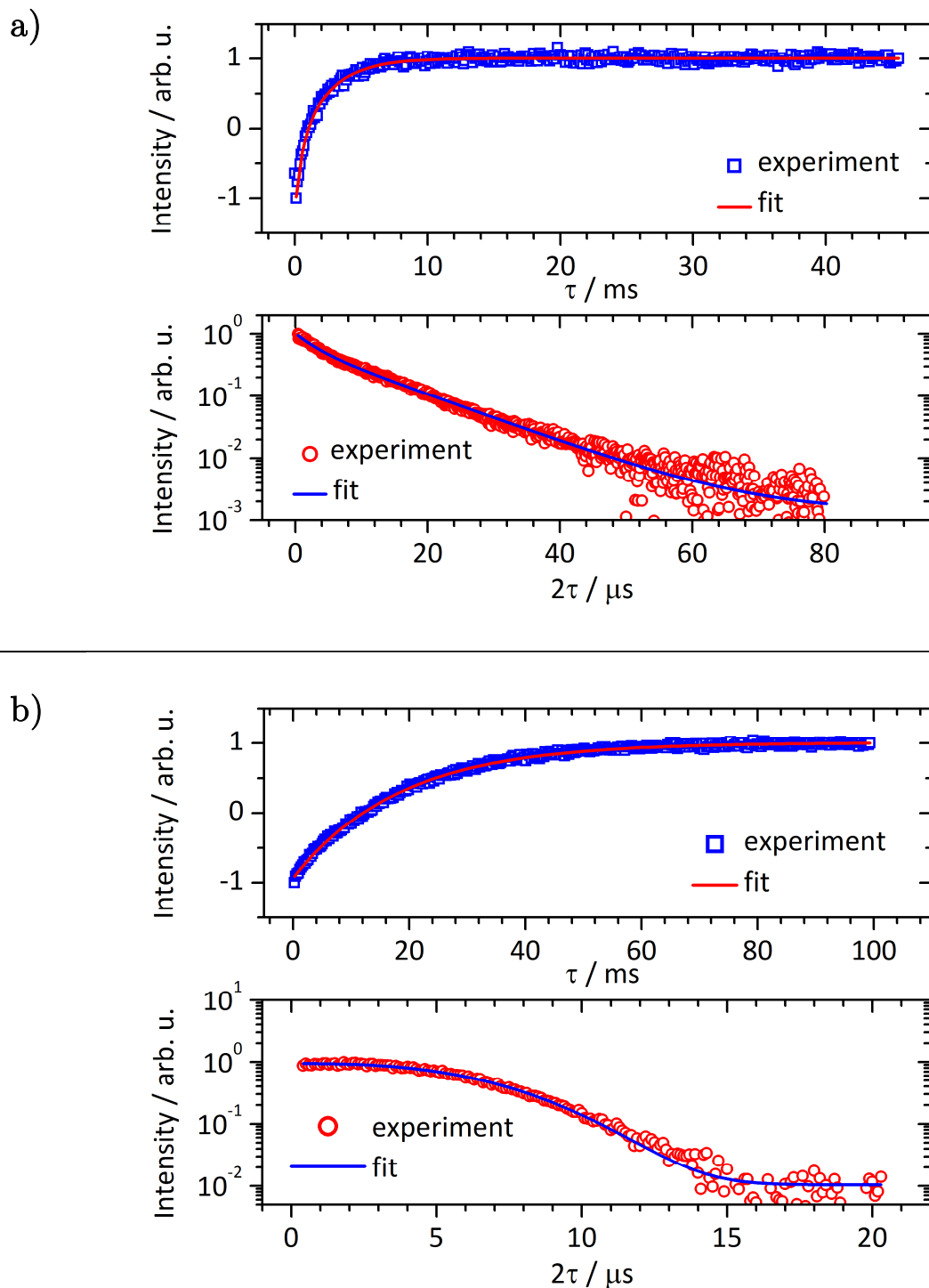


Figure 15: Electron spin relaxation measurements and fits of a) **Cu-Oacac** in 0.001 M solution (1:1 CD₂Cl₂/CS₂) and b) **Cu-Odbm_{0.001%}** measured at Q-band (35.000 GHz in both cases) and 7 K. The magnetic field was fixed to the position indicated by the asterisk in the corresponding ESE-detected EPR spectrum shown in Figure 12 and Figure 14, respectively. Top panels of a) and b): Inversion recovery experiment. Blue, open squares indicate experimental data and red, solid line represents fit function (fit parameters see Table 10 and Table 12). Bottom panels of a) and b): Hahn echo experiment. Red, open circles indicate experimental data and blue, solid line represents fit function (fit parameters see Table 13 and Table 15).

Table 10: Parameters of biexponential fit functions according to equation (90) and standard deviations for inversion recovery experiments of investigated compounds with O-donor ligands in 0.001 M solution (1:1 CD₂Cl₂/CS₂) recorded at Q-band (35.000 GHz in all cases) and 7 K.

compound	B_0 / mT	A_f	$T_{1,f}$ / ms	A_s	$T_{1,s}$ / ms
Cu-Oacac	1218.4	-0.80 ± 0.07	0.47 ± 0.08	-1.39 ± 0.08	2.4 ± 0.1
Cu-Otfac	1216.0	-0.89 ± 0.02	0.53 ± 0.02	-1.15 ± 0.02	2.35 ± 0.03
Cu-Ohfac	1210.0	-2.1 ± 0.2	1.5 ± 0.3	-1.1 ± 0.3	6.2 ± 0.9
Cu-Ofod	1246.0	-1.02 ± 0.06	0.74 ± 0.06	-1.13 ± 0.06	3.2 ± 0.1
Cu-Obzac	1217.0	-1.16 ± 0.02	0.68 ± 0.02	-0.93 ± 0.02	4.09 ± 0.07
Cu-Odbm	1216.0	-0.92 ± 0.02	0.85 ± 0.03	-1.1 ± 0.02	3.74 ± 0.05

Table 11: Parameters of biexponential fit functions according to equation (90) and standard deviations for inversion recovery experiments of **Cu-Odbm** in different solvents (0.001 M) recorded at Q-band (35.000 GHz) and 7 K.

solvent	B_0 / mT	A_f	$T_{1,f}$ / ms	A_s	$T_{1,s}$ / ms
CH ₂ Cl ₂	1216.5	-1.43 ± 0.05	4.4 ± 0.2	-0.56 ± 0.05	14.9 ± 0.9
CHCl ₃	1216.0	-0.37 ± 0.07	2.2 ± 0.6	-1.74 ± 0.08	8.7 ± 0.3
CD ₂ Cl ₂	1216.5	-0.78 ± 0.03	1.9 ± 0.1	-1.34 ± 0.04	7.1 ± 0.1
CDCl ₃	1216.0	-0.4 ± 0.1	2.1 ± 0.8	-1.7 ± 0.1	7.5 ± 0.4
CS ₂	1216.0	-0.8 ± 0.1	0.7 ± 0.2	-1.28 ± 0.09	4.7 ± 0.3
1:1 CD ₂ Cl ₂ /CS ₂	1216.0	-0.92 ± 0.02	0.85 ± 0.03	-1.1 ± 0.02	3.74 ± 0.05

Table 12: Parameters of monoexponential fit function according to equation (90) and standard deviations for inversion recovery experiment of **Cu-Odbm_{0.001%}** recorded at Q-band (35.000 GHz) and 7 K.

B_0 / mT	A_f	$T_{1,f}$ / ms	A_s	$T_{1,s}$ / ms
1217.8	-	-	-1.943 ± 0.006	18.3 ± 0.1

Table 13: Parameters of biexponential fit functions according to equation (63) and standard deviations for Hahn echo experiments of investigated compounds with O-donor ligands in 0.001 M solution (1:1 CD₂Cl₂/CS₂) recorded at Q-band (35.000 GHz in all cases) and 7 K.

compound	B_0 / mT	A_f	$T_{M,f}$ / μ s	A_s	$T_{M,s}$ / μ s
Cu-Oacac	1218.4	0.39 ± 0.01	2.8 ± 0.1	0.63 ± 0.01	11.2 ± 0.2
Cu-Otfac	1216.0	0.8 ± 0.1	4.0 ± 0.2	0.3 ± 0.1	6.9 ± 0.9
Cu-Ohfac	1210.0	0.612 ± 0.007	5.0 ± 0.1	0.416 ± 0.007	29.0 ± 0.5
Cu-Ofod	1246.0	0.92 ± 0.02	1.69 ± 0.07	0.27 ± 0.01	18.1 ± 0.8
Cu-Obzac	1217.0	0.743 ± 0.008	2.20 ± 0.04	0.349 ± 0.005	19.3 ± 0.3
Cu-Odbm	1216.0	0.547 ± 0.007	3.21 ± 0.07	0.509 ± 0.005	25.3 ± 0.3

Table 14: Parameters of biexponential or stretched exponential fit functions according to equations (63) and (64) and standard deviations for Hahn echo experiments of **Cu-Odbm** in different solvents (0.001 M) recorded at Q-band (35.000 GHz in all cases) and 7 K.

solvent	B_0 / mT	A_f	$T_{M,f}$ / μ s	A_s	$T_{M,s}$ / μ s	k
CH₂Cl₂	1216.5	-	-	0.962 ± 0.007	7.94 ± 0.06	1.50 ± 0.02
CHCl₃	1216.0	-	-	0.968 ± 0.006	18.7 ± 0.2	-
CD₂Cl₂	1216.5	0.40 ± 0.02	3.0 ± 0.2	0.712 ± 0.007	39.0 ± 0.7	-
CDCl₃	1216.0	0.395 ± 0.009	4.2 ± 0.2	0.664 ± 0.007	33.7 ± 0.5	-
CS₂	1216.0	0.50 ± 0.03	2.1 ± 0.2	0.481 ± 0.007	48 ± 2	-
1:1 CD₂Cl₂/CS₂	1216.0	0.547 ± 0.007	3.21 ± 0.07	0.509 ± 0.005	25.3 ± 0.3	-

Table 15: Parameters of stretched exponential fit function according to equations (64) and standard deviations for Hahn echo experiment of **Cu-Odbm_{0.001%}** recorded at Q-band (35.000 GHz in all cases) and 7 K.

B_0 / mT	A_s	$T_{M,s}$ / μ s	k
1218.8	0.940 ± 0.005	7.74 ± 0.03	2.69 ± 0.04

Discussion of the Influences of the Ligand on Electron Spin Dynamics for Compounds with O-Donor Ligands

Figure 16 graphically summarizes the ligand dependence of spin-lattice and spin-spin relaxation times in compounds with O-donor ligands in 0.001 M frozen solution (CD₂Cl₂/CS₂, 1:1). Error bars indicated in Figure 16 are standard deviations of the fit parameters and the experimental uncertainty is around 10 %, as indicated previously (see footnote p.83). The relative contributions of the fast and slow process to the overall inversion recovery curve are visualized by the size of the symbols, which corresponds to the relative sizes of the exponential prefactors. From Figure 16 it can be seen, that the variation of the ratio is small and close to a 50:50-contribution of both processes of spin-lattice relaxation. The absolute values of the slow spin-lattice relaxation process show slight variations, which could be assigned to differences in the rigidity of the ligands. The rigidity of ligands with the same core structure is determined by the mobility of the substituents.^[24-26, 55] In **Cu-Ohfac** the CF₃-substituents^[24-26, 55] are rigid and possess only few groups as source of librations, leading to one of the longest spin-lattice relaxation times in the ligand-dependence series. Similarly, the rigid phenyl-substituents in **Cu-Obzac** and **Cu-Odbm** provide low mobilities, which results in long spin-lattice relaxation times.

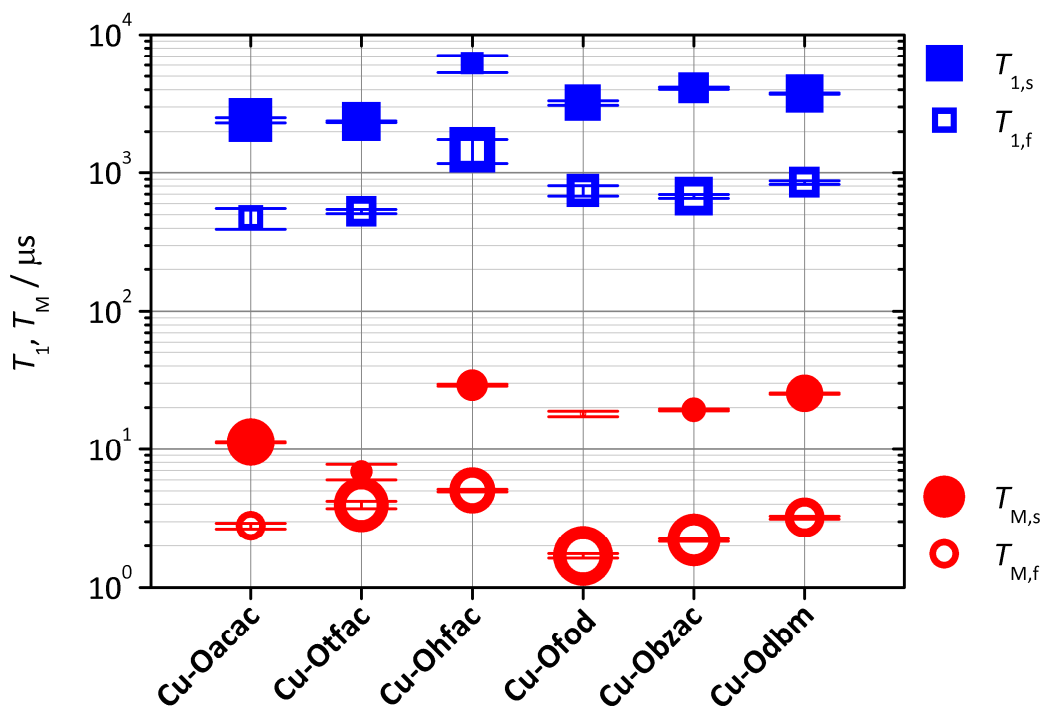


Figure 16: Ligand dependence of spin-lattice- and spin-spin relaxation times in microseconds of compounds with O-donor ligands in 0.001 M solution (1:1 $\text{CD}_2\text{Cl}_2/\text{CS}_2$), recorded at Q-band (35.000 GHz in all cases) and 7 K; values extracted from fit functions according to Table 10 and Table 13. Blue, filled squares (red, filled circles) indicate the slow process of spin-lattice (spin-spin) relaxation and blue, open squares (red, open circles) represent the fast process of spin-lattice (spin-spin) relaxation. Error bars correspond to the standard deviations of the fit functions. The size of the symbols corresponds to the relative size of the exponential prefactors A_f and A_s of the fast and slow process of spin-lattice and spin-spin relaxation time, respectively, extracted from fit functions.

In **Cu-Ofod** six CH_3 -groups are present, which can perform rotations via quantum tunneling processes even at very low temperatures,^[3] introducing substantial motional dynamics in the ligand. The CH_3 -groups are part of a *tert*-butyl group in **Cu-Ofod** and therefore sterically hindered, so the compound shows slightly slower spin-lattice relaxation compared to **Cu-Otfac** and **Cu-Oacac** with two or four sterically unhindered methyl-groups, respectively.

The variations of relative contributions of the fast and slow spin-spin relaxation process in dependence of the ligand appear slightly more pronounced than in the case of spin-lattice relaxation at first sight. However, concerning an experimental error of 10 % as explained above, the variations are negligible (except for **Cu-Ofod**) and mostly an equal contributions of the fast and the slow process are found. Comparing the absolute values of the slow phase memory times of all investigated compounds, the literature-known tendency of decreasing phase memory times

in the presence of methyl groups^[3] is confirmed. The $T_{M,s}$ time almost triples going from **Cu-Oacac** and **Cu-Otfac** to the CH₃-free compounds **Cu-Ohfac** and **Cu-Odbm**. The latter two compounds show the longest phase memory times in this series. Both have very similar values of $T_{M,s} > 25 \mu\text{s}$, although having different compositions and rigidities as discussed above. Hence, rigidity is not the limiting factor. Also the number and kind of contained magnetic nuclei, as well as the distance of the magnetic nuclei are strong influences on dephasing. The dipolar coupling between electron- and nuclear spins scales with r^{-3} (see section 2.2.3), which further contributes to the complex interplay of influences on electron spin relaxation.

Discussion of the Influences of the Solvent on Electron Spin Dynamics for Compounds with O-Donor Ligands

Figure 17 graphically summarizes the solvent dependence of spin-lattice and spin-spin relaxation times in **Cu-Odbm** in 0.001 M frozen solution.

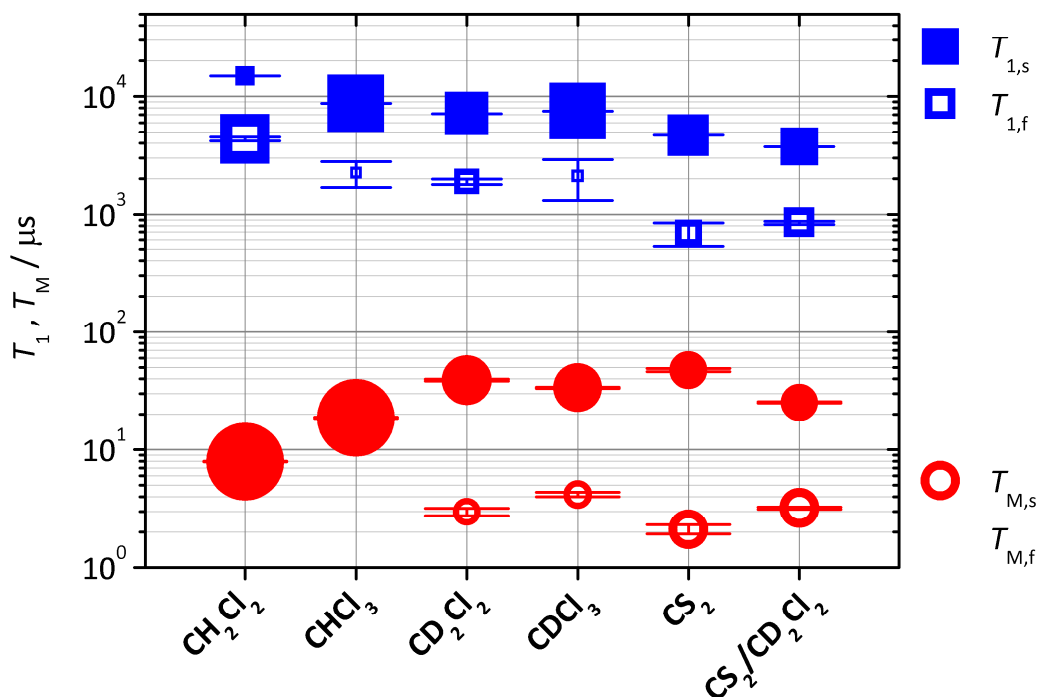


Figure 17: Solvent dependence of spin-lattice- and spin-spin relaxation times in microseconds of **Cu-Odbm** in different solvents, recorded at Q-band (35.000 GHz in all cases) and 7 K; values extracted from fit functions according to Table 11 and Table 14. Blue, filled squares (red, filled circles) indicate the slow process of spin-lattice (spin-spin) relaxation and blue, open squares (red, open circles) represent the fast process of spin-lattice (spin-spin) relaxation. Error bars correspond to the standard deviations of the fit functions. The size of the symbols corresponds to the relative size of the exponential prefactors A_f and A_s of the fast and slow process of spin-lattice and spin-spin relaxation time, respectively, extracted from fit functions.

Cu-Odbm was selected, as it shows the longest phase memory times together with **Cu-Otfac**. Furthermore, **Cu-Odbm** was found to be less hygroscopic than **Cu-Otfac**. When exposed to air, **Cu-Otfac** rapidly changes color from dark turquoise to pale green, indicating a hydrate formation. In contrast, the elemental analysis of **Cu-Odbm** indicated the pure compound even after days of exposition to air. **Cu-Odbm** is thus easier to handle and simplifies obtaining consistent results.

First, the contributions of fast and slow spin-lattice relaxation are discussed. Figure 17 shows in nearly all cases a dominant slow process of spin-lattice relaxation. For CH_2Cl_2 an inverse behavior is observed, here the fast process dominates with over 70 %. These variations are more pronounced here compared to the ligand dependence measurement series discussed further above, where equal contributions of both processes for all samples were found. This finding substantiates the initially stated hypothesis of the fast process belonging to a solvent adduct species. Within this reasoning, the variation in these contributions could be associated with a different degree of solvent adduct formation as mentioned further above. However, it is not assured whether solvent adducts would display much shorter relaxation times than the pure compounds. The real origin of the biexponential behavior remains ambiguous and needs further investigation. As stated above with the presentation of the results of electron spin relaxation measurements, also a different degree of cluster formation or spectral diffusion could account for the fast relaxation.

For the phase memory times, the relative contributions of fast and slow components of the biexponential decay curves are similar to what was found for the spin-lattice relaxation times. Regarding the absolute values of the slow phase memory times, some interesting features can be found. Substituting the contained protons in the solvents by deuterons increases the phase memory time by a factor of ca. three. Removing the remaining magnetic nuclei leads to a very long phase memory time of almost 50 μs of **Cu-Odbm** in CS_2 , which is among the longest values for transition metal compounds in frozen solutions.^[1-2] Not only the absolute phase memory time values, but also the shape of the Hahn echo decay curves reveals information on electron spin relaxation. **Cu-Odbm** in protonated solvents shows non-biexponential Hahn echo decay curves. **Cu-Odbm** in CHCl_3 can be fitted with a monoexponential function. In CH_2Cl_2 , **Cu-Odbm** exhibits a stretched exponential Hahn echo decay curve according to equation (64). The stretch factor of $k = 1.50 \pm 0.02$ indicates physical motion of magnetic nuclei as main decoherence

process.^[3] This in turn means, that in this system the mobility of the compound and the surrounding matrix has major influence on the relaxation properties. In order to increase phase memory times, the glassy matrix needs to be replaced by a more rigid one.

Discussion of the Influences of the Matrix on Electron Spin Dynamics for Compounds with O-Donor Ligands

A comparison of **Cu-Odbm** in frozen solution and in a doped powder will give insight in the influence of the rigidity and three dimensional structure of the matrix on electron spin dynamics.

The extracted spin-lattice relaxation time $T_{1,s}$ for the doped powder is 18.3 ± 0.1 ms which is up to ca. seven times longer than in the frozen solution samples of **Cu-Odbm**. This is attributed to the higher rigidity of the microcrystalline matrix, leading to fewer available low energy vibration modes. The absence of a second spin-lattice relaxation process in the doped powder corroborates the presence of a second species in solution, presumably a solvent adduct.

The phase memory time extracted from a stretched exponential fit with $T_{M,s} = 7.74 \pm 0.03$ μ s is comparable to the values determined for **Cu-Odbm** in the protonated solvents and in CD_2Cl_2/CS_2 , but much lower than in the other deuterated solvents. This can be explained by the higher number of protons in vicinity to the electron spin, located in the ligands of neighboring molecules in the microcrystalline matrix. The stretch parameter is 2.69 ± 0.04 , which indicates nuclear spin diffusion as main decoherence process^[3] in **Cu-Odbm**_{0.001%}. The found stretch parameter of ca. 1.5 in the measurement of **Cu-Odbm** in CH_2Cl_2 indicates physical motion of magnetic nuclei as main decoherence process. The findings on stretch parameters underline the higher rigidity of the powder matrix compared to the glassy solutions.

Summary regarding Spin Dynamics in Compounds with O-Donor Ligands

The influences of ligand and matrix composition in copper(II)-coordination compounds with Oacac-type ligands were investigated systematically and the study revealed valuable insights. We found multiple EPR-active species in frozen solution, which are probably caused by a mixture of the coordination compounds (major compound) and solvent adducts (minor component) in varying degree. Biexponential relaxation curves were found in most cases. Slow components were assigned to the actual spin-lattice or spin-spin relaxation process, respectively. The fast processes

can be due to be spectral diffusion, clusters of paramagnetic species in the frozen solutions or solvent adducts, but no unambiguous assignment was possible.

A dependence of the electron spin relaxation times on ligands and also on the matrix was found. In general, a decreased mobility and higher rigidity of ligand and matrix leads to longer spin-lattice relaxation times. An interplay between the rigidity of the system and surrounding as well as the number and kind of magnetic nuclei in vicinity of the observed electron spin is the most important influence on phase memory times. Methyl groups were found to act strongly dephasing and longer phase memory times were found in deuterated compared to protonated solvents. In proton-containing solvents, physical movements of magnetic nuclei were found as main decoherence process, displaying the conformational lability of the ligands and matrix. The dephasing processes and relative contributions were not clearly separable in the frozen solution measurements. In contrast, one defined paramagnetic species and one relaxation process was found in the doped powder **Cu-Odbm**_{0.001%}. The spin-lattice relaxation was slower compared to $T_{1,s}$ in solution samples of **Cu-Odbm**, which was attributed to the higher rigidity. Due to the higher local proton concentration in the doped powder compared to deuterated frozen solutions, a much shorter phase memory time was found. Nuclear spin diffusion was found as main decoherence process in the doped powder sample rather than in the case of frozen solutions, where physical movement of magnetic nuclei governs dephasing. This contrast displays the higher rigidity of the powder matrix.

Although the investigations of compounds with O-donor ligands revealed respectable phase memory times of up to 48 μ s, these systems are not yet eligible for quantum computing applications due to several reasons. First, even longer phase memory times are needed. The extracted values for the investigated compounds are long, but still not long enough to allow fault-tolerant quantum computation (figure of merit ≤ 2500 , required: ≥ 10000). Second, the qubit-species are not well defined in most cases. This inhibits a quantitative understanding of decoherence processes in the systems which was inter alia aimed to achieve in this investigation. In addition, ill-defined species militate against qubit applications according to the DiVincenzo criteria.^[13] Finally, the observed spin-lattice relaxation times are not exceptionally long at low temperatures, which could be a limiting factor for applications at higher temperatures.

An exchange of protons in the ligand by nuclei with smaller gyromagnetic ratio (e.g. deuterium) could further decrease decoherence and therefore displays a potential solution towards the first issue. For complete substitution of H by D, an increase of the phase memory times by a factor of six can be expected, according to the six times smaller gyromagnetic moment of D compared to H nuclei.^[28] Moving from the frozen solutions to the doped powder already resulted in better defined EPR-active species. This could be further improved by investigating single crystal or atomically flat ordered arrays of the compound. Well-defined, isolated systems potentially allow the unambiguous assignment of relaxation processes and a quantitative understanding of influences. The third named problem of the studied compounds with O-donor ligands discovered in this investigation will probably remain unchanged by deuterating the ligand and moving to different sample matrices. Longer spin-lattice relaxation times afford more rigid compounds, which can only be achieved by employing different ligands, such as π -conjugated bidentate- or ring-ligands.

3.1.2 Spin Dynamics in Compounds with N-Donor Ligands

In this section, the results of the investigation of spin dynamics in coordination compounds with phthalocyanine-type ligands (“N-donor ligands”) will be introduced and discussed. The key questions here were the influences of ligand substitution and the effect of the central transition metal ion on electron spin dynamics in order to develop a deeper understanding of electron spin relaxation. A series of transition metal phthalocyanines was chosen as target compounds for the systematic investigation (Figure 18).

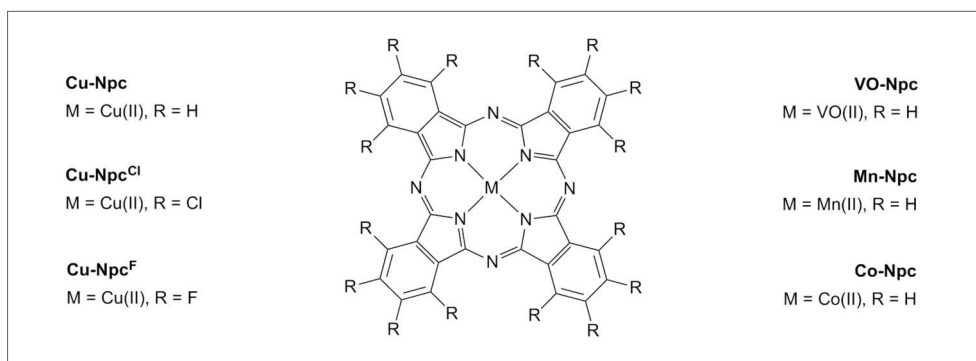


Figure 18: Investigated compounds with N-donor ligands. Figure adapted from K. Bader et al., *Chem. Commun.* 2016, 52, 3623–3626.^[70]

The group of transition metal phthalocyanines offers a range of advantages for qubit-purposes. Phthalocyanine complexes are present in nature and industry as dyes or in cosmetics, DVDs and solar cells. This broad range of applications and large interest from many sides makes them not only commercially cheaply available on an industrial scale, but has also led to a sophisticated materials science.^[85-86] Furthermore, transition metal phthalocyanines are highly chemically stable. The charge-neutral phthalocyanine complexes can be evaporated, which offers the opportunity of molecular beam surface deposition for manufacturing of thin films. The qubit properties of copper(II)-phthalocyanine (**Cu-Npc**) in bulk and in thin films were reported recently.^[21] Despite the variety of applications of transition metal phthalocyanines and the connected well-established material science, little is known of their electron spin dynamics.^[21, 87] In terms of systematic EPR studies, so far only the influence of solvents on molecular orbitals of transition metal phthalocyanines as well as the involved change in g - and A -tensors was reported.^[88-89]

All compounds with N-donor ligands were investigated under the same conditions. The samples were 0.5 mM frozen solutions of the compounds in D₂SO₄. Previous investigations assured that electron spin relaxation is concentration-independent in this regime.^[90] The solubility of phthalocyanines is poor in most common solvents; this can be improved by substitution of ligand protons by halides or organic groups. The solvent D₂SO₄ provides high solubility for the compounds and simultaneously contains a low number of nuclear spins. A comparative investigation of **Cu-Npc**, **Cu-Npc^{Cl}** and **Cu-Npc^F** should give insight in the influences of different ligand substitution. This substitution pattern was investigated previously regarding the effect on electron spin dynamics in Cr₇Ni-MQBs.^[57] There, an increase in phase memory time for the substitution of protons by magnetically similar fluorine nuclei in the ligands was found.

A variation of the central metal ion (VO²⁺, Mn²⁺, Co²⁺, Cu²⁺) enables the comparison of the effect of spin-orbit-coupling (SOC), different coordination geometries (square-planar *versus* square-pyramidal) as well as different spin quantum number (all $S = 1/2$, except **Mn-Npc**: $S = 3/2$)^[91-92] on electron spin relaxation. In terms of the central transition metal ion in MQBs, little is known about influences on electron spin relaxation. Increasing spin-lattice relaxation rates were reported for increasing spin-orbit coupling of the central ion,^[24-25, 31, 55] but this effect is not always visible.^[56]

In the following, the systematic investigation of influences on electron spin relaxation in transition metal phthalocyanines is presented. First, the ESE-detected EPR spectra will be displayed and discussed according to the influences of ligand and central metal ion. Second, the results of the electron spin dynamics investigation regarding the influences of solvent, ligand and central metal ion is presented. The compounds were purchased and used without further purification. Details on sample preparation, collection and evaluation of data can be found in the Experimental Section (5.2). Measurements presented in this section were performed in the B.Sc.-project of Mario Winkler.^[90] A part of this investigation was published in *Chemical Communications* in 2016.^[70]

ESE-detected EPR Spectra

ESE-detected EPR spectra were recorded for all samples prior to spin dynamics measurements. The results including simulations are shown in Figure 19 and the corresponding simulation parameters are listed in Table 16. The spectra of **Cu-Npc**, **Cu-Npc^{Cl}** and **Cu-Npc^F** are very similar. In all three cases, two main signals are visible in the range of 1100–1250 mT with a resolved fine structure on the signal located at lower fields. The spectra were simulated with an $S = 1/2$, $I = 3/2$ -spin system with axial g - and A -tensors, which is common for square-planar copper(II)-coordination compounds. The values of g - and A -components of the three complexes are similar, although not identical. This reflects the similarity of the compounds in terms of coordination geometry and Cu^{2+} as central ion in all cases, the minor variations are attributed to the different peripheral substituents on the phthalocyanine ligand (H, Cl, F). The ligands probably introduce subtle changes in the energies of the MOs of the compounds, which then can be observed by small variations in g and A . Such an effect in MQBs was already reported in literature.^[89]

The EPR-spectra of the compounds with the same ligand but different central ion (**Cu-Npc**, **VO-Npc**, **Mn-Npc** and **Co-Npc**) vary strongly. For **Mn-Npc** and **Co-Npc** two sets of signals are visible, like in the case of **Cu-Npc** discussed above. The spectrum of **Mn-Npc** was simulated with an $S = 3/2$, $I = 5/2$ -spin system with axial g - and A -tensors (natural isotopes: 100 % ^{55}Mn , $I = 5/2$). The axial and perpendicular g -components of **Mn-Npc** are very similar, whereas for the hyperfine coupling tensor only a parallel component was included (i.e. A_{\perp} was fixed to 0).

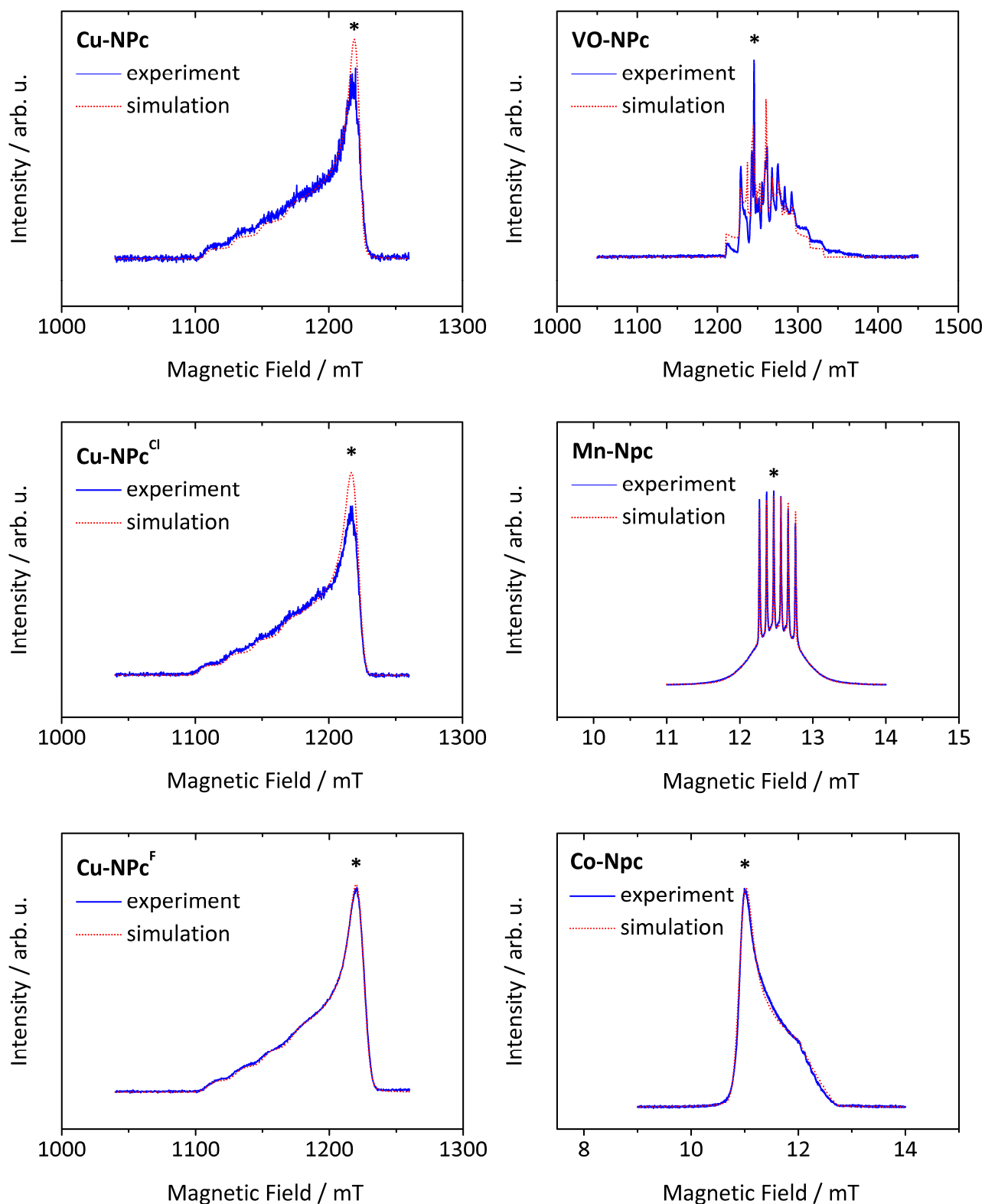


Figure 19: ESE-detected EPR spectra of investigated compounds with N-donor ligands in 0.5 mM solution (D_2SO_4) recorded at Q-band (35.000 GHz in all cases) and 7 K. Blue, solid lines represent experimental data and red, dotted lines indicate corresponding simulations. Simulation parameters can be found in Table 16. The asterisks indicate field positions for spin dynamics measurements.

3. Results & Discussion

Table 16: Simulation parameters for ESE-detected EPR spectra (Figure 19) of investigated compounds with N-donor ligands in 0.5 mM solution (D_2SO_4) recorded at Q-band (35.000 GHz in all cases) and 7 K.

compound	g_{\parallel}	g_{\perp} or (g_{yy}, g_{xx})	A_{\parallel} / MHz	A_{\perp} or (A_{yy}, A_{xx}) / MHz	ΔB_{twpp} / mT
Cu-Npc	2.1965 ± 0.0005	2.0502 ± 0.0005	610 ± 10	30 ± 10	[4 0.5]
Cu-Npc^{Cl}	2.2050 ± 0.0005	2.0525 ± 0.0005	620 ± 10	30 ± 10	[7 0]
Cu-Npc^F	2.1925 ± 0.0005	2.0470 ± 0.0005	630 ± 10	15 ± 10	[7.5 0.5]
VO-Npc	1.9975 ± 0.0005	$(1.9760, 1.9760) \pm 0.0005$	480 ± 10	$(220, 85) \pm 10$	[0.5 0]
Mn-Npc	2.0000 ± 0.0005	1.9978 ± 0.0005	278 ± 10	0 (fixed)	[0.6 0]
Co-Npc	2.0232 ± 0.0005	2.2830 ± 0.0005	259 ± 10	60 ± 10	[0 2]

For **Co-Npc** an $S = 1/2$, $I = 7/2$ -spin system with axial g - and A -tensors was used for the simulation (natural isotopes: 100 % ^{59}Co , $I = 7/2$). Here the axial is larger than the perpendicular g -component, which is the opposite for the other compounds observed in this study. According to the nuclear spin of cobalt of $7/2$, eight hyperfine-split resonance lines are expected, but only seven lines are resolved in the high-field part of the spectrum due to a low S/N -ratio. Similar to the case of **Cu-Npc** and **Mn-Npc**, the hyperfine coupling in **Co-Npc** is only resolved for the parallel component. In these three cases, the hyperfine splitting is smaller than the linewidth and therefore not resolved. Although the errors were carefully determined by variations of fit parameters until a deviation between experiment and simulation became visible, the real uncertainty in the perpendicular hyperfine coupling components could be larger than indicated in Table 16 for **Cu-Npc**, **Mn-Npc** and **Co-Npc**, as they are smaller than the linewidth as indicated above.

The spectrum of **VO-Npc** differs strongly from those of the above discussed compounds; the simulation of the spectrum includes an $S = 1/2$, $I = 7/2$ -spin system with an axial g - and a rhombic A -tensor (natural isotopes: 99.75 % ^{51}V , $I = 7/2$; 0.75 % ^{50}V , $I = 6$). Here, the metal ion is coordinated in a square-pyramidal geometry in contrast to the square-planar ones discussed above, which explains the observed different tensor-symmetries.

In summary, the spectra of the investigated compounds with N-donor ligands display different features due to their electron- and nuclear spin quantum numbers, the coordination geometries as well as the ligand substitutions. All these factors influence the electronic structure, i.e. the molecular orbitals of the compounds which is translated into variations in the symmetry and the magnitude of components of g - and A -tensors.

Results of Electron Spin Relaxation Measurements of Compounds with N-Donor Ligands

After observing pronounced differences in the ESE-detected EPR spectra for the phthalocyanines compounds, the electron spin dynamics were investigated. In all spin dynamics measurements the magnetic field was fixed to the position of the most intense spectral line, indicated by the asterisks in Figure 19.

Initial spin dynamics measurements of **Cu-Npc** were performed in 0.5 mM solution for H_2SO_4 and D_2SO_4 as solvents. The result of inversion recovery- and Hahn echo experiments are shown in Figure 20 (ESE-detected spectrum of **Cu-Npc** in H_2SO_4 including simulation see Supplementary Figure 11). For the further investigations, D_2SO_4 was used as solvent. The experimental inversion recovery- and Hahn echo results as well as the according fit curves are shown in the Appendix (Supplementary Figure 12-Supplementary Figure 16).

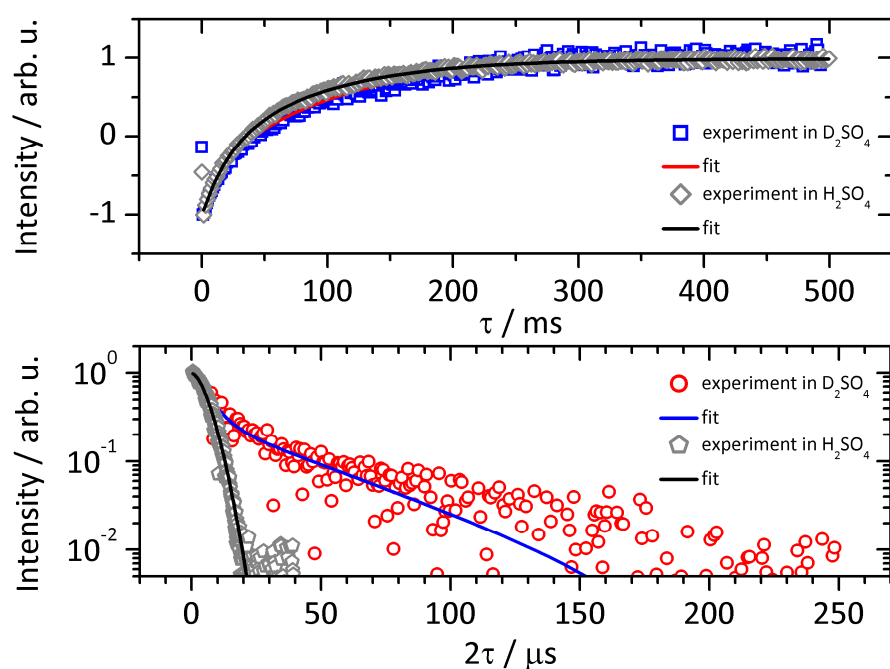


Figure 20: Electron spin relaxation measurements and fits of **Cu-Npc** in 0.5 mM solution (D_2SO_4 and H_2SO_4 in comparison) measured at Q-band (35.000 GHz) and 7 K. Magnetic field was fixed to the position indicated by the asterisk in the corresponding ESE-detected EPR spectra shown in Figure 19 and Supplementary Figure 11, respectively. Top panel: Inversion recovery experiment. Blue, open squares (grey, open diamonds) indicate experimental data and red (black), solid line represents fit function (fit parameters see Table 17). Bottom panel: Hahn echo experiment. Red, open circles (grey, open pentagons) indicate experimental data and blue (black), solid line represents fit function (fit parameters see Table 18). Figure adapted from K. Bader et al., *Chem. Commun.* 2016, 52, 3623–3626.^[70]

All inversion recovery curves were fitted with biexponential functions (fit parameters see Table 17) and the extracted spin-lattice relaxation times span a wide range of $T_{1,f} = 0.134 - 226$ ms and $T_{1,s} = 0.69 - 2405$ ms. The Hahn echo decay curves were also fitted with biexponential functions in most cases, only for H_2SO_4 a stretched exponential was more appropriate (fit parameters: Table 18). The extracted phase memory times are between $T_{M,f} = 2.1 - 6.1$ μs and $T_{M,s} = 7.78 - 43$ μs . In the biexponential echo decay curves for both spin-lattice- and spin-spin relaxation, the slow relaxation time is attributed to the actual relaxation processes. The origin of the fast process cannot be determined definitively from this set of data. Possible explanations are the occurrence of spectral diffusion or a second paramagnetic species (clusters, solvent adducts) with faster relaxation compared to the main species, as introduced in the previous Section.

A graphical summary of the relaxation data (D_2SO_4 samples) is shown in Figure 21.

Table 17: Parameters of biexponential fit functions according to equation (90) and standard deviations for inversion recovery experiments of investigated compounds with N-donor ligands in 0.5 mM solution (D_2SO_4) recorded at Q-band (35.000 GHz in all cases) and 7 K. Asterisk assigns sample in H_2SO_4 .

compound	B_0 / mT	A_f	$T_{1,f} / \text{ms}$	A_s	$T_{1,s} / \text{ms}$
Cu-Npc*	1218.8	-0.71 ± 0.03	20 ± 1	-1.29 ± 0.04	85 ± 2
Cu-Npc	1218.8	-0.58 ± 0.04	14 ± 2	-1.52 ± 0.04	103 ± 3
Cu-Npc^{Cl}	1216.9	-1.7 ± 0.2	36 ± 4	-0.3 ± 0.2	140 ± 56
Cu-Npc^F	1219.7	-0.9 ± 0.1	14 ± 2	-1.1 ± 0.1	60 ± 4
VO-Npc	1245.0	-1.49 ± 0.06	226 ± 18	-0.59 ± 0.04	2405 ± 268
Mn-Npc	1246.4	-0.93 ± 0.02	0.134 ± 0.005	-1.06 ± 0.02	0.69 ± 0.01
Co-Npc	1100.0	-0.95 ± 0.03	2.7 ± 0.1	-1.13 ± 0.03	11.1 ± 0.2

* Asterisk assigns sample in H_2SO_4 .

Table 18: Parameters of mono-, bi- or stretched exponential fit functions according to equations (63) and (64) and standard deviations for Hahn echo experiments of investigated compounds with N-donor ligands in 0.5 mM solution (D_2SO_4) recorded at Q-band (35.000 GHz in all cases) and 7 K. Asterisk assigns sample in H_2SO_4 .

compound	B_0 / mT	A_f	$T_{M,f} / \mu\text{s}$	A_s	$T_{M,s} / \mu\text{s}$	k
Cu-Npc*	1218.8	-	-	0.999 ± 0.005	7.78 ± 0.04	1.66 ± 0.02
Cu-Npc	1218.8	0.79 ± 0.03	6.1 ± 0.5	0.32 ± 0.03	41 ± 4	-
Cu-Npc^{Cl}	1216.9	-	-	1.01 ± 0.01	43 ± 1	-
Cu-Npc^F	1219.7	0.45 ± 0.04	3.8 ± 0.6	0.62 ± 0.02	40 ± 2	-
VO-Npc	1245.0	0.61 ± 0.08	2.1 ± 0.5	0.27 ± 0.04	22 ± 5	-
Mn-Npc	1246.4	0.37 ± 0.01	4.1 ± 0.2	0.65 ± 0.01	14.0 ± 0.2	-
Co-Npc	1100.0	-	-	0.961 ± 0.005	9.44 ± 0.07	-

* Asterisk assigns sample in H_2SO_4 .

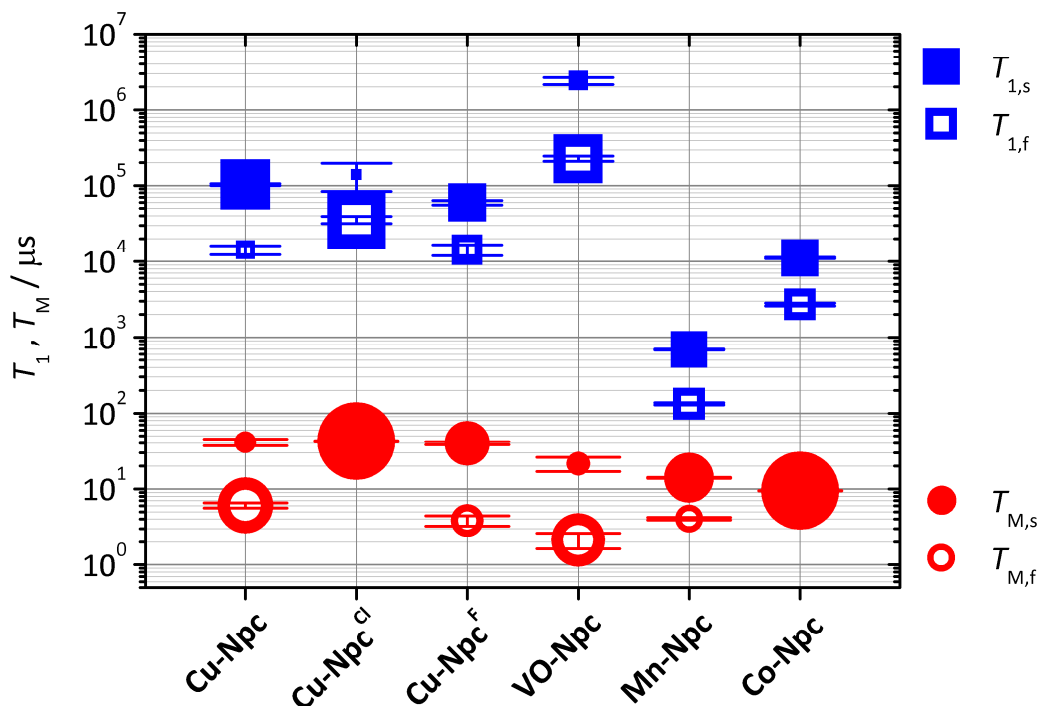


Figure 21: Ligand- and metal ion dependence of spin-lattice- and spin-spin relaxation times in microseconds of compounds with N-donor ligands in 0.5 mM solution (D_2SO_4), recorded at Q-band (35.000 GHz in all cases) and 7 K; values extracted from fit functions according to Table 17 and Table 18). Blue, filled squares (red, filled circles) indicate the slow process of spin-lattice (spin-spin) relaxation and blue, open squares (red, open circles) represent the fast process of spin-lattice (spin-spin) relaxation. Error bars correspond to the standard deviations of the fit functions. The size of the symbols corresponds to the relative size of the exponential prefactors A_f and A_s of the fast and slow process of spin-lattice and spin-spin relaxation time, respectively, extracted from fit functions. Figure adapted from K. Bader et al., *Chem. Commun.* 2016, 52, 3623–3626.^[70]

Discussion of the Influences of the Solvent on Electron Spin Dynamics for Compounds with N-Donor Ligands

The influence of the solvent on relaxation in compounds with N-donor ligands was studied for **Cu-Npc** (Figure 20). The extracted fast and slow spin-lattice relaxation times of **Cu-Npc** in H_2SO_4 and D_2SO_4 are quite similar, so the solvent has no influence on spin-lattice relaxation. In contrast, the results of Hahn echo measurements of **Cu-Npc** in the two solvents are different. The phase memory time in H_2SO_4 is approximately five times shorter than $T_{M,s}$ in D_2SO_4 . This is in agreement with the expected trend from literature that replacing magnetic nuclei by ones with smaller gyromagnetic ratio increases the phase memory times.^[28-30] Furthermore, in protonated sulfuric acid a stretched exponential rather than a biexponential Hahn echo decay is found. The

stretch parameter of $k = 1.66 \pm 0.02$ indicates physical motion of magnetic nuclei as main dephasing process. The phthalocyanine ligand is a quite rigid system, but the solvent matrix provides a large number of weakly bound protons (*via* hydrogen bridges) which are possibly the main source of dephasing in this system. As the deuterated solvent leads to more favorable phase memory times, the remaining investigations were carried out in D_2SO_4 .

Discussion of the Influences of the Ligand on Electron Spin Dynamics for Compounds with N-Donor Ligands

The influence of the ligand on spin-lattice relaxation in the investigated compounds with N-donor ligands can be probed by comparing the values for $T_{1,s}$ of **Cu-Npc**, **Cu-Npc^{Cl}** and **Cu-Npc^F**. For the first two compounds, values around 100 ms were obtained, whereas for the last one $T_{1,s}$ is only about half of that. This decrease is attributed to changes in the phonon spectrum, which are caused by the change in electronic structure due to the different ligand substituents.^[70] The large electronegativity of the fluorine substituents compared to chlorine and hydrogen probably induces changes in the molecular orbitals of the compounds. Furthermore, intermolecular interactions (Van-der-Waals forces, hydrogen-bridges) between solvent matrix and the complex change with different ligand substitution. These effects then may lead to unequal overall rigidities of the compounds which can be translated into changes in the phonon spectrum. The fast spin-lattice relaxation times of **Cu-Npc**, **Cu-Npc^F** and **Cu-Npc^{Cl}** are similar, but the contribution of the fast process increases in the named order.

The slow phase memory times of the differently substituted copper(II)phthalocyanines are almost independent on the ligand. This is interesting, as the hydrogen and fluorine substituents have similar gyromagnetic ratio, but that of $^{35,37}Cl$ is only ca. 1/10 of the former ones. The remote location of the substituents with respect to the paramagnetic transition metal ion probably damps the effect of nuclear spin induced spectral diffusion, as dipolar coupling thorough space scales with r^{-3} between the electron- and nuclear spin. Nuclear spin diffusion requires a large number of nuclear spins forming a bath, where flip-flop processes are possible. Such a bath is formed for example by the deuterium-nuclei of the solvent matrix. Furthermore, the aforementioned change in electronic structure which influenced the spin-lattice relaxation does not seem to have an influence on spin-spin relaxation, so other effects must be dominant here.

The slow phase memory times of **Cu-Npc**, **Cu-Npc^F** and **Cu-Npc^{Cl}** are around 40 μs , which is among the highest reported values for transition metal compounds in frozen solution and in doped powder. ^[1, 56, 69-70] The contribution of the fast process is 50 % or more, except for **Cu-Npc^{Cl}** where it is not visible. A possible explanation for this could be differences in the efficiency of nuclear spin diffusion. Although nuclear spin diffusion does seem not to be the dominant process it can severely influence spin dynamics (dominant nuclear spin diffusion would manifest itself in a stretched exponential Hahn echo decay with a stretch parameter of $k \approx 2-3$, see section 2.2.3). Conceivably, the nuclear spin flip-flop transfer from the solvent matrix nuclei to the ligand nuclei depends on the similarity of their magnetic properties. Fluorine and hydrogen are magnetically similar but chlorine is not, so presumably the described transfer process is inhibited in the case of **Cu-Npc^{Cl}**.^[70]

Discussion of the Influences of the Central Metal Ion on Electron Spin Dynamics for Compounds with N-Donor Ligands

A comparison of the compounds with unsubstituted phthalocyanine ligands and varying central metal ions should give insight in the dependence of electron spin dynamics on the transition metal ion. The inversion recovery curves of **Cu-Npc**, **VO-Npc**, **Mn-Npc** and **Co-Npc** are biexponential. The fast process of spin-lattice relaxation contributes to 50 % or more in all cases except for **Cu-Npc**, where a dominant slow process is observed. No correlation between this behavior and the chemical properties of the compounds is obvious. Maybe the fast relaxing species is indeed a solvent adduct, like proposed in the case of Oacac-compounds discussed in section 3.1.1, but for a definitive assignment more data is needed.

The absolute values of $T_{1,f}$ and $T_{1,s}$ follow the same trend. A decrease of the spin-lattice relaxation time by one order of magnitude each is observed for **VO-Npc**, **Cu-Npc**, **Co-Npc**, **Mn-Npc** in the named order. For **VO-Npc**, the slow process of spin-lattice relaxation is in the range of seconds, which is unusually long for transition metal complexes in frozen solutions. The chemical properties of this potential MQB are ideal for exhibiting such long relaxation times. **VO-Npc** is a $S = 1/2$, for which no Orbach process of spin-lattice relaxation is operative (section 2.2.4). A decreased efficiency of the Orbach process enables longer relaxation times. Furthermore, the compound has a square-pyramidal coordination geometry. Octahedral and related

coordination geometries were reported to be favorable for long spin-lattice relaxation times.^[26] In addition, **VO-Npc** exhibits the smallest SOC in the investigated series of compounds. As described in section 2.2.4, a smaller SOC leads to longer spin-lattice relaxation times. For **Cu-Npc**, **Co-Npc** and **Mn-Npc** no correlation between SOC and $T_{1,s}$ is observed, so other influences must be dominant. Considering the electronic structure of all investigated compounds with N-donor ligands, a correlation between the orbitals with unpaired electrons and spin-lattice relaxation is unraveled. In **Mn-Npc** and **Co-Npc** at least one unpaired electron is located in an orbital with d_z -contribution (d_{z^2} and/or d_{xy} , d_{yz}).^[93-94] In **Cu-Npc** and **VO-Npc** this is not the case ($d_{x^2-y^2}$ and d_{xy} , respectively).^[93, 95] An unpaired electron in orbitals with d_z -contribution is possibly more susceptible to fluctuations in the environment: These orbitals are oriented perpendicular to the phthalocyanine-ring plane, so the electron in these orbitals experiences a strong interaction with the matrix compared to electrons in orbitals in the ring plane. Electrons in orbitals with d_z -contributions are highly exposed to fluctuations in the surrounding in this kind of compounds, which leads to faster spin-lattice relaxation.^[70]

The phase memory times of **Cu-Npc**, **VO-Npc**, **Mn-Npc** and **Co-Npc** show smaller variations compared to the above discussed variations in spin-lattice relaxation times. Here again we find biexponential Hahn echo decay curves, except for **Co-Npc**. The $T_{M,s}$ -values of **Cu-Npc** and **VO-Npc** are slightly longer than those of **Mn-Npc** and **Co-Npc**. This is in agreement with the previously discussed location of unpaired electrons in these compounds. A higher exposition of the electron to the surrounding in the last two could account for the smaller phase memory times. Surprisingly, the slow phase memory time of **VO-Npc** is only half of the value for **Cu-Npc**, although the spin-lattice relaxation of the former compound was about a magnitude slower compared to the latter one. The difference in orbitals bearing the unpaired electron spin or a different degree of delocalization of the electron could account for that. The variations in phase memory times are in general not as pronounced observed for the spin-lattice relaxation times, so other, so far not identified influences on spin-spin relaxation must be important as well. Most probably this involves nuclear spin diffusion by weakly coupled nuclear spins in ligand and matrix (H, N, D).

Summary regarding Spin Dynamics in Compounds with N-Donor Ligands

The influences of ligand substitution and central ion in transition metal phthalocyanine complexes were investigated systematically. We found biexponential relaxation characteristics in most cases, where the slow process was assigned to the actual spin-lattice or spin-spin relaxation, respectively. The origin of the fast process was assumed to be either solvent adducts clusters of paramagnetic species or spectral diffusion. The comparative study of copper(II)-compounds with variously substituted phthalocyanine ligands (H, Cl, F) showed that peripheral ligand substituents alter the g - and A -tensors as well as the electronic composition. These changes are weak and have no pronounced effect on spin dynamics. In general, the phase memory times of the investigated copper compounds are long. The figure of merit (see 1.1) of **Cu-Npc^{Cl}** is about 2000, which is among the highest reported ones for transition metal complexes in frozen solution.^[1-2] Furthermore, the Hahn echo decay of **Cu-Npc^{Cl}** is monoexponential, provides a high controllability of the qubit system.

The comparative investigation of electron spin relaxation properties in phthalocyanine complexes with different central metal ions (VO^{2+} , Mn^{2+} , Co^{2+} , Cu^{2+}) revealed valuable information on influences on spin dynamics. We found spin-lattice relaxation times in the range of seconds for **VO-Npc**, which arises from the stable coordination geometry (square-pyramidal), the rigidity of the ligand, the absence of an Orbach process ($S = 1/2$ -system) as well as the low SOC. Furthermore, the orientation of the orbital bearing the unpaired electron with respect to the phthalocyanine ring was identified as major influence on electron spin relaxation. Electron spins in orbitals perpendicular to the ring plane have a higher sensitivity towards environmental fluctuations, as the overlap with the surrounding is larger compared to orbitals parallel to the ring plane. Therefore faster spin dynamics can be expected for electron spins in orbitals with larger contact with the environment.

In conclusion, transition metal phthalocyanines are promising MQB candidates. They exhibit long relaxation times in combination with a chemical robustness, which is favorable for real quantum computing devices. If the limiting processes for phase memory time in this class of compound could be identified and removed, possibly coherence times in the order seconds could be achieved. At this point of the investigation it is assumed, that the limiting factor are the deuterium nuclear spins in the solvent. This bath of nuclear spins does not exist in a doped

powder, which could for example be prepared with **Zn-Npc** as diamagnetic host for the paramagnetic compounds. However, for an exact determination of the limiting factor on coherence in the investigated compounds with N-ligands, a wider range of relaxation data should be analyzed. For example, more systematic studies involving a variation of the matrix (e.g. frozen solutions of different solvents, doped powders, single crystals) and deuteration of the ligand or further functionalization could help solving this problem. In addition, variation of physical parameters could give more insight in the underlying relaxation mechanisms and processes. Finally, studying electron spin relaxation properties of a molecular monolayer of transition metal phthalocyanines would be interesting in order to probe the effect of fundamental changes in the MQBs surrounding on spin dynamics.

3.1.3 Spin Dynamics in Compounds with S-Donor Ligands

In this section, the results of the investigation of spin dynamics in compounds with S-donor ligands will be presented and discussed. We aim to pinpoint and quantify the influences on electron spin relaxation in MQBs by varying sample matrix, counter ion, ligands and central metal ion in a comparative pulsed EPR-study. The main interest here is to analyze the interplay of structural influences on electron spin dynamics, such as the rigidity and composition of ligands and matrix, and effects of nuclear spins in various distances and coupling strengths to the potential MQB's electron spin (e.g. nuclear spin of the central metal ion, on the ligands, in the counter ions or sample matrix). For this study 1,2-dithiolenes were selected as S-donor ligands, since they show a range of advantageous feature for the aspired investigation. Transition metal complexes with 1,2-dithiolene ligands are very well investigated systems.^[96] Besides showing a rich coordination chemistry, they also show interesting conductivity and magnetic properties in the solid state.^[97] They form stable complexes with many transition metals in a multitude of oxidation states.^{[98-99]**}

** Unpaired electrons are actually delocalized between the metal ion and the ligand due to the non-innocent character of dithiolene-ligands. The dative bonds are also highly covalent in general.^[99] Note that the assignment of oxidation states in this Section is only a formalism applied for distinguishing paramagnetic from diamagnetic compounds.

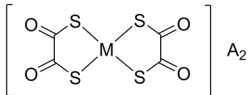
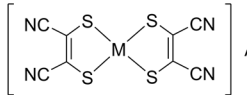
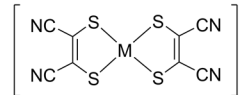
A^+			
$(PPh_4)^+$	M-Sdto^P	M-Smnt^P	M-Smnt^P_{para}
$(d_{20}\text{-}PPh_4)^+$	M-Sdto^{P/d}	M-Smnt^{P/d}	M-Smnt^{P/d}_{para}
$(d_{20}\text{-}AsPh_4)^+$	M-Sdto^{As/d}	M-Smnt^{As/d}	-
Na^+	-	M-Smnt^{Na}	-
	M = Cu^{2+} , Ni^{2+}	M = Cu^{2+} , Ni^{2+}	M = Ni^{3+}

Figure 22: Investigated compounds with S-donor ligands.

Figure 22 shows the compounds investigated in this section. In all cases, a square planar coordination environment is present as qubit core. This geometry was shown to enable longer relaxation times than tetrahedral distorted ones.^[26] Furthermore the singly occupied molecular orbital (SOMO) of both copper(II)- and nickel(III)-dithiolene complexes points in the plane of square-planar coordinating ligands,^[100] which we supposed beforehand (3.1.2) as favorable for long electron spin relaxation times.^[70] The selected ligands are 1,2-dithiooxalate (Sdto) and maleonitrile-1,2-dithiolate (or 1,2-dicyanoethylene-1,2-dithiolate, Smnt). The former consist of C, O and S which makes it a nuclear-spin-free ligand. The latter contains nitrogen, which naturally consists of $I \neq 0$ - isotopes only. Nevertheless, the coupling to the remote nitrogen nuclear spins in paramagnetic Smnt-coordination compounds is small, and the close vicinity of the electron spin is essentially nuclear-spin-free.^[101-102] Both ligands, Smnt and Sdto, yield complexes with similar MS_n -coordinations, where M is Cu^{2+} , Ni^{2+} or Ni^{3+} . A comparison of Smnt- and Sdto-compounds should therefore give insight into the influence of weakly coupled ligand nuclear spins on electron spin relaxation in otherwise very similar compounds. The number and magnitude of nuclear spins in the qubits vicinity was further varied by employing a range of counter ions of the complexes. The chosen cations are (perdeutero)-tetraphenylphosphonium (**P** and **P/d**), perdeuterotetra-phenylarsonium (**As/d**) and sodium (**Na**). The cations **P**, **P/d** and **As/d** provide good solubility of the compounds in organic solvents and lead to interesting, columnar packing of the complex anions in the solid state,^[103-104] which will be discussed later on. **Na** was chosen as small counter ion for comparison an for exploring the effect of structural changes on relaxation.

Furthermore a comparison of different matrices, namely solution vs. doped powders, was performed to shed light on the impact of changes in the qubit periphery on the relaxation properties. The solvents of choice were $\text{CH}_2\text{Cl}_2/\text{CS}_2$ (1:1) and $\text{CD}_2\text{Cl}_2/\text{CS}_2$ (1:1). The mixtures provide good solubility towards the investigated compounds and do not enhance redox-reactions in contrast to other solvents, such as alcohols.^[98] Furthermore, the chosen solvents were also used in the investigation of compounds with O-donor ligands (section 3.1.1), so the results are comparable.

In all doped powders, a diamagnetic Ni^{2+} -analogue of the paramagnetic compound was used as host. The concentration of the paramagnetic species in the diamagnetic host lattice was ≤ 0.01 %. Previous investigations assured that electron spin relaxation is concentration independent for the selected concentrations for doped powders and frozen solutions.

Finally the influence of the central metal ion was investigated for one of the compounds with S-donor ligands. It is known, that weakly coupled nuclear spins decrease the coherence time, where particularly protons have a very strong effect due to their large magnetic moments.^[28-30] In contrast, no influence on electron spin relaxation was found for strongly coupled nuclear spins of the paramagnetic metal ion.^[24-25, 31] Nevertheless, strongly coupled nuclear spins can enhance decoherence under certain circumstances, e.g. in the case of forbidden spin transitions induced by hard microwave pulses.^{††} In this thesis, the influence of nuclear spins of central metal ions in complexes with S-donor ligands was investigated. **Ni-Smnt_{para}** was chosen as “nuclear-spin-free” reference specimen for **Cu-Smnt**, which conveniently allows a direct comparison of almost identical compounds: both have a square-planar coordination geometries with similar bond lengths and -angles.^[104] Nickel naturally consists of over 98 % nuclear-spin-free isotopes (1.14 % ^{61}Ni , $I = 3/2$) and copper exclusively has natural isotopes with $I \neq 0$ (^{63}Cu , ^{65}Cu , $I = 3/2$). Table 19 gives an overview of all investigated samples for the probed compounds with S-donor ligands. In the following, the systematic investigation of influences on electron spin relaxation in compounds with S-donor ligands is presented. First the ESE-detected EPR spectra will be

^{††} Hard MW pulses are typically of 2-20 ns for 3d transition metal compounds. According to equation (89), the excitation bandwidth for such pulses is 600 - 60 MHz, which is comparable to many values of hyperfine coupling strength of the named compounds.

displayed and discussed according to the influences of central metal ion, ligand and sample matrix. Second, the results of the electron spin dynamics investigations are presented. The discussion here is split into Cu^{2+} - and Ni^{3+} -based compounds with S-donor ligands.

Table 19: Overview investigated samples matrices for compound with S-donor ligands.

compound	$\text{CH}_2\text{Cl}_2/\text{CS}_2$	$\text{CD}_2\text{Cl}_2/\text{CS}_2$	doped powder
Cu-Sdto^P	✓	✓	✓
Cu-Sdto^{P/d}	✓	✓	✓
Cu-Sdto^{As/d}	-	-	✓
Cu-Smnt^P	✓	✓	✓
Cu-Smnt^{P/d}	✓	✓	✓
Cu-Smnt^{As/d}	-	-	✓
Cu-Smnt^{Na}	-	-	✓
Ni-Smnt^P_{para}	-	-	✓
Ni-Smnt^{P/d}_{para}	-	✓	✓

The investigated compounds were synthesized following literature procedures.^[104-110] Perdeuterotetraphenylarsonium bromide was kindly synthesized by Simon Schlindwein from the Institute of Inorganic Chemistry, University of Stuttgart. Details on all synthetic procedures are given in the Experimental Section (5.1.8-5.1.27). First EPR test measurements on **Cu-Smnt^P** were performed during the B.Sc. thesis of Samuel Lenz.^[111] Part of the investigations on **Cu-Smnt^P** and **Cu-Smnt^{P/d}** has been published in *Nature Communications* in 2014.^[69]

ESE-Detected EPR Spectra of Compounds with S-Donor Ligands

Electron spin echo detected EPR spectra of the compounds with S-donor ligands were recorded on frozen solutions (1:1 $\text{CH}_2\text{Cl}_2/\text{CS}_2$ or $\text{CD}_2\text{Cl}_2/\text{CS}_2$, 1 mM for **Cu-Smnt^P**, **Cu-Smnt^{P/d}**, **Cu-Sdto^P**, **Cu-Sdto^{P/d}**, **Ni-Smnt^{P/d}_{para}**) and on doped powders (0.01 % of the paramagnetic Cu^{2+} - or Ni^{3+} -compound in the diamagnetic Ni^{2+} equivalent, all compounds except **Cu_mnt^P**: 0.001 %). The results are shown in Figure 23, Figure 24 and Figure 25 as well as in the Appendix (Supplementary Figure 17–Supplementary Figure 25). Simulation parameters are summarized in Table 20–Table 23.

Figure 23 shows the spectra of **Ni-Smnt^{P/d}_{para}** in frozen solution and as doped powder. The frozen solution spectrum shows three clearly resolved spectral features, which were simulated with a rhombic $S = 1/2$ -system without HF-interaction (Table 20). The line shapes were simulated with a Voigtian convolution, accounting for homogeneous broadening effects, in combination with a g -

strain, accounting for orientation-dependent effects. The observed values of g -tensor components are typical for square-planar monoanionic Ni(III)-bis-dithiolenes.^[112]

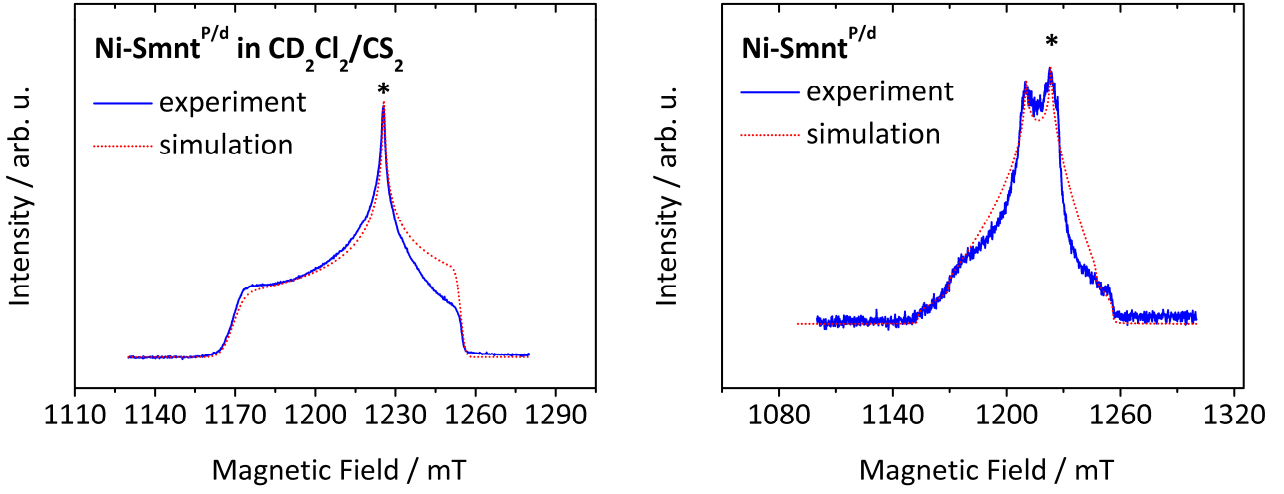


Figure 23: ESE-detected EPR spectra of Ni-Smnt^{P/d} in 1 mM solution (left panel, solvent as indicated) and as 0.01 % doped powders (right panel) recorded at Q-band (all 35.000 GHz) and 7 K. Blue, solid lines represent experimental data and red, dotted lines indicate corresponding simulations. Simulation parameters can be found in Table 20 and Table 21. The asterisks indicate field positions for spin dynamics measurements.

Table 20: Simulation parameters for ESE-detected EPR spectra (Q-band: 35.000 GHz and 7 K) of Ni-Smnt^{P/d}_{para} in 1 mM solution (1:1 CD₂Cl₂/CS₂).

compound	g_{zz}	g_{yy}	g_{xx}	ΔB_{lwpp} / mT	g -strain / MHz
Ni-Smnt ^{P/d} _{para} (solution)	2.1390 ± 0.0005	2.0404 ± 0.0005	1.9935 ± 0.0005	[0.6 0.1]	[0.005 0 0.015]

Table 21: Simulation parameters for ESE-detected EPR spectra (Q-band: 35.000 GHz and 7 K) of investigated Ni³⁺-compounds with Smnt-ligands in 0.01 % doped powder.

compound	Spin System	weight	g_{zz}	g_{yy}	g_{xx}	ΔB_{lwpp} / mT
Ni-Smnt ^P _{para}	1	1	2.166 ± 0.001	2.0440 ± 0.0005	1.991 ± 0.001	[0.2 0.3]
	2	0.9	2.148 ± 0.001	2.0660 ± 0.0005	2.005 ± 0.001	[0.2 0.3]
Ni-Smnt ^{P/d} _{para}	1	1	2.1980 ± 0.0005	2.0440 ± 0.0005	1.9905 ± 0.0005	[0.2 0.3]
	2	0.9	2.1680 ± 0.0005	2.0660 ± 0.0005	2.0050 ± 0.0005	[0.2 0.3]

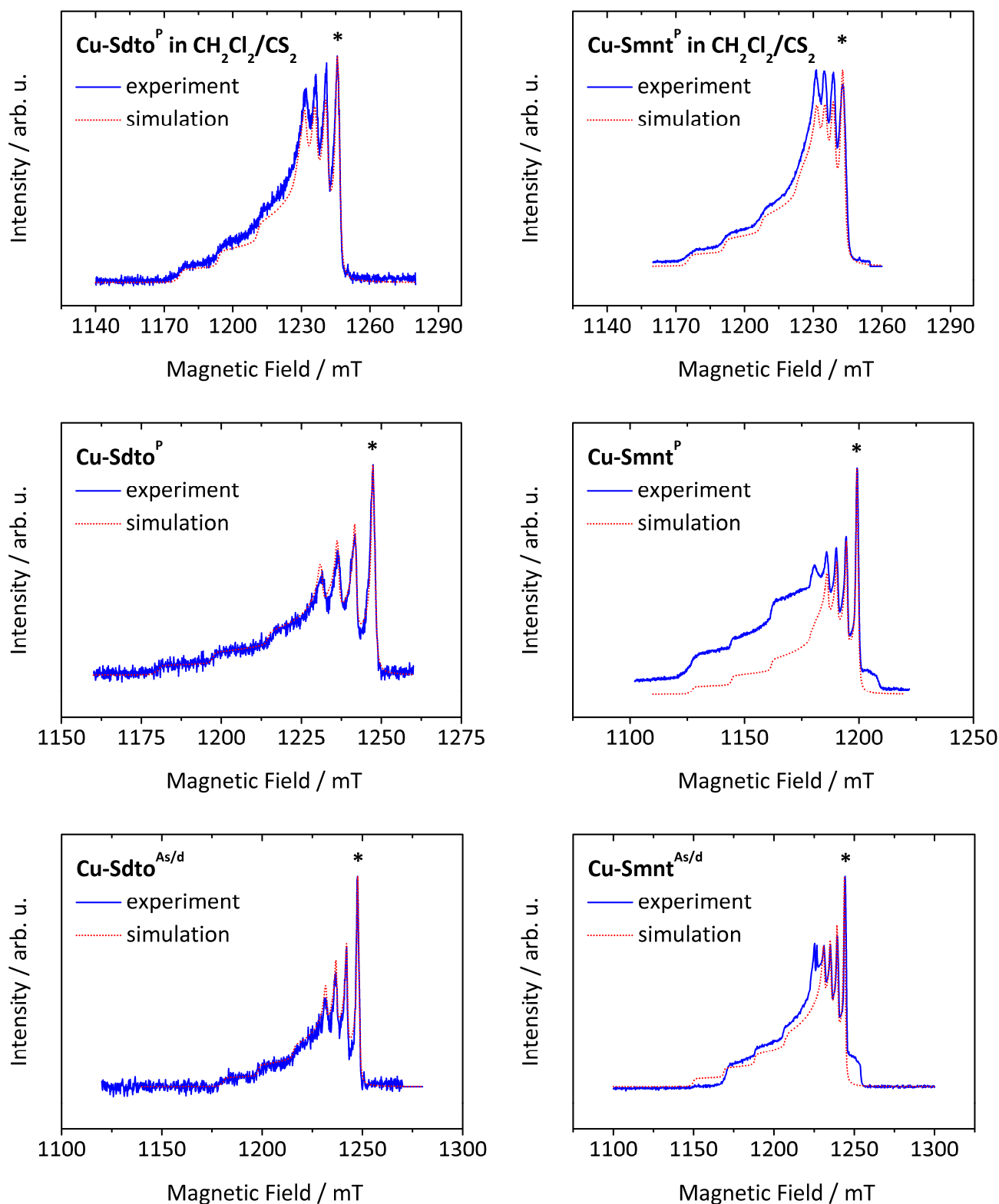


Figure 24: ESE-detected EPR spectra of investigated Cu-compounds with Sdto- and Smnt-ligands and different counter ions in 1 mM solution (solvent as indicated) and as 0.01 % doped powders (except $\text{Cu-Smnt}^{\text{P}}$: 0.001 %) recorded at Q-band and 7 K. Blue, solid lines represent experimental data and red, dotted lines indicate corresponding simulations. Simulation parameters can be found in Table 22 and Table 23. The asterisks indicate field positions for spin dynamics measurements.

3. Results & Discussion

Table 22: Simulation parameters for ESE-detected EPR spectra (Q-band and 7 K) of investigated Cu-compounds with Sdto-donor ligands in 1 mM solution (solvent indicated in brackets, a: CH₂Cl₂/CS₂, b: CD₂Cl₂/CS₂, both 1:1) or 0.01 % doped powder (except **Cu-Smnt^P**: 0.001 %; pwd indicated in brackets).

compound	ν_{MW} / GHz	g_{\parallel}	g_{\perp}	$A_{\parallel} / \text{MHz}$	A_{\perp} / MHz	$\Delta B_{lwpp} / \text{mT}$
Cu-Sdto^P (a)	34.995	2.0795 ± 0.0005	2.0180 ± 0.0005	490 ± 5	130 ± 5	[1.0 0.6]
Cu-Sdto^P (b)	34.999	2.0795 ± 0.0005	2.0180 ± 0.0005	490 ± 5	130 ± 5	[1.0 0.6]
Cu-Sdto^{P/d} (a)	34.999	2.0795 ± 0.0005	2.0180 ± 0.0005	490 ± 5	130 ± 5	[1.0 0.6]
Cu-Sdto^{P/d} (b)	35.000	2.0795 ± 0.0005	2.0180 ± 0.0005	490 ± 5	130 ± 5	[1.0 0.6]
Cu-Sdto^P (pwd)	35.000	2.0735 ± 0.0005	2.0175 ± 0.0005	490 ± 5	150 ± 5	[0.4 0.4]
Cu-Sdto^{P/d} (pwd)	35.000	2.0720 ± 0.0005	2.0165 ± 0.0005	500 ± 5	145 ± 5	[0.5 0.5]
Cu-Sdto^{As/d} (pwd)	35.000	2.0720 ± 0.0005	2.0167 ± 0.0005	500 ± 5	145 ± 5	[0.4 0.4]

Table 23: Simulation parameters for ESE-detected EPR spectra (Q-band and 7 K) of investigated Cu-compounds with Smnt-ligands in 1 mM solution (solvent indicated in brackets, a: CH₂Cl₂/CS₂, b: CD₂Cl₂/CS₂, both 1:1) or 0.01 % doped powder (except **Cu-Smnt^P**: 0.001 %; pwd indicated in brackets).

compound	ν_{MW} / GHz	g_{\parallel}	g_{\perp}	$A_{\parallel} / \text{MHz}$	A_{\perp} / MHz	$\Delta B_{lwpp} / \text{mT}$
Cu-Smnt^P (a)	34.998	2.0850 ± 0.0005	2.0205 ± 0.0005	455 ± 5	100 ± 5	[1.0 0.6]
Cu-Smnt^P (b)	34.999	2.0850 ± 0.0005	2.0205 ± 0.0005	455 ± 5	100 ± 5	[1.0 0.6]
Cu-Smnt^{P/d} (a)	35.001	2.0850 ± 0.0005	2.0205 ± 0.0005	455 ± 5	100 ± 5	[1.0 0.6]
Cu-Smnt^{P/d} (b)	35.001	2.0850 ± 0.0005	2.0205 ± 0.0005	455 ± 5	100 ± 5	[1.0 0.6]
Cu-Smnt^P (pwd)	33.770	2.0925 ± 0.0005	2.0227 ± 0.0005	500 ± 5	118 ± 5	[0.2 0.2]
Cu-Smnt^{P/d} (pwd)	34.994	2.0900 ± 0.0005	2.0203 ± 0.0005	515 ± 5	118 ± 5	[0.2 0.2]
Cu-Smnt^{As/d} (pwd)	35.000	2.1220 ± 0.0005	2.0303 ± 0.0005	560 ± 5	118 ± 5	[0.4 0.4]
Cu-Smnt^{Na} (pwd)	35.000	2.0750 ± 0.0005	2.0160 ± 0.0005	550 ± 5	135 ± 5	[0.4 0.4]

In the doped powder, more spectral features are visible and a lower S/N compared to the frozen solution measurement complicates the interpretation. A simulation with two rhombic $S = 1/2$ -spin systems with almost equal weights (Table 21) leads to a very good agreement of experiment and simulation. Almost identical spectral features and similar simulation parameters (except g_{zz}) are observed for **Ni-Smnt^P_{para}** (Supplementary Figure 17). The two observed paramagnetic species could be assigned to two different local geometries for **Ni-Smnt_{para}** in the diamagnetic Ni²⁺-host, which has been reported previously for similar compounds.^[113] Local strain in for **Ni-Smnt_{para}** is likely, as different charges of the dopant and host complex anions are accompanied with different crystal structure of the pure compounds.^[104]

Figure 24 shows the spectra of the investigated Cu-compounds with S-donor ligands. They have similar overall appearances, showing two sets of four equidistant features which are attributed to axial g - and A -tensors of the $S = 1/2$, $I = 3/2$ Cu^{2+} -cores. The g - and A -tensor values of the Cu^{2+} -based Smnt-systems obtained from the simulations are 2.0750–2.0925 for g_{\parallel} and 2.0160–2.0303 for g_{\perp} , as well as 455–560 MHz for A_{\parallel} and 100–135 MHz for A_{\perp} , which is in agreement with literature values of similar compounds.^[49-50, 114-115] For the Cu^{2+} -based Sdto-compounds values of 2.0720–2.0795 for g_{\parallel} and 2.0167–2.0180 for g_{\perp} , as well as 490–500 MHz for A_{\parallel} and 130–150 MHz for A_{\perp} are found. Due to the comparable electronic structures in the Smnt- and Sdto-compounds, their EPR-parameters are very similar.^[100, 116] For both Cu^{2+} -Smnt- and -Sdto-compounds, the region of the g_{\perp} -resonances is better resolved in the doped powder spectra, which is attributed to a lower linewidth compared to the frozen solution spectra.

Careful examination shows differences between intensities of the experimental spectra and simulations of variable degree for the investigated Cu^{2+} -compounds with Smnt-ligands. This difference is very pronounced in the case of **Cu-Smnt^{Na}** (Figure 25). The overall appearance of the spectrum of a 1 % doped powder sample is in agreement with the other investigated Cu^{2+} -compounds with Smnt-ligands. In contrast, the spectrum of the 0.01 % doped powder sample shows only very weak Cu^{2+} -features. The main species here is a rhombic $S = 1/2$ -system with similar g -tensor values as **Ni-Smnt_{para}^{Na}** in solution. This can be explained with the formation of **Ni-Smnt_{para}^{Na}** out of **Ni-Smnt^{Na}** during the synthesis of the doped powder. Rhombic features were detected for all investigated Cu^{2+} -compounds with Smnt-ligands to varying extents. In general, these features were found below doping percentages of 0.01 % and even in the pure Ni^{2+} -compound (intensities of Ni^{3+} -features comparable to most 0.01 % doped powder samples, not shown). For doping of approximately 1 % and higher, the Cu^{2+} -signals completely covers the Ni^{3+} -signals. Furthermore, a correlation between the synthetic protocol of **Ni-Smnt** and the intensity of the Ni^{3+} -signal was found: The shorter the time between formation of the complex in solution and precipitation of the final product, the higher the intensity of the Ni^{3+} -signal in the pure compound (not shown, details on synthesis see 5.1). Presumably, kinetically driven air-oxidation (or traces of other redox-active species) is responsible for the Ni^{3+} -species and longer reaction time favors the thermodynamically favored product Ni^{2+} .

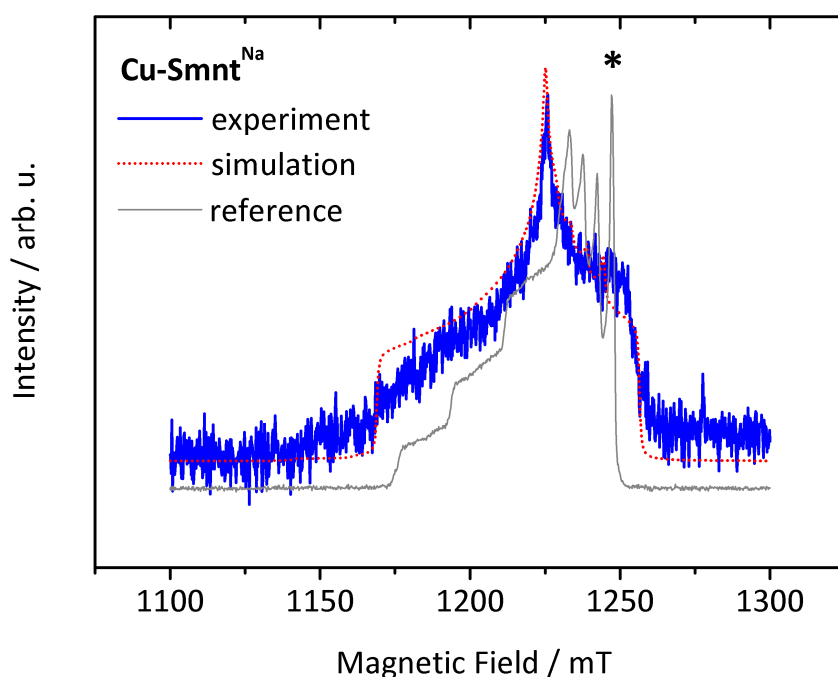


Figure 25: ESE-detected EPR spectrum of **Cu-Smnt^{Na}** as 0.01 % doped powder recorded at Q-band (35.000 GHz) and 7 K. Blue, solid line represents experimental data. Red, dotted line indicates simulation with two spin systems (System 1 as indicated in Table 23, weight: 0.08; System 2: $g_{zz} = 2.139 \pm 0.0005$, $g_{yy} = 2.041 \pm 0.0005$, $g_{xx} = 1.990 \pm 0.0005$, $\Delta B_{Iwpp}/\text{mT}$: [0.4 0.4], weight: 1). Grey, solid line represents reference data of **Cu-Smnt^{Na}** as 1 % doped powder. The asterisk marks magnetic field position for spin dynamics measurements.

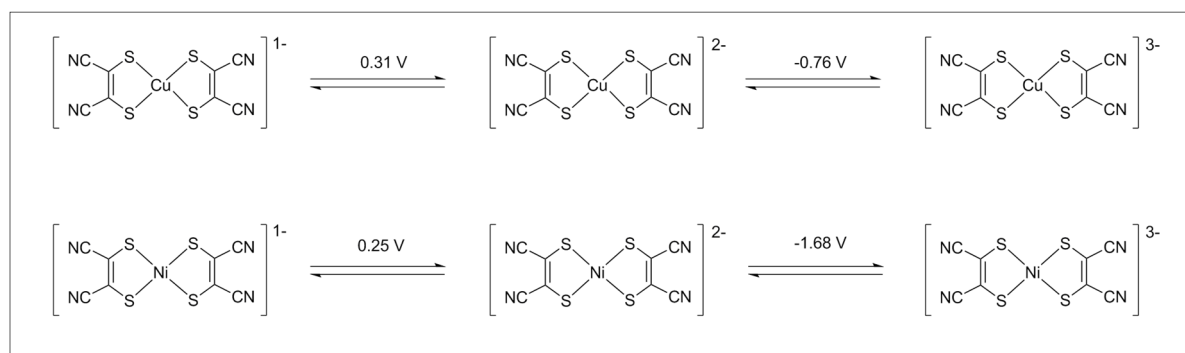


Figure 26: Redox-potentials of Cu- and Ni-Smnt species according to Wang *et al.*^[98]

The redox potential for **Cu-Smnt**- and **Ni-Smnt**-anions are shown in Figure 26. Although the oxidation potential for M^{2+}/M^{3+} for both investigated metals is negative (also under consideration of the relevant concentrations by means of the Nernst equation), the reaction is assumed to take place enhanced by influences of temperature, pressure, kind and amount of impurities in the

sample, etc. The Ni³⁺- and Cu³⁺-species are air-stable, but can be reduced by weakly Lewis-basic solvents such as alcohols.^[98]

Besides the amount of Ni³⁺ formed during the synthesis of **Ni-Smnt**-compounds, also the amount of Cu²⁺-compound incorporated into the diamagnetic host lattice determines the relative intensities of the “axial” Cu²⁺- and the “rhombic” Ni³⁺-signals in the doped powders. The amount is mainly determined by the crystal structures of dopant and host lattice. Structural variations will be discussed later in detail.

In the Sdto-compounds, no evidence of Ni³⁺-species formation was found. **Cu-Sdto** is known to be highly labile towards redox active impurities (e.g. uncoordinated Cu²⁺-ions) and even light: a one electron-oxidation leads to the decomposition of one of the ligands.^[110] This was also experimentally observed during the data collection on solution samples of **Cu-Sdto** for this investigation: after ca. 30 min in solution, the initially green solutions changed color to light brown, even in sealed sample tubes. Storage in the dark and at -60 °C retards the decomposition. Probably the situation is similar for **Ni-Sdto**, and a decomposition involved in an oxidation prevents the appearance of **Ni-Sdto_{para}**-signals in the corresponding EPR spectra.^{‡‡}

The actual Cu²⁺-concentration in the doped powders remains unclear. However, for the relaxation measurement it is only important that a certain threshold concentration of the paramagnetic species is not exceeded, above which the relaxation times get concentration dependent due to instantaneous diffusion. A lower actual concentration compared to the nominal one will thus have no influence on the electron spin relaxation times. The nominal concentration of 0.01 % was identified for **Cu-Smnt^{P/d}** being in the concentration independent regime.

Results of Spin Dynamics Measurements for Compounds with S-Donor Ligands

In order to determine the spin-lattice relaxation times and phase memory times of the investigated compounds, inversion recovery- and Hahn echo experiments were performed in deuterated and protonated frozen solution and in doped powders. As an example, Figure 27 shows the experimental results of **Cu-Smnt^P** in 1 mM solution (1:1 CH₂Cl₂/CS₂).

^{‡‡} The lability of the Sdto-compounds is also the reason, why no Sdto-coordination compound with small counter ion was involved in this investigation. Although **Ni-Sdto^K** and **Cu-Sdto^K** have been synthesized, the doped powders (prepared by following a literature procedure)^[117] did not show EPR-signals, tested up to 10 % nominal doping.

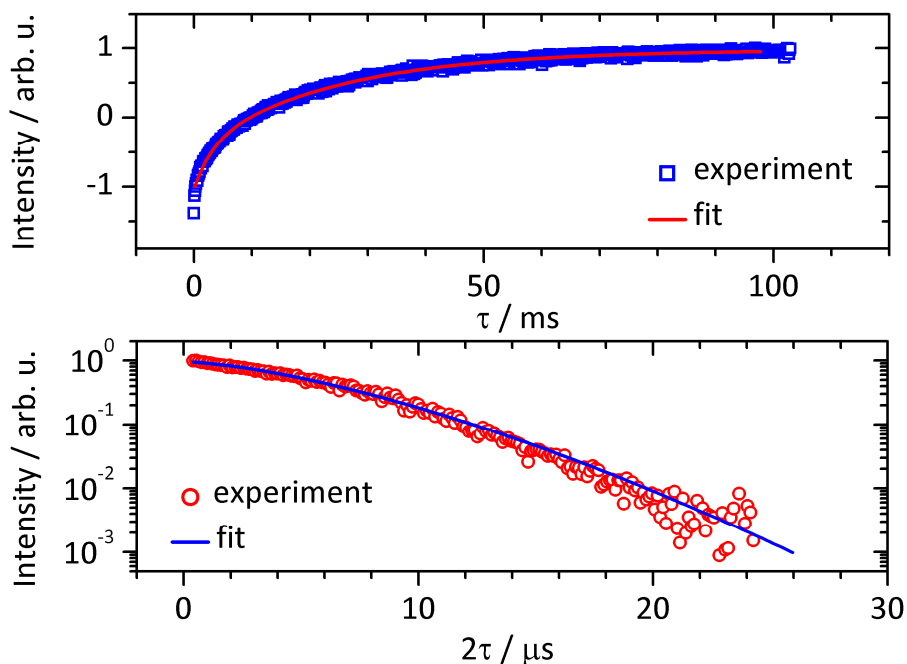


Figure 27: Electron spin relaxation measurements and fits of **Cu-Smnt^P** in 1 mM CH₂Cl₂/CS₂ solution (1:1) measured at Q-band (35.000 GHz) and 7 K. Magnetic field was fixed to the position indicated by the asterisk in the corresponding ESE-detected EPR spectra shown in Figure 24. Top panel: Inversion recovery experiment. Blue, open squares indicate experimental data and red, solid line represents fit function (fit parameters see Table 24). Bottom panel: Hahn echo experiment. Red, open circles indicate experimental data and blue, solid line represents fit function (fit parameters see Table 25).

Table 24: Parameters of biexponential fit functions according to equation (90) and standard deviations for inversion recovery experiments of investigated compounds with S-donor ligands in 1 mM solution (1:1 X/CS₂) recorded at Q-band (35.000 GHz in all cases) and 7 K.

compound	X	B_0 / mT	A_f	$T_{1,f}$ / ms	A_s	$T_{1,s}$ / ms
Cu-Sdto^P	CH ₂ Cl ₂	1245.8	-0.52 ± 0.01	2.3 ± 0.1	-1.17 ± 0.01	16.3 ± 0.2
Cu-Sdto^P	CD ₂ Cl ₂	1245.6	-0.89 ± 0.08	4.1 ± 0.6	-0.69 ± 0.08	20 ± 2
Cu-Sdto^{P/d}	CH ₂ Cl ₂	1245.9	-0.59 ± 0.02	3.7 ± 0.3	-0.97 ± 0.03	19.4 ± 0.5
Cu-Sdto^{P/d}	CD ₂ Cl ₂	1245.8	-0.59 ± 0.01	3.2 ± 0.1	-0.90 ± 0.01	21.1 ± 0.3
Cu-Smnt^P	CH ₂ Cl ₂	1242.8	-0.60 ± 0.01	3.2 ± 0.1	-1.40 ± 0.01	24.5 ± 0.3
Cu-Smnt^P	CD ₂ Cl ₂	1242.6	-0.70 ± 0.03	2.1 ± 0.2	-0.68 ± 0.01	39 ± 2
Cu-Smnt^{P/d}	CH ₂ Cl ₂	1243.1	-1.3 ± 0.1	3.9 ± 0.5	-1.1 ± 0.1	20 ± 2
Cu-Smnt^{P/d}	CD ₂ Cl ₂	1243.1	-0.89 ± 0.04	6.1 ± 0.4	-0.63 ± 0.04	32 ± 2
Ni-Smnt^{P/d}	CD ₂ Cl ₂	12273	-0.99 ± 0.06	1.6 ± 0.2	-1.03 ± 0.06	8.5 ± 0.5

Table 25: Parameters of mono-, bi- or stretched exponential fit functions according to equations (63) and (64) and standard deviations for Hahn echo experiments of investigated compounds with S-donor ligands in 1 mM solution (1:1 X/CS₂) recorded at Q-band and 7 K.

compound	X	B_0 / mT	A_f	$T_{M,f}$ / μ s	A_s	$T_{M,s}$ / μ s	k
Cu-Sdto^P	CH ₂ Cl ₂	1245.8	-	-	0.97 ± 0.01	8.9 ± 0.1	1.45 ± 0.03
Cu-Sdto^P	CD ₂ Cl ₂	1245.6	0.26 ± 0.01	3.3 ± 0.3	0.77 ± 0.01	22.7 ± 0.3	-
Cu-Sdto^{P/d}	CH ₂ Cl ₂	1245.9	-	-	0.967 ± 0.005	9.44 ± 0.05	1.51 ± 0.02
Cu-Sdto^{P/d}	CD ₂ Cl ₂	1245.8	0.37 ± 0.03	2.4 ± 0.4	0.757 ± 0.009	67 ± 2	-
Cu-Smnt^P	CH ₂ Cl ₂	1242.8	-	-	0.955 ± 0.007	7.15 ± 0.06	1.50 ± 0.02
Cu-Smnt^P	CD ₂ Cl ₂	1242.6	0.79 ± 0.05	0.88 ± 0.07	0.511 ± 0.009	15.2 ± 0.6	-
Cu-Smnt^{P/d}	CH ₂ Cl ₂	1243.1	-	-	0.968 ± 0.007	6.27 ± 0.05	1.22 ± 0.01
Cu-Smnt^{P/d}	CD ₂ Cl ₂	1243.1	0.23 ± 0.02	3.3 ± 0.5	0.81 ± 0.02	20.7 ± 0.4	-
Ni-Smnt^{P/d}	CD ₂ Cl ₂	12273	0.34 ± 0.02	3.7 ± 0.5	0.74 ± 0.01	38.7 ± 0.08	-

Table 26: Parameters of biexponential fit functions according to equation (90) and standard deviations for inversion recovery experiments of investigated compounds with S-donor ligands in 0.01 % doped powders (except **Cu-Smnt^P**: 0.001 %) recorded at Q-band and 7 K. MW frequency was 35.000 GHz in all cases except **Cu-Smnt^P**: 33.766 GHz.

compound	B_0 / mT	A_f	$T_{1,f}$ / ms	A_s	$T_{1,s}$ / ms
Cu-Sdto^P	1248.2	-	-	-1.39 ± 0.03	20.0 ± 0.7
Cu-Sdto^{P/d}	1248.5	-0.9 ± 0.3	8 ± 3	-0.6 ± 0.3	29 ± 10
Cu-Sdto^{As/d}	1247.6	-0.63 ± 0.06	8 ± 2	-1.02 ± 0.06	53 ± 3
Cu-Smnt^P	1217.2	-0.272 ± 0.004	6.9 ± 0.2	-1.683 ± 0.002	87.4 ± 0.2
Cu-Smnt^{P/d}	1244.9	-0.7 ± 0.2	7 ± 3	-0.86 ± 0.06	96 ± 10
Cu-Smnt^{As/d}	1244.1	-0.27 ± 0.05	7 ± 2	-1.58 ± 0.02	74 ± 1
Cu-Smnt^{Na}	1245.8	-1.4 ± 0.1	0.8 ± 0.2	-0.61 ± 0.08	8 ± 2
Ni-Smnt^P	1220.9	-0.80 ± 0.04	0.79 ± 0.06	-1.24 ± 0.04	3.8 ± 0.1
Ni-Smnt^{P/d}	1222.7	-0.91 ± 0.04	0.93 ± 0.06	-0.99 ± 0.06	4.0 ± 0.1

Table 27: Parameters of mono-, bi- or stretched exponential fit functions according to equations (63) and (64) and standard deviations for Hahn echo experiments of investigated compounds with S-donor ligands in 0.01 % doped powders (except **Cu-Smnt^P**: 0.001 %) recorded at Q-band and 7 K. MW frequency was 35.000 GHz in all cases except **Cu-Smnt^P**: 33.766 GHz.

compound	B_0 / mT	A_f	$T_{M,f}$ / μ s	A_s	$T_{M,s}$ / μ s	k
Cu-Sdto^P	1248.2	-	-	1.02 ± 0.01	7.0 ± 0.1	1.38 ± 0.03
Cu-Sdto^{P/d}	1248.5	0.42 ± 0.03	1.6 ± 0.2	0.69 ± 0.01	20.1 ± 0.5	-
Cu-Sdto^{As/d}	1247.6	0.67 ± 0.06	1.1 ± 0.2	0.48 ± 0.02	13.8 ± 0.7	-
Cu-Smnt^P	1217.2	-	-	1.018 ± 0.001	9.23 ± 0.01	2.48 ± 0.01
Cu-Smnt^{P/d}	1244.9	0.59 ± 0.02	4.2 ± 0.3	0.692 ± 0.007	68 ± 3	-
Cu-Smnt^{As/d}	1244.1	-	-	1.047 ± 0.008	34.4 ± 0.5	-
Cu-Smnt^{Na}	1245.8	1.3 ± 0.2	0.7 ± 0.1	0.26 ± 0.02	15 ± 2	-
Ni-Smnt^P	1220.9	-	-	7.78 ± 0.03	1.90 ± 0.02	-
Ni-Smnt^{P/d}	1222.7	0.21 ± 0.04	0.7 ± 0.1	1.131 ± 0.005	19.8 ± 0.1	-

The other relaxation measurement curves can be found in the Appendix (Supplementary Figure 26–Supplementary Figure 38). All inversion recovery curves were fit with mono- or biexponential functions according to equation (90). Hahn echo curves were mainly fit with mono- or biexponential functions according to equation (63); in some cases a stretched exponential according to equation (64) was used. The fit parameters for all these spin dynamics experiments can be found in Table 23–Table 26. The determined spin-lattice and phase memory times of all investigated compounds with S-donor ligands will be briefly summarized and compared here.

The spin dynamics of compounds with S-donor ligands exhibit two processes in most cases. As mentioned in the previous sections, the slow process is thought to represent the actual (spin-lattice- or spin-spin-) relaxation, whereas the fast process represents either spectral diffusion or faster relaxation of an additional paramagnetic species (cluster, solvent adducts etc.).^[3, 59]

The spin-lattice relaxation values for the investigated Cu²⁺-based Smnt-compounds in solution are quite similar with $T_{1,f} = 2.1$ – 6.1 ms and $T_{1,s} = 20$ – 39 ms. In the doped powders of Cu²⁺-based Smnt-compounds a wider distribution of values is found with $T_{1,f} = 0.8$ – 7 ms and $T_{1,s} = 8$ – 96 ms. For the Cu²⁺-based Sdto-compounds the results are comparable with overall slightly lower values, $T_{1,f} = 2.3$ – 4.1 ms and $T_{1,s} = 16.3$ – 21.1 ms in solution and a variation in the doped powders of $T_{1,f} = 0$ – 8 ms and $T_{1,s} = 20$ – 53 ms. For **Ni-Smnt**, values of $T_{1,f} = 1.73$ – 1.6 ms and $T_{1,s} = 3.8$ – 8.5 ms are found. The slow process of spin-lattice relaxation in the doped powder is twice as fast as in frozen solution.

In contrast to the mostly biexponential inversion recovery curves, the shape of the Hahn echo decay varies with the absolute number of protons in the vicinity of the paramagnetic center. For the Cu²⁺-based Smnt-compounds in deuterated solvents, biexponential decay curves with $T_{M,f} = 0.88$ – 3.3 μ s and $T_{M,s} = 15.2$ – 20.7 μ s are found. In protonated solutions of the Cu²⁺-based Smnt-compounds, stretched exponentials are observed with $T_{M,s} = 6.27$ – 7.15 μ s and stretch parameters of 1.22–1.50, which indicates physical motion of magnetic nuclei as main dephasing process. The doped Cu²⁺-based Smnt-powders show biexponential Hahn echo decays with a range of with $T_{M,f} = 0.7$ – 4.2 μ s and $T_{M,s} = 15$ – 68 μ s. Solely **Cu-Smnt^P** exhibits a stretched exponential in the doped powder, here $T_{M,s}$ is around 9 μ s and other than in solution ($k \approx 1.5$), the stretch parameter indicates here nuclear spin flip-flops as main dephasing process ($k \approx 2.5$).

Again, similar trends as discussed for Cu^{2+} -based Smnt are observed for the phase memory times of the Sdto-compounds. The maximum $T_{M,s}$ is here ca. 67 μs in solution, whereas the doped powder values cover the range of $T_{M,s} = 7.0\text{-}20.1 \mu\text{s}$. The coherence time of $\text{Ni-mnt}^{\text{P/d}}_{\text{para}}$ in frozen solution is almost 40 μs , which is similar to many state of the art MQBs.^[22, 69-70] The phase memory time of $\text{Ni-mnt}^{\text{P/d}}_{\text{para}}$ in the doped powder is approximately 20 μs (slow process), which is ca. 2.5 times longer than in the protonated derivative $\text{Ni-mnt}^{\text{P}}_{\text{para}}$. To the best of our knowledge, this study represents the first phase memory time measurements reported in literature for a nickel(III)-coordination compound.

Figure 28 gives a graphical overview on determined relaxation times for the investigated Cu^{2+} -compounds with S-donor ligands as basis for the discussion in the following subsections (graphical summary for Ni^{3+} -compounds: see subsection on central metal ion dependence).

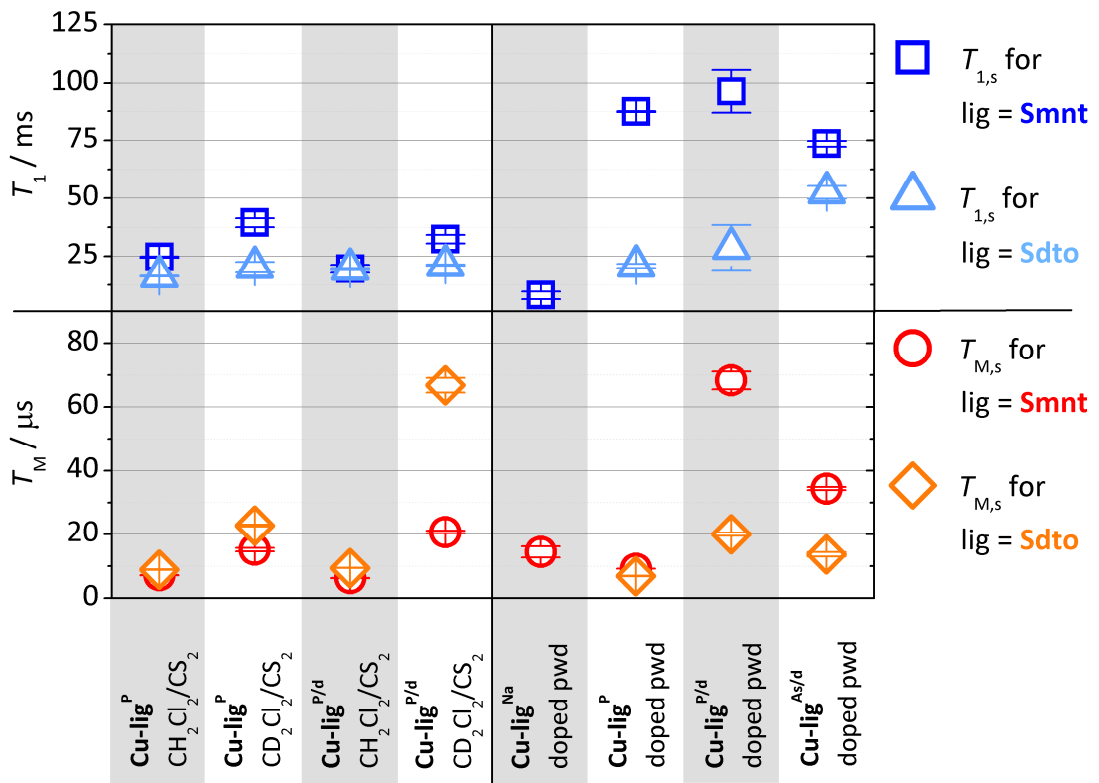


Figure 28: Spin-lattice relaxation times in milliseconds and spin-spin relaxation times in microseconds of compounds with S-donor ligands in 1 mM solution (solvent as indicated) and as 0.01 % doped powders (except **Cu-Smnt^P**: 0.001 %) recorded at Q-band and 7 K; values extracted from fit functions according to Table 24–Table 27). Blue, open squares (red, open circles) indicate the slow process of spin-lattice (spin-spin) relaxation of Smnt-compounds. Light blue, open triangles (orange, open diamonds) represent the slow process of spin-lattice (spin-spin) relaxation of Sdto-compounds. Error bars correspond to the standard deviations of the fit functions. In contrast to other figures of this type, no scaling was applied to the size of the symbols for reasons of clarity.

In the following sub-sections, an in-depth discussion of various influences on spin dynamics in compounds with S-donor ligands is presented. First, only the Cu²⁺-containing compounds will be discussed. Here we proceed from the core of the Cu²⁺-containing MQBs - the electronic structure of the paramagnetic ion and the first coordination sphere - further outside via the ligands towards the close and far surrounding of the potential qubit, i. e. the matrix (solvents and doped powders) and the three dimensional crystal structure. Finally, the similarities and differences of spin dynamics in the investigated Cu²⁺- and Ni³⁺-compounds will be discussed.

Discussion of Influences of the Coordination Geometry on Electron Spin Dynamics for Cu-Compounds with S-Donor Ligands

All investigated Cu²⁺-compounds have a Cu(II)S₄-core, where the SOMO is “in-plane” of ligands in all cases.^[99] In the investigation of compounds with N-donor ligands (previous Section), such an in-plane orbital geometry was found to be beneficial for long relaxation times in contrast to orbitals perpendicular to the molecular plane.^[70] The molecular orbital energies of the SOMOs vary slightly, which is displayed in little variations of g - and A -values, as previously mentioned in the discussion of the ESE-detected EPR spectra. Peisach & Blumberg discovered a linear relationship between $g_{||}$ and $A_{||}$ for CuX₄-compounds, where the charge of the complex determines the absolute position on the correlation line.^[118] Hoffmann *et al.* pursued this idea and they explained the larger slope of CuS₄-correlation lines compared to those of CuO₄- and CuN₄-complexes by a high degree of spin delocalization onto the ligation atoms, *i.e.* a high degree of covalency of the Cu-S-bonds.^[116] Furthermore they reported that the position in the Peisach-Blumberg-plots is also influenced by the degree of tetrahedral distortion. Fielding *et al.* discovered that spin-lattice relaxation is up to six times faster in pseudo-tetrahedral complexes compared to square-planar ones.^[26] In here, these two ideas are combined. A Peisach-Blumberg plot adopted from Hoffmann *et al.*^[116] was created from the data of Cu²⁺-complexes with S-donor ligands investigated in this section (Figure 29). The data points are scaled in size according to the detected $T_{1,s}$ of the corresponding compound, to assess whether an influence of tetrahedral distortion on the spin-lattice relaxation times is visible. Literature data of **Cu-Smnt**-^[114] and **Cu-Sdto**-compounds^[117] were also included. In some of these cases also pulsed measurements (mainly T_1 -data) were reported,^[49-50, 115] but the data was collected without exception on

concentrated systems, where electron spin relaxation is governed by instantaneous diffusion and therefore no T_1 -scaling was applied for the literature data points in this case. From the $T_{1,s}$ -scaled Peisach-Blumberg plot (Figure 29) we see, that predicted correlation is fulfilled by all investigated and literature systems. For the investigated compounds, the dihedral angles are similar and the complexes are close to an ideal square-planar geometry, which is reflected by the clustered position of their data points in Figure 29.

No direct correlation between the dihedral angle and spin-lattice relaxation is obvious, in agreement with the observations of Fielding *et al.* for compounds with N-donor ligands.^[26] An analogous plot to Figure 29 with T_M -scaling for the investigated compounds with S-donor ligands did also not reveal such a correlation (not shown). From these facts it can be stated that for the investigated systems, the first coordination sphere is no major influence on electron spin relaxation. Looking closely at the crystal structures of the investigated compounds, the angle between the S-C-C-S and O-C-C-O-plane within one dithiooxalate-ligand (“bend angle”) in the diamagnetic host **Ni-Sdto^P** attracted our attention. The diamagnetic host shows a NiS₄-plane, but one of the ligands is bent away from that plane, with a bend angle of almost 15° in **Ni-Sdto^P**.^[119]

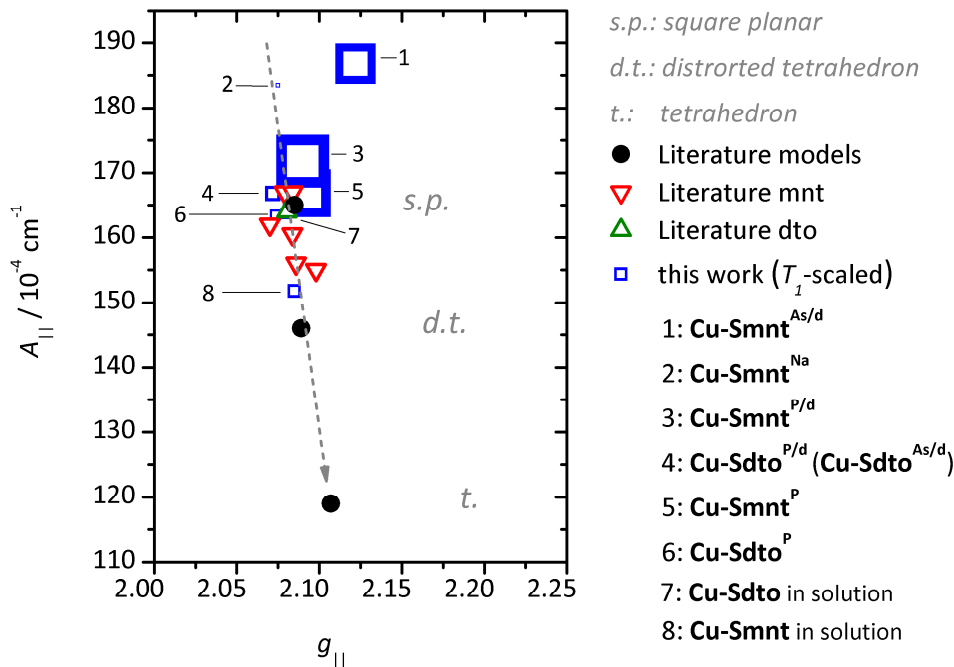


Figure 29: Peisach-Blumberg plot adopted from Hoffmann *et al.*^[116] created with data of **Cu-Smnt**- and **Cu-Sdto**-complexes investigated in this section (data points scaled in size according to $T_{1,s}$) and literature values (without size scaling as mostly no $T_{1,s}$ -data available).^[26, 114, 116-117]

This structural variation is absent in **Ni-Sdto^{As}**, which possesses planar, centrosymmetric complex anions.^[119] These differences between Ni-host lattice structures impact the detected spin-lattice relaxation times of **Cu-Sdto^P**, **Cu-Sdto^{P/d}** and **Cu-Sdto^{As/d}** in doped powders. Thus we find a significant increase of $T_{1,s}$ from 20.0 ± 0.7 ms resp. 29 ± 10 ms for the phosphonium-compounds to 53 ± 3 ms in **Cu-Sdto^{As/d}**. The fast processes of spin-lattice relaxation are both around 8 ms for **Cu-Sdto^{P/d}** and **Cu-Sdto^{As/d}**, which suggests the assignment of the fast process to spectral diffusion, as for compound-related fast processes (clusters, adducts etc.), compound specific fast relaxation processes should be expected. In **Cu-Sdto^P** only a monoexponential decay is found, we assume here that the fast process of spin-lattice relaxation vanishes in the measurement noise. In contrast to the findings for the spin-lattice relaxation, we do not see a correlation between the ligand-bend-angle and the phase memory time, which means that here other parameters must have a stronger influence, which will be identified in the course of the discussion.

Discussion of the Influences of the Ligand on Electron Spin Dynamics for Cu-Compounds with S-Donor Ligands

Revisiting Figure 28, an overall trend of longer $T_{1,s}$ times for Smnt-compounds compared to Sdto-compound is evident. For the investigated Cu(II)S₄-systems, the direct and Raman-process are possible processes of spin-lattice relaxation. In the “phonon-approach” of electron spin-relaxation theory (Section 2.2), the energy released by the spin during relaxation is taken up by the lattice in terms of quanta of collective lattice vibrations (phonons). In both cases, direct and Raman process, a more flexible lattice enhances the probability for spin-lattice relaxation by providing a higher density of lattice modes. The rigidity of ligand and matrix in **Cu-Smnt^P** and **Cu-Smnt^{P/d}** causes the observed slow electron spin dynamics.^[69] This is in agreement with literature, where trends of increasing spin-lattice relaxation times with decreasing flexibility of coordination geometry and decreasing mobility in the vicinity of the paramagnetic center are reported.^[24-26]

In literature, localized bond vibrations were reported to contribute in two-phonon relaxation processes:^[7] Atzori *et al.* assign faster relaxation in an octahedral V(IV)-dithiolene compared to a square-pyramidal vanadyl(IV)-dithiolene compound to the much lower energy of the valence vibration of the V–S- compared to the V=O-bond. In general, the assignment of ν_{MS} is difficult

for CuS_4 -complexes and especially for Smnt-complexes due to the high degree of delocalization and a strong mixing with other vibrations. Still it was found that in **Ni-Smnt** various vibrations with contributions of $\nu_{\text{N+S}}$ are found at slightly higher energies than the corresponding vibrations in **Ni-Sdto**-derivatives.^[120] For the complex anion **Cu-Smnt**, Escalera Moreno *et al.* theoretically modeled the spin-phonon coupling.^[9] By means of DFT calculations they determined the vibrational modes in the complex which are involved in spin-lattice relaxation, which are vibrations without covalent bond stretching. The most crucially spin-relaxation-influencing vibrations were found to be distortions of the Cu^{2+} -coordination sphere with energies of up to some ca. 300 cm^{-1} . Experimentally, a comparison of **Cu-Smnt** and **Cu-Sdto** in terms of molecular vibration energies could be performed with far-infrared measurements, covering the relevant spectral energies as indicated by Escalera Moreno *et al.* For the course of the further discussion, the qualitative assignment of a higher rigidity of the investigated Smnt-complexes compared to the investigated Sdto-complexes is sufficient at this point.

The observed spin-lattice relaxation times are orders of magnitude longer than the corresponding phase memory times, so a limiting effect of $T_{1,s}$ on $T_{M,s}$ by can be excluded. The effect of the ligand on the phase memory times is not as explicit as in the case of spin-lattice-relaxation. However, a more differentiated analysis helps revealing the interplay of competing effects on phase memory time in the investigated systems. Going from **Cu-Smnt^{P/d}** to **Cu-Sdto^{P/d}** in deuterated solution leads to a dramatic increase in phase memory time from $20.7 \pm 0.4 \mu\text{s}$ to $67 \pm 2 \mu\text{s}$. Hence, removal of nuclear spins in proximity of the paramagnetic center, here N-nuclear spins, increases phase memory time as stated in literature.^[3, 28-30] This ligand-effect is obscured if protonated counter ions or solvents are present in the frozen solution samples.

In the doped powder samples with **P**-counter ions, for both ligands stretched exponentials are found. In case of **Cu-Sdto^P**, the stretch parameter of 1.38 ± 0.03 indicates physical motion of magnetic nuclei as main dephasing process. The lability of the matrix is here the main coherence limiting factor. For **Cu-Smnt^P** in contrast, the stretch parameter is 2.48 ± 0.01 , which indicates nuclear spin flip-flops as main dephasing process as mentioned in Section 2.2.3. This supports the assumption stated above, that the Smnt-compounds represent a more rigid matrix than the Sdto-compounds. In agreement with this ligand-effect, the slow components of the phase memory times for **Cu-Smnt^{P/d}** and **Cu-Smnt^{As/d}** are much longer compared to the corresponding Sdto-

compounds. The effect is erased by the dephasing effect of proton nuclear spins: in the corresponding compounds with **P**-counter ions, the phase memory times are almost identical for Sdto- and Smnt-ligands.

Discussion of the Influences of the Sample Matrix on Electron Spin Dynamics for Cu-Compounds with S-Donor Ligands

The effects of the sample matrices on spin-lattice relaxation (and further below on spin-spin relaxation) are discussed separately for the two ligands employed, as different dominant effects can be observed. In case of the Sdto-compounds, where the flexible ligand is a major contributor to spin-lattice relaxation, the relaxation times do not substantially vary for the investigated matrices. Spin-lattice relaxation times in solution and in the doped powders are very similar (around 20 ms). The only exception here is **Cu-Sdto^{As/d}**, where the previously mentioned all-planar conformation of the ligand leads to more favorably $T_{1,s}$ -values compared to the cases of the crystal structures showing the bent ligand conformation.

For the Smnt-compounds the situation is different: here the rigid ligand has no major influence on spin-lattice relaxation and influences of the sample matrix are visible. The values for $T_{1,s}$ in the doped powder samples of Smnt-compounds are systematically longer than in solution (neglecting the exceptionally fast spin-lattice relaxation of **Cu-Smnt^{Na}**, which will be discussed in the subsequent sub-section). The doped powders possess a micro-crystalline environment with a high degree of three dimensionally structured regions, which presumably provides a more rigid matrix than the glassy solutions. Regarding the frozen solution samples of the Smnt-compounds, even a difference in $T_{1,s}$ between deuterated and protonated solvents is evident. A significant increase of $T_{1,s}$ by a factor of 1.6 is observed in the deuterated solvents compared to protonated solutions. The field fluctuation theory (Section 2.2.2) is considered here as basis for an explanation. This theory is valid for very anharmonic motions in the sample, i.e. when the phonon-model with the assumption of a Debye-lattice is no good approximation. As previously introduced, magnetic field fluctuations with suitable frequencies can induce electron spin transitions. The fluctuation frequency in terms of a basic harmonic oscillator is lower for C-D compared to C-H and the magnetic moment of D-nuclei is much smaller than H-nuclei. Hence it is suggested, that the correlation time of field fluctuations is longer in deuterated compared to

protonated disordered matrices. A longer correlation time leads to sharper spectral densities which in turn results in lower transition probabilities for the electron spin (i.e. longer spin-lattice relaxation times). This explanation matches the observed effects of longer relaxation times in deuterated compared to protonated frozen solutions. For the frozen solution measurements it is difficult to decide which theoretical model of spin relaxation is suited best for a correct description (phonon- or fluctuating field-approach). The interpretation above should be considered as starting point for further investigations. Increasing spin-lattice relaxation times for deuterated species were found in literature before, where the effect was assigned to an isotope effect, too.^{[6][120-121]} This isotope effect was so far only observed, if the HF anisotropy contributes to relaxation and a dominant Raman process or local vibrational mode was present. In agreement with our findings, Owenius *et al.* reported an increase in relaxation times by a factor of 1.5 for the isotope effect in C–H(D) vibration.^[121]

The effects of the frozen solution sample matrices on spin-spin relaxation are remarkable, too. In protonated solvents, stretched exponential Hahn echo decays are found, where the stretch parameters indicate physical motion of magnetic nuclei as main dephasing process in all cases. Hence the mechanical flexibility of the matrix is a major influence on dephasing in protonated frozen solution. In deuterated solvents, biexponential Hahn echo decays are observed. The values of $T_{M,s}$ increase for decreasing number of nuclear spins (H, N) in the investigated compounds. Hence the absolute number of nuclear spins present in the compound (H, N) seems to be a major influence on dephasing in frozen, deuterated solution. The comparison between frozen solution matrices and doped powder samples leads to different conclusions for Smnt- and Sdto-containing compounds. The phase memory times of the Sdto-compounds in the investigated doped powder- and frozen solution samples show comparable values (except **Cu-Sdto^{P/d}** in deuterated solution). As discussed above, here the ligand flexibility seems to be the major source of electron spin relaxation. Also dephasing is governed by this effect as indicated by the found stretch parameters, so no matrix effects can be observed. In contrast, phase memory times in doped powders of deuterated Smnt-compounds are substantially longer than in corresponding frozen solutions (except **Cu-Smnt^{Na}**, this will be discussed below). For a given number and kind of nuclear spins, the rigidity of the matrix seems to have the most substantial effect onto electron spin dephasing. The structural differences of the investigated compounds will be discussed in the next section.

Discussion of the Influence of the Counter Ion on Electron Spin Dynamics for Cu-Compounds with S-Donor Ligands

A variation of the counter ion can change structural and magnetic properties of the investigated system. Crystal structures of Smnt-complexes were extensively studied in literature. For example it is known that either bulky or planar, organic counter ions lead to columnar stacking of the complex anions, separated by cation-stacks,^[122] which often leads to interesting magnetic and electronic properties such as exchange interactions or conductivity. For **Ni-Smnt^P** and **Cu-Smnt^P**^[123], **Ni-Smnt^{As}**^[124] we find such a columnar packing with space groups as indicated in Table 28. As we saw no structural changes upon deuterating **Cu-Smnt^P** (not shown), it is probable that the other deuterated compounds behave similarly. Furthermore **Ni-Smnt^P** and **Cu-Smnt^P** are isostructural,^[123] therefore we focus the structural discussions on the diamagnetic host lattices. For **Ni-Smnt^{Na}** and **Cu-Smnt^{Na}** only crystal structure data for similar compounds (with NH₄⁺, K⁺, Rb⁺ as counter ions)^[125-127] were found in literature along with the statement, that the structures of **Ni-Smnt^{Na}** and **Cu-Smnt^{Na}** are very similar to reported structures of (NH₄)₂[Ni(mnt)₂]·H₂O (“**Ni-Smnt^{NH4}**”),^[128-129] which possesses a square planar complex geometry, again with columnar stacking of the complex anion. Besides in terms of their space groups, the crystal structures of the **Ni-Smnt^P**, **Ni-Smnt^{As}** and **Ni-Smnt^{Na}** can be distinguished by the uniformity of the stack arrangement in the unit cell (Figure 30), which decreases in the named order. As mentioned before, in **Ni-Sdto^P** a significant deviation from planarity of the complex anion is observed, whereas in **Ni-Sdto^{As/d}** the complex anion is centrosymmetric and planar.^[119]

Table 28: Literature data for crystal structures of investigated compounds or related ones. Bend angle describes angle between S-C-C-S-plane and C-C-C-C-plane in Smnt or between S-C-C-S-plane and O-C-C-O-plane in Sdto, respectively.

compound	bend angle	crystal sytem	space group	reference
Ni-Smnt^P	< 1°	monoclinic	P2 ₁ /n	Lewis <i>et al.</i> ^[104]
Ni-Smnt^{As}	< 1°	monoclinic	P2 ₁ /n	Golic <i>et al.</i> ^[124]
Ni-Smnt^{NH4}	< 1°	orthorhombic	Pnam	Underhill <i>et al.</i> ^[128]
Ni-Sdto^P	ca. 15°	triclinic	P $\bar{1}$	Román <i>et al.</i> ^[119]
Ni-Sdto^{As}	< 1°	triclinic	P $\bar{1}$	Román <i>et al.</i> ^[119]

Comparing Smnt- and Sdto-compounds, the different orientations of the complex anions with respect to the stacking direction is striking (Figure 31). In Smnt-based compounds, a parallel

stacking of the complexes is present, whereas in the Sdto-compounds the complexes stack sideways in a herringbone pattern, which inhibits π -type interactions. The lack of π -interactions suggests a lower rigidity of Sdto-based crystal structures compared to Smnt-based ones.

Changes in spin-lattice relaxation due to changing the structural parameters are observed. Figure 28 shows that the spin-lattice relaxation times of **Cu-Smnt^P** and **Cu-Smnt^{P/d}** are significantly higher than $T_{1,s}$ of **Cu-Smnt^{As}**, and all three of them being an order of magnitude longer than $T_{1,s}$ of **Cu-Smnt^{Na}**. The effect is related to the above mentioned decreasing uniformity of stack arrangement in the crystal structures. Therefore it is supposed, that a higher degree of uniformity of stack arrangement leads to longer spin-lattice relaxation times in the investigated compounds with S-donor ligands. In literature, a dependence of the acoustic phonon spectrum on the crystal unit cell size and content was suggested.^[6]

Lower spin-lattice relaxation times were found for doped powders of Smnt- compared to Sdto-donor ligand containing compounds. This finding is connected with a more rigid stack-arrangement of Smnt-complexes in the corresponding crystal structures. In addition, a higher planarity of the complex anion leads to longer spin-lattice relaxation time, as demonstrated by **Ni-Sdto^P** and **Ni-Sdto^{As/d}**.

Before structural influences on phase memory times are discussed, the effects of the different magnetic nuclei being present in the different crystal structures are examined. Starting from **Cu-Smnt^P** and **Cu-Sdto^P**, the number, distance and gyromagnetic ratio of nuclear spins in the proximity of the molecular nanomagnets can be varied by deuterating the counter ion (**P/d**), exchanging the tetraphenyl-phosphonium- by tetraphenylarsonium-cations (**As/d**) or even going from these bulky to much smaller cations (**Na**). Table 29 gives an overview of magnetic properties of nuclear spin carrying isotopes present in the investigated compounds. As reported previously, a deuteration of the tetraphenylphosphonium cation prolongs the phase memory time, as deuterium nuclei have a much smaller gyromagnetic ratio compared to protons. The exchange of **P/d** with **As/d** strongly decreases the phase memory time in the Smnt-compound from $68 \pm 3 \mu\text{s}$ to $34.4 \pm 0.5 \mu\text{s}$ which is surprising at first glance: the gyromagnetic ratio of arsenic is approximately half of that of phosphorous, which would imply a weaker influence on dephasing. However, the dipolar coupling also scales with r^{-3} , so the distances of nuclear- and electron spins need to be considered.

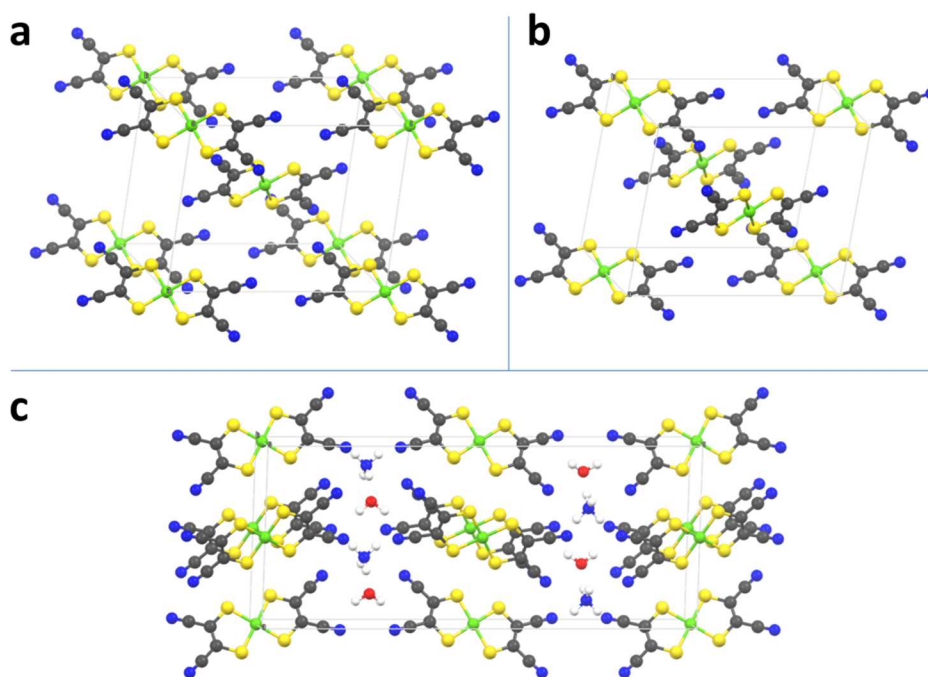


Figure 30: Packing diagram of Ni-Smnt-compounds for illustration of degree of uniformity in the different unit cells, colors: green - Ni, yellow - S, black - C, blue - N, red - O, white - H. **a:** Packing diagram of Ni-Smnt^P, crystal structure data from Lewis *et al.*,^[104] cations omitted for clarity. **b:** Packing diagram of Ni-Smnt^{As}, crystal structure data from Golic *et al.*,^[124] cations omitted for clarity. **c:** Packing diagram of Ni-Smnt^{NH₄}, crystal structure data from Underhill *et al.*^[128]

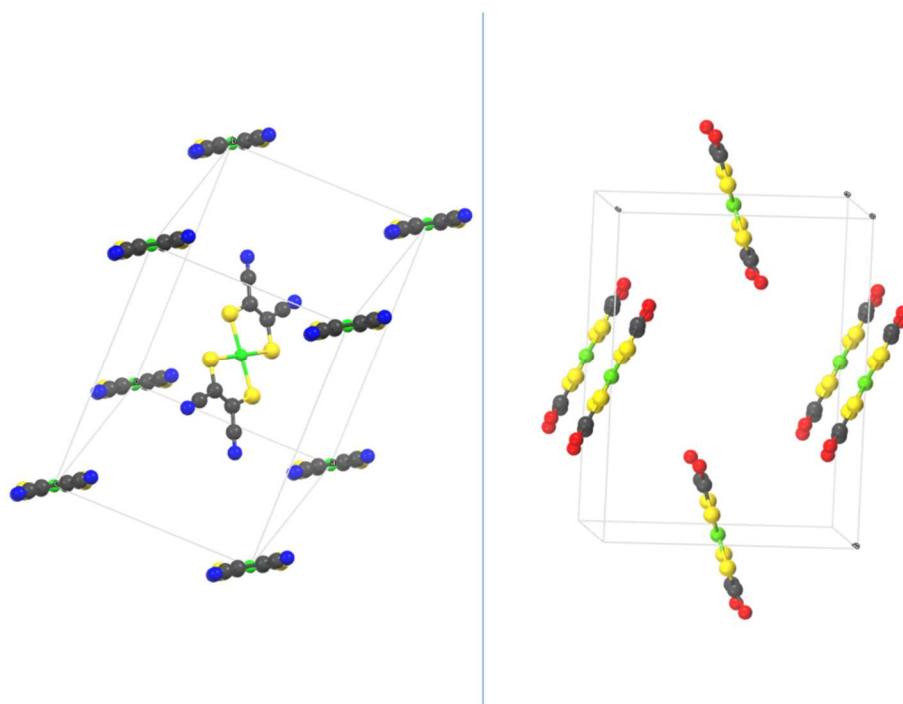


Figure 31: Packing diagram of Ni-Smnt^P (left) and Ni-Sdto^{As} (right). Cations omitted for clarity, crystal structure data from Lewis *et al.*^[104] and Román *et al.*^[119] Colors: green - Ni, yellow - S, black - C, blue - N, red - O.

Table 29: Magnetic properties of nuclear spin carrying counter ion atoms in investigated compounds with S-donor ligands.

isotope	I	$\gamma / \text{rad} \cdot \text{T}^{-1} \cdot \text{s}^{-1}$
^1H	1/2	26.752
$^2\text{H} = \text{D}$	1	4.107
^{23}Na	3/2	7.081
^{31}P	1/2	10.839
^{75}As	3/2	4.595

Hydrogens are not assigned in the literature crystal structure data. However, the closest Ni-As-distance is 6.622 Å, whereas the closest Ni-P-distance is 6.693 Å. Therefore it is assumed, that the closest Ni-D-distance is smaller in the **As/d** containing compound compared to the **P/d** containing compound, being responsible for the longer phase memory time in the **As/d** compound.

Finally, it is supposed that phase memory times are also longer for higher symmetries of the complexes and higher uniformity in the unit cells (see examples in discussion of spin-lattice relaxation above). In agreement with the statements for spin-lattice relaxation, a higher symmetry/uniformity provides higher rigidity of the complexes or the crystal structures, respectively. A higher rigidity in turn means less physical movement of nuclear spins and therefore lower field fluctuations, which act dephasing on the electron spins. For **Cu-Sdto^P** in doped powder, this was above identified as main dephasing process ($k = 1.38 \pm 0.03$, Table 27).

Results and Discussion of Central Metal Ion Dependence of Electron Spin Dynamics in Compounds with S-Donor Ligands

Cu-Smnt^{P/d} exhibits one of the slowest electron spin dynamics of the investigated compounds with S-donor ligands and is furthermore redox-stable under ambient conditions in solid state and solution. Therefore we selected **Cu-Smnt^{P/d}** and **Ni-Smnt^{P/d}_{para}** as subjects for the investigation of central metal ion dependence of electron spin dynamics. Figure 32 shows a graphical summary of detected spin-lattice and spin-spin relaxation times of the two compounds in frozen solution (1:1 CD₂Cl₂/CS₂) and doped powder according to Table 24–Table 27.

For **Cu-Smnt^{P/d}**, spin-lattice relaxation is faster in the frozen solution than in the doped powder. In contrast, for **Ni-Smnt^{P/d}_{para}** in frozen solution T_{1s} is twice as long as in the doped powder.

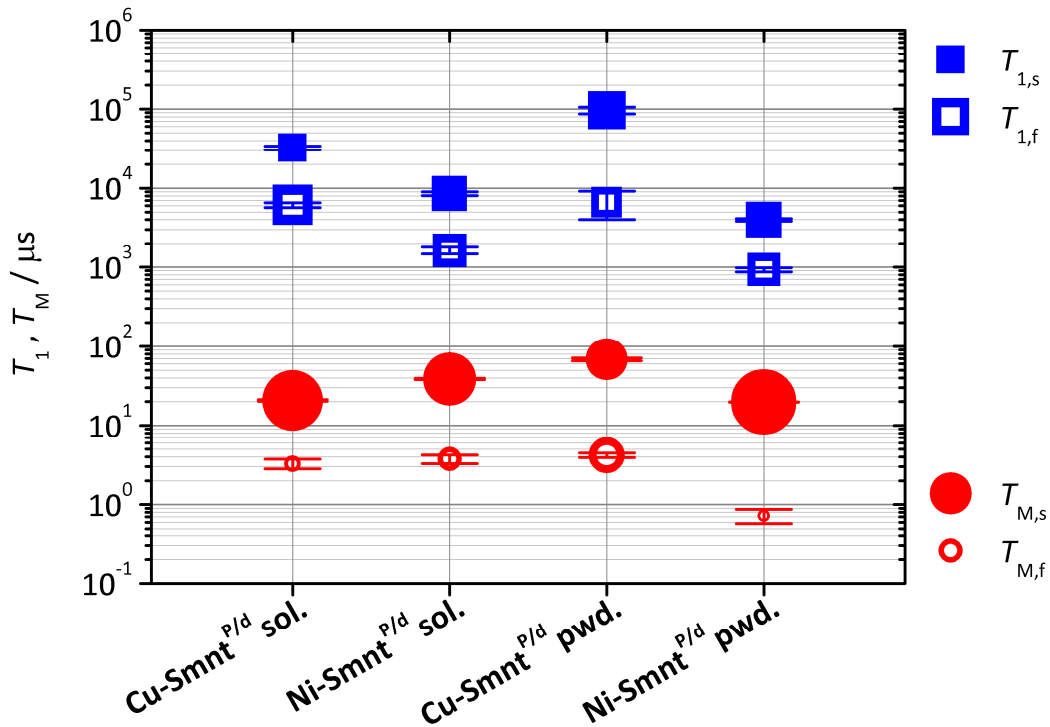


Figure 32: Spin-lattice- and spin-spin relaxation times in microseconds of $\text{Cu-Smnt}^{\text{P/d}}$ and $\text{Ni-Smnt}^{\text{P/d}}$ in 1 mM solution (1:1 $\text{CD}_2\text{Cl}_2/\text{CS}_2$; “sol.”) and as 0.01 % doped powders (“pwd.”) recorded at Q-band and 7 K; values extracted from fit functions according to Table 24–Table 27). Blue, filled squares (red, filled circles) indicate the slow process of spin-lattice (spin-spin) relaxation. Blue, open squares (red, open circles) indicate the fast process of spin-lattice (spin-spin) relaxation. Error bars correspond to the standard deviations of the fit functions. In contrast to other figures of this type, no scaling was applied to the size of the symbols. The size of the symbols corresponds to the relative size of the exponential prefactors A_f and A_s of the fast and slow process of spin-lattice and spin-spin relaxation time, respectively, extracted from fit functions.

As previously stated, the incorporation of $\text{Ni-Smnt}^{\text{P/d}}_{\text{para}}$ in the diamagnetic host $\text{Ni-Smnt}^{\text{P/d}}_{\text{para}}$ is expected to result in a distorted structure, due to the different crystal structures.^[104] The resulting lattice strain could be responsible for the faster spin-lattice relaxation of the Ni^{3+} -compound in the doped powder compared to the frozen solution sample.

Comparing the spin-lattice relaxation times of the Cu^{2+} - and the Ni^{3+} -compound, one sees that the fast and slow processes of $\text{Cu-Smnt}^{\text{P/d}}$ are slower than those of $\text{Ni-Smnt}^{\text{P/d}}_{\text{para}}$ in both matrices. $\text{Cu-Smnt}^{\text{P/d}}$ is isostructural with its diamagnetic Ni^{2+} host^[104] in contrast to $\text{Ni-Smnt}^{\text{P/d}}_{\text{para}}$ as discussed above, which makes a comparison of the two doped powders difficult.. The discrepancy in spin-lattice relaxation of the two compounds in frozen solution is not fully understood so far. A possible explanation for this observation are the different in SOMOs of the two compounds, which both lie in the molecular planes, but their orientation with respect to the

dative bonds differs ($d_{x^2-y^2}$ in the case of the Cu^{2+} -compound; d_{xy} for the Ni^{3+} -compound).^[99]

This could affect the degree of delocalization of unpaired electrons, which may change the rigidity of the complex, which in turn affects T_1 .

The comparison of phase memory times in the doped powders for the Cu^{2+} - and Ni^{3+} -compounds leads to the same conclusions as in the case of spin-lattice relaxation. Interestingly, $T_{M,s}$ of **Ni-Smnt^{P/d}_{para}** in solution is twice as long as for **Cu-Smnt^{P/d}**. This effect is not fully understood at this point, but some thoughts on this are given here. As stated in the beginning of this Section, for hard MW pulses spin forbidden transitions can enhance electron spin relaxation. For this study, 20 ns $\pi/2$ -pulses were applied in all measurements, which corresponds to an excitation bandwidth of 60 MHz, which can be rated as rather soft pulse for **Cu-Smnt^{P/d}** (with a hyperfine coupling strength of 118 ± 5 MHz for the probed g -tensor orientation in the doped powder). Hence the effect of MW-pulse length on dephasing can be excluded in this case. Another possibility for the faster dephasing in **Cu-Smnt^{P/d}** compared to **Ni-Smnt^{P/d}_{para}** could be related to the presence of hyperfine coupling in the former: due to that, a lower fraction of the spectrum is excited in these experiments compared to **Ni-Smnt^{P/d}_{para}**. This in turn means, that overall more electronic B-spins are present in the Cu^{2+} -sample, offering higher probability for spectral diffusion. Furthermore, not excited Cu^{2+} -nuclear spins represent additional sources of local B -field inhomogeneities, which enhance electron spin dephasing. This in turn would mean that the nuclear spin of the central metal ion does indirectly influence spin-spin relaxation in the case of partly spectral excitation. At this point of the investigation it is not clear, whether such an effect could be visible at the applied low concentrations of the paramagnetic species in the frozen solution samples. More data needs to be collected for a clear assignment.

Summary regarding Spin Dynamics in Compounds with S-Donor Ligands

By our systematic study, we were able to characterize and weigh the various influences on electron spin dynamics in compounds with S-donor ligands. Subtle differences in the electronic structure of copper(II)-dithiolene complexes were found to have no major influence on electron spin dynamics. The main influences on spin-lattice relaxation in square planar copper(II)-dithiolenes with decreasing importance are the rigidity and conformation of the ligands, of the close environment of the potential qubit (ordered crystalline environment or random glassy

matrix) and of the three-dimensional degree of ordering, i.e. the crystal structure. For the phase memory time, the number and distance of nuclear spins are the major limiting factor in most cases. Less (and more distant) nuclear spins result in longer phase memory times. In addition, also strong influences of rigidity and degree of ordering of the close and peripheral environment of the potential MQBs were identified as considerable determinants for T_M . More labile and disordered environments generally lead to more local magnetic field distributions and allow more physical motions of magnetic nuclei, which both are severe sources of dephasing. The validity of these results should not be affected by the presence of nickel(III)-impurities in the doped powder samples of the **Cu-Smnt**-compounds. The amount of Ni^{3+} being present in these samples is estimated to be similar in all cases (except **Cu-Smnt^{Na}**), as the spurious signal intensities are comparable to the main signal. Furthermore, additional paramagnetic species will mainly enhance the probability for spectral diffusion and for clusters of paramagnetic species. However, for qubit devices a high purity and controllability is required. Further development should include the synthesis of Ni^{3+} -free doped powders.

Future work should also include an extension of the comparison of Cu^{2+} - and Ni^{3+} -compounds with S-donor ligands: The investigation of **Ni-Smnt^{P/d}_{para}** and **Cu-Smnt^{P/d}** in doped powders should be repeated with an isostructural diamagnetic host for the former. The corresponding Cu^{3+} -compound^[104] could serve this purpose. Furthermore, a better understanding of the differences in spin relaxation times in frozen solution of these compounds needs to be developed. An extension of the measurement series with additional Ni^{3+} - and Cu^{2+} -compounds could help here. However, this study involves the first coherence measurement of Ni^{3+} -species to the best of our knowledge. Previously, monoanionic Ni-bis-1,2-dithiolenes in biological systems were investigated by the means of ESEEM and ENDOR as model-compounds for hydrogenase enzymes.^[130-132] Further pulsed and cw EPR experiments were published,^[101, 112, 133-134] but none of them involved measurements of spin-spin relaxation time. In here it was demonstrated, that nickel(III)-dithiolenes are applicable as building blocks for novel MQBs.

3.2 Physical Influences on Electron Spin Relaxation

In this Section, the physical influences on electron spin relaxation are investigated. **Cu-Smnt^{P/d}_{0.01%}** was selected as target compound for this purpose (Figure 33). In the previous section, this compound was identified as most promising potential MQB due to the record phase memory times and its chemical stability.

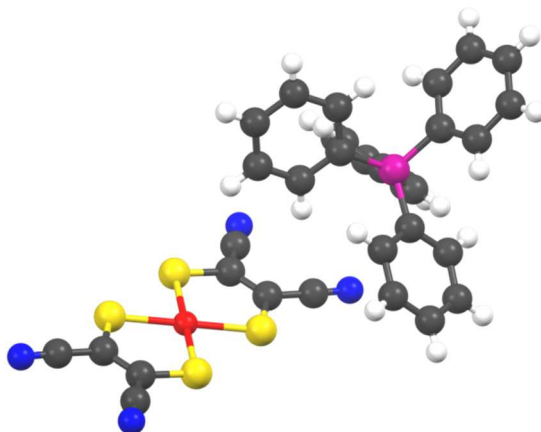


Figure 33: Crystal structure of **Cu-Smnt^P** (excerpt, complex dianion and one counter ion shown). Colors: red - Cu, yellow - S, black - C, blue - N, magenta - P, white - H. Figure adopted from K. Bader *et al.*, *Nat. Commun.* 2014, 5, 5304.^[69]

Smnt-coordination compounds are very well investigated systems. Measurements of cw EPR-spectra of paramagnetic dithiolene and especially Smnt-compounds were reported already in the early 1960s^[135] and also more recent studies are available.^[112, 136-137] Rich literature exists on ENDOR-experiments^[101, 138-140] and even some pulsed studies on relaxation times are available for Smnt- and comparable dithiolene-complexes.^[49-50]

We want to tie in here and utilize **Cu-Smnt^{P/d}_{0.01%}** to explore the physical influences on electron spin relaxation. This offers the opportunity to develop a fundamental understanding of the influence of experimental parameters on relaxation. The first step of the systematic study is the investigation of magnetic field dependence of spin dynamics in **Cu-Smnt^{P/d}_{0.01%}** at Q-band. From this, the best-suited magnetic field position for further spin dynamics experiments will be identified. In the next step, the temperature dependence of spin dynamics at Q-band at a fixed magnetic field is probed from cryogenic- up to room temperature. The third part of the study comprises a uniquely extensive investigation of the frequency dependence of spin dynamics in

Cu-Smnt^{P/d}_{0.01%} for 3.7–240 GHz at 7 K. In the fourth and last part, the couplings between electron and nuclear spin in **Cu-Smnt^{P/d}_{0.01%}** are probed. There, the frequency dependence of weak couplings is shown in ESEEM-experiments at S-, X- and Q-band frequencies. Strong couplings between electron- and nuclear spins are revealed in ENDOR-experiments at Q-band. Advanced pulse experiments, such as CPMG and nuclear nutations are presented as first prove of principle of the applicability of **Cu-Smnt^{P/d}_{0.01%}** as a MQB in quantum information processing and quantum information storage.

3.2.1 *Magnetic Field Dependence of Spin Dynamics*

The dependence of electron spin relaxation on the magnetic field for a fixed MW frequency was investigated. Measurements of electron spin dynamics at different spectral positions enable the investigation of two effects. First, the effect of the orientation of the molecular g -tensor towards the external magnetic field can be probed, as introduced in section 2.3.1. Second, the influence of the nuclear spin quantum number m_I can be investigated for nuclear-spin carrying paramagnetic centers. In this section, these two effects will be analyzed for **Cu-Smnt^P_{0.001%}** and **Cu-Smnt^{P/d}_{0.01%}** with different experiments presented in the proceeding text. The measurements were performed in Stuttgart and in Frankfurt at Q-band with two different spectrometers (details see Experimental Section, 5.2).

The magnetic field dependence of electron spin relaxation in for **Cu-Smnt^P_{0.001%}** was investigated with the aid of ESE-detected EPR spectra. For this purpose, spectra with a range of interpulse distances τ were recorded at Q-band (33.77 GHz, Frankfurt) and 15 K. Figure 34 shows an example of such a spectrum, which has equivalent features as **Cu-Smnt^P_{0.001%}** at 7 K discussed in section 3.1.3 (corresponding spectrum see Figure 24, simulation parameters Table 23). In total, 88 spectra were collected a variation of τ in steps of 150 ns from 140–13120 ns. Figure 35 shows the three-dimensional representation of these spectra as surface-plot. From the surface representation, Hahn echo decay curves were constructed by plotting signal intensities against pulse delay time (which corresponds to 2τ) for a fixed magnetic field value. The constructed Hahn echo decay curves are marked with black, solid lines in Figure 35. Figure 36 shows a part of these constructed Hahn echo decay curves (remaining curves: Supplementary Figure 39).

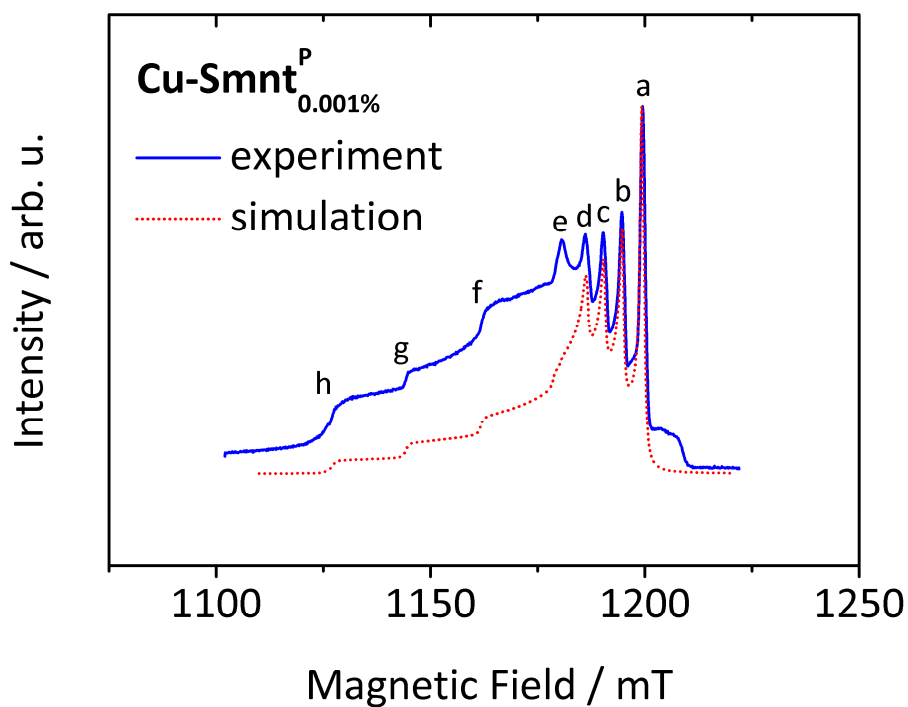


Figure 34: ESE-detected EPR spectrum of **Cu-Smnt^P_{0.001%}** recorded at Q-band (33.77 GHz, Frankfurt) and 15 K, interpulse distance: $\tau = 220$ ns. Blue, solid line represents experimental data. Red, dotted line indicates simulation (simulation parameters: Table 23).

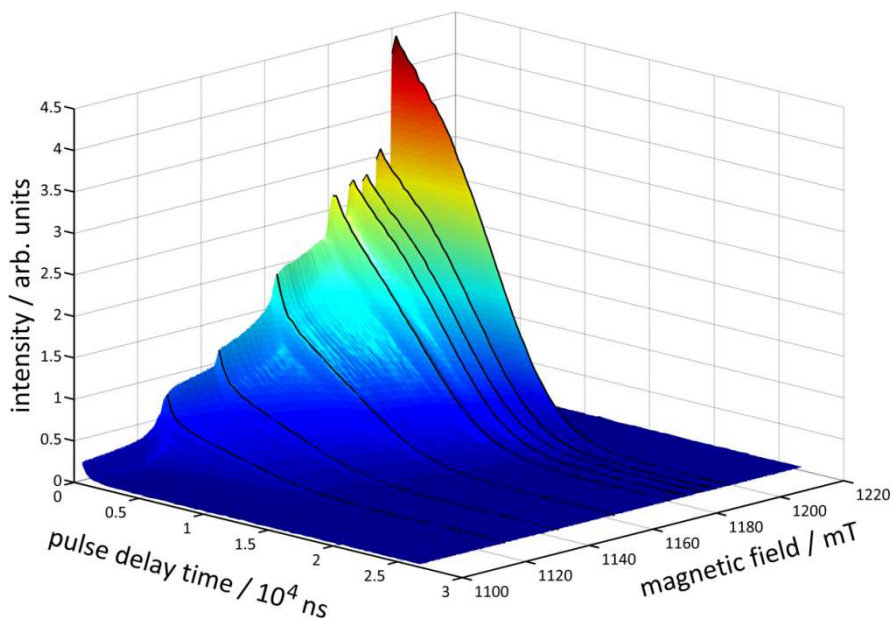


Figure 35: Surface representation of ESE-detected EPR spectra of **Cu-Smnt^P_{0.001%}** in dependence of pulse delay time (corresponds to 2τ), recorded at Q-band (33.77 GHz, Frankfurt) and 15 K, where τ was stepped from 140–13120 ns with increments of 150 ns. Black, solid lines indicate constructed Hahn echo decay curves shown in Figure 36. Figure adopted from K. Bader *et al.*, *Nat. Commun.* **2014**, *5*, 5304.^[69]

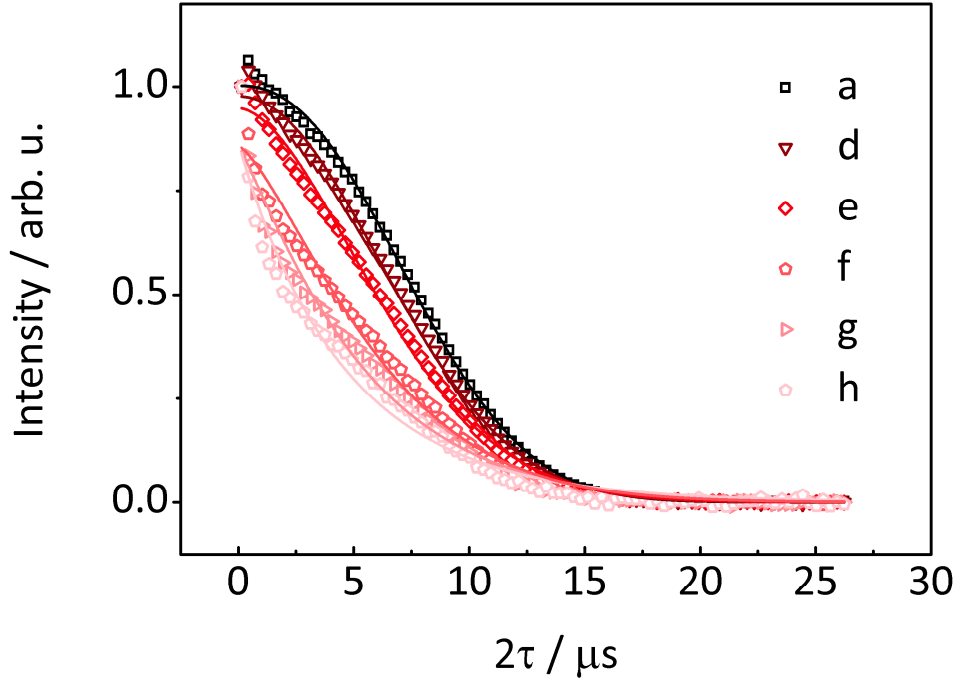


Figure 36: Hahn echo decay curves constructed from surface representation of ESE-detected EPR spectra of **Cu-SmntP_{0.001%}** and fits, recorded at Q-band (33.77 GHz, Frankfurt) and 15 K. Open symbols correspond to the ESE-Intensities at the corresponding pulse delay time (Figure 35) and at the magnetic field positions indicated by labels a-h, exemplary shown for one pulse delay in Figure 34. Solid lines represent stretched exponential fits according to Table 30.

Table 30: Parameters of stretched exponential fit functions according to equation (64) and standard deviations for constructed Hahn echo decay curves of **Cu-SmntP_{0.001%}** at Q-band (33.77 GHz, Frankfurt) and 15 K according to Figure 36.

B_0 -label	B_0 / mT	$T_{M,s}$ / μ s	k
a	1199.5	9.02 ± 0.03	2.29 ± 0.03
b	1194.6	8.78 ± 0.04	2.20 ± 0.03
c	1190.3	8.64 ± 0.04	2.08 ± 0.03
d	1186.1	8.42 ± 0.04	2.05 ± 0.03
e	1180.7	7.70 ± 0.06	1.76 ± 0.03
f	1163.2	6.57 ± 0.13	1.38 ± 0.05
g	1145.0	5.53 ± 0.18	1.13 ± 0.05
h	1128.7	4.65 ± 0.23	0.96 ± 0.05

The constructed Hahn echo decay curves were fit with stretched exponential functions; the results are listed in Table 30. For the magnetic field value marked “a” in Figure 34 and Figure 36, the extracted values of $T_{M,s}$ and k are identical to those extracted from a conventional Hahn echo decay experiment (see further below, section 3.2.2), considering a 10 % measurement uncertainty.

This shows the accuracy of the here extracted phase memory times and stretch parameters. Note

that with decreasing magnetic field value, an oscillation of the experimental data around the fits is increasingly visible (Figure 36). This oscillation is not caused by an ESEEM-effect (electron spin echo envelope modulation, compare section 2.4.2), but by instabilities of experimental conditions such as temperature, MW phase and -frequency. The actual time between collecting two subsequent points of the constructed Hahn echo decay curves is extremely long (in the range of hours) compared to a conventional detection (in the range of seconds) for the investigated system. The oscillation is more pronounced at lower field lines due to the lower S/N with decreasing magnetic field position in the spectra.

For a validation of the results on magnetic field dependence of electron spin relaxation in $\text{Cu-Smnt}^{\text{P}}_{0.001\%}$, “conventional” orientation dependent electron spin dynamics measurements were performed for $\text{Cu-Smnt}^{\text{P/d}}_{0.01\%}$ at 50 K and Q-band (35.000 GHz, Stuttgart). First, an ESE-detected EPR spectrum was recorded (Figure 37). The spectrum shows the same features as $\text{Cu-Smnt}^{\text{P/d}}_{0.01\%}$ at 7 K as discussed in Section 3.1.3 (Supplementary Figure 24) and the simulation parameters applied there (Table 23) were also used here.

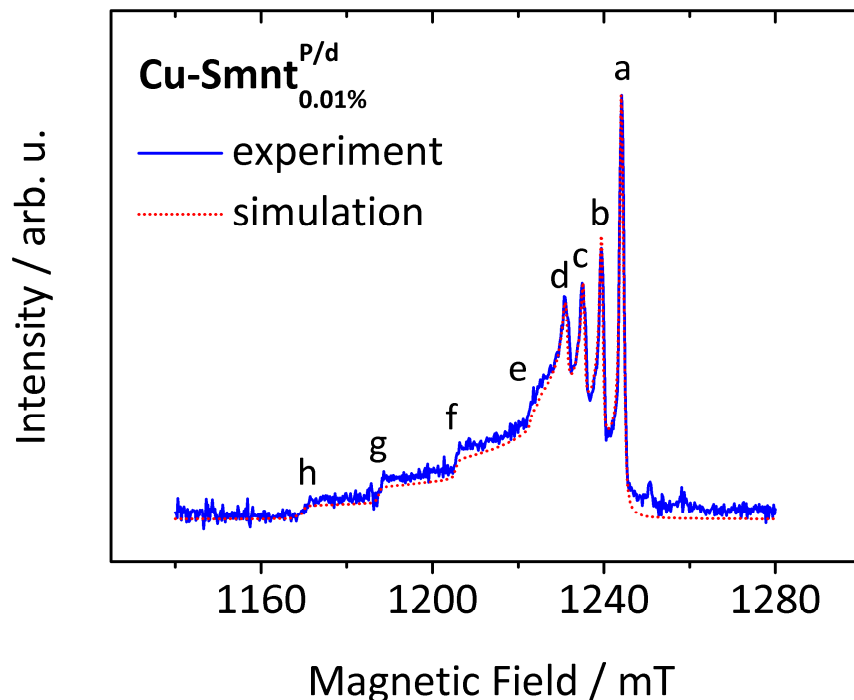


Figure 37: ESE-detected EPR spectra of $\text{Cu-Smnt}^{\text{P/d}}_{0.01\%}$ recorded at Q-band (35.000 GHz, Stuttgart) and 50 K. Blue, solid line represent experimental data and red, dotted line indicated corresponding simulation. Simulation parameters can be found in Table 23.

The magnetic field positions for spin dynamics measurements are marked with labels a-h in analogy to the results presented above. Inversion recovery- and Hahn echo experiments were performed for magnetic field positions a-h. An example of the experimental results is shown in Figure 38 (remaining experiments see Appendix, Supplementary Figure 40–Supplementary Figure 46). Monoexponential fits were employed to extract spin-lattice and phase memory times from the experimental data. The corresponding fit parameters are shown in Table 31. Figure 39 graphically summarizes the detected orientation dependence of spin-spin-relaxation in **Cu-Smnt^P_{0.001%}** and the same is shown in Figure 40 for **Cu-Smnt^{P/d}_{0.01%}** (spin-spin and spin-lattice relaxation). In the following, first the findings for the magnetic field dependence of spin-spin relaxation of both investigated systems will be discussed. Subsequently, the examination for the magnetic field dependence of spin-lattice relaxation in **Cu-Smnt^{P/d}_{0.01%}** will be presented.

The extracted phase memory times (ca. 9 μ s) and stretch parameters ($k \approx 2$) of **Cu-Smnt^P_{0.001%}** for the magnetic field positions a-d are invariant within a 10 % error margin. The magnetic field positions a-d correspond to an excitation of g_{\perp} . The extracted parameters for magnetic field positions e-h (corresponding to an excitation of g_{\parallel}) are smaller than the ones discussed above. Furthermore, a dependence of the phase memory times and stretch parameters on the nuclear spin quantum number m_I is present for the magnetic field positions e-h. Here, $T_{M,s}$ varies from 4.65–7.70 μ s and $k \approx 0.96$ –1.76, where both parameters decrease with decreasing magnetic field value. For **Cu-Smnt^{P/d}_{0.01%}**, same trends of phase memory times are found: for magnetic field positions a-e $T_{M,s}$ is invariant within 10 % error margins, whereas for positions e-h overall smaller values of $T_{M,s}$ are found including a dependence on the nuclear spin quantum number.

These findings indicate faster spin-spin relaxation for magnetic field orientations perpendicular to the molecular plane compared to parallel orientations.^{§§} In experiments with other copper(II)-dithiolene coordination compounds, also anisotropic phase memory times were found.^[141]

^{§§} Molecular axes refer to axes associated with the square-planar complex anions. The molecular x - and y -axes are assumed here to point along the plane span by the ligands, which corresponds to the orientation of g_{\perp} . The molecular z -axis is assumed to be collinear with the normal of the plane span by the ligands and collinear with g_{\parallel} . This is in agreement with literature data for similar compounds.^[50, 133, 139]

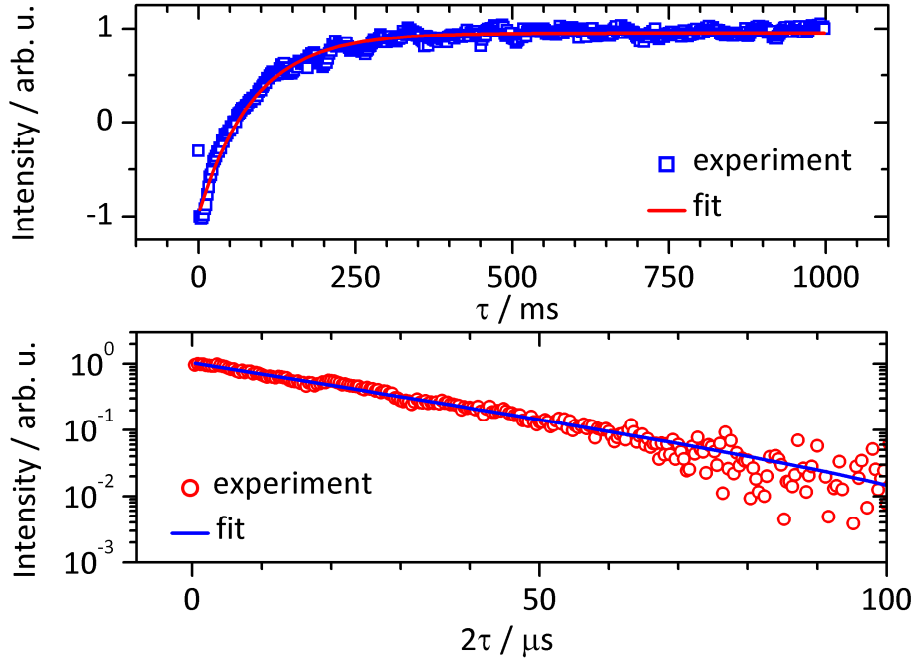


Figure 38: Electron spin relaxation measurements and fits of $\text{Cu-Smnt}^{\text{P/d}_{0.01\%}}$ recorded at Q-band (35.000 GHz, Stuttgart) and 50 K. Magnetic field was fixed to the position indicated by the label “a” in the corresponding ESE-detected EPR spectra shown in Figure 37. Top panel: Inversion recovery experiment. Blue, open squares indicate experimental data and red, solid line represents fit function (fit parameters see Table 31). Bottom panel: Hahn echo experiment. Red, open circles indicate experimental data and blue, solid line represents fit function (fit parameters see Table 31).

Table 31: Parameters of monoexponential fit functions according to equation (90) and (63) and standard deviations for inversion recovery and Hahn echo decay experiments of $\text{Cu-Smnt}^{\text{P/d}_{0.01\%}}$ recorded at Q-band (35.000 GHz, Stuttgart) and 50 K.

B_0 – label	B_0 / mT	$T_{1,s}$ / ms	$T_{M,s}$ / μs
a	1244.2	87 ± 1	25.7 ± 0.2
b	1239.3	75.4 ± 0.8	23.2 ± 0.2
c	1234.9	76.8 ± 0.8	23.3 ± 0.2
d	1230.7	70.9 ± 0.8	22.9 ± 0.2
e	1222.9	70 ± 1	19.4 ± 0.4
f	1205.7	72 ± 2	18.3 ± 0.5
g	1188.5	69 ± 5	18.2 ± 0.7
h	1171.4	64 ± 4	13.7 ± 0.4

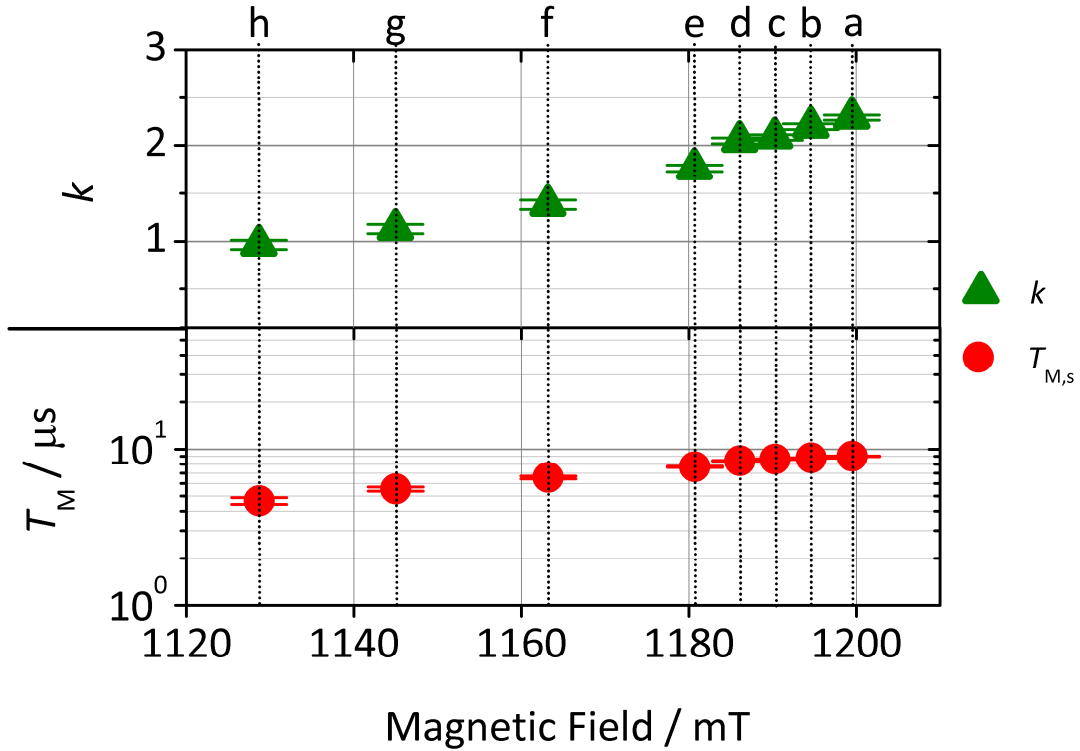


Figure 39: Orientation Dependence of stretch parameters (green, filled triangles) and phase memory times (red, filled circles) in $\text{Cu-SmntP}_{0.001\%}$ extracted from stretched exponential fits of constructed Hahn echo decay curves according to Table 30 (experimental conditions: Q-band, 33.77 GHz, Frankfurt and 15 K). The labels a-h assign magnetic field positions according to Figure 34. Error bars correspond to the standard deviations of the fit functions.

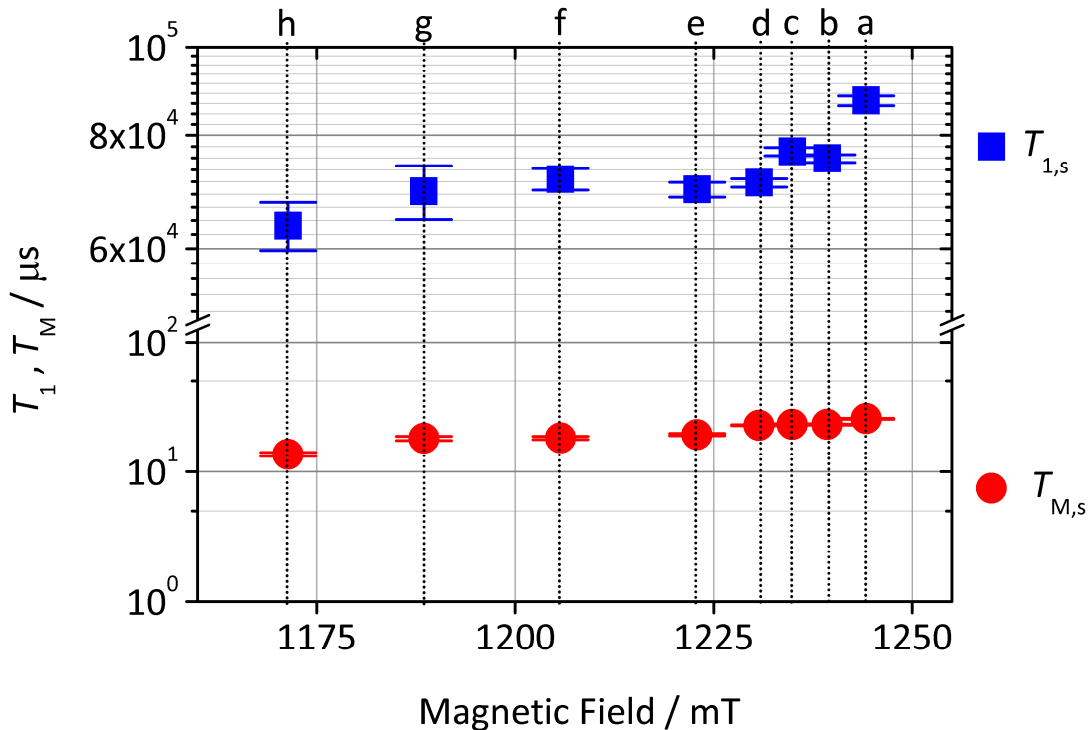


Figure 40: Orientation Dependence of spin-lattice- (blue, filled squares) and phase memory times (red, filled circles) in $\text{Cu-SmntP}_{0.01\%}$ according to Table 31 (experimental conditions: Q-band, 35.000 GHz, Stuttgart and 50 K). The labels a-h assign magnetic field positions according to Figure 37. Error bars correspond to the standard deviations of the fit functions.

In general, longer phase memory times for higher field parts of the corresponding EPR spectra are commonly found for transition metal complexes, as stated in 2.3.1. Different dominant relaxation processes for the two assigned molecular directions are a plausible explanation for the observed phase memory time anisotropy. The found stretch parameters for **Cu-Smnt^P_{0.001%}** indicate nuclear spin diffusion as dominant dephasing process in the molecular plane (i.e. magnetic field positions a-d). In contrast, for perpendicular orientations, physical motion of magnetic nuclei seems to be dominant. The magnetic field position e is also assigned to a resonance of perpendicularly oriented molecules, but the stretch parameter is close to 2 in contrast to positions f-h. This is assigned to the high overlap of resonance lines at field position e. The observation of changing dominant dephasing processes with orientation of the paramagnetic molecules towards the external field could be connected with the square-planar geometry of the molecule and with the columnar π -stacking of the complex molecules in the crystal structure as outlined in section 3.1.3. These geometrical constraints could lead to less hindered movements of magnetic nuclei along the direction of the molecular z -axis compared to the directions of the x - and y -axis. The finding of a dependence of spin-spin relaxation on the nuclear spin quantum number exclusively for the magnetic field positions associated with g_{\parallel} for both investigated systems is generally in agreement with a report of Kirmse *et al.*^[50] They found the same behavior for a similar compound, **Cu-Simnt^{NBu₄}_{2%}** (where Simnt = iso-maleonitriledithiolate or 1,1-dicyanoethylene-2,2-dithiolate). In their concentrated doped single crystal, the reported phase memory times are only around 0.5 μ s due to the presence of instantaneous diffusion. Nevertheless, they reported a faster spin-spin relaxation for magnetic field positions associated with g_{\parallel} and $m_I = \pm 1/2$ compared to $m_I = \pm 3/2$. Kirmse *et al.* explain this with a higher cross-relaxation probability at the $m_I = \pm 1/2$ -resonance lines due to the higher overlap of resonance lines caused by ⁶³Cu- and ⁶⁵Cu-derivatives of the compound (natural isotopic mixture).^[50] This detail is not observed here. Probably the effect is not resolved here due to the higher linewidth associated with the doped powder compared to a doped single crystal.

The variation of spin-lattice relaxation in **Cu-Smnt^P_{0.001%}** with the magnetic field position is much more subtle than in the previously discussed case of spin-spin relaxation. Under the consideration of 10 % error margins, the values of $T_{1,s}$ are almost identical and close to 70 ms. An overall trend

of increasing spin-lattice relaxation time for increasing perpendicular orientation of the complex towards the external magnetic field is detected.

A variation of spin-lattice relaxation times is generally expected, if a strong anisotropy of contributions in the Hamiltonian is present,^[23] as introduced in Section 2.3. Compared to other systems investigated in this thesis, the anisotropy of the g -tensor is quite low here, which could account for the relative invariance of spin-lattice relaxation times. Another factor to be considered is the measurement temperature, which was quite high in the presented experiments on spin-lattice relaxation (50 K). Manoharan *et al.* report a study of orientation dependent spin-lattice relaxation measurements at various temperatures on ^{63}Cu -dithiolene complexes in doped single crystals.^[49] In that study, a field dependence was found at 10 K, which was absent at higher temperatures. The orientation dependence was only visible in the case of a dominant direct process of spin-lattice relaxation. The dominant process can be identified by temperature dependent relaxation measurements, which will be presented in the following section.

3.2.2 Temperature Dependence of Spin Dynamics

The temperature dependence of electron spin relaxation for a fixed MW frequency and fixed magnetic field position was probed for **Cu-Smnt^P_{0.001%}** and **Cu-Smnt^{P/d}_{0.01%}**. The measurements were performed in Stuttgart and in Frankfurt at Q-band with two different spectrometers (details see Experimental Section, 5.2). A part of the investigation presented in the following was published in *Nature Communications* in 2014.^[69]

ESE-Detected EPR Spectra

First of all, ESE-detected EPR spectra were collected at Q-band and various temperatures between 7 K and room temperature for the two samples. Figure 41 shows the results for **Cu-Smnt^P_{0.001%}**, the spectra of **Cu-Smnt^{P/d}_{0.01%}** are shown in the Appendix (Supplementary Figure 47–Supplementary Figure 49). In both cases, the spectra are equivalent to the ones discussed in Section 3.1.3 (Figure 24, Supplementary Figure 24 and Table 23) at low temperatures.

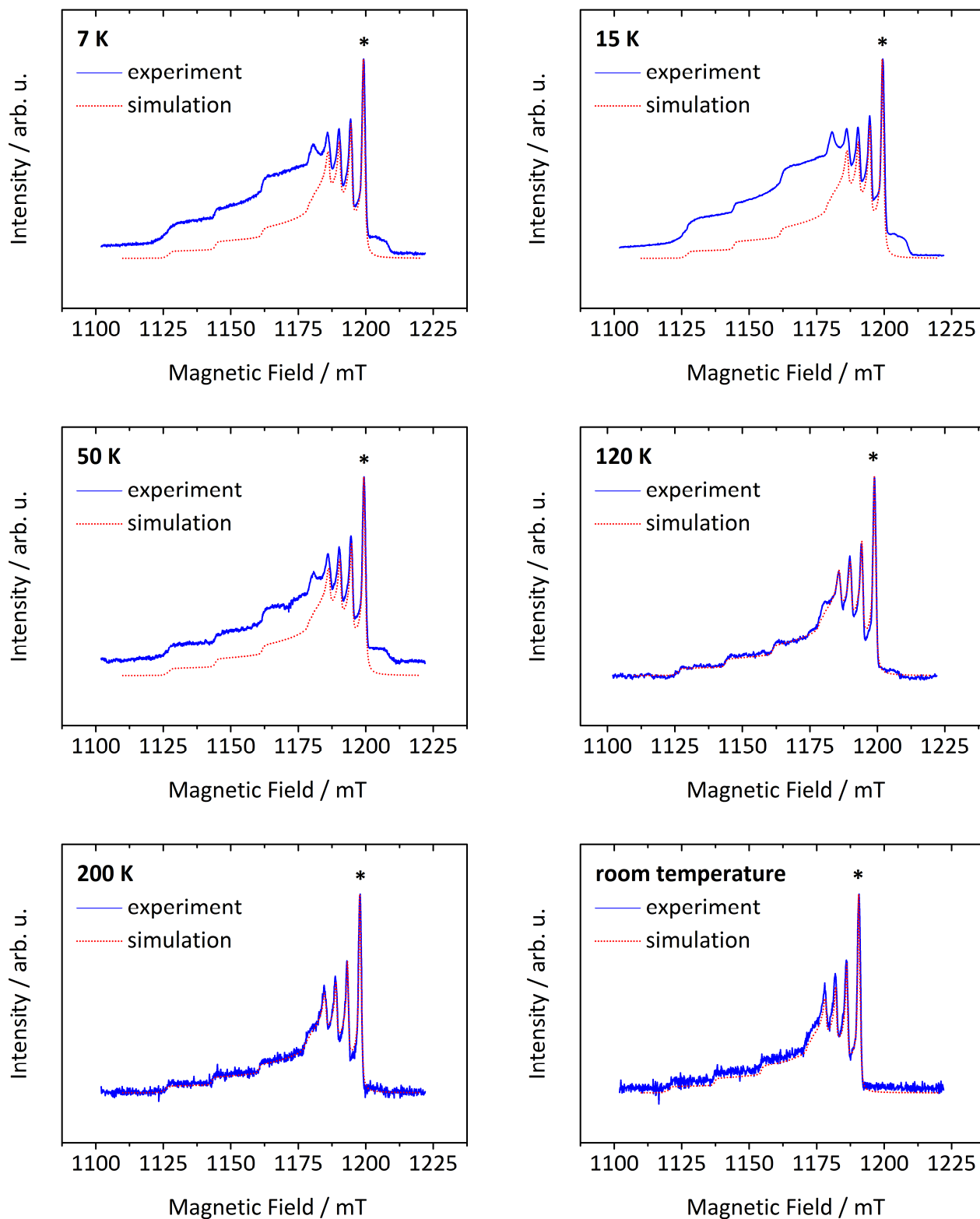


Figure 41: ESE-detected EPR spectra of $\text{Cu-Smmt}^{\text{P}}_{0.001\%}$ recorded at Q-band (33.77 GHz, Frankfurt) and various temperatures as indicated. Blue, solid lines represent experimental data and red, dotted lines indicate corresponding simulations. Simulation parameters can be found in Table 32. The asterisks indicate field positions for spin dynamics measurements. Figure adapted from K. Bader *et al.*, *Nat. Commun.* 2014, 5, 5304.^[69]

The simulation parameters of the spectra at different temperatures are predominantly equivalent within the assigned error margins for **Cu-Smnt^P_{0.001%}** (Table 32) and **Cu-Smnt^{P/d}_{0.01%}** (here in all cases parameters from Table 23 used). For both compounds, the intensity difference between experiment and simulation decreases with increasing temperature. Above 120 K, no such difference is visible anymore. As discussed in Section 3.1.3, the intensity differences are attributed to a spurious signal of **Ni-Smnt^P_{para}** or **Ni-Smnt^{P/d}_{para}**, respectively, presumably formed via air-oxidation during the preparation of the doped powders. From the temperature dependence of the signal intensities it is concluded, that the relaxation times of the paramagnetic Ni³⁺-compounds are below the detection window for temperatures of 120 K and higher. The signals of the corresponding Cu²⁺-compounds can be easily detected for higher temperatures and even up to room temperature, indicating the overall slower electron spin dynamics compared to the Ni³⁺-compounds.

Table 32: Simulation parameters for ESE-detected EPR spectra (Figure 19) of **Cu-Smnt^P_{0.001%}** recorded at Q-band (33.77 GHz, Frankfurt) and various temperatures as indicated.

T / K	g_{\parallel}	g_{\perp}	$A_{\parallel} / \text{MHz}$	A_{\perp} / MHz	$\Delta B_{\text{lwpp}} / \text{mT}$
7	2.0925 ± 0.0005	2.0227 ± 0.0005	500 ± 5	118 ± 5	[0 0.4]
15	2.0925 ± 0.0005	2.0224 ± 0.0005	500 ± 5	118 ± 5	[0 0.4]
50	2.0925 ± 0.0005	2.0224 ± 0.0005	500 ± 5	118 ± 5	[0 0.4]
120	2.0935 ± 0.0005	2.0232 ± 0.0005	505 ± 5	118 ± 5	[0 0.4]
200	2.0920 ± 0.0005	2.0222 ± 0.0005	500 ± 5	118 ± 5	[0 0.35]
rt	2.0905 ± 0.0005	2.0225 ± 0.0005	495 ± 5	112 ± 5	[0 0.4]

Electron Spin Dynamics Investigation

Temperature dependent inversion recovery and Hahn echo decay experiments were performed for **Cu-Smnt^P_{0.001%}** and **Cu-Smnt^{P/d}_{0.01%}** at Q-band and the magnetic field fixed to the position indicated by the asterisk in the corresponding ESE-detected EPR spectrum (Figure 41, Supplementary Figure 47–Supplementary Figure 49). These magnetic field positions in the g_{\perp} -region are assigned to the $|m_s, m_I\rangle = |-1/2, +3/2\rangle$ to $|+1/2, +3/2\rangle$ transition. This field position was selected for the temperature dependent study, because the relaxation times here were the longest ones observed in the magnetic field dependence (Section 3.2.1). The temperature dependent inversion recovery and Hahn echo decay curves of **Cu-Smnt^P_{0.001%}** are shown in Figure 42 and Figure 43 (for **Cu-Smnt^{P/d}_{0.01%}**: Supplementary Figure 50–Supplementary Figure 52).

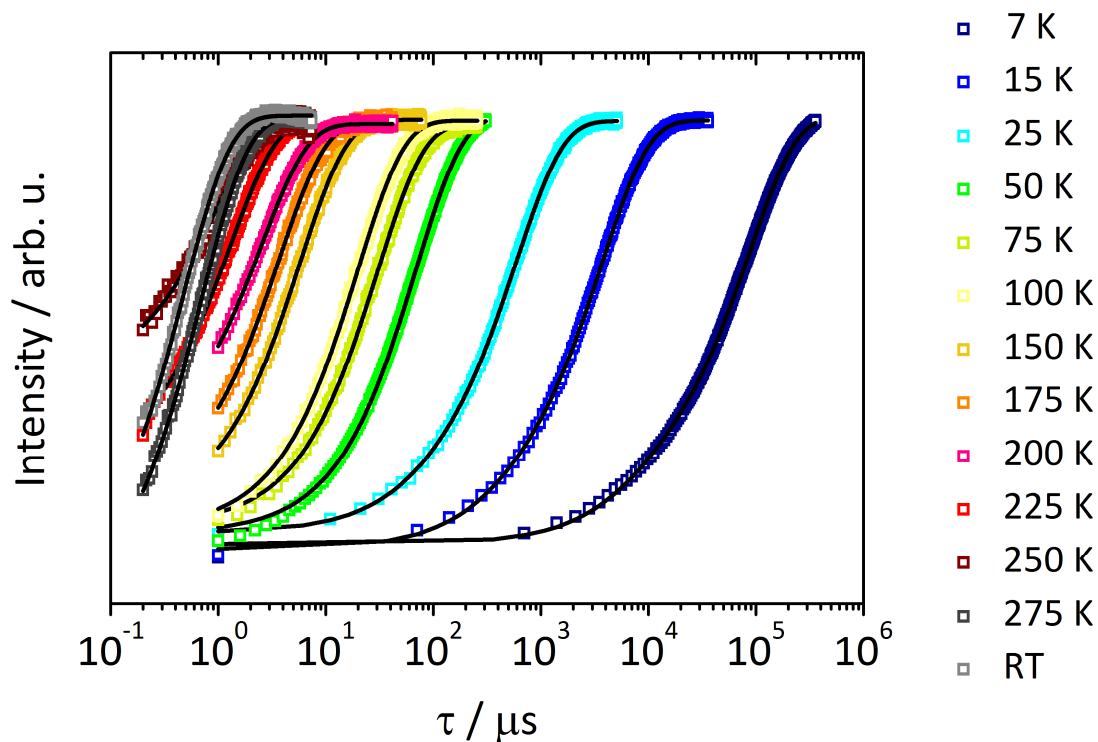


Figure 42: Inversion recovery measurements (open symbols) and fits (solid lines) of $\text{Cu-SmntP}_{0.001\%}$ recorded at Q-band (33.77 GHz, Frankfurt) and various temperatures as indicated. Magnetic field was fixed to the position indicated by the asterisks in the corresponding ESE-detected EPR spectra shown in Figure 41. Fit parameters see Table 33. Figure adapted from K. Bader et al., *Nat. Commun.* 2014, 5, 5304.^[69]

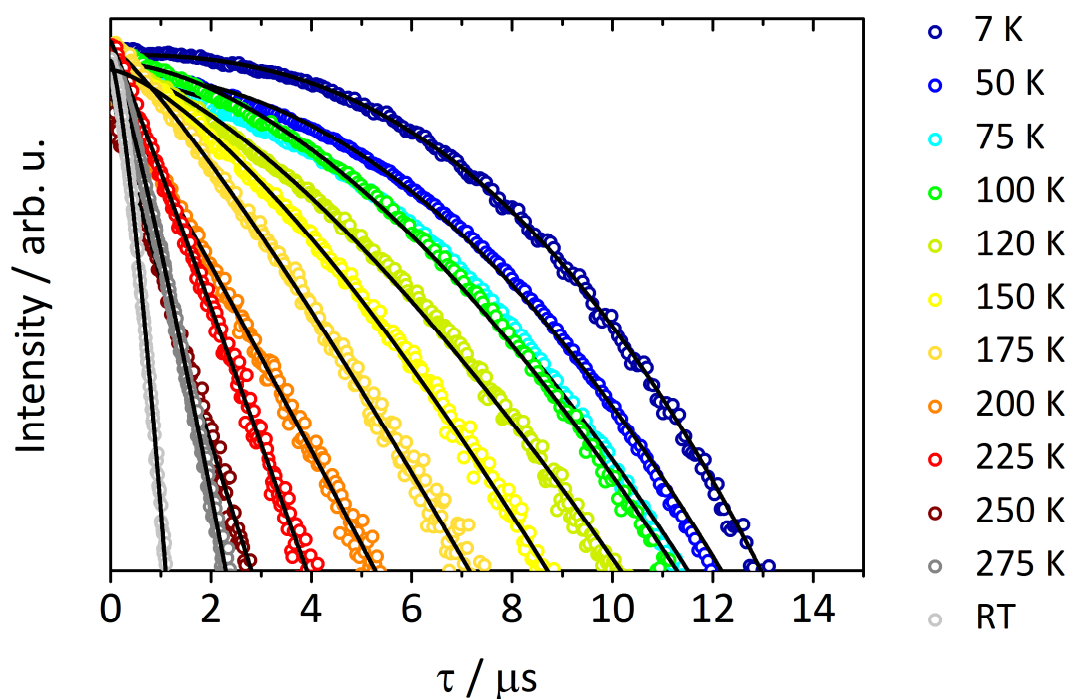


Figure 43: Hahn echo decay measurements (open symbols) and fits (solid lines) of $\text{Cu-SmntP}_{0.001\%}$ recorded at Q-band (33.77 GHz, Frankfurt) and various temperatures as indicated. Magnetic field was fixed to the position indicated by the asterisks in the corresponding ESE-detected EPR spectra shown in Figure 41. Fit parameters see Table 33. Figure adapted from K. Bader et al., *Nat. Commun.* 2014, 5, 5304.^[69]

Mono-, bi- or stretched exponential functions were applied for fitting and the corresponding parameters are summarized in Table 33–Table 34. Figure 44 gives an overview of the extracted slow spin-lattice and phase memory times in dependence of temperature.

The detected spin-lattice relaxation times of **Cu-Smnt^P_{0.001%}** vary from ca. 87 ms to 0.5 μ s in the range from 7 K up to room temperature. Below 50 K, biexponential inversion recovery curves were found. The contribution of the fast process decreases from 7 K to 50 K and was not detected for higher temperatures. In this low temperature regime, the spin-lattice relaxation shows a strong temperature dependence. Above ca. 50 K, the changes in $T_{1,s}$ are much smaller.

Table 33: Parameters of mono-, bi- or stretched exponential fit functions according to equations (90), (63) and (64) and standard deviations for inversion recovery and Hahn echo experiments of **Cu-Smnt^P_{0.001%}** recorded at Q-band (33.77 GHz, Frankfurt) and various temperatures as indicated. Magnetic field was fixed to the position indicated by the asterisks in the corresponding ESE-detected EPR spectra shown in Figure 41.

T / K	$T_{1,f} / \mu\text{s}$	$T_{1,s} / \mu\text{s}$	$T_{M,s} / \mu\text{s}$	k
7	6852 ± 195	87380 ± 209	9.229 ± 0.010	2.480 ± 0.010
15	358 ± 17	3707 ± 7	9.128 ± 0.011	2.445 ± 0.011
25	58 ± 4	592 ± 1	8.950 ± 0.015	2.350 ± 0.014
50	-	69.1 ± 0.1	8.301 ± 0.022	2.099 ± 0.017
75	-	30.32 ± 0.08	7.458 ± 0.025	1.828 ± 0.016
100	-	19.79 ± 0.05	6.951 ± 0.023	1.709 ± 0.013
120	-	9.51 ± 0.02	5.804 ± 0.017	1.457 ± 0.008
150	-	5.74 ± 0.02	4.869 ± 0.019	1.401 ± 0.010
175	-	3.67 ± 0.01	3.463 ± 0.014	1.181 ± 0.007
200	-	2.520 ± 0.007	2.528 ± 0.017	1.045 ± 0.008
225	-	1.291 ± 0.005	1.679 ± 0.010	1.027 ± 0.007
250	-	0.910 ± 0.008	1.168 ± 0.013	0.892 ± 0.010
275	-	0.692 ± 0.002	1.121 ± 0.003	1.173 ± 0.004
293	-	0.477 ± 0.002	0.600 ± 0.002	1.379 ± 0.006

Table 34: Parameters of mono- or biexponential fit functions according to equation (90) and (63) and standard deviations for inversion recovery experiments of **Cu-Smnt^P_{0.01%}** recorded at Q-band (35.000 GHz, Stuttgart) and various temperatures as indicated.

T / K	$T_{1,f} / \mu\text{s}$	$T_{1,s} / \mu\text{s}$	$T_{M,f} / \mu\text{s}$	$T_{M,s} / \mu\text{s}$
7	7 ± 3	96197 ± 9356	4.2 ± 0.3	68 ± 3
50	-	83.5 ± 0.7	-	19.8 ± 0.1
150	-	1.60 ± 0.05	-	4.2 ± 0.2

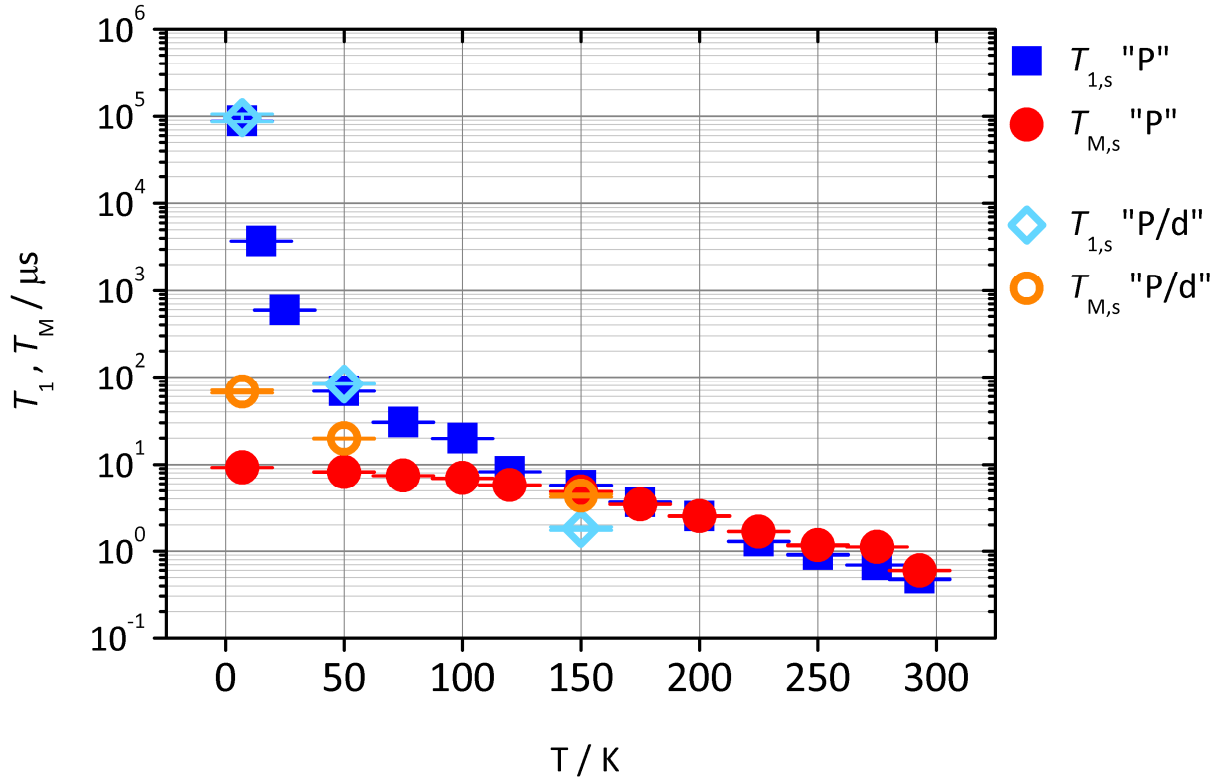


Figure 44: Temperature dependence of spin-lattice- and spin-spin relaxation times in microseconds of **Cu-Smnt^P_{0.001%}** (“P” in legend) recorded at Q-band (33.77 GHz, Frankfurt) and **Cu-Smnt^{P/d}_{0.01%}** (“P/d” in legend) recorded at Q-band (35.000 GHz, Stuttgart); values extracted from fit functions according to Table 33–Table 34. Blue, filled squares (red, filled circles) indicate the slow process of spin-lattice (spin-spin) relaxation in **Cu-Smnt^P_{0.001%}**. Light blue, open diamonds (orange, open circles) indicate the slow process of spin-lattice (spin-spin) relaxation in **Cu-Smnt^{P/d}_{0.01%}**. Error bars correspond to the standard deviations of the fit functions. Figure adapted from K. Bader et al., *Nat. Commun.* 2014, 5, 5304.^[69]

Cu-Smnt^{P/d}_{0.01%} shows the same temperature dependence of spin-lattice relaxation. However, at 150 K the detected spin-lattice relaxation time is shorter than the corresponding phase memory time. This is due to the very low S/N of the samples at this temperature in the used spectrometer. A three-pulse sequence is applied for detecting spin-lattice relaxation times, whereas a two-pulse sequence is used for the phase memory times. Presumably, this leads to an experimental error higher than the previously outlined 10 % in the inversion recovery experiments. The low S/N in the Stuttgart-spectrometer is also the reason, why no signal could be detected for **Cu-Smnt^{P/d}_{0.01%}** above 200 K. It is assumed, that the temperature dependence of spin-lattice relaxation of the two examined systems are identical for the whole investigated temperature range. Figure 44 indicates two distinct regions with different temperature dependent behavior. The experimental temperature dependence of spin-lattice relaxation rates of

Cu-Smnt^P_{0.001%} was modeled with a Raman process according to the phenomenological expression in equation (81), displayed in Figure 45. An inclusion of further processes resulted in an over-parametrization of the fit (not shown). A proportionality of the spin-lattice relaxation rate to approximately T^3 was found. Typically, an exponent of 9 would be expected for the Raman process (see Section 2.3.1). A deviation from this expectation is typical for highly covalent for S-containing Cu-complexes.^[49-50] In recent literature, similar exponents were found for vanadium-based coordination compounds, which were attributed to the involvement of not only acoustical but also optical phonons in spin-lattice relaxation.^[6] Manoharan *et al.* furthermore suggested the deviating exponents as being indicative for a transition from a dominant direct to a Raman process.^[49] This is probably also the case here, as two different regimes are visible in Figure 44, as indicated above. To ensure this by theory, measurements and modeling below 7 K are necessary. Alternatively, the exponent is not 9 probably because the condition $T \ll \theta_D$ is not fulfilled in the detected interval.^[49-50] For $T > \theta_D$, a quadratic temperature dependence of the spin-lattice rate is expected, which is not observed here. Due to this, it is assumed that the Debye-temperature is closely above 300 K.

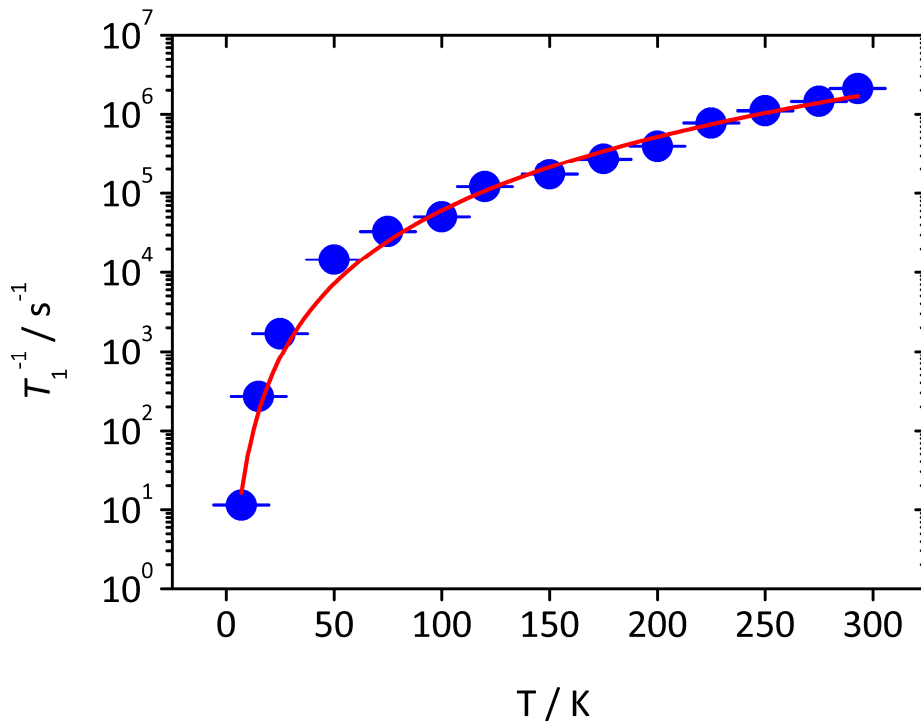


Figure 45: Experimental temperature dependence of spin-lattice relaxation rate of **Cu-Smnt^P_{0.001%}** (blue, filled circles) recorded at Q-band (33.77 GHz, Frankfurt) and fit with phenomenological model (red, solid line) for a Raman process $T_1^{-1} = ax^b$ with $a = 0.04 \pm 0.01$ and $b = 3.09 \pm 0.08$.

Literature on single crystals of other copper(II)-dithiolene coordination compounds report Debye-temperatures of 100–300 K.^[48-50] A modeling of the temperature dependence according to equations (78) and (82) for the extraction of a Debye-temperature was not successful for the collected data. Presumably a wider temperature range needs to be investigated in order to do so. The phase memory times of **Cu-Smnt^P_{0.001%}** vary from ca. 9–0.6 μ s in the range from 7 K up to room temperature. The values are temperature independent up to approximately 100 K, beyond that coherence is limited by spin-lattice relaxation. Over the whole temperature range, stretched exponential Hahn echo decay curves were found. Below 100 K, the stretch parameters are close to 2 or larger, which indicated nuclear spin diffusion as dominant dephasing process. At higher temperature, the stretch parameters are close to 1, which is indicative of physical motion of magnetic nuclei as coherence limiting factor. The phase memory time at room temperature is $0.600 \pm 0.002 \mu$ s, which is longer than commonly observed values for coordination compounds at low temperatures^[3-4] and very close to the record value of MQB-coherence times at room temperature of 0.83 μ s.^[6] The phase memory times of **Cu-Smnt^{P/d}_{0.01%}** are up to 7 times longer than the ones of its protonated analogue at the lower investigated temperatures. At 150 K, the phase memory times of both compounds are equivalent. The phase memory time of **Cu-Smnt^{P/d}_{0.01%}** at 7 K is among the highest reported values for potential MQBs.^[1-2]

3.2.3 Frequency Dependence of Spin Dynamics

The frequency dependence of electron spin relaxation was investigated for **Cu-Smnt^{P/d}_{0.01%}** in the range of 3.7–240 GHz. Numerous spectrometers were used and the measurements were performed with the help of numerous collaborators as indicated in the Experimental Section (5.2). The measurement temperature was 7 K, unless stated otherwise. This temperature was selected as it showed to be one of the lowest stable ones on all employed setups.

ESE-Detected EPR Spectra

ESE-detected EPR spectra were recorded on **Cu-Smnt^{P/d}_{0.01%}** at 7 K and S-band (3.700 GHz), X-band (9.563 GHz), Q-band (35.000 GHz), W-band (94.021 GHz), F-band (120 GHz) and Y-band (240 GHz).

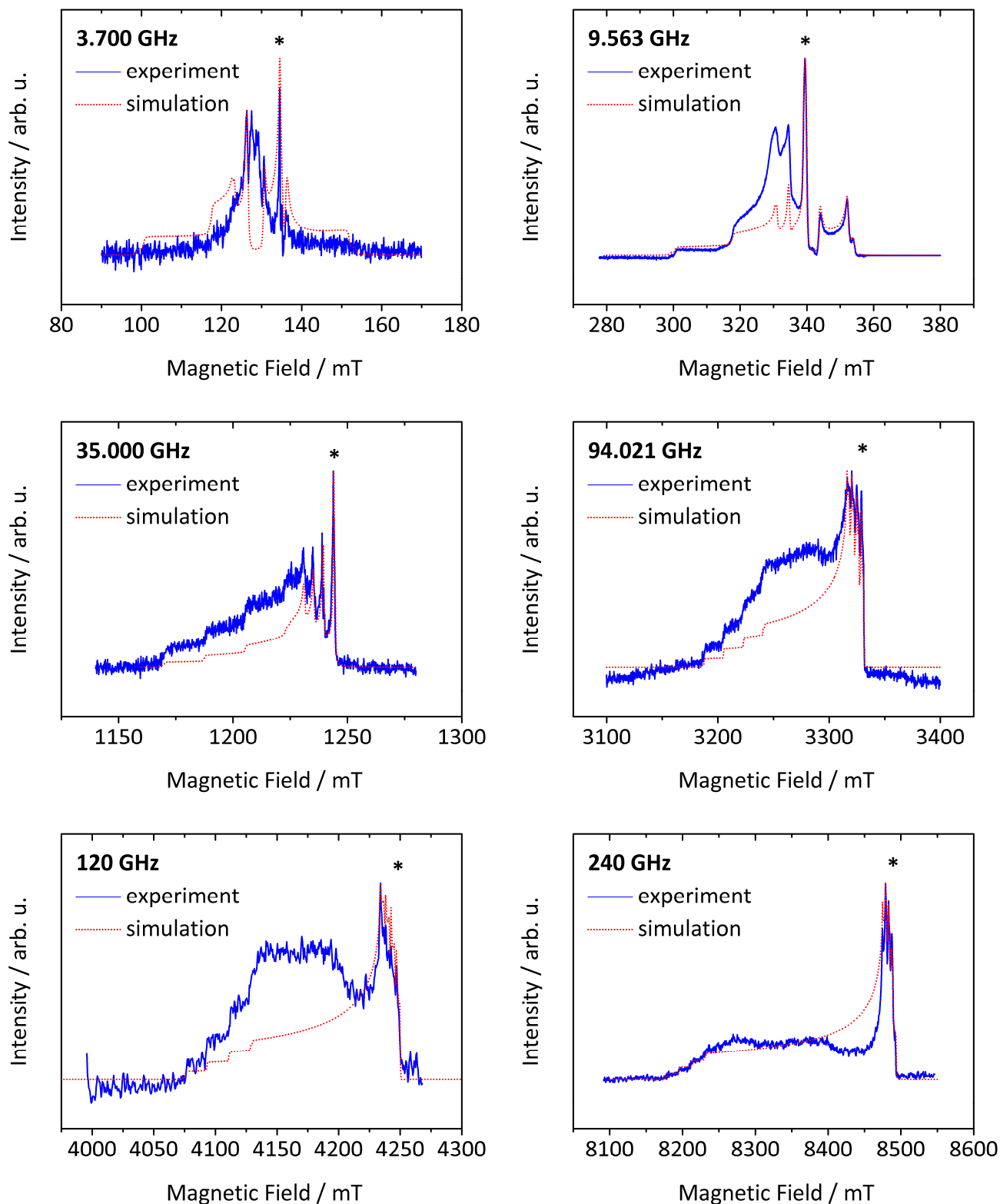


Figure 46: ESE-detected EPR spectra of $\text{Cu-Smnt}^{\text{P}/4}_{0.01\%}$ recorded at 7 K, MW frequency as indicated. Blue, solid lines represent experimental data and red, dotted lines indicate corresponding simulations. Simulation parameters can be found in Table 35 and Table 36. The asterisks indicate field positions for spin dynamics measurements.

Table 35: Simulation parameters for ESE-detected EPR spectra of $\text{Cu-Smnt}^{\text{P/d}}_{0.01\%}$ recorded at 7 K and S-, X-, Q-band (MW frequency as indicated).

ν_{MW} / GHz	g_{\parallel}	g_{\perp}	$A_{\parallel} / \text{MHz}$	A_{\perp} / MHz	$\Delta B_{l_{wpp}} / \text{mT}$
3.700	2.0900 ± 0.005	2.0203 ± 0.005	515 ± 5	118 ± 5	[0.2 0.2]
9.563	2.0900 ± 0.005	2.0203 ± 0.005	515 ± 5	118 ± 5	[0.2 0.2]
35.000	2.0900 ± 0.005	2.0203 ± 0.005	515 ± 5	118 ± 5	[0.2 0.2]

Table 36: Simulation parameters for ESE-detected EPR spectra of $\text{Cu-Smnt}^{\text{P/d}}_{0.01\%}$ recorded at 7 K and W-, F- and Y-band (MW frequency as indicated).

ν_{MW} / GHz	g_{zz}	g_{yy}	g_{xx}	A_{zz} / MHz	A_{yy} / MHz	A_{xx} / MHz	$\Delta B_{l_{wpp}} / \text{mT}$
94.021	2.0900 ± 0.005	2.0218 ± 0.005	2.0203 ± 0.005	515 ± 5	118 ± 5	118 ± 5	[0.3 0.3]
120	2.0900 ± 0.005	2.0218 ± 0.005	2.0203 ± 0.005	515 ± 5	118 ± 5	118 ± 5	[0.3 0.3]
240	2.0900 ± 0.005	2.0218 ± 0.005	2.0203 ± 0.005	515 ± 5	118 ± 5	118 ± 5	[0.1 0.1]

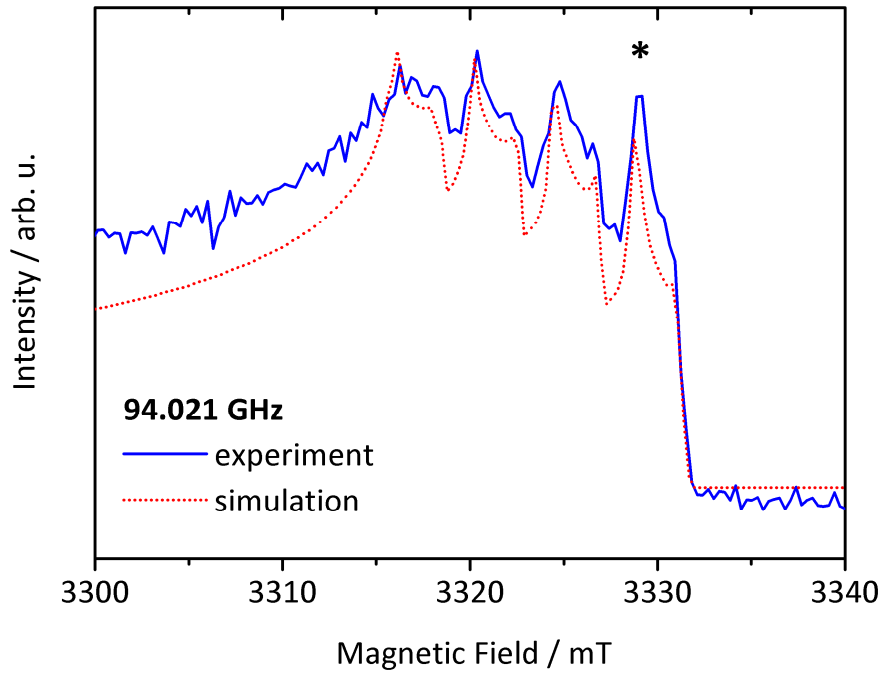
**Figure 47:** Detail of ESE-detected EPR spectra of $\text{Cu-Smnt}^{\text{P/d}}_{0.01\%}$ recorded at 7 K and W-band (94.021 GHz). Blue, solid lines represent experimental data and red, dotted lines indicate corresponding simulations. Simulation parameters can be found in Table 36. The asterisks indicate field positions for spin dynamics measurements.

Figure 46 shows the results including simulation with parameters according to Table 35 and Table 36. In all cases, differences between experiment and simulation are visible, which are attributed to a paramagnetic Ni^{3+} -species, as indicated in the previous sections (3.1.3 and 3.2.2). At S-band, some of the signals predicted by the simulation are not clearly observed in the experiment. This is a result of the low S/N, what can be concluded from a comparison with the spectrum of a more highly concentrated sample (**Cu-Smnt^{P/d}_{2%}**, Supplementary Figure 53).

The spectra can be divided into two groups: high and low frequency spectra. At low frequencies, i.e. S-, X- and Q-band, axial g - and A -tensors in the simulation with equivalent components as indicated previously for **Cu-Smnt^{P/d}_{0.01%}** are sufficient to reproduce the experiments (Table 35). The spectra at S- and X-band look more complicated compared to higher frequencies, as the HF-split lines of the g_{\parallel} - and g_{\perp} -components intermingle. At Q-band, the signals assigned to g_{\parallel} and g_{\perp} are separated from each other, which simplifies the interpretation. At high frequencies, i.e. W-, F- and Y-band a slight rhombicity of the g - and A -tensors is resolved (Table 36). For better visibility, a part of the W-band spectrum is magnified in Figure 47, where two sets of signals are visible in the g_{\parallel} -region, assigned to $g_x \neq g_y$. This was also observed in literature for similar compounds in measurements of (undoped) single crystals. ^[139, 142-143]

Electron Spin Dynamics Investigation

Inversion recovery and Hahn echo measurements were performed for **Cu-Smnt^{P/d}_{0.01%}** at 7 K at all named frequencies and the magnetic field was set to the positions marked with an asterisks in Figure 46. This signal in the g_{\perp} -region is assigned to the $|m_s, m_I\rangle = |-1/2, +3/2\rangle$ to $|+1/2, +3/2\rangle$ transition. For S- and X-band, the S/N was low at that transition, so measurements were performed at the most intense spectral line instead. Preliminary experiments ensured, that the slow component of relaxation is equivalent at both magnetic field positions. The corresponding experimental curves and fits are shown in the Appendix (Supplementary Figure 54–Supplementary Figure 59). The corresponding fit parameters are listed in Table 37 and Table 38 and Figure 48 graphically summarized the frequency dependence of spin dynamics in **Cu-Smnt^{P/d}_{0.01%}** at 7 K. In the following, first the results for spin-lattice relaxation are presented, where applied fit models, extracted values and the frequency dependence are discussed. Subsequently, the same is presented for the results of spin-spin relaxation.

Table 37: Parameters of biexponential fit functions according to equation (90) and standard deviations for inversion recovery experiments of $\text{Cu-Smnt}^{\text{P/d}}_{0.01\%}$ recorded at 7 K, MW frequency and magnetic field as indicated.

ν_{MW} / GHz	B_0 / mT	A_f	$T_{1,f}$ / ms	A_s	$T_{1,s}$ / ms
3.700	134.4	-0.5 ± 0.2	8 ± 4	-1.5 ± 0.2	44 ± 4
9.563	339.5	-0.43 ± 0.01	40 ± 2	-1.43 ± 0.01	218 ± 2
35.000	1244.9	-0.7 ± 0.2	7 ± 3	-0.86 ± 0.06	96 ± 9
94.021	3329.2	-1.75 ± 0.01	2.72 ± 0.01	-0.27 ± 0.01	8.4 ± 0.2
120.000	4247.1	-1.9 ± 0.2	1.5 ± 0.3	-0.9 ± 0.3	4.9 ± 0.8
240.000	8487.0	-1.8 ± 0.4	0.15 ± 0.06	-0.9 ± 0.3	1.1 ± 0.9

Table 38: Parameters of mono-, biexponential or augmented fit functions according to equations (63) and (95) and standard deviations for Hahn echo experiments of $\text{Cu-Smnt}^{\text{P/d}}_{0.01\%}$ recorded at 7 K, MW frequency and magnetic field as indicated.

ν_{MW} / GHz	B_0 / mT	A_f	$T_{M,f}$ / μs	A_s	$T_{M,s}$ / μs	T_{SD} / μs
3.700	134.4	-	-	1.05 ± 0.05	74 ± 9	-
9.563	339.5	0.32 ± 0.08	18 ± 3	0.64 ± 0.08	53 ± 4	-
35.000	1244.9	0.59 ± 0.02	4.2 ± 0.3	0.692 ± 0.007	68 ± 3	-
94.021	3329.2	0.10 ± 0.01	1.3 ± 0.3	0.967 ± 0.003	50.1 ± 0.5	-
120.000	4247.1	-	-	<i>fixed to 1</i>	68.5 ± 0.6	109 ± 1
240.000	8487.0	0.16 ± 0.02	4.5 ± 0.7	0.23 ± 0.02	19 ± 1	-

Two processes of spin-lattice relaxation were detected for all investigated MW frequencies. The spin-lattice relaxation times of the fast process range between 0.15–40 ms and those of the slow process between 1.1–218 ms. In both cases, the shortest spin-lattice relaxation times were detected at the 240 GHz, whereas the longest ones were found at 9.563 GHz. The slow process dominates the inversion-recovery curves at the investigated low MW frequencies (S-, X-band). The contribution of the fast process increases with ν_{MW} and it is the dominant process for the higher MW frequencies. The frequency dependences of fast and slow spin-lattice relaxation processes are in agreement with the expected behavior from theory: at higher MW frequencies, higher phonon densities are present, leading to higher transition probabilities and therefore shorter spin-lattice relaxation times (see Sections 2.2.4 and 2.3.1). If the fast process is caused by spectral diffusion, a lower contribution at higher MW frequencies would be expected due to the higher spectral dispersion. This leads effectively to fewer spins per Gauss, lowering the probability for spectral diffusion.^[3] As the inverse is observed - an increase of the fast process with increasing MW frequency - the frequency dependence of the fast process must therefore be dominated by another effect, such as e.g. faster relaxation in pairs and clusters.

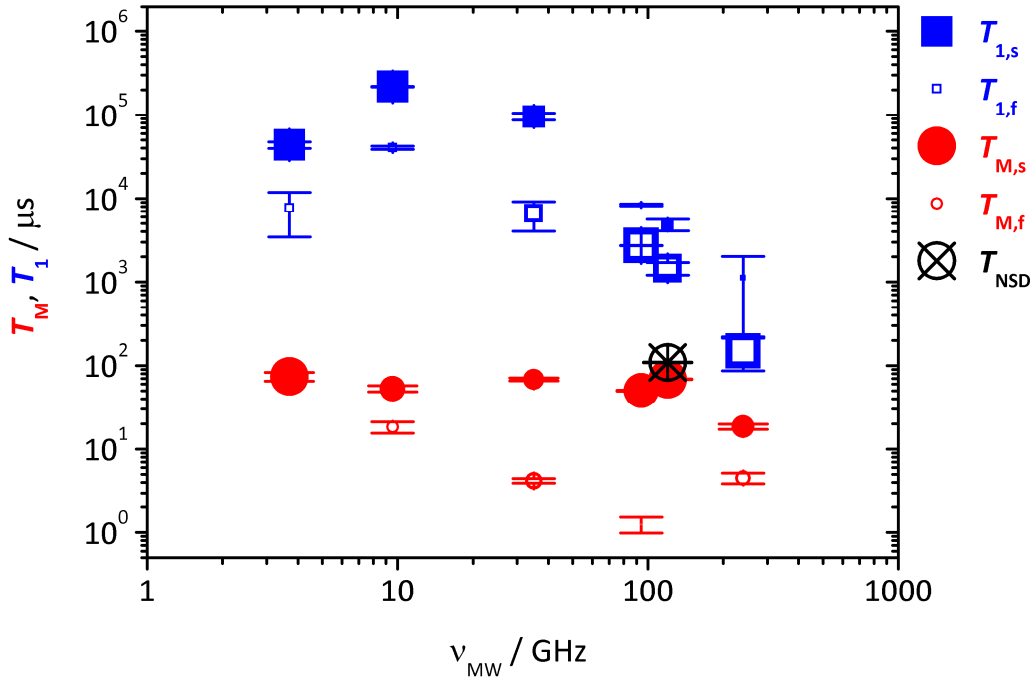


Figure 48: Frequency dependence of spin-lattice- and spin-spin relaxation times in microseconds of $\text{Cu-Smmt}^{P/d}_{0.01\%}$, values extracted from fit functions according to Table 37–Table 38. Blue, filled squares (red, filled circles) indicate the slow process of spin-lattice (spin-spin) relaxation. Blue, open squares (red, open circles) indicate the fast process of spin-lattice (spin-spin) relaxation. The nuclear spin diffusion characteristic time T_{NSD} is represented by black, open circle with cross. The size of the symbols corresponds to the relative size of the exponential prefactors A_f and A_s of the fast and slow process of spin-lattice and spin-spin relaxation time, respectively, extracted from fit functions. Error bars correspond to the standard deviations of the fit functions.

The frequency dependence of $T_{1,s}$ and $T_{1,f}$ was modeled in order to gain information on the spin-lattice relaxation process. In order to avoid over-parametrization of the fit, the relaxation rates were fit with a simple power functions aT^b . Figure 49 shows the results, including the equations of the model functions in the legend. The fit functions show good agreement with the experimental data at higher frequencies. For lower frequencies, strong deviations are observed. Furthermore, the standard deviations of the prefactors a are very large, so no quantitative assignments are made from the model functions. Nevertheless, qualitatively in both cases the exponents b indicate a mixture of direct and Raman process controlling spin-lattice relaxation. From theory, for a dominant direct process $T_1^{-1} \propto \nu_{MW}^4$ is expected. For the $S = 1/2$ Kramers ion no Orbach process is possible, so the exponents lower than 4 are assigned to the contribution of a Raman process, which is frequency independent at the investigated temperature (compare Section 2.3.1).

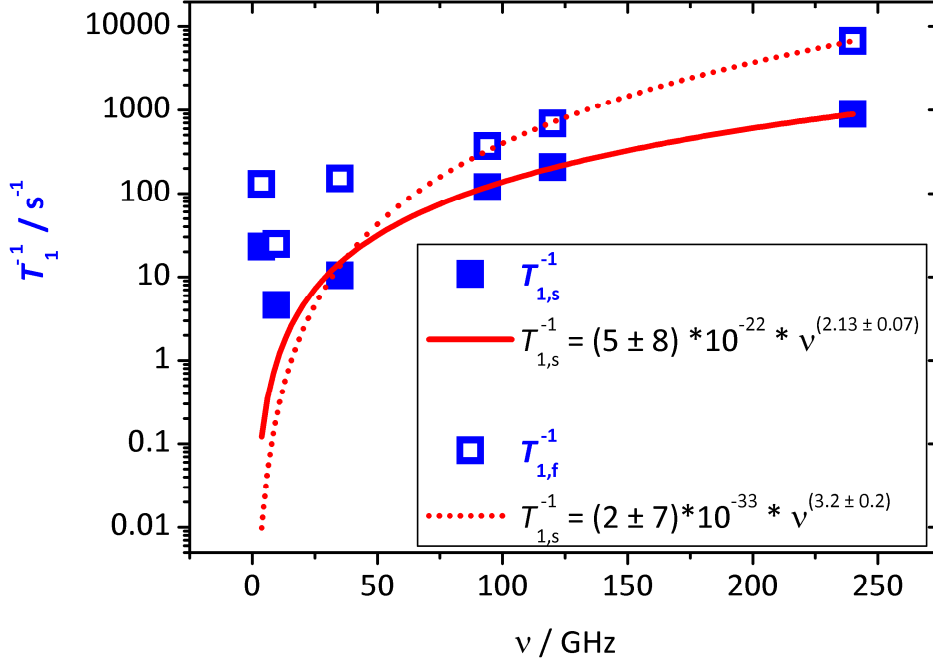


Figure 49: Frequency dependence and model function of spin-lattice- and spin-spin relaxation rates in Hz of $\text{Cu-Smnt}^{\text{P/d}}_{0.01\%}$, values extracted from fit functions according to Table 37–Table 38. Blue, filled squares (blue, open squares) indicate the slow (fast) process of spin-lattice relaxation, the red solid line (red dotted line) indicates the model function for the frequency dependence of the slow (fast) spin-lattice relaxation process, functions as indicated in legend.

In the previous section, the dominant spin-lattice relaxation mechanism at Q-band was attributed to a Raman process. The direct process is generally expected to be observed at low temperatures. Low and high temperatures can be determined by the ratio of thermal- and MW energy (Table 39). As the measurement temperature of 7 K compared to the MW energy in units of K transitions from a “high” to a “rather low” temperature, not only a Raman but also the direct process is observed in this frequency dependent study. This transition of thermal energy regime could also account for the large deviation of the fit at lower frequencies.

A deviation from $T_1^{-1} \propto \nu_{MW}^4$ was also found for a similar dithiolene-coordination compound in a doped single crystal.^[50] Kirmse *et al.* connected the found lower exponent to a low probability for the direct process at the employed MW frequencies (9 and 28.7 GHz) and suggested additionally the presence of anharmonic lattice librations. Eaton *et al.* reported a very small frequency dependence of spin-lattice relaxation for another dithiolene system (measurements at X- and W-band, modeling with a combination of a Raman process and a local mode).^[144]

Table 39: Comparison of measurement temperature and MW energy ($h\nu k_B^{-1}$) at different employed MW frequencies. The coloring shall indicate the transition from “rather low” (blue) to “high” (red) temperature conditions.

ν_{MW}	T / K	$h\nu k_B^{-1} / \text{K}$
3.700	7	0.2
9.563	7	0.5
35.000	7	1.7
94.021	7	4.5
120.000	7	5.8
240.000	7	11.5

The findings from the experiments found in literature and performed in this Ph.-D.-project show, how crucially the amount of data and selected measurement conditions influence the interpretation of the results. The frequency dependent spin-spin relaxation investigation yielded in most cases two phase memory times. For the fast process, values of 1.3–18 μs were found and for the slow process 19 μs up to ca. 70 μs . At S-band, the S/N was very low and instead of fitting the Hahn echo decay curve with a (bi)exponential function as in the other cases, a linear fit to the natural logarithm of the experimental intensity values was applied. The extracted phase memory times seem to be rather frequency independent at lower frequencies. At 120 GHz (F-band), the experimental Hahn echo decay cannot be fitted with a (bi)exponential or stretched exponential function. The Hahn echo decay curves including fits at two selected MW frequencies are shown in Figure 50. For the non-exponential decay at 120 GHz, an augmented fit model according to Feretti *et al.* was applied:^[7]

$$I(2\tau) = A_s \exp[-2\tau/T_{M_s} - (2\tau/T_{NSD})^3] \quad (95)$$

With the nuclear spin diffusion characteristic time T_{NSD} and the other parameters having their usual meaning. The fit parameters T_{M_s} and T_{NSD} show a strong inverse correlation (Pearson correlation coefficient of -0.7), so the exact values of the parameters are difficult to obtain correctly. However, this effect is presumably not an artefact, as also for other measurement temperatures at 120 GHz non-exponential decays were found (see Appendix: Supplementary Figure 60 and Supplementary Figure 61). Furthermore, measurements with the same spectrometer at another frequency (240 GHz) and various temperatures yielded in (bi)exponential Hahn echo decay curves (see Appendix Supplementary Figure 62 and Supplementary Figure 63).

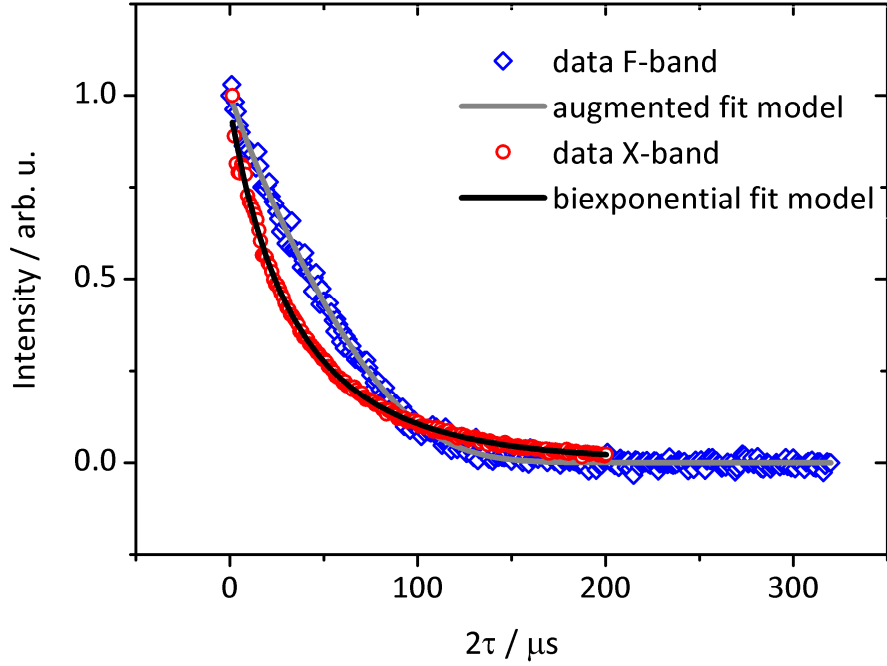


Figure 50: Hahn echo decay measurements and fits of $\text{Cu-Smnt}^{P/d}_{0.01\%}$ recorded at 7 K and two different MW frequencies. Magnetic field was fixed to the position indicated by the asterisks in the corresponding ESE-detected EPR spectra shown in Figure 46. Red, open circles (black, solid line) indicate experimental data (fit function) at X-band (9.563 GHz) and blue, open diamonds (grey, solid line) represents experimental data (fit function) at F-band (120 GHz), fit parameters see Table 38.

Table 40: Parameters of biexponential fit functions according to equation (90) and standard deviations for inversion recovery experiments of $\text{Cu-Smnt}^{P/d}_{0.01\%}$ recorded at various low temperatures, MW frequency and magnetic field as indicated.

ν_{MW} / GHz	B_0 / mT	T / K	A_f	$T_{1,f} / \text{ms}$	A_s	$T_{1,s} / \text{ms}$
120.000	4247.1	1.5	-2.0 ± 0.5	2.7 ± 0.8	-1.6 ± 0.3	89 ± 34
		3	-1.67 ± 0.02	3.74 ± 0.07	-0.61 ± 0.02	23.5 ± 0.6
		7	-1.9 ± 0.2	1.5 ± 0.3	-0.9 ± 0.3	4.9 ± 0.8
240.000	8487.0	1.5	-	-	-	-
		3	-3 ± 1	0.03 ± 0.02	-1.3 ± 0.4	0.23 ± 0.05
		7	-1.8 ± 0.4	0.15 ± 0.06	-0.3 ± 0.3	1.1 ± 0.9

3. Results & Discussion

Table 41: Parameters of biexponential and augmented fit models according to equations (63) and (95) and standard deviations for Hahn echo experiments of $\text{Cu-Smnt}^{P/d_{0.01\%}}$ recorded at various low temperatures, MW frequency and magnetic field as indicated.

ν_{MW} / GHz	B_0 / mT	T / K	A_f	$T_{M,f} / \mu\text{s}$	A_s	$T_{M,s} / \mu\text{s}$	$T_{NSD} / \mu\text{s}$
120.000	4247.1	1.5	0.43 ± 0.02	4.0 ± 0.3	0.564 ± 0.005	265 ± 8	285 ± 4
		3	-	-	0.985 ± 0.002	114.8 ± 0.8	198 ± 7
		7	-	-	fixed to 1	68.5 ± 0.6	109 ± 1
240.000	8487.0	1.5	0.35 ± 0.06	2.3 ± 0.8	0.70 ± 0.02	83 ± 4	-
		3	0.06 ± 0.02	1.1 ± 0.8	0.570 ± 0.006	47.1 ± 0.8	-
		7	0.16 ± 0.02	4.5 ± 0.7	0.23 ± 0.02	19 ± 1	-

Interestingly, the slow phase memory time at 240 GHz is much shorter compared to the other investigated frequencies. Table 40 and Table 41 summarize the extracted relaxation times at high frequencies and various temperatures. Reviewing the relevant theory (compare Section 2.3), the frequency dependence between 3.7 and 120 GHz is in agreement with literature known influences of nuclear spin dynamics. The selected measurement temperature of 7 K is a relatively high temperature in comparison to the MW energy, as mentioned previously (Table 39). It is assumed that the correlation time of nuclear spin flip-flop processes τ_c is relatively short and motional narrowing leads to a standard exponential Hahn echo decay. Increasing the MW frequency while keeping the same temperature leads then to longer correlation times. At 120 GHz, 7 K represents a rather low temperature, which leads to the assumption, that the condition $T_M \gg \tau_c$ is fulfilled, leading to the observation of a Gaussian echo decay (compare equation (86)). Within this reasoning, the correlation time of nuclear spin flip-flops should be even longer at 240 GHz and also a Gaussian decay should be observed. This is clearly not the case. Standard exponentials can also be observed for $\tau \gg T_{1,n}$ (compare equations (87) and (88)), if nuclear spin diffusion is quenched by strong nuclear spin polarization accompanied by an increase of the observed phase memory time.^[53] The nuclear Zeeman energies are orders of magnitude smaller than the thermal energy at 7 K for all investigated frequencies, which is visualized by Figure 51. Therefore, an infinite temperature state of the nuclear spin bath at 7 K can be safely assumed and quenched nuclear spin diffusion is not the reason for the decrease in $T_{M,s}$ from 120 to 240 GHz. However, the electronic spin-lattice relaxation could account for that. Revisiting Figure 48, it can be seen that $T_{1,s}$ is in the same order of magnitude as $T_{M,s}$ at 240 GHz and spin-lattice relaxation limited coherence could be present.

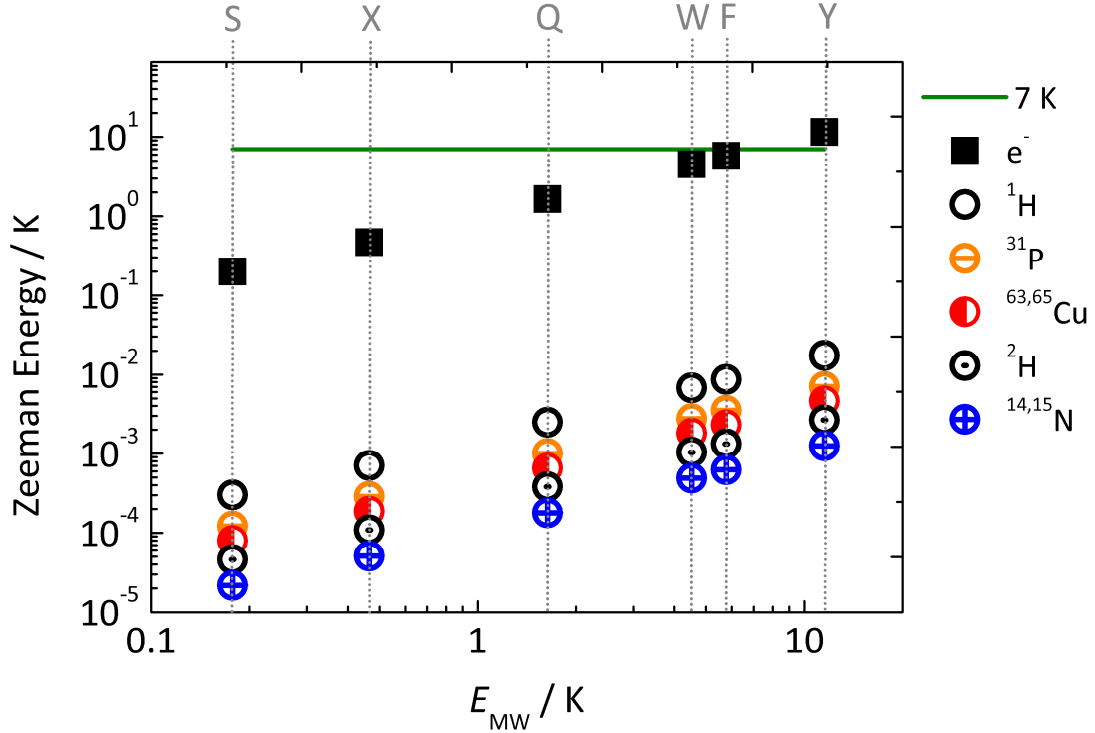


Figure 51: Zeeman energy in dependence of MW-energy, both in units of Kelvin. Green line indicates thermal energy at 7 K. Black, filled squares represent electronic (“e⁻”) Zeeman energies at the investigated MW-energies for $g = 2.02$. Symbols for nuclear Zeeman energy at investigated MW-energies as indicated in figure legend. Data point of ^{63}Cu (^{15}N) covered by point of ^{65}Cu (^{15}N).

Further frequency- and temperature dependent measurements on $\text{Cu-Smnt}^{\text{P/d}}_{0.01\%}$ could be performed to underline this hypothesis, which is beyond the scope of this dissertation. In addition it should be mentioned, that the theory on influences of nuclear spin diffusion on electron spin relaxation are strictly speaking valid for $I = 1/2$ and the validity of the model for systems with higher nuclear spin quantum numbers (and a mixture of nuclear spin carriers) is unproven.

3.2.4 Couplings to Nuclear Spins

The coupling of nuclear spins strongly influences the electron spin dynamics, as seen in the previous sections. Consequently, an in-depth investigation of couplings to nuclear spins should shed further light on the complex interplay of physical and chemical influences on electron spin dynamics in MQBs. In the first part, couplings between electron and nuclear spin will be investigated by the means of ESEEM-experiments at various frequencies. This investigation is deepened afterwards with ENDOR-spectroscopy at Q-band. On top, advanced pulsed EPR experiments were performed on $\text{Cu-Smnt}^{\text{P/d}}_{0.01\%}$, showing its principal applicability as MQB in

quantum information processing and quantum information storage. This is displayed by CPMG-experiments and transient nutations of electron- and nuclear spin.

The experiments presented in this Subsection were performed in Zürich (S-band, 3.700 GHz), Manchester (X-band, 9.688 GHz), Frankfurt (Q-band, 33.771 GHz), Oxford (Q-band, 34.091 GHz) and Antwerp (W-band, 94.019 GHz). Unless stated differently, the magnetic field was fixed to the position assigned to the $|m_s, m_I\rangle = |-1/2, +3/2\rangle$ to $|+1/2, +3/2\rangle$ transition in the g_{\perp} -region in these experiments.

ESEEM-Experiments

As introduced in Section 2.4.2, ESEEM-experiments are identical to Hahn echo decay (two-pulse ESEEM) and stimulated echo experiments (three-pulse ESEEM), but with smaller τ -increments are for better resolution of the modulations. Typically, weak dipolar couplings between electron and nuclear spins are observed with higher sensitivity than couplings >5 MHz.^[145] ESEEM-effects were observed at S-, X- and Q-band frequencies. The resulting two-pulse ESEEM-spectra at 15 K including results of data processing including FFT are shown in Figure 52.

In all three cases, a distinct peak is observed after data processing including FFT. At S-band, an FFT-shift of 0.469 MHz is observed, at X-band a peak at 2.279 MHz and at Q-band a peak at 7.917 MHz. For the assignment of the ESEEM-effects to nuclear spin, the Larmor frequencies of relevant nuclear spin carrying isotopes in **Cu-Smmt**^{P/d}_{0.01%} were calculated (Figure 43). From this it is obvious, that the ESEEM-effect at S-band is mainly caused by the ¹⁴N nuclear spin, while at X- and Q-band the ²H nuclear spin is responsible for the modulation.

Why are ESEEM-effects observed only at the lowest three investigated frequencies and why are coupling of only ¹⁴N and the ²H observed? In order to answer these questions, the proportionality of the modulation depth parameter in ESEEM-experiments of various parameters needs to be considered. In equation (93), the magnetic field and distance r between the corresponding nuclear spin and the MQBs electron spin are the only variable parameters for a fixed electron and nuclear spin and fixed orientation, so the modulation depth parameter can be described by:

$$k \propto \left(\frac{1}{B_0}\right)^2 \frac{1}{r^6} \quad (96)$$

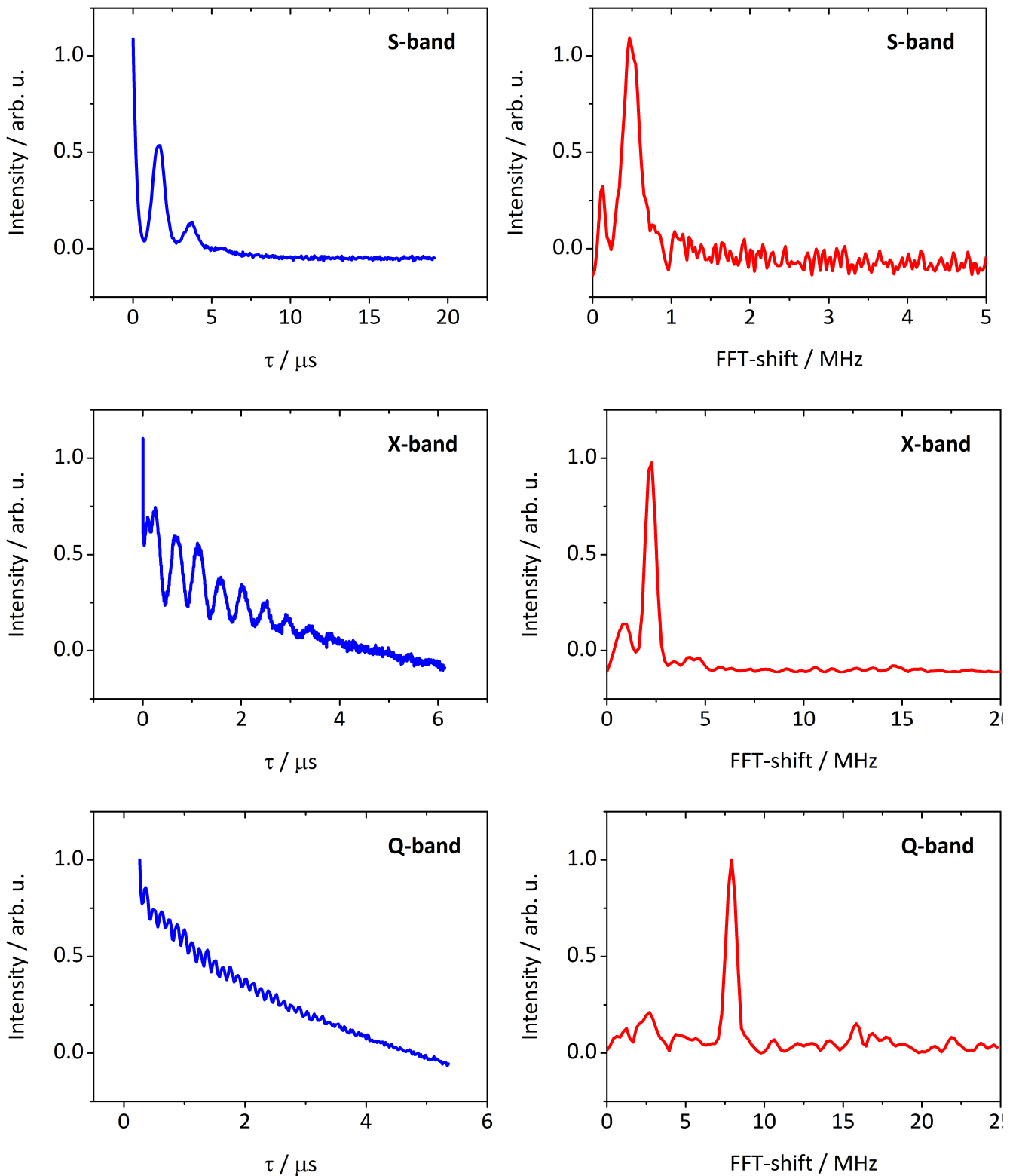


Figure 52: 2-pulse ESEEM experiments and FFT-results of $\text{Cu-Smnt}^{\text{P}/d_{0.01\%}}$ recorded at various frequencies as indicated and 7 K, the magnetic field was fixed to the position assigned by the asterisks in the corresponding ESE-detected EPR spectra in Figure 46. Left column: experimental data (blue, solid lines). Right column: FFT-results (red, solid lines). Calculated nuclear Larmor frequencies for the investigated MW frequencies and magnetic fields see Table 42.

Table 42: Calculated nuclear Larmor frequencies for **Cu-Smnt^{P/d}_{0.01%}** at the three MW frequencies.

conditions	S-band: 3.700 GHz, 0.147 T	X-band: 9.688 GHz, 0.346 T	Q-band: 34.091 GHz, 1.212 T
isotope	ν_L / MHz	ν_L / MHz	ν_L / MHz
¹ H	6.259	14.732	51.604
² H	0.961	2.261	7.922
¹⁴ N	0.452	1.065	3.730
¹⁵ N	0.635	1.494	5.233
³¹ P	2.536	5.969	20.909
⁶³ Cu	1.661	3.910	13.695
⁶⁵ Cu	1.779	4.188	14.669

Presumably, the modulation depth of ESEEM-effects of weakly coupled nuclear spins becomes too low to be observed beyond Q-band frequency for this sample.

From the crystal structure of **Cu-Smnt^{P/d}**, the relevant distances can be extracted. In Table 43 they are displayed together with the dipolar coupling strengths according to equation (19) of relevant nuclear spin carrying isotopes in **Cu-Smnt^{P/d}_{0.01%}**. The deuteration grade of the compound is high enough, that the contribution of ¹H can be neglected and that the natural abundance of ¹⁵N is similarly low enough to be ignored. The dipolar coupling strengths of ¹⁴N and the ²H are significantly stronger than the ones of the other relevant nuclei, so supposedly the modulation depths of ESEEM caused by the other nuclei is too low to be observed. Revisiting Figure 51, the nuclear Zeeman energies of ¹⁴N and the ²H are furthermore the weakest of the relevant isotopes in **Cu-Smnt^{P/d}_{0.01%}**.

Table 43: Calculated dipolar couplings for magnetic nuclei in **Cu-Smnt^{P/d}_{0.01%}** according to equation (19). Distance r represents closest distance of the indicated type of magnetic nuclei.

isotope	g_n	r / Å	$T_{dd,zz}^D$ / MHz	$T_{dd,xx}^D = T_{dd,yy}^D$ / MHz
¹ H	5.586	4.078	2.332	-1.166
² H	0.857	4.078	0.358	-0.179
¹⁴ N	0.404	5.598	0.065	-0.033
¹⁵ N	-0.566	5.598	-0.091	0.046
³¹ P	2.263	6.561	0.009	-0.005
⁶³ Cu	1.482	11.236	0.030	-0.015
⁶⁵ Cu	1.588	11.236	0.032	-0.016

ENDOR-Experiments

For a further investigation of couplings between electron and nuclear spins, stochastic-mode Davies-ENDOR experiments were performed. Preliminary investigations by Davies-ENDOR in standard detection mode did not yield in any resonances, presumably due to a long nuclear spin-lattice relaxation time. The experiments presented here were performed in stochastic mode, i.e. the radio frequency was not swept with a linear increment, but stochastically random. This prevents saturation of the nuclear spins.

Experiments were performed on **Cu-Smnt^{P/d}_{0.01%}** and **Cu-Smnt^{P/d}_{10%}** at Q-band and 15 K, Figure 53 and Figure 54 show the experimental results. As the S/N was rather low in the case of **Cu-Smnt^{P/d}_{0.01%}** and signal averaging proved to be tedious due to the long electronic spin-lattice relaxation time (compare Section 3.2.2), **Cu-Smnt^{P/d}_{10%}** was investigated as reference. In the more highly concentrated doped powder, not only the expected signals are more intense, but also the electron spin dynamics is much faster. This allows efficient signal averaging and results in better S/N, yielding more reliable results. The ENDOR spectra of both samples show two intense main features with several shoulders between 45–150 MHz. In case of **Cu-Smnt^{P/d}_{0.01%}**, additional features are observed below 45 MHz. The signals resemble the shape and distance of the two main features. The low-field features are harmonics of the main signals occurring due to power saturation. The spectrum of **Cu-Smnt^{P/d}_{0.01%}** was recorded with full RF power, whereas for **Cu-Smnt^{P/d}_{10%}** a 6 dB attenuation was applied. For the latter, no power harmonics are observed. A comparative measurement for **Cu-Smnt^{P/d}_{10%}** without and with RF-attenuation is shown in the appendix (Supplementary Figure 64).

The interpretation of the Davies-ENDOR spectra is not trivial. The signal center of weakly dipolar coupled nuclei (i.e. $\nu_{L,n} > A/2$) is expected at their Larmor frequency and the signal should be separated by the value of the HF-coupling constant. For strong HF couplings ($\nu_{L,n} < A/2$), it is vice versa: the signal center of these couplings appears at half of the value of the HF-coupling constant and is split by the twice the Larmor frequency of the corresponding nucleus.^[145]

The best fit between simulation and experiment for both investigated samples was achieved with a minimal parameter set (Table 44). This includes a rhombic g -tensor of an $S = 1/2$ system and a rhombic A -tensor of strongly coupled Cu-nuclei (isotopic ratio as naturally abundant).

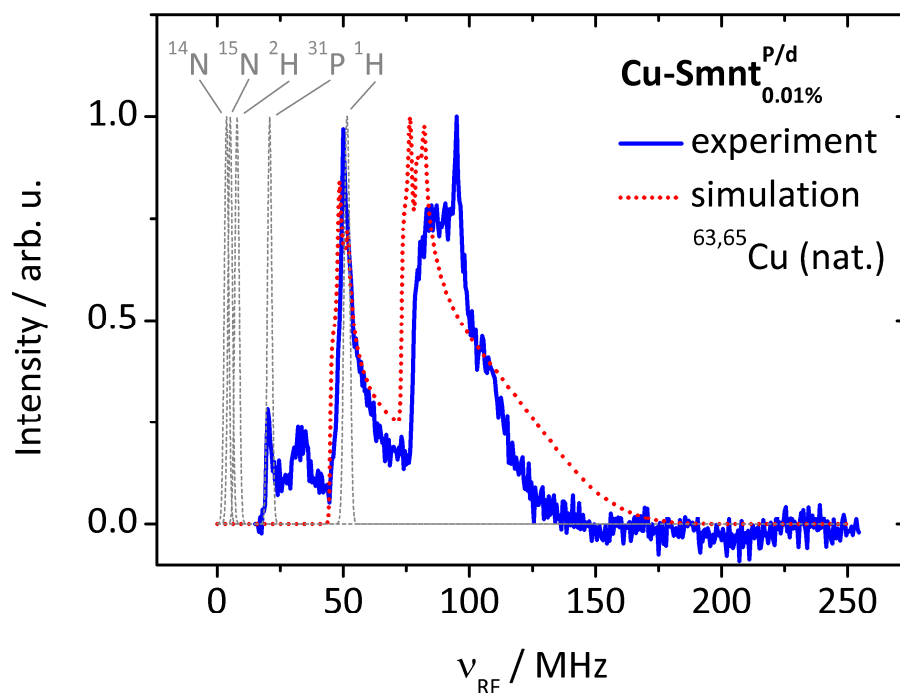


Figure 53: Davies-ENDOR for $\text{Cu-Smnt}^{\text{P/d}}_{0.001\%}$ at Q-band (34.090 GHz), 15 K and 1211.9 mT. Experimental data (blue, solid line) and simulation (red, dotted line), parameters see Table 44. Grey, broken lines represent ENDOR-resonances of dipolar couplings of nuclei which are contained in the compound, but were not included in the final simulation, parameters see Table 43.

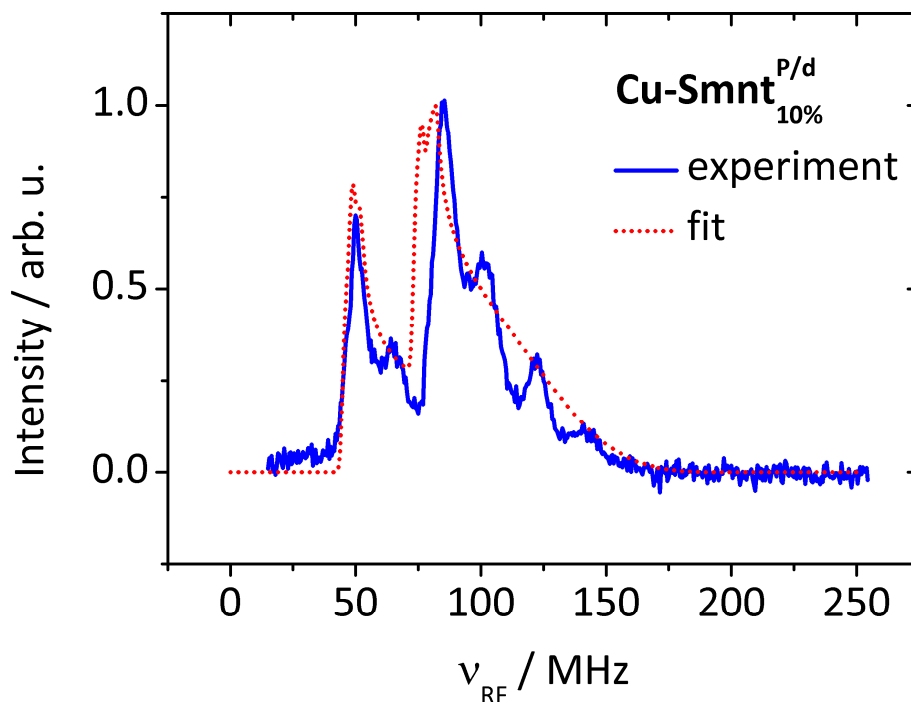


Figure 54: Davies-ENDOR for $\text{Cu-Smnt}^{\text{P/d}}_{10\%}$ at Q-band (34.067 GHz), 15 K and 1211.3 mT, experimental data (blue, solid line) and simulation (red, dotted line). Simulation parameters see Table 44.

Table 44: Simulation parameters applied for Davies-ENDOR of both **Cu-Smnt^{P/d}_{0.001%}** at Q-band (34.090 GHz), 15 K and 1211.9 mT and **Cu-Smnt^{P/d}_{10%}** at Q-band (34.067 GHz), 15 K and 1211.3 mT.

g_{zz}	g_{yy}	g_{xx}	A_{zz} / MHz	A_{yy} / MHz	A_{xx} / MHz	$\Delta B_{lwp} / \text{mT}$	Nuclei
2.0900	2.0218	2.0203	515	121	114	2	⁶³ Cu, ⁶⁵ Cu; nat. abund.

In Figure 53, simulations for the other contained nuclei are shown (grey, broken lines) with dipolar coupling constants calculated from their distances to the electron spin center (Table 43). This illustrates, that presumably none of these weak dipolar couplings contribute to the ENDOR spectra of **Cu-Smnt^{P/d}_{0.01%}** and **Cu-Smnt^{P/d}_{10%}**.

The simulation parameters of the electron spin g -tensor are in good agreement with the parameters obtained in the frequency dependent study for ESE-detected EPR spectra at W-, Y- and F-band (Table 36). In contrast, the extracted values for components of the HF-coupling tensor disagree with those previously identified (Table 36). No uncertainties are indicated in Table 44 for the simulation parameters of the ENDOR-spectra, as for a set of seven variables surely other combinations can be found, leading to a similarly satisfying result. Additionally, the agreement of simulation and experiment is not very high and should be improved. ENDOR-measurements on powders with randomly oriented crystallites are very demanding and simpler spectra could be obtained from single-crystal measurements. Nevertheless, the obtained parameters are comparable to literature values for a similar system.^[138] Furthermore, at this point of the investigation an assignment of strong and weak couplings of nuclei in **Cu-Smnt^{P/d}_{0.01%}** is satisfactory. The weak couplings are targeted in the following section by CPMG, which aimed to eliminate their coherence destroying influence. In the last paragraph of this subsection, first qubit manipulations will be shown, employing the identified strong coupling between the electron spin and the copper nuclear spin for a demonstration of coherence transfer.

CPMG-Experiments

Over the course of the Results & Discussion Section of this thesis, weakly dipolar coupled nuclear spins were identified as one of the main coherence destroying influences in **Cu-Smnt^{P/d}_{0.01%}**. As introduced in the description of pulsed experiments in Section 2.4.2, the CPMG experiment can filter out such time-dependent processes by multiple refocusing of the spin echo.

CPMG-experiments were performed on $\text{Cu-Smnt}^{\text{P/d}}_{0.01\%}$ at 7 K and Q- and W-band, the results are displayed in Figure 55. In the Q-band experiment, a high resolution was achieved by applying 398 refocusing π -pulses. At W-band only 32 refocusing pulses were applied, due to instrumental limitations. In both cases, the upper envelope of the CPMG-data was fit with exponential functions. The fit parameters are shown in Table 45 together with the fit parameters obtained from Hahn echo decay measurements in Section 3.2.3. At Q-band, two decay processes are found in the CPMG-experiment, whereas at W-band only a monoexponential is found. Presumably the fast decay is not observed due to the higher interpulse-distance at W-band, i.e. the lower resolution as mentioned above.

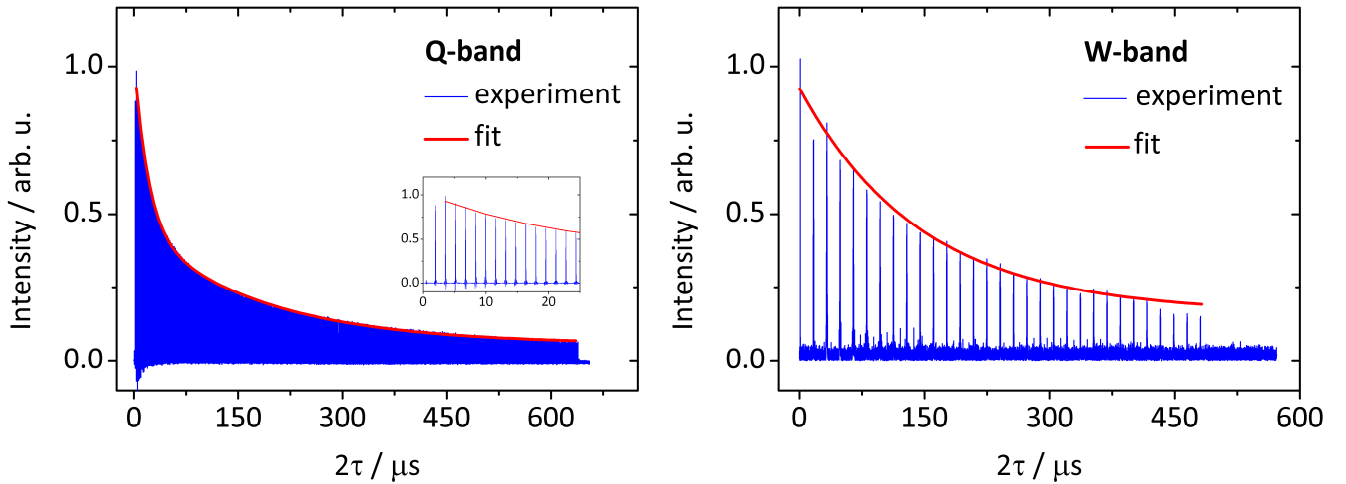


Figure 55: CPMG measurements and fits of $\text{Cu-Smnt}^{\text{P/d}}_{0.01\%}$ recorded at 7 K and two different MW frequency bands as indicated and 7 K. Magnetic field was fixed to the position indicated by the asterisks in the corresponding ESE-detected EPR spectra shown in Figure 46. Blue, solid lines correspond to experimental data and red, solid lines to fits, parameters see Table 45. Left panel: Q-band (34.091 GHz), 398 refocusing π -pulses applied; inset: view zoomed in for illustration of spin echoes. Right panel: W-band (94.019 GHz), number of pulses was limited by the applied spectrometer, experiment was conducted in 8 sub-experiments of 4 refocusing π -pulses (total 32 refocusing π -pulses).

Table 45: Parameters of mono- or biexponential fit functions according to equation (63) and standard deviations for upper envelope of CPMG experiments and comparison to results from previously discussed Hahn echo decay experiments of $\text{Cu-Smnt}^{\text{P/d}}_{0.01\%}$ recorded at 7 K, MW frequency and magnetic field as indicated.

MW-band	experiment	A_f	$T_{M,f} / \mu\text{s}$	A_s	$T_{M,s} / \mu\text{s}$
Q-band	CPMG	0.4830 ± 0.0004	20.63 ± 0.03	0.3307 ± 0.0003	182 ± 3
	HE-decay	0.59 ± 0.02	4.2 ± 0.3	0.692 ± 0.007	68 ± 3
W-band	CPMG	-	-	0.76 ± 0.02	147 ± 12
	HE-decay	0.10 ± 0.01	1.3 ± 0.3	0.967 ± 0.003	50.1 ± 0.5

The slow phase memory time is at both frequencies approximately three times longer in the CPMG- compared to the Hahn echo experiments, proving that nuclear spin dynamics crucially control the coherence in **Cu-Smnt^{P/d}_{0.01%}** for the investigated experimental conditions. If e.g. the coordination geometry is the coherence limiting factor, nearly no effect by applying CPMG instead of the Hahn echo sequence is observed.^[6] Recalling the corresponding spin-lattice relaxation times (Table 37), which are still two to three orders of magnitude longer than the CPMG-detected phase memory times, indicates that there are still other coherence limiting factors, inhibiting the phase memory time to approach the values of spin-lattice relaxation time. In dithiolene-based MQBS these are most probably the rigidity and conformation of the ligand and the degree of ordering in the proximity of the qubit and the three dimensional lattice. In order to design better MQBs, these factors need to be optimized.

Nutation Experiments

Although the qubit properties of **Cu-Smnt^{P/d}_{0.01%}** can still be improved, first qubit manipulation experiments were carried out, proving its viability as a MQB. Transient electron spin nutation of **Cu-Smnt^P_{0.001%}** and coherence transfer from the electron- to the nuclear spin valve for **Cu-Smnt^{P/d}_{0.01%}** by the means of EPR-detected transient nuclear spin nutations were carried out. The measurements were both performed at Q-band and 15 K, Figure 56 and Figure 57 show the results. Two different power levels were applied in the transient electron spin nutation experiment to exclude ESEEM-effects being responsible for the nutation. The experiment proves that even with the deuterated analogue **Cu-Smnt^P_{0.001%}**, simple coherent manipulations can be performed. For detecting transient nuclear spin nutations, a Davies-ENDOR sequence with the radio frequency fixed to 78.5 MHz (Cu-resonance) was applied. The length of the RF pulse was kept constant in this experiment, but its phase was inverted after a varying time t , as introduced by Gromov *et al.*^[146] Figure 57 displays a nutation of the nuclear spin with a oscillation period of 2.2 μ s. The EPR-based detection of nuclear spin nutation serves as proof of principle for coherence transfer between the electron- and nuclear spin valves. The successful detection of nuclear nutation manifests the qubit viability of **Cu-Smnt^P_{0.001%}** and further proves the principal applicability of the MQB not only in quantum information processing, but also in quantum information storage.

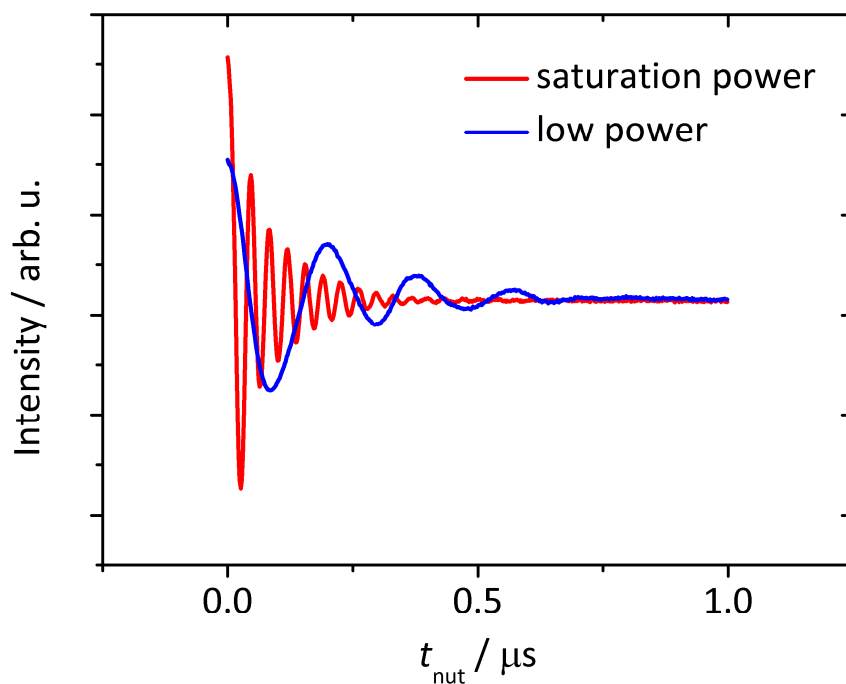


Figure 56: Transient electron spin nutation experiment for $\text{Cu-Smnt}^{\text{P}_{0.001\%}}$ at Q-band (33.771 GHz), 15 K, 1217.2 mT.

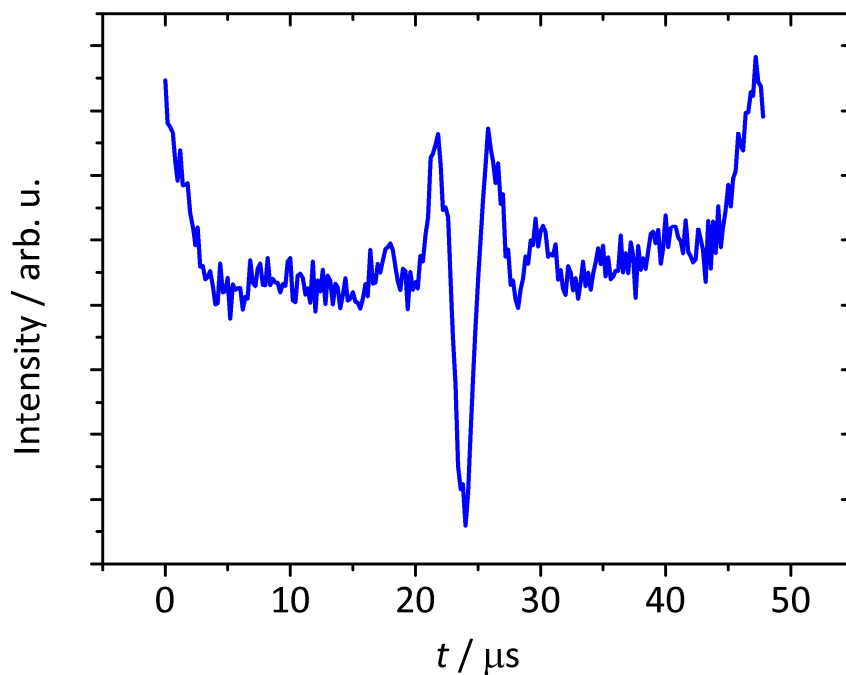


Figure 57: Transient nuclear spin nutation experiment for $\text{Cu-Smnt}^{\text{P}/d_{10\%}}$ at Q-band (34.067 GHz), 15 K, 1211.3 mT. Nutation was detected via Davies-ENDOR at fixed RF $\nu_{\text{RF}} = 78.5$ MHz with rotary echo (inversion of phase of RF-pulse after varying time t while keeping the length of the RF-pulse constant).

3.2.5 Summary regarding Physical Influences on Electron Spin Relaxation

The systematic study of influences on electron spin relaxation in **Cu-Smnt^{P/d}_{0.01%}** yielded in valuable findings. First, an orientation dependent study of relaxation in **Cu-Smnt^P_{0.001%}** and **Cu-Smnt^{P/d}_{0.01%}** at Q-band was performed. Spin-lattice relaxation proved to be independent of the orientation of the complex towards the external magnetic field, which was attributed to the low anisotropy of the g -tensor. Dephasing varies with the orientation of the complex towards the external magnetic field. The phase memory times are longer in the plane of the complex, i.e. when the magnetic field position corresponds to a transition assigned to the g_{\perp} -component, compared to orientations perpendicular to the complex plane, i.e. when the magnetic field position corresponds to a transition assigned to the g_{\parallel} -component. This observation was connected to the square-planar coordination geometry and columnar packing in the crystal structure, which presumably leads to lower mobility of magnetic nuclei in the plane of the complex (molecular x - and y -axis) compared to the perpendicular direction (molecular z -axis). This is underlined by the fact, that in the plane of the complex, nuclear spin diffusion was identified as dominant dephasing process, whereas in the perpendicular direction, motion of magnetic nuclei is the dominant process. Besides standard Hahn echo decay measurements, ESE detected EPR spectra with various interpulse distances were recorded, from which Hahn echo decay curves were constructed. Both methods yielded comparable phase memory times.

For **Cu-Smnt^P_{0.001%}** and **Cu-Smnt^{P/d}_{0.01%}**, the temperature dependence of relaxation was studied at Q-band. Pulsed EPR measurements were performed from 7 K up to room temperature, indicating the compounds as potential MQBs with extraordinary stable electron spin dynamics. Spin-lattice relaxation times for **Cu-Smnt^P_{0.001%}** vary between ca. 87 ms to 0.5 μ s in the investigated temperature range. The temperature dependence was modeled with a phenomenological model for a Raman process. The temperature dependence was found to be $T_{1,s}^{-1} \propto T^3$ was found, which is typical for highly covalent Cu-dithiolene complexes.^[49-50] The phase memory times of **Cu-Smnt^{P/d}_{0.01%}** both at 7 K and room temperature are among the highest reported values for MQBs.^[1-6] From the stretch parameters found for **Cu-Smnt^P_{0.001%}**, nuclear spin diffusion was identified as dominant dephasing process below 100 K. At higher temperatures, the

phase memory times are limited by spin-lattice relaxation and physical motion of magnetic nuclei was found as coherence limiting factor.

Cu-Smnt^{P/d}_{0.01%} was further employed as target compound in an unprecedentedly detailed frequency dependent electron spin dynamics study. Pulsed EPR measurements were performed at 7 K for MW frequencies between 3.7 and 240 GHz. Two processes of spin-lattice relaxation were found for all investigated MW frequencies, where values for fast process between 0.15–40 ms were found and for the slow process 1.1–218 ms. Spectral diffusion can be excluded as source of the fast spin-lattice relaxation process, which might be present due to faster relaxation in pairs and clusters of the paramagnetic species in the doped powder. The overall tendency for both processes is faster spin-lattice relaxation for higher MW-frequencies. This is in agreement with theory, where higher phonon densities at higher frequencies predict higher transition probabilities. Modeling of the frequency dependence of the fast and slow process of spin-lattice relaxation revealed a combination of direct and Raman process controlling spin dynamics in the investigated frequency range at 7 K. The frequency dependence of phase memory times prove to be more complicated to understand. In most cases, the Hahn echo decay measurements yielded in biexponential decay curves with values of 1.3–18 μ s for the fast process and 19 μ s up to ca. 70 μ s for the slow process. No direct frequency dependence of the phase memory time is directly obvious. At 120 GHz (F-band), a non-exponential decay curve was found for which an augmented fit model according to Feretti *et al.* was applied.^[7] The change in spin dynamics was assigned to a transition from high to rather low thermal energy conditions. At 120 GHz, nuclear spin diffusion is visible in the echo decay and not motionally narrowed as for the lower frequencies. The strong decrease of $T_{M,s}$ from $68.5 \pm 0.6 \mu$ s at 120 GHz to $19 \pm 1 \mu$ s at 120 GHz and the finding of a standard exponential Hahn echo decay at the higher frequency is presumably caused by a limitation of $T_{M,f}$ by spin-lattice relaxation. For a full understanding, not only further experiments, but also new theoretical considerations are necessary.

In the last part of the study, couplings to nuclear spins and their applicability in quantum manipulations were explored by means of different experiment. ESEEM effects were found at S-, X- and Q-band frequencies (3.7, 9.7, 36.1 GHz). The modulations were assigned to D- and ¹⁴N-nuclei, which presumably have the strongest dipolar couplings in **Cu-Smnt**^{P/d}_{0.01%}. At higher frequencies, no ESEEM was observed which was attributed to an insignificant modulation depth.

Davies ENDOR experiments revealed strong coupling between the electron spin and the nuclear spin of the Cu^{2+} transition metal centers in **Cu-Smnt^{P/d}_{0.01%}**. Hints for a rhombicity of the HF-coupling tensor were found, but further measurements for quantitative simulation of the spectra are necessary. The phase memory times of **Cu-Smnt^{P/d}_{0.01%}** without the dephasing influence of nuclear spins were examined with CPMG experiments at Q- and W-band. In both cases, the CPMG sequence leads to phase memory times of $182 \pm 3 \mu\text{s}$ (Q-band) and $147 \pm 12 \mu\text{s}$, which is approximately three times longer compared to phase memory times extracted from Hahn echo decays. However, the CPMG-detected phase memory times are still two to three orders of magnitude shorter than the corresponding spin-lattice relaxation times. This means, that other dominant processes are operative in dephasing and the design of a more robust MQB requires eliminating these.

Finally, first simple qubit manipulations and coherence transfer were conducted. Rabi oscillations and nuclear spin transient nutations show the principle applicability of **Cu-Smnt^P_{0.001%}** and **Cu-Smnt^{P/d}_{0.01%}** in quantum information processing and quantum information storage.

4 Conclusion

In this thesis, the factors influencing electron spin relaxation in mononuclear, homoleptic $S = 1/2$ transition metal coordination compounds was studied by the means of systematic pulsed EPR measurements. The investigation of chemical and physical influences on electron spin relaxation in potential MQBs revealed valuable information.

In the investigation of chemical influences on electron spin relaxation, three groups of compounds were investigated employing a range of ligands, central ions and sample matrices. A cross-comparison of the results gained from the three compound classes allows the setup of some general design principles for MQBs with long relaxation times. The most dominant chemical influence on spin-lattice relaxation was found to be the conformational rigidity of ligands and matrix: the higher the conformational rigidity of atoms and groups, the longer the spin-lattice relaxation times. Furthermore, a higher degree of ordering of the MQBs surrounding as well as a low exposition of the SOMO to environmental fluctuations and a low SOC of the central metal ion lead to slow spin-lattice relaxation. The longest spin-lattice relaxation time of the investigated compounds was found for **VO-Npc** ($T_{1,s} = 2405 \pm 268$ ms), where high stability is provided by a square-pyramidal coordination geometry in combination with a rigid, π -conjugated ring ligand, a low SOC is present and the unpaired electron resides in an orbital which lies in the ring plane, ensuring high protection from environmental fluctuations.

Spin-spin relaxation is mainly influenced by the number, distance and magnitude of magnetic moments of nuclear spins present in the MQB and its surrounding. In general, the lower the number of nuclear spins, the lower the magnitude of their magnetic moments and the higher the distance to the electron spin of interest, the longer the phase memory times. Compounds with nuclear-spin-free ligands are therefore promising MQB candidates, as demonstrated recently with phase memory times in the range of milliseconds.^[2] The principal feasibility of Ni³⁺-based MQBs was demonstrated for the first time in this thesis, which enables the design of entirely nuclear-spin-free MQBs.

Besides nuclear spins, also structural parameters were found to crucially influence spin-spin relaxation. As in the case of spin-lattice relaxation, lower mobility of groups and atoms in the MQBs ligands and surrounding as well as a higher degree of three-dimensional ordering and minimal overlap between the SOMO and the environment enable long coherence times. Higher rigidity can be achieved by less flexible ligands, such as per-conjugated, multi-dental ring- or cage-ligands with sterically demanding substituents. The degree of three-dimensional ordering is mainly influenced by the kind of sample matrix. Glassy solutions are completely disordered and lead to a low degree of controllability of the MQBs environment. Doped powders were found to be advantageous over frozen solutions for first assessment of relaxation times, due to the microcrystalline qubit surrounding. The crystal structure of the systems is also an important factor influencing relaxation. Here a high degree of symmetry is favorable in combination with high rigidity, e.g. in presence of π -stacking interactions. In future quantum computing devices, most probably MQBs will be present in form of nano-single crystals or atomically flat molecular arrays. For testing the applicability of MQBs in real devices, a similar solid-state environments is crucial, as fundamental changes in spin dynamics could accompany the transition from bulk material to single MQBs.

In terms of physical influences of electron spin relaxation it was shown that again single experiments only show a part of the whole picture. For quantitative understanding of fundamental electron spin relaxation mechanisms and processes, systematic studies are necessary. The main findings from the investigation of physical influences on electron spin relaxation are in agreement with the conclusions from the chemical dependence study. Electron spin relaxation is controlled by the rigidity of the system and by nuclear spin dynamics. This was shown with the anisotropy of dephasing in **Cu-Smnt^{P/d}_{0.01%}**, which is connected to anisotropy of rigidity in this system. Elimination of the nuclear spin-driven processes by CPMG showed that the phase memory times are still orders of magnitude shorter than spin-lattice relaxation times. In general, coherence is stable over a very wide temperature and frequency range. Even with the detailed investigations presented in this thesis, still not all effects of the frequency dependence of electron spin relaxation of **Cu-Smnt^{P/d}_{0.01%}** are understood. Besides further measurements, development in terms of theoretical models is required here.

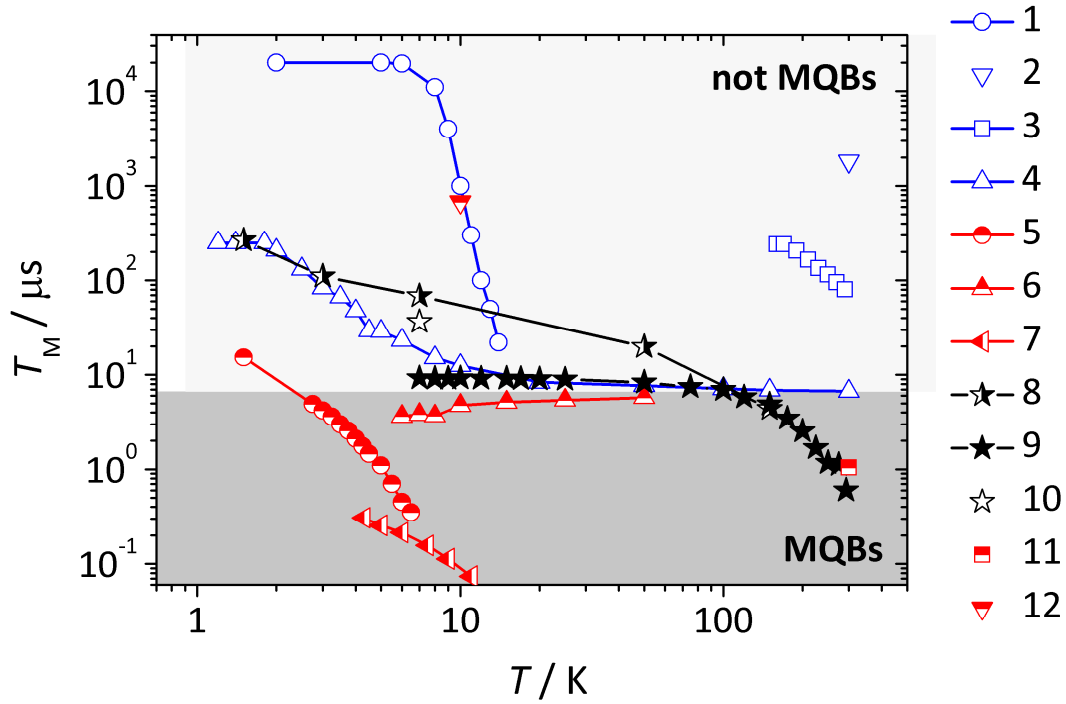


Figure 58: Comparison of coherence times of electron spin qubits. Blue symbols assign not-MQB electron spin qubits, i.e. mainly inorganic systems. Red symbols assign MQBs (literature values) and black symbols assign MQBs investigated in this thesis. 1 - P:Si,^[19] 2 - NV in diamond-¹²C,^[147] 3 - N@C₆₀,^[148] 4 - NV in diamond,^[53] 5 - Cr₇Ni,^[28] 6 - Cu₃L,^[149] 7 - Fe₄,^[29] 8 - **Cu-Smnt^{P/d}_{0.01%}** (this work), 9 - **Cu-Smnt^P_{0.001%}** (this work), 10 - **Ni-Smnt^{P/d}_{para}** (this work), 11 - VO-dmit,^[6] 12 - V(C₈S₈)₃.^[2] Figure inspired by Warner *et al.*^[21]

Figure 58 shows a graphical comparison of phase memory times of state-of-the-art electron spin qubits. From this it can be seen, that the phase memory times of **Cu-Smnt^{P/d}_{0.01%}**, **Cu-Smnt^P_{0.001%}** and **Ni-Smnt^{P/d}_{para}** are not only close to the record values for MQBs over the whole shown temperature range, but they also compete with so far unrivaled phase memory times of purely inorganic based electron spin qubits.

In conclusion, a range of potential MQBs was investigated in this thesis with promising electron spin relaxation times. Systematic studies were employed to find design principles for new MQBs. We hope that our investigations lead to more experimental and theoretical studies of electron spin relaxation in molecular systems, in order to enable quantitative understanding of spin dynamics and the development of nuclear-spin-free MQBs.

5 Experimental Section

5.1 Syntheses

5.1.1 General Remarks on Syntheses and Characterization Methods

All reagents and solvents were used as purchased from commercial sources. Elemental analyses were performed with a *PerkinElmer 2400CHNS/O Analyser* by Barbara Förtsch at the Institute of Inorganic Chemistry at the University of Stuttgart. NMR-spectra were recorded by Uta Twiehaus-Heynhold and Sascha Wegner at the Institute of Organic Chemistry at the University of Stuttgart on a *Bruker Avance 300* and on a *Bruker Avance 500* in deuterated solvents, reported chemical shifts in ppm are referenced on tetramethylsilane (internal standard). X-ray structures were collected on a *Bruker Kappa APEX II DUO* Diffractometer by Dr. Wolfgang Frey (measurement and structure solutions) at the Institute of Organic Chemistry at the University of Stuttgart. IR-spectra were recorded on a *Bruker ALPHA* FT-IR-spectrometer on samples in KBr-disks at room temperature, bands are reported as $\tilde{\nu}$ in cm^{-1} . UV/VIS-spectra were recorded on a PerkinElmer Lambda 2 at room temperature in different solvents, peak maxima are reported as λ_{max} in nm.

5.1.2 *Cu(Otfacac)₂*, *Cu-Otfacac*

Cu-Otfacac was synthesized according to a literature procedure of Linn Belford *et al.*^[75] The starting material copper(II) acetate monohydrate (1 mmol, 199.6 mg) was dissolved in hot demineralized water (10 ml, 80 °C) under stirring followed by dropwise addition of the ligand 1,1,1-trifluoro-2,4-pentanedione (2 mmol, 308.2 mg) in ethanol (1.7 ml). Sodium carbonate (0.226 mmol, 24 mg) was added under vigorous stirring. After stirring 15 min at 90 °C, the crude product was filtered. It was washed with 2 x 20 ml demineralized water, subsequently dried under reduced pressure and recrystallized from 1:1 ethanol/water (6 ml). The purple solid was stored in a desiccator over P₂O₅ under reduced pressure (two weeks).

Elemental analysis: found (calcd.) for C₁₀H₈CuF₆O₄ in %: C: 32.51 (32.49), H: 2.246 (2.180).

UV/VIS in chloroform: λ_{max} in nm: 298, 316, 546, 678.

IR (KBr-pellet): $\tilde{\nu}$ in cm^{-1} : 1611, 1587, 1531, 1518, 1478, 1417, 1367, 1312, 1226, 1196, 1168, 1139.

5.1.3 *Cu(Ohfac)₂*, *Cu-Ohfac*

Cu-Ohfac was synthesized according to a literature procedure of Linn Belford *et al.*^[75] To a hot solution of copper(II) acetate monohydrate (2.5 mmol, 499.1 mg) in 20 ml demineralized water (90 °C) the ligand 1,1,1,5,5,5-Hexafluoro-2,4-pentanedione (5 mmol, 0.708 ml) was added dropwise. Then a 4 N NaOH solution was pipetted slowly to the hot solution and it was stirred for five minutes. The resulting bright green solid precipitated was filtered. Washing of the solid product with 2 x 10 ml demineralized water and drying for two weeks (desiccator, P₂O₅) yielded in the final product, which was dark turquoise.

Elemental analysis: found (calcd.) for C₁₀H₂CuF₁₂O₄ in %: C: 25.08 (25.12), H: 0.683 (0.420).

UV/VIS in chloroform: λ_{max} in nm: 309, 328, 571, 712.

IR (KBr-pellet): $\tilde{\nu}$ in cm^{-1} : 1646, 1612, 1562, 1536, 1473, 1443, 1365, 1259, 1217, 1150, 1105.

5.1.4 *Cu(Ofod)₂*, *Cu-Ofod*

Cu-Ofod was synthesized by Samuel Lenz during his M.Sc.-thesis^[74] according to a variation of a literature procedure for a similar compound by Linn Belford *et al.*^[75] A solution of copper(II) acetate monohydrate (1 mmol, 200 mg) in 50 ml methanol was prepared. Subsequently, a solution of sodium methoxide (2 mmol, 108 mg) and the ligand 6,6,7,7,8,8,8-heptafluoro-2,2-dimethyl-3,5-octanedione (2 mmol, 0.47 ml) in 25 ml methanol was added dropwise and the mixture was stirred for 30 min at 60 °C. After cooling, the solvent was evaporated completely and the residue re-dissolved in DCM. Evaporation of the solvent resulted in a blue solid. The compound was dried under reduced pressure and this yielded in a purple product.

Elemental analysis: found (calcd.) for C₂₀H₂₀CuF₁₄O₄ in %: C: 36.76 (36.74), H: 3.27 (3.08).

UV/VIS in dichloromethane: λ_{max} in nm: 244, 302, 317, 688.

IR (KBr-pellet): $\tilde{\nu}$ in cm^{-1} : 2977, 2938, 2916, 2874, 1615, 1514, 1458, 1347, 1229.

5.1.5 *Cu(Obzac)₂*, *Cu-Obzac*

Cu-Obzac was synthesized by Samuel Lenz during his M.Sc.-thesis^[74] according to a literature procedure of Ma *et al.*^[77] A solution of the starting material copper(II) acetate monohydrate

(2 mmol, 400 mg) in ethanol (40 ml) was combined dropwise with benzoylacetone (4 mmol, 650 mg) in ethanol (5 ml) and stirred for 30 minutes. The formed precipitate was filtered and the crude product was recrystallized (1:1 DCM/n-hexane), which resulted in the final green product.

Elemental analysis: found (calcd.) for $C_{20}H_{18}CuO_4$ in %: C: 62.02 (62.25), H: 4.68 (4.70).

UV/VIS in dichloromethane: λ_{max} in nm: 258, 323, 552, 653.

IR (KBr-pellet): $\tilde{\nu}$ in cm^{-1} : 3044, 2989, 2922, 1560, 1461, 1415, 1354, 1309, 1288, 1212.

5.1.6 $Cu(Odbm)_2$, $Cu-Odbm$

Cu-Odbm was synthesized by Samuel Lenz during his M.Sc.-thesis^[74] according to a literature procedure of Ma *et al.*^[77] To an aqueous solution of copper(II) sulfate (1 mmol, 160 mg in 15 ml demineralized water) a mixture of the ligand dibenzoylmethane (2 mmol, 458 mg) and sodium hydroxide (2 mmol, 79 mg) in ethanol/water (15:1) was slowly added and stirred for 30 minutes. The crude product was filtered, washed (water, DET) and recrystallized (DCM), which resulted in a final green product.

Elemental analysis: found (calcd.) for $C_{30}H_{22}CuO_4$ in %: C: 70.60 (70.65), H: 4.33 (4.35).

UV/VIS in dichloromethane: λ_{max} in nm: 266, 283, 350, 555, 649.

IR (KBr-pellet): $\tilde{\nu}$ in cm^{-1} : 3063, 3026, 1591, 1539, 1485, 1454, 1403, 1314, 1232.

5.1.7 $Pd(Odbm)_2$, $Pd-Odbm$

Pd-Odbm was synthesized by Samuel Lenz during his M.Sc.-thesis^[74] according to a literature procedure of Okeya *et al.*^[76] The starting product palladium(II) chloride (1 mmol, 180 mg) was dissolved with sodium chloride (1.2 mmol, 70 mg) in 4:1 ethanol/water (10 ml). Subsequently, dibenzoylmethane (2 mmol, 460 mg) in ethanol (10 ml) and sodium hydroxide in water (1 mmol, 40 mg in 2 ml) were slowly added to the reaction mixture. The resulting green solid was filtered, washed (water, DET) and recrystallized (DCM), which resulted in a yellow product.

Elemental analysis: found (calcd.) for $C_{30}H_{22}O_4Pd$ in %: C: 65.16 (65.17), H: 4.09 (4.01).

IR (KBr-pellet): $\tilde{\nu}$ in cm^{-1} : 1587, 1534, 1522, 1490, 1483, 1465, 1452, 1379, 1312, 1300, 1233.

5.1.8 (*d*₂₀-PPh₄)Br

Perdeuterotetraphenylphosphonium bromide was synthesized according to a procedure of Horner *et al.*^[105] The starting material, anhydrous nickel(II)bromide (0.3933 g, 1.8 mmol), deuterated triphenylphosphine (1.0000 g, 3.6 mmol) and deuterated phenylbromide (0.76 ml, 7.2 mmol) were heated in a pressure cylinder (180 °C) for three hours. The resulting blue-green mixture was cooled, demineralized water (50 ml) was added and stirred for 15 min at 75 °C. The resulting light blue solution and fawn precipitate were cooled to 0 °C. Subsequently, the mixture was extracted with 3 x 50 ml of diethylether. The aqueous phase was further extracted with 3 x 50 ml chloroform. The product in the organic phase was isolated by removing the solvent and drying under reduced pressure.

¹³C NMR (500MHz, in CDCl₃): δ in ppm: 135.41 (t), 133.96 (td), 130.82 (td), 117.56, 116.85.

5.1.9 (*d*₂₀-AsPh₄)Br

Perdeuterotetraphenylarsonium bromide, (*d*₂₀-AsPh₄)Br, was synthesized by Simon Schlindwein according to a procedure of Chatt *et al.*^[106]

¹³C NMR (500MHz, in CDCl₃): δ in ppm: 134.2 (t), 132.5 (td), 131.8 (dt), 120.0..

5.1.10 (PPh₄)₂[Cu(Smnt)₂], Cu-Smnt^P

Bis-(tetraphenylphosphonium)-bis-(maleonitriledithiolato)cuprate(II), **Cu-Smnt^P**, was synthesized according to a procedure of Lewis *et al.*^[104] A solution of copper chloride dihydrate (128 mg, 0.75 mmol in 5 ml ethanol) was added dropwise to a solution of sodium maleonitriledithiolate (279 mg, 1.5 mmol, in 5 ml ethanol and 2 ml demineralized water). Tetraphenylphosphonium bromide (629 mg, 1.50 mmol) dissolved in 15 ml warm ethanol was added under stirring. After 5 mins of stirring the brown product was filtered and washed with 3 x 5 ml ethanol. Drying under reduced pressure gave the final product in a yield of 576 mg (75.01 % based on Cu).

Elemental analysis: found (calcd) for C₅₆H₄₀CuN₄P₂S₄ in %: C: 65.42 (65.77), H: 3.90 (3.94), N: 5.48 (5.48), S: 12.70 (12.54).

UV/VIS (DCM): λ_{max} in nm: 476, 426, 368, 348, 317, 276, 227.

IR (KBr-pellet): $\tilde{\nu}$ in cm⁻¹ and assignment in brackets: 2195 ($\nu_{C\equiv N}$), 1459 ($\nu_{C=C}$).

5.1.11 $(PPh_4)_2[Ni(Smnt)_2]$, $Ni-Smnt^P$

Bis-(tetraphenylphosphonium)-bis-(maleonitriledithiolato)nickelate(II), $Ni-Smnt^P$ was synthesized following a similar procedure as described for $Cu-Smnt^P$ (see 5.1.10), where nickel chloride hexahydrate (178 mg, 0.75 mmol) was used instead of copper chloride dihydrate. The red product was isolated with a yield of 614 mg (80.4 % based on Ni).

Elemental analysis: found (calcd) for $C_{56}H_{40}NiN_4P_2S_4$: C: 65.75 (66.08), H: 3.94 (3.96), N: 5.46 (5.50), S: 12.83 (12.60).

UV/VIS (MeCN): λ_{max} in nm: 474, 379, 315, 270.

IR (KBr-pellet): $\tilde{\nu}$ in cm^{-1} and assignment in brackets: 2196 ($\nu_{C\equiv N}$), 1479 ($\nu_{C=C}$).

5.1.12 $(PPh_4)[Ni(Smnt)_2]$, $Ni-Smnt^P_{para}$

Tetraphenylphosphonium-bis-(maleonitriledithiolato)nickelat(III), $Ni-Smnt^P_{para}$, was synthesized according to a procedure of Ning *et al.*^[107] $Ni-Smnt^P$ (150 mg, 0.15 mmol) was dissolved in 5 ml acetonitrile. Iodine (45 mg, 0.18 mmol) dissolved in in 1.5 ml methanol was added dropwise under stirring. A grey, fluffy solid precipitated which was filtered and washed (5 ml methanol, 5 ml demineralited water, 5 ml diethylether). After three re-precipitations from 1 : 3 acetone/pentane in an ice bath, a final recrystallization from acetone yielded in the product, which contains PPh_4I as side-product.

Elemental analysis: found (calcd.) for $C_{32}H_{20}NiN_4PS_4$: C: 56.65 (57.46), H: 3.622 (2.970), N: 6.74 (8.26), S: 15.57 (18.90).

UV/VIS in DCM: λ_{max} in nm: 866, 606, 481, 349 (sh), 314, 272, 237.

IR (KBr-pellet): $\tilde{\nu}$ in cm^{-1} and assignment in brackets: 2205 ($\nu_{C\equiv N}$), 1436 ($\nu_{C=C}$).

5.1.13 $(d_{20}-PPh_4)_2[Cu(Smnt)_2]$, $Cu-Smnt^{P/d}$

Bis-(perdeuterotetraphenylphosphonium)-bis-(maleonitriledithiolato)cuprat(II), $Cu-Smnt^{P/d}$, was synthesized following a similar procedure as described for $Cu-Smnt^P$ (see 5.1.10), where a fifth of the amount of substances as indicated above was used and $d_{20}-PPh_4Br$ (131.8 mg, 0.30 mmol) instead of PPh_4Br . The red-brown product was isolated with a yield of 113.1 mg (70.9 % based on Cu).

Elemental analysis: found (calcd) for $C_{56}D_{40}CuN_4P_2S_4$: C: 63.01 (63.28), D: 7.47 (7.58), N: 5.24 (5.27), S: 12.49 (12.66).

UV/VIS in DCM: λ_{max} in nm: 476, 426, 368, 348, 317, 276, 227.

IR (KBr-pellet): $\tilde{\nu}$ in cm^{-1} and assignment in brackets: 2195 ($\nu_{C\equiv N}$), 1459 ($\nu_{C=C}$).

5.1.14 (d_{20} -PPh₄)₂[Ni(Smnt)₂], Ni-Smnt^{P/d}

Bis-(perdeuterotetraphenylphosphonium)-bis-(maleonitriledithiolato)nickelat(II), **Ni-Smnt^{P/d}**, was synthesized following a similar procedure as described for **Ni-Smnt^P** (see 5.1.11), where a fifth of the amount of substances as indicated above was used and d_{20} -PPh₄Br (131.8 mg, 0.30 mmol) instead of PPh₄Br. The red product was isolated with a yield of 117.9 mg (74.3 % based on Ni).

Elemental analysis: found (calcd) for $C_{56}D_{40}N_4NiP_2S_4$: C: 63.43 (63.57), D: 7.70 (7.61), N: 5.27 (5.30), S: 12.77 (12.12).

UV/VIS in DCM: λ_{max} in nm: 479, 384, 317, 273, 230.

IR (KBr-pellet): $\tilde{\nu}$ in cm^{-1} and assignment in brackets: 2196 ($\nu_{C\equiv N}$), 1479 ($\nu_{C=C}$).

5.1.15 (d_{20} -PPh₄)[Ni(Smnt)₂], Ni-Smnt^{P/d_{para}}

Perdeuterotetraphenylphosphonium-bis-(maleonitriledithiolato)nickelat(III), **Ni-Smnt^{P/d_{para}}**, was synthesized following a similar procedure as described for **Ni-Smnt^{P_{para}}** (see 5.1.12), where 156 mg of **Ni-Smnt^{P/d}** (0.15 mmol) was used as starting material instead of **Ni-Smnt^P**. The final product contains PPh₄I as side-product.

Elemental analysis: found (calcd.) for $C_{32}D_{20}NiN_4PS_4$: C: 54.18 (55.02), H: 2.93 (5.77), N: 7.33 (8.02), S: 17.03 (18.36).

UV/VIS in DCM: λ_{max} in nm: 866, 606, 481, 349 (sh), 314, 272, 237.

IR (KBr-pellet): $\tilde{\nu}$ in cm^{-1} and assignment in brackets: 2205 ($\nu_{C\equiv N}$), 1436 ($\nu_{C=C}$).

5.1.16 (d_{20} -AsPh₄)₂[Cu(Smnt)₂], Cu-Smnt^{As/d}

Bis-(perdeuterotetraphenylarsonium)-bis-(maleonitriledithiolato)cuprat(II), **Cu-Smnt^{As/d}**, was synthesized following a similar procedure as described for **Cu-Smnt^P** (see 5.1.10), where a fifth of the amount of substances as indicated above was used and d_{20} -AsPh₄Br (147.7 mg, 0.3 mmol)

instead of PPh₄Br. The red-brown product was isolated with a yield of 117.2 mg (67.9 % based on Cu).

Elemental analysis: found (calcd) for C₅₆D₄₀CuN₄As₂S₄: C: 57.92 (58.45), D: 6.96 (7.00), N: 4.94 (4.87), S: 11.58 (11.14).

UV/VIS (DCM): λ_{max} in nm: 476, 426, 368, 317, 282, 276, 264, 233.

IR (KBr-pellet): $\tilde{\nu}$ in cm⁻¹ and assignment in brackets: 2195 ($\nu_{\text{C}\equiv\text{N}}$), 1459 ($\nu_{\text{C}=\text{C}}$).

5.1.17 (*d*₂₀-AsPh₄)₂[Ni(*Smnt*)₂], *Ni-Smnt*^{As/d}

Bis-(perdeuterotetraphenylarsonium)-bis-(maleonitriledithiolato)nickelat(II), **Ni-Smnt^{As/d}**, was synthesized following a similar procedure as described for **Ni-Smnt^P** (see 5.1.11), where a fifth of the amount of substances as indicated above was used and *d*₂₀-AsPh₄Br (147.7 mg, 0.30 mmol) instead of PPh₄Br. The red product was isolated with a yield of 113.5 mg (66.0 % based on Ni).

Elemental analysis: found (calcd) for C₅₆D₄₀N₄NiAs₂S₄: C: 58.65 (58.69), D: 7.16 (7.03), N: 4.85 (4.89), S: 11.52 (11.19).

UV/VIS in DCM: λ_{max} in nm: 479, 384, 317, 273, 230.

IR (KBr-pellet): $\tilde{\nu}$ in cm⁻¹ and assignment in brackets: 2194 ($\nu_{\text{C}\equiv\text{N}}$), 1478 ($\nu_{\text{C}=\text{C}}$).

5.1.18 Na₂[Cu(*Smnt*)₂] · D₂O, *Cu-Smnt*^{Na}

Bis-(sodium)-bis-(maleonitriledithiolato)cuprat(II) d₂-monohydrat, **Cu-Smnt^{Na}**, was synthesized according to a procedure of Pearson *et al.*^[108] A warm solution CuSO₄ · 5 H₂O (124.9 mg, 0.5 mmol) in 0.6 ml D₂O was combined dropwise with sodium maleonitriledithiolate (186.2 mg, 1.0 mmol) in 0.6 ml D₂O. The solvent was removed under reduced pressure and gentle warming and the resulting dark brown residue was recrystallized from deuterated methanol. The final product contains 0.1 eq Na₂SO₄ as side product (yield: 150.4 mg, 70.9 % based on Cu).

Elemental analysis: found (calcd) for C₈CuN₄Na₂S₄ · D₂O · 0.1 Na₂SO₄: C: 21.93 (22.66), D: 0.899 (0.900), N: 12.69 (13.21), S: 30.62 (31.00).

IR (KBr-pellet): $\tilde{\nu}$ in cm⁻¹ and assignment in brackets: 2198 ($\nu_{\text{C}\equiv\text{N}}$), 1470 ($\nu_{\text{C}=\text{C}}$).

5.1.19 $\text{Na}_2[\text{Ni}(\text{Smnt})_2] \cdot \text{D}_2\text{O}$, $\text{Ni-Smnt}^{\text{Na}}$

Bis-(sodium)-bis-(maleonitriledithiolato)nickelat(II) d₂-monohydrat, **Ni-Smnt^{Na}**, was synthesized following a similar procedure as described for **Cu-Smnt^{Na}** (see 5.1.18), where nickel chloride hexahydrate (131.4 mg, 0.5 mmol) was used instead of copper chloride dihydrate. The final product contains 0.2 eq Na₂SO₄ as side product (yield: 147.6 mg, 70 % based on Ni).

Elemental analysis: found (calcd) for C₈NiNa₂N₄P₂S₄ · D₂O · 0.2 Na₂SO₄: C: 22.07 (22.17), D: 1.05 (0.92), N: 12.77 (12.93), S: 30.14 (31.07).

IR (KBr-pellet): $\tilde{\nu}$ in cm⁻¹ and assignment in brackets: 2216 ($\nu_{\text{C}\equiv\text{N}}$), 1484 ($\nu_{\text{C}=\text{C}}$).

5.1.20 K_2Sdto

Bis-(potassium)-1,2-dithiooxalate, **K₂Sdto**, was synthesized following a procedure of Wenzel *et al.*^[109] Hydrogen sulfide was passed through a solution of potassium (4.5 g, 115 mmol) in 150 ml dry ethanol, until a light yellow solid precipitated (after ca. 4 h). Subsequently, the solution was flushed with nitrogen gas for 20 mins to remove excess H₂S. Diphenyl oxalate (6.056 g, 25 mmol) was added to the mixture and a dirty white solid formed. After stirring for 24 h at room temperature, the product was filtered and washed with a minimum volume of ethanol. After drying in a dessicator over NaOH, the pale yellow product was isolated with a yield of 4.358 g (87.9 % based on diphenyl oxalate).

Elemental analysis: found (calcd) for C₂K₂O₂S₂: C: 12.44 (12.11), S: 21.30 (32.33).

¹³C-NMR (62.9 MHz, in D₂O) δ in ppm: 217.04 (COS).

IR (KBr-pellet): $\tilde{\nu}$ in cm⁻¹ and assignment in brackets: 1519 ($\nu_{\text{C-O}}$), 1371 ($\nu_{\text{C-C-O}}$), 1115 ($\nu_{\text{C-C-S}}$), 878 ($\nu_{\text{C-S}}$).

5.1.21 $(\text{PPh}_4)_2[\text{Cu}(\text{Sdto})_2]$, $\text{Cu-Sdto}^{\text{P}}$

Bis-(tetraphenylphosphonium)-bis-(dithiooxalato)cuprate(II), **Cu-Sdto^P**, was synthesized following a procedure of Imamura *et al.*^[110] A warm solution of copper chloride dihydrate (127.9 mg, 0.75 mmol) was added slowly to a n aqueous solution of the ligand salt potassium dithiooxalate (297.5 mg, 1.5 mmol, in 15 ml demineralized water). Subsequently, a warm solution of tetraphenylphosphonium bromide (628.9 mg, 1.5 mmol) in methanol/demineralized water (5 ml/20 ml) was added. The mixture was stirred for 10 mins at room temperature and the

precipitate was separated from the solution. Afterwards washing with 5 x 50 ml demineralized water and drying for 5 h under reduced pressure led to a crude product, which was finally recrystallized from DCM/pentane (1.5 : 1) in an ice bath. After 7 h drying under reduced pressure, the olive compound was isolated in a yield of 451.3 mg ($y = 61\%$ based on Cu).

Elemental analysis: found (calculated) in % for $C_{52}H_{40}O_4P_2S_4Cu$: C: 62.85 (63.53), H: 4.08 (4.10), S: 13.04 (13.05).

UV/VIS in DCM: λ_{max} in nm: 693, 619, 568, 406, 320, 276, 269, 262, 238.

IR (KBr pellet): $\tilde{\nu}$ in cm^{-1} and assignment in brackets: 1610 ($\nu_{C=O}$), 1583 ($\nu_{C=O}$), 1038 (ν_{C-C} , ν_{C-S}), 910 (τ_{O-C-S}).

5.1.22 $(PPh_4)_2[Ni(Sdto)_2]$, $Ni-Sdto^P$

Bis-(tetraphenylphosphonium)-bis-(dithiooxalato)nickelat(II), **Ni-Sdto^P**, was synthesized following a similar procedure as described for **Cu-Sdto^P** (see 5.1.21), where nickel chloride hexahydrate (178.3 mg, 0.75 mmol) instead of copper chloride dihydrate was used. The pink product was isolated with a yield of 637.6 mg ($y = 86.7\%$ based on Ni).

Elemental analysis: found (calculated) in % for $C_{52}H_{40}O_4P_2S_4Ni$: C: 61.12 (63.56), H: 4.04 (4.12), S: 12.37 (13.12).

UV/VIS in DCM: λ_{max} in nm: 552, 503, 360, 304, 376, 268, 262, 230.

IR (KBr pellet): $\tilde{\nu}$ in cm^{-1} and assignment in brackets: 1604 ($\nu_{C=O}$), 1584 ($\nu_{C=O}$), 1054 (ν_{C-C} , ν_{C-S}), 914 (τ_{O-C-S}).

5.1.23 $(d_{20}\text{-}PPh_4)_2[Cu(Sdto)_2]$, $Cu-Sdto^{P/d}$

Bis-(perdeuterotetraphenylphosphonium)-bis-(dithiooxalato)cuprat(II), **Cu-Sdto^{P/d}**, was synthesized following a similar procedure as described for **Cu-Sdto^P** (see 5.1.21), where a fifth of the amount of substances as indicated above was used and $d_{20}\text{-}PPh_4Br$ (131.8 mg, 0.3 mmol) instead of PPh_4Br . The dark green compound was isolated with a yield of 69.7 mg (46.7 % based on Cu).

Elemental analysis: found (calculated) in % for $C_{52}D_{40}O_4P_2S_4Cu$: C: 60.46 (61.06), D: 7.81 (7.88), S: 12.55 (12.54).

UV/VIS in DCM: λ_{max} in nm: 566, 403, 320, 275, 268, 228.

IR (KBr pellet): $\tilde{\nu}$ in cm^{-1} and assignment in brackets: 1610 ($\nu_{\text{C=O}}$), 1587 ($\nu_{\text{C=O}}$), 1036 ($\nu_{\text{C-C}}$, $\nu_{\text{C-S}}$), 911 ($\tau_{\text{O-C-S}}$).

5.1.24 ($d_{20}\text{-PPh}_4$)₂[Ni(Sdto)₂], Ni-Sdto^{P/d}

Bis-(perdeuterotetraphenylphosphonium)-bis-(dithiooxalato)nickelat(II), **Ni-Sdto^{P/d}**, was synthesized following a similar procedure as described for **Ni-Sdto^P** (see 5.1.22), where two fifths of the amount of starting material was used and with $d_{20}\text{-PPh}_4\text{Br}$ (263.7 mg, 0.6 mmol) instead of PPh_4Br . The pink compound was isolated with a yield of 252.8 mg (82.8 % based on Ni).

Elemental analysis: found (calculated) in % for $\text{C}_{52}\text{D}_{40}\text{O}_4\text{P}_2\text{S}_4\text{Ni}$: C: 58.79 (61.35), D: 7.88 (7.91), S: 12.24 (12.60).

UV/VIS in DCM: λ_{max} in nm: 552, 503, 360, 304, 276, 268, 262, 233.

IR (KBr pellet): $\tilde{\nu}$ in cm^{-1} and assignment in brackets: 1604 ($\nu_{\text{C=O}}$), 1544 ($\nu_{\text{C=O}}$), 1056 ($\nu_{\text{C-C}}$, $\nu_{\text{C-S}}$), 916 ($\tau_{\text{O-C-S}}$).

5.1.25 ($d_{20}\text{-AsPh}_4$)₂[Cu(Sdto)₂], Cu-Sdto^{As/d}

Bis-(perdeuterotetraphenylarsonium)-bis-(dithiooxalato)cuprat(II), **Cu-Sdto^{As/d}**, was synthesized following a similar procedure as described for **Cu-Sdto^P** (see 5.1.21), where a fifth of the amount of starting material was used and with $d_{20}\text{-AsPh}_4\text{Br}$ (147.7 mg, 0.3 mmol) instead of PPh_4Br . The olive compound was isolated with a yield of 106.4 mg (64.0 % based on Cu).

Elemental analysis: found (calculated) in % for $\text{C}_{52}\text{D}_{40}\text{As}_2\text{CuO}_4\text{S}_4$: $\text{C}_{52}\text{D}_{40}\text{As}_2\text{CuO}_4\text{S}_4$: C: 55.41 (56.23), H: 6.96 (7.25), S: 12.31 (11.55).

UV/VIS in DCM: λ_{max} in nm: 693, 593, 383, 320, 291, 270, 264, 258, 232.

IR (KBr pellet): $\tilde{\nu}$ in cm^{-1} and assignment in brackets: 1610 ($\nu_{\text{C=O}}$), 1578 ($\nu_{\text{C=O}}$), 1036 ($\nu_{\text{C-C}}$, $\nu_{\text{C-S}}$), 910 ($\tau_{\text{O-C-S}}$).

5.1.26 ($d_{20}\text{-AsPh}_4$)₂[Ni(Sdto)₂], Ni-Sdto^{As/d}

Bis-(perdeuterotetraphenylarsonium)-bis-(dithiooxalato)nickelat(II), **Ni-Sdto^{As/d}**, was synthesized following a similar procedure as described for **Ni-Sdto^P** (see 5.1.22), where a fifth of the amount of starting material was used and with $d_{20}\text{-AsPh}_4\text{Br}$ (147.7 mg, 0.3 mmol) instead of PPh_4Br . The olive compound was isolated with a yield of 115.1 mg (69.4 % based on Ni).

Elemental analysis: found (calculated) in % for $C_{52}D_{40}As_2NiO_4S_4$: C: 54.55 (56.48), H: 7.13 (7.28), S: 11.67 (11.60).

UV/VIS in DCM: λ_{\max} in nm: 552, 503, 360, 304, 270, 264, 258, 229.

IR (KBr pellet): $\tilde{\nu}$ in cm^{-1} and assignment in brackets: 1604 ($\nu_{C=O}$), 1544 ($\nu_{C=O}$), 1056 (ν_{C-C} , ν_{C-S}), 917 (τ_{O-C-S}).

5.1.27 Synthesis of doped powders

All doped powders were synthesized by dissolving the required paramagnetic compound and a diamagnetic host with similar or identical crystal structure in an appropriate solvent (minimum volume, e.g. acetone, water, dichloromethane). The molar ratio of the compounds was chosen corresponding to the required doping percentage, where a full inclusion of the dopant in the host was assumed. After mixing, the solvent was evaporated and the compounds were dried under reduced pressure. All doped powders were finely ground prior to spectroscopic measurements.

5.2 EPR Measurements

5.2.1 Sample Preparation

Solution samples were filled in quartz- or suprasil-EPR sample tubes and degassed by three freeze-pump-thaw cycles. The tubes were subsequently flame-sealed. Doped powder samples were finely ground, filled in quartz- or suprasil-EPR sample tubes and evacuated to remove oxygen. The tubes were either flame-sealed (for pulsed Q-band measurements in Stuttgart) or sealed with Teflon tape, respectively. All sample tubes were cleaned accurately prior to insertion in the spectrometers.

5.2.2 Spectrometers

Pulsed EPR measurements at **S-band** frequencies were performed with the help of Renée Tschaggelar in the Jeschke group at the Laboratory of Physical Chemistry, Department of Chemistry and Applied Bioscience, ETH Zürich (Vladimir-Prelog-Weg 1-5/10, 8093 Zürich, Switzerland). A homebuilt S-band spectrometer with a bridged loop-gap resonator^[150] was used in combination with a Oxford Instruments CF935 cryostat. Typical MW-pulse lengths for the

investigated samples were $\pi/2 = 16$ ns and $\pi = 32$ ns. Pulsed EPR measurements at **X-band** frequencies were performed on two different spectrometers. Measurements in Frankfurt were performed with the help of Dr. Burkhard Endeward in the Prisner group at the Centre for Biomolecular Magnetic Resonance, Institute of Physical and Theoretical Chemistry, Goethe University Frankfurt (Max-von-Laue-Str. 7, 60438 Frankfurt am Main, Germany). Measurements in Manchester were performed with the help of Dr. Alistair Fielding and Dr. Amgalanbaatar Baldansuren at the National EPR Facility and Service at the School of Chemistry at the University of Manchester (Oxford Road, Manchester, M13 9PL, UK). In both cases, a BRUKER Elexsys E580 X-/Q-band spectrometer equipped with a BRUKER MS-3 split-ring resonator and a Oxford Instruments CF935 cryostat was employed for the experiments. Typical MW-pulse lengths for the investigated samples were $\pi/2 = 16$ ns and $\pi = 32$ ns. Pulsed EPR measurements at **Q-band** frequencies were performed on three different spectrometers. For measurements in Stuttgart, a homebuilt pulsed Q-band in combination with a cylindrical TE₀₁₁ resonator^[58] and a Oxford Instruments CF935 cryostat was used. Measurements at Q-band in Frankfurt were performed with the help of Dr. Burkhard Endeward on the above named BRUKER Elexsys E580 X-/Q-band spectrometer (specifications see there). Pulsed EPR-measurements at Q-band in Oxford were performed with the help of Prof. Dr. Arzhang Ardavan, Dr. William Myers and Dr. Alice Bowen at CAESR ESR Facility, Inorganic Chemistry at the University of Oxford (South Parks Road, OX1 3QR, UK). Here, a BRUKER ElexSys E580 X-/Q-band pulse/cw spectrometer was used in combination with a dielectric ring and dielectric ring ENDOR-resonator and a Oxford Instruments CF935 cryostat. Typical MW-pulse lengths for the investigated samples were $\pi/2 = 16$ ns and $\pi = 32$ ns in all three cases (Q-band in Stuttgart, Frankfurt and Oxford). Pulsed **W-band** EPR measurements were performed with the help of Prof. Dr. Etienne Goovaerts and Prof. Dr. Sabine van Doorslaer at the Departement of Physics, University of Antwerp (Campus Drie Eiken, Universiteitsplein 1, 2610 Wilrijk, Belgium). A BRUKER X-/W-band spectrometer was used for the measurements equipped with a Oxford Instruments CF935 cryostat. Typical MW-pulse lengths for the investigated samples were $\pi/2 = 120$ ns and $\pi = 240$ ns.

Pulsed **F- and Y-band** measurements were performed with the help of Dr. Johan van Tol at the Center for Interdisciplinary Magnetic Resonance, National High Magnetic Field Laboratory (1800

E. Paul Dirac Dr., Tallahassee, USA). A homebuilt multifrequency heterodyne quasi-optical spectrometer^[151] was used without resonator and dynamic flow cryostat. Very low temperatures (i.e. 1.5-5 K) were reached with minimal He-flow and continuous pumping on the cryostat. Typical MW-pulse lengths for the investigated samples were $\pi/2 = 900$ ns and $\pi = 1200$ ns at both MW frequencies (120 GHz and 240 GHz).

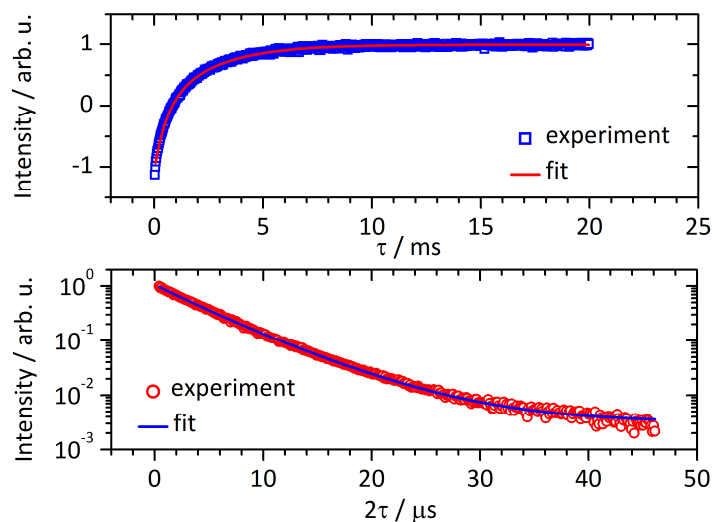
5.2.3 Experiment Design and Data Analysis

MW pulse lengths in pulsed EPR experiments were optimized in order to yield a maximum spin echo. The pulse sequence repetition time was set to at least five times $T_{1,s}$ to prevent saturation effects. Inversion recovery- and Hahn echo experiments were performed from small interpulse distances τ to at least $\tau = 5T_{1,s}$ or $= 5T_{M,s}$, respectively. Otherwise the uncertainty of parameters extracted from fits will be much larger than the experimental error. The experimental error for relaxation measurements with pulsed EPR spectrometers is in general around 10 %, due to instrument specific noise and instabilities. For example, the instability of the microwave frequency and of the magnetic field should be named here and also temperature variations. Further contributors to this error are sample preparation related inconsistencies like the freezing procedure of the EPR-samples or the possibility of incomplete glass formation.

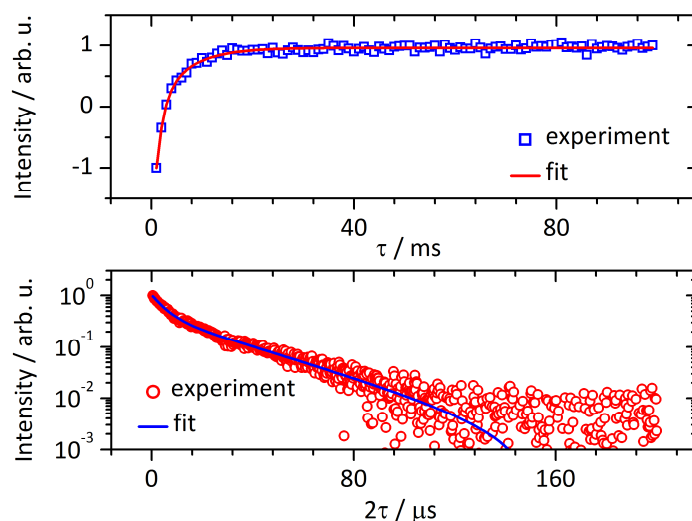
Data of ESE-detected EPR spectra were normalized to the most intense signal and simulated with the Matlab-toolbox EasySpin.^[80] Data from Hahn echo (and inversion recovery-) experiments were normalized to the first (and last) point and fits were performed with Origin. In the case of inversion recovery experiments, the respective first data point was excluded for the fits, as here usually spin-echo saturation effects occur due to the ring-down of MW power in the resonator. Data from ESEEM-experiments was processed with a self-written MATLAB-script. In there, first a baseline correction with a polynomial function was applied. On the first half of the time-trace, an apodization window (Hamming) was applied and the second half was truncated and subsequently zero-filling was applied. Finally, FFT of the processed data yielded in the FFT-shifts. ENDOR data were used as recorded and simulated with the Matlab-toolbox EasySpin.^[80] CPMG-data were used as recorded and fitting was performed with Origin, where the upper envelope of the data trace was fitted with exponential functions. Transient nutation data are displayed as recorded.

6 Appendix

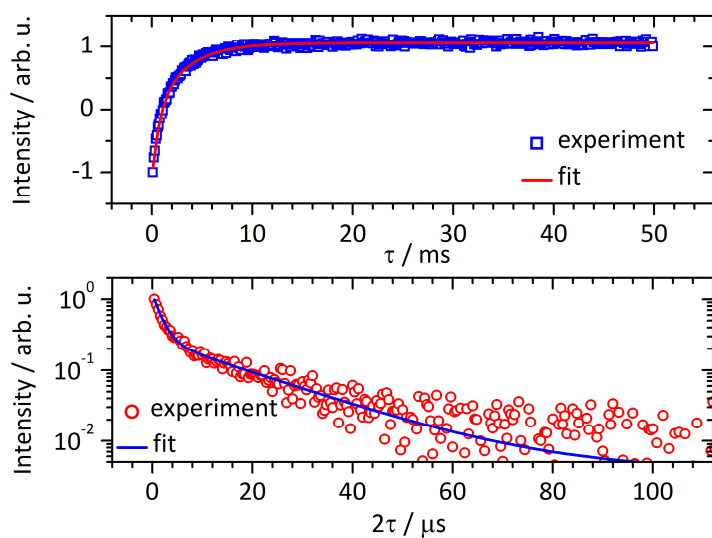
6.1 Supplementary Information to Spin Dynamics in Compounds with O-Donor Ligands



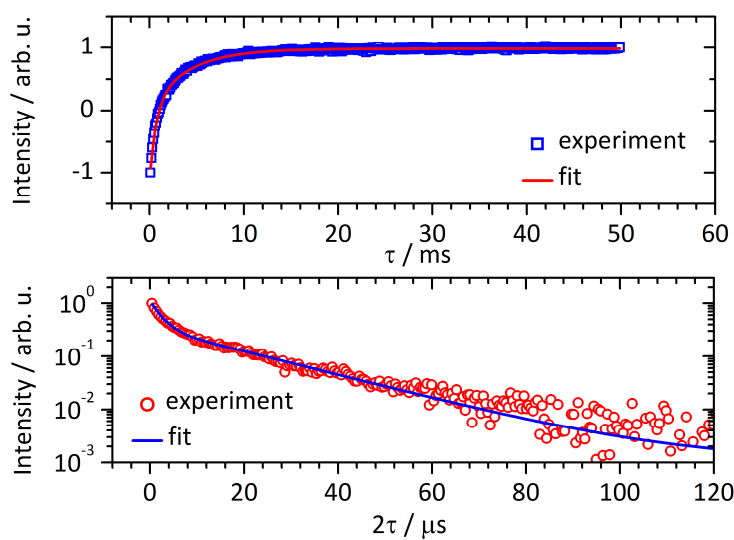
Supplementary Figure 1: Electron spin relaxation measurements and fits of **Cu-Otfac** in 0.001 M solution (1:1 $\text{CD}_2\text{Cl}_2/\text{CS}_2$) measured at Q-band (35.000 GHz in both cases) and 7 K. Top panel: Inversion recovery experiment. Blue, open squares indicate experimental data and red, solid line represents fit function. Bottom panel: Hahn echo experiment. Red, open circles indicate experimental data and blue, solid line represents fit function.



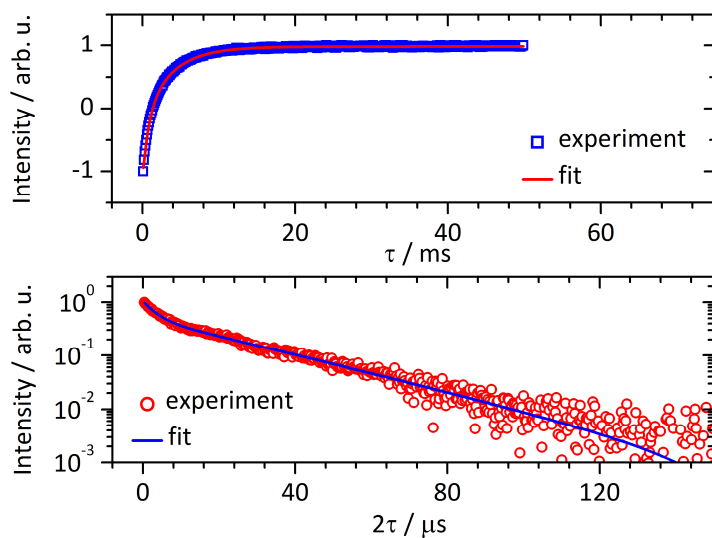
Supplementary Figure 2: Electron spin relaxation measurements and fits of **Cu-Ohfac** in 0.001 M solution (1:1 $\text{CD}_2\text{Cl}_2/\text{CS}_2$) measured at Q-band (35.000 GHz in both cases) and 7 K. Top panel: Inversion recovery experiment. Blue, open squares indicate experimental data and red, solid line represents fit function. Bottom panel: Hahn echo experiment. Red, open circles indicate experimental data and blue, solid line represents fit function.



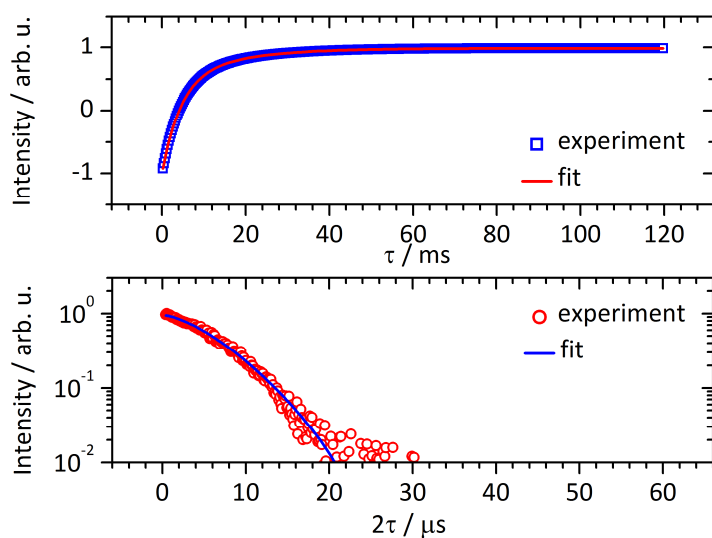
Supplementary Figure 3: Electron spin relaxation measurements and fits of **Cu-Ofod** in 0.001 M solution (1:1 $\text{CD}_2\text{Cl}_2/\text{CS}_2$) measured at Q-band (35.000 GHz in both cases) and 7 K. Top panel: Inversion recovery experiment. Blue, open squares indicate experimental data and red, solid line represents fit function. Bottom panel: Hahn echo experiment. Red, open circles indicate experimental data and blue, solid line represents fit function.



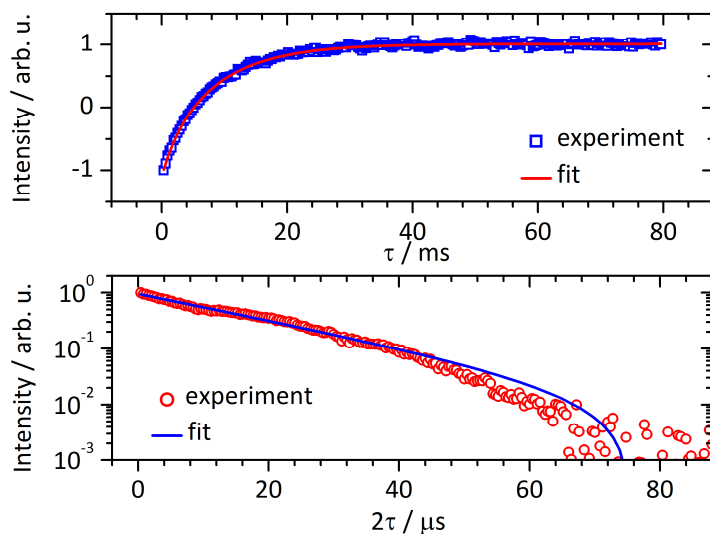
Supplementary Figure 4: Electron spin relaxation measurements and fits of **Cu-Obzac** in 0.001 M solution (1:1 $\text{CD}_2\text{Cl}_2/\text{CS}_2$) measured at Q-band (35.000 GHz in both cases) and 7 K. Top panel: Inversion recovery experiment. Blue, open squares indicate experimental data and red, solid line represents fit function. Bottom panel: Hahn echo experiment. Red, open circles indicate experimental data and blue, solid line represents fit function.



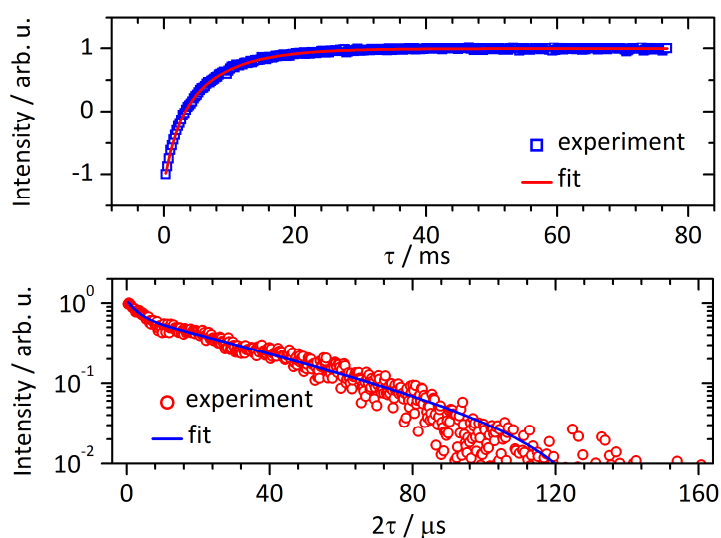
Supplementary Figure 5: Electron spin relaxation measurements and fits of **Cu-Odbm** in 0.001 M solution (1:1 $\text{CD}_2\text{Cl}_2/\text{CS}_2$) measured at Q-band (35.000 GHz in both cases) and 7 K. Top panel: Inversion recovery experiment. Blue, open squares indicate experimental data and red, solid line represents fit function. Bottom panel: Hahn echo experiment. Red, open circles indicate experimental data and blue, solid line represents fit function.



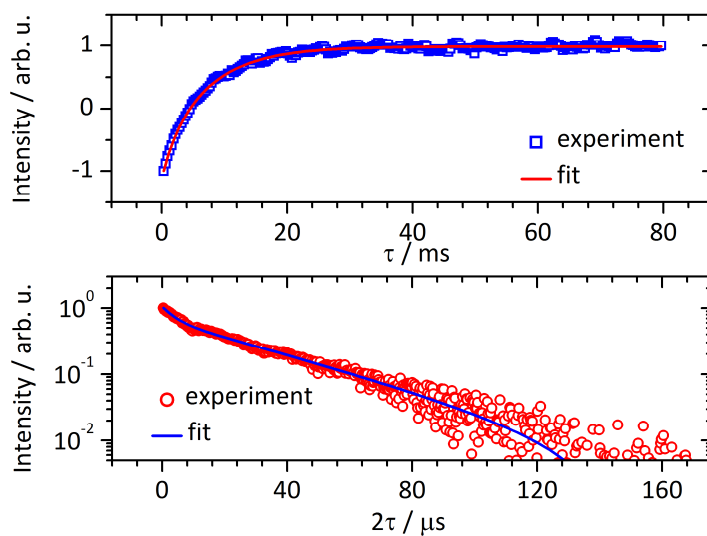
Supplementary Figure 6: Electron spin relaxation measurements and fits of **Cu-Odbm** in CH_2Cl_2 (0.001 M) measured at Q-band (35.000 GHz in both cases) and 7 K. Top panel: Inversion recovery experiment. Blue, open squares indicate experimental data and red, solid line represents fit function. Bottom panel: Hahn echo experiment. Red, open circles indicate experimental data and blue, solid line represents fit function.



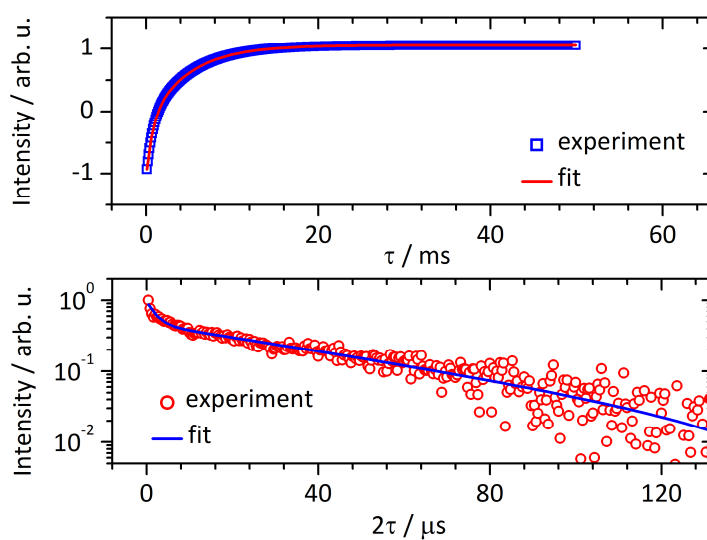
Supplementary Figure 7: Electron spin relaxation measurements and fits of **Cu-Odbm** in **CHCl₃** (0.001 M) measured at Q-band (35.000 GHz in both cases) and 7 K. Oscillations are due to spectrometer specific instabilities. Top panel: Inversion recovery experiment. Blue, open squares indicate experimental data and red, solid line represents fit function. Bottom panel: Hahn echo experiment. Red, open circles indicate experimental data and blue, solid line represents fit function.



Supplementary Figure 8: Electron spin relaxation measurements and fits of **Cu-Odbm** in **CD₂Cl₂** (0.001 M) measured at Q-band (35.000 GHz in both cases) and 7 K. Oscillations are due to spectrometer specific instabilities. Top panel: Inversion recovery experiment. Blue, open squares indicate experimental data and red, solid line represents fit function. Bottom panel: Hahn echo experiment. Red, open circles indicate experimental data and blue, solid line represents fit function.

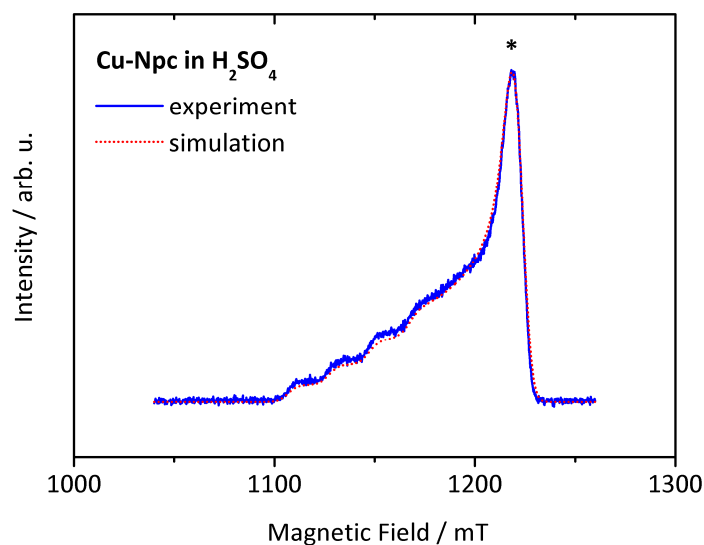


Supplementary Figure 9: Electron spin relaxation measurements and fits of **Cu-Odbm** in **CDCl₃** (0.001 M) measured at Q-band (35.000 GHz in both cases) and 7 K. Oscillations are due to spectrometer specific instabilities. Top panel: Inversion recovery experiment. Blue, open squares indicate experimental data and red, solid line represents fit function. Bottom panel: Hahn echo experiment. Red, open circles indicate experimental data and blue, solid line represents fit function.

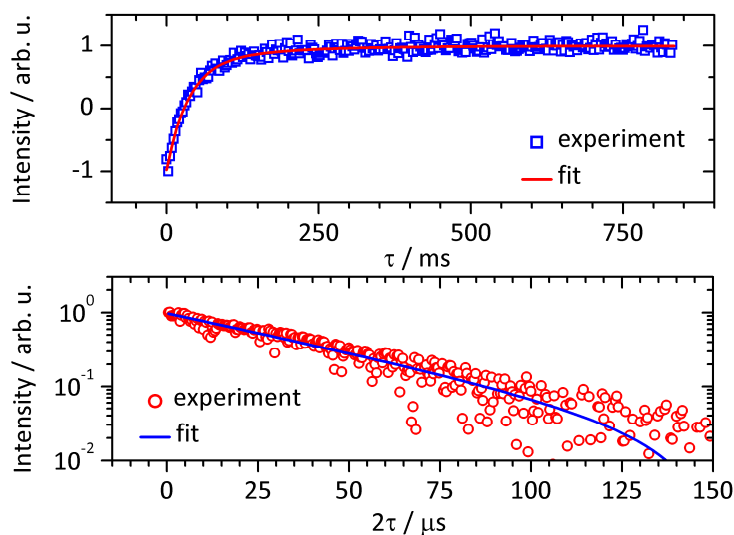


Supplementary Figure 10: Electron spin relaxation measurements and fits of **Cu-Odbm** in **CS₂** (0.001 M) measured at Q-band (35.000 GHz in both cases) and 7 K. Top panel: Inversion recovery experiment. Blue, open squares indicate experimental data and red, solid line represents fit function. Bottom panel: Hahn echo experiment. Red, open circles indicate experimental data and blue, solid line represents fit function.

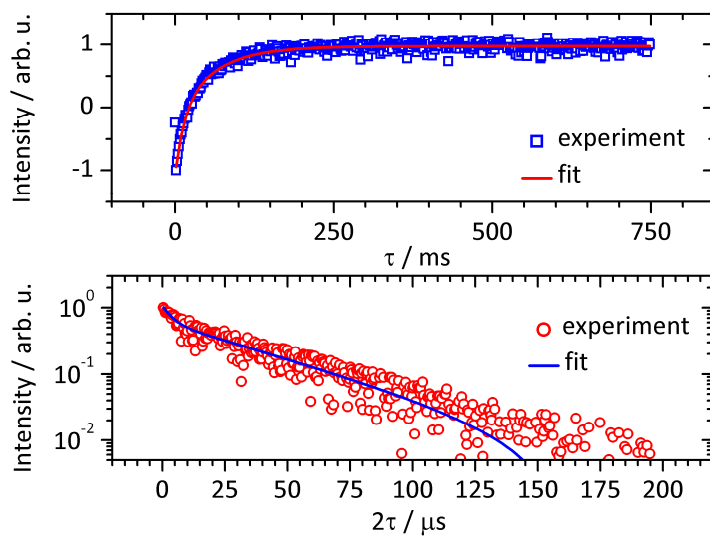
6.2 Supplementary Information to Spin Dynamics in Compounds with N-Donor Ligands



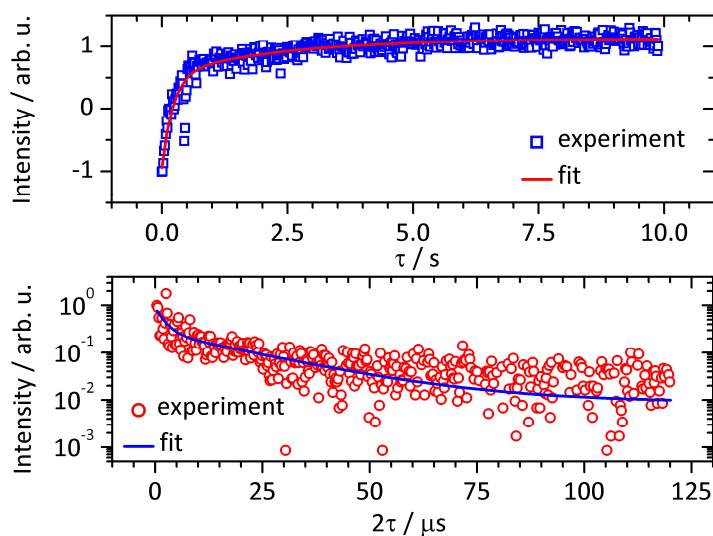
Supplementary Figure 11: ESE-detected EPR spectra of **Cu-Npc** in 0.5 mM solution (H_2SO_4) recorded at Q-band (35.000 GHz) and 7 K. Blue, solid line represents experimental data. Red, dotted line indicates simulation with parameters: $g_{\parallel} = 2.1990 \pm 0.0005$, $g_{\perp} = 2.0496 \pm 0.0005$, $A_{\parallel} = 630 \pm 10$ MHz, $A_{\perp} = 15 \pm 10$ MHz, $\Delta B_{lwp} = [7.2 \ 0]$. The entry for ΔB_{lwp} gives the Gaussian and Lorentzian linewidth of a Voigtian convolution. The asterisk marks magnetic field position for spin dynamics measurements.



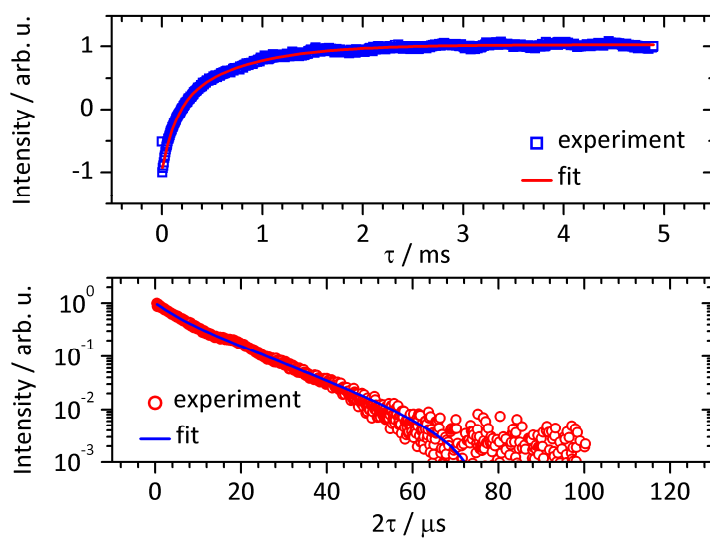
Supplementary Figure 12: Electron spin relaxation measurements and fits of **Cu-Npc^{Cl}** in 0.5 mM solution (D_2SO_4) measured at Q-band (35.000 GHz in both cases) and 7 K. Top panel: Inversion recovery experiment. Blue, open squares indicate experimental data and red, solid line represents fit function. Bottom panel: Hahn echo experiment. Red, open circles indicate experimental data and blue, solid line represents fit function.



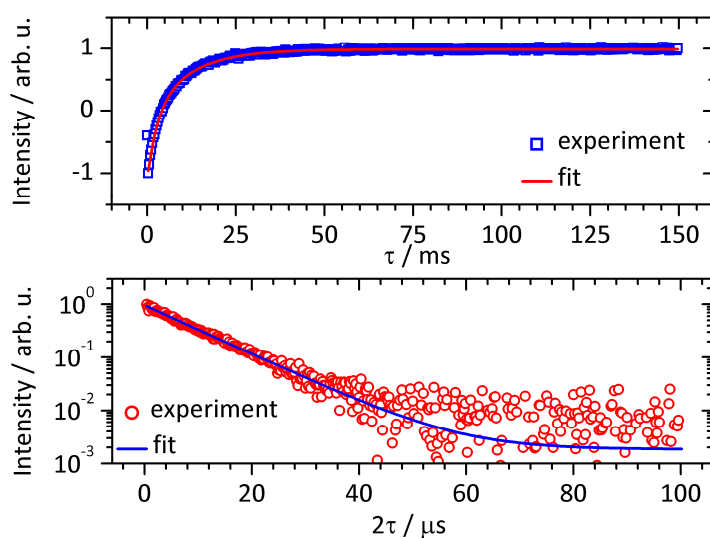
Supplementary Figure 13: Electron spin relaxation measurements and fits of **Cu-Npc^F** in 0.5 mM solution (D_2SO_4) measured at Q-band (35.000 GHz in both cases) and 7 K. Top panel: Inversion recovery experiment. Blue, open squares indicate experimental data and red, solid line represents fit function. Bottom panel: Hahn echo experiment. Red, open circles indicate experimental data and blue, solid line represents fit function.



Supplementary Figure 14: Electron spin relaxation measurements and fits of **VO-Npc** in 0.5 mM solution (D_2SO_4) measured at Q-band (35.000 GHz in both cases) and 7 K. Top panel: Inversion recovery experiment. Blue, open squares indicate experimental data and red, solid line represents fit function. Bottom panel: Hahn echo experiment. Red, open circles indicate experimental data and blue, solid line represents fit function.

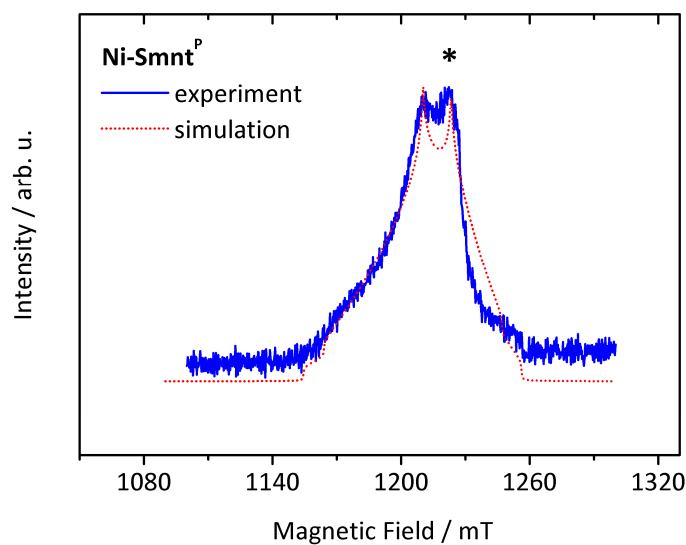


Supplementary Figure 15: Electron spin relaxation measurements and fits of **Mn-Npc** in 0.5 mM solution (D_2SO_4) measured at Q-band (35.000 GHz in both cases) and 7 K. Top panel: Inversion recovery experiment. Blue, open squares indicate experimental data and red, solid line represents fit function. Bottom panel: Hahn echo experiment. Red, open circles indicate experimental data and blue, solid line represents fit function.

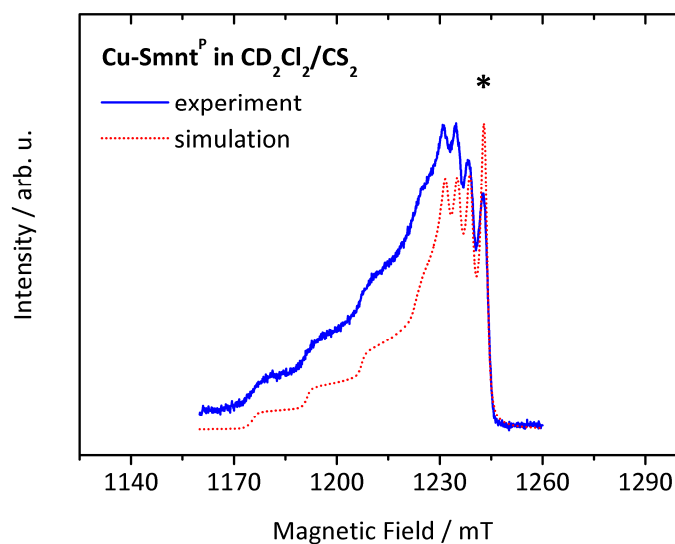


Supplementary Figure 16: Electron spin relaxation measurements and fits of **Co-Npc** in 0.5 mM solution (D_2SO_4) measured at Q-band (35.000 GHz in both cases) and 7 K. Top panel: Inversion recovery experiment. Blue, open squares indicate experimental data and red, solid line represents fit function. Bottom panel: Hahn echo experiment. Red, open circles indicate experimental data and blue, solid line represents fit function.

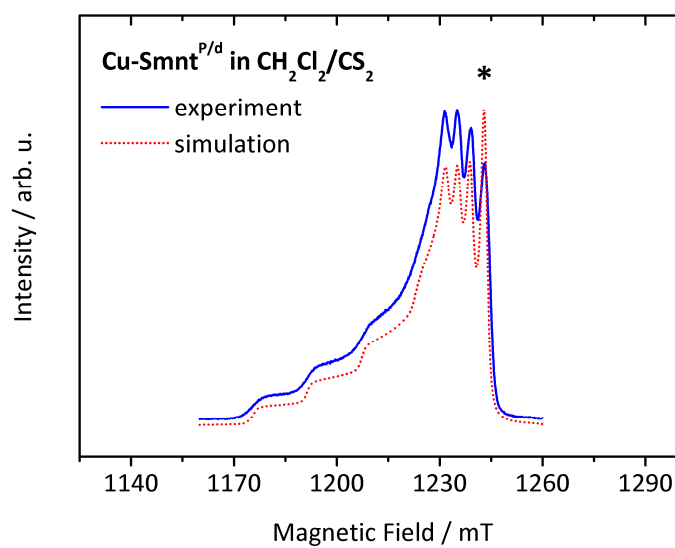
6.3 Supplementary Information to Spin Dynamics in Compounds with S-Donor Ligands



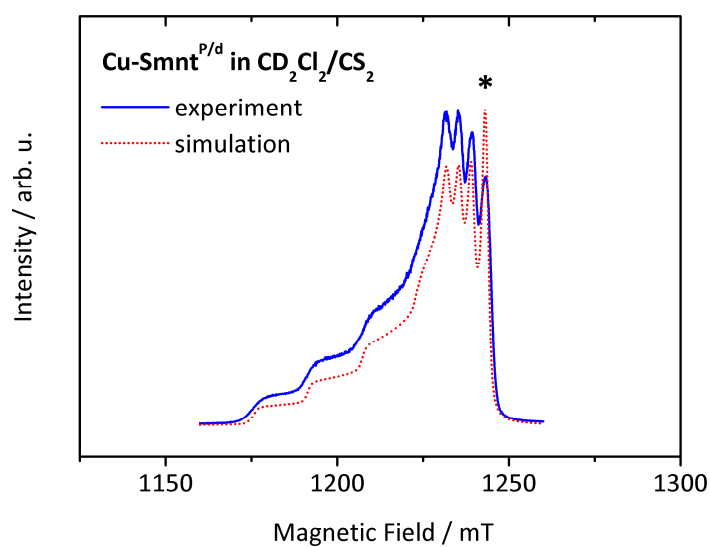
Supplementary Figure 17: ESE-detected EPR spectra of Ni-Sdto^{P/d} as 0.01 % doped powder recorded at Q-band (35.000 GHz) and 7 K. Blue, solid line represents experimental data. Red, dotted line indicates simulation. The asterisk marks magnetic field position for spin dynamics measurements.



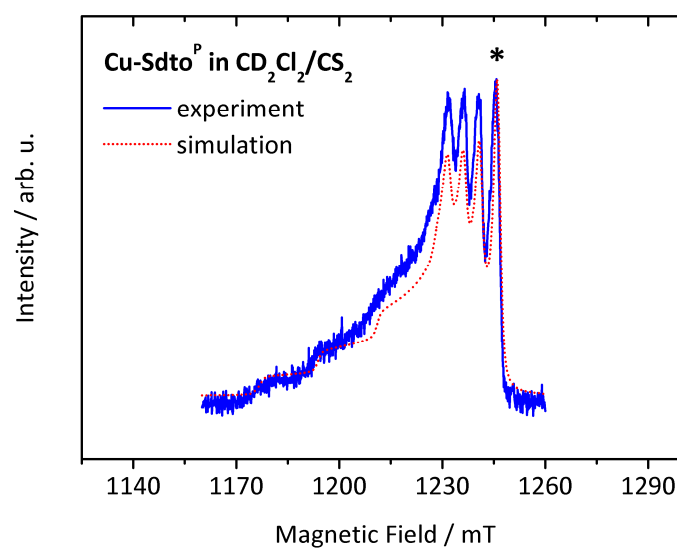
Supplementary Figure 18: ESE-detected EPR spectra of Cu-Smnt^P in 1 mM solution in CD₂Cl₂/CS₂ (1:1) recorded at Q-band (34.999 GHz) and 7 K. Blue, solid line represents experimental data. Red, dotted line indicates simulation. The asterisk marks magnetic field position for spin dynamics measurements.



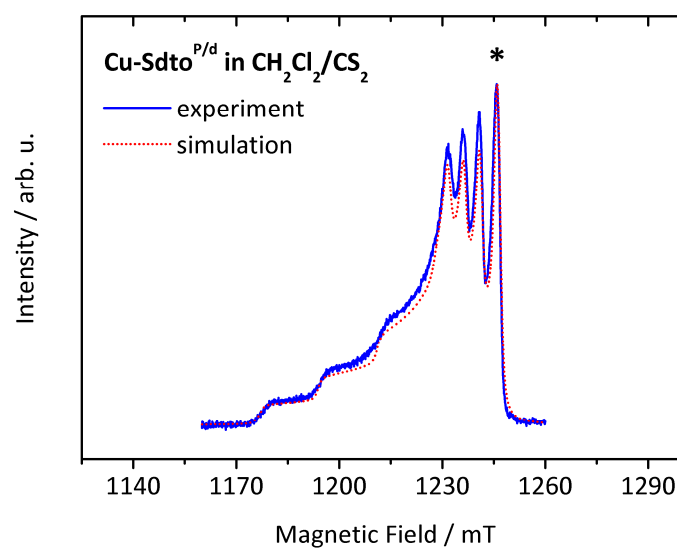
Supplementary Figure 19: ESE-detected EPR spectra of **Cu-Smnt^{P/d}** in 1 mM solution in CH₂Cl₂/CS₂ (1:1) recorded at Q-band (35.001 GHz) and 7 K. Blue, solid line represents experimental data. Red, dotted line indicates simulation. The asterisk marks magnetic field position for spin dynamics measurements.



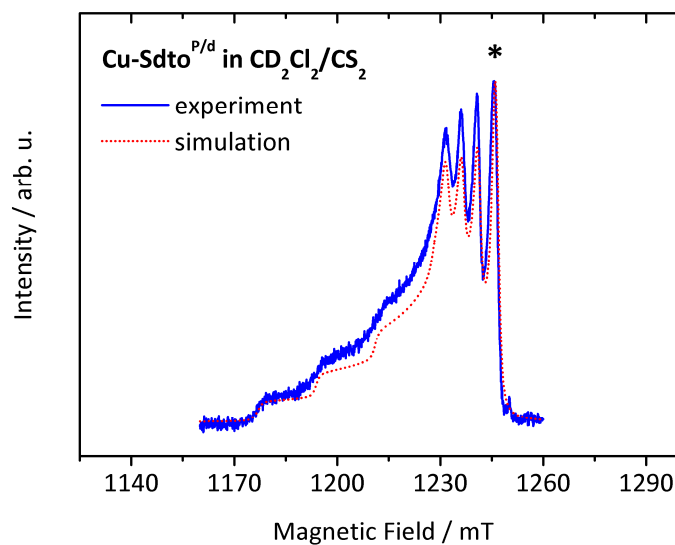
Supplementary Figure 20: ESE-detected EPR spectra of **Cu-Smnt^{P/d}** in 1 mM solution in CD₂Cl₂/CS₂ (1:1) recorded at Q-band (35.001 GHz) and 7 K. Blue, solid line represents experimental data. Red, dotted line indicates simulation. The asterisk marks magnetic field position for spin dynamics measurements.



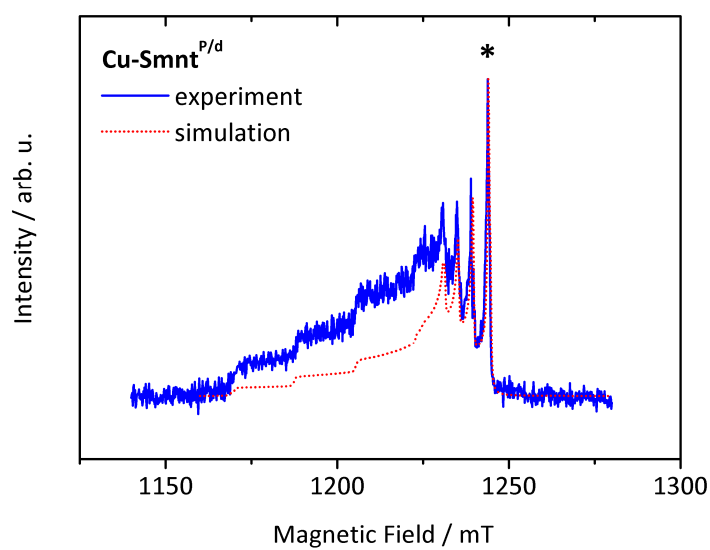
Supplementary Figure 21: ESE-detected EPR spectra of **Cu-Sdto^P** in 1 mM solution in CD₂Cl₂/CS₂ (1:1) recorded at Q-band (34.999 GHz) and 7 K. Blue, solid line represents experimental data. Red, dotted line indicates simulation. The asterisk marks magnetic field position for spin dynamics measurements.



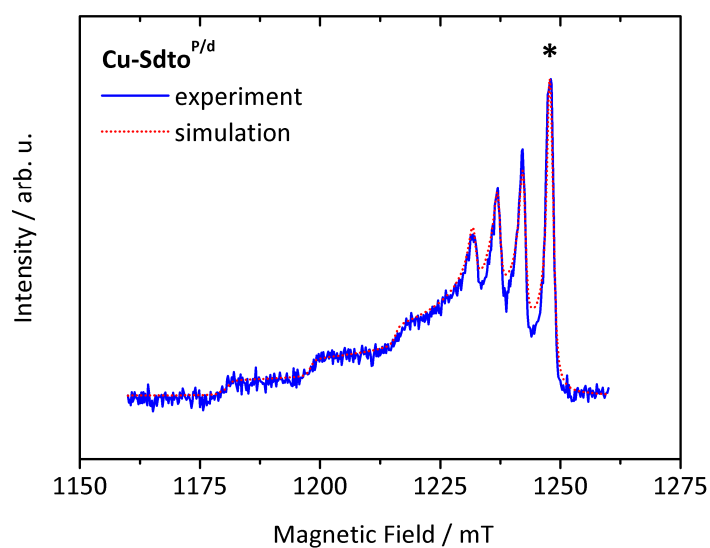
Supplementary Figure 22: ESE-detected EPR spectra of **Cu-Sdto^{P/d}** in 1 mM solution in CH₂Cl₂/CS₂ (1:1) recorded at Q-band (34.999 GHz) and 7 K. Blue, solid line represents experimental data. Red, dotted line indicates simulation. The asterisk marks magnetic field position for spin dynamics measurements.



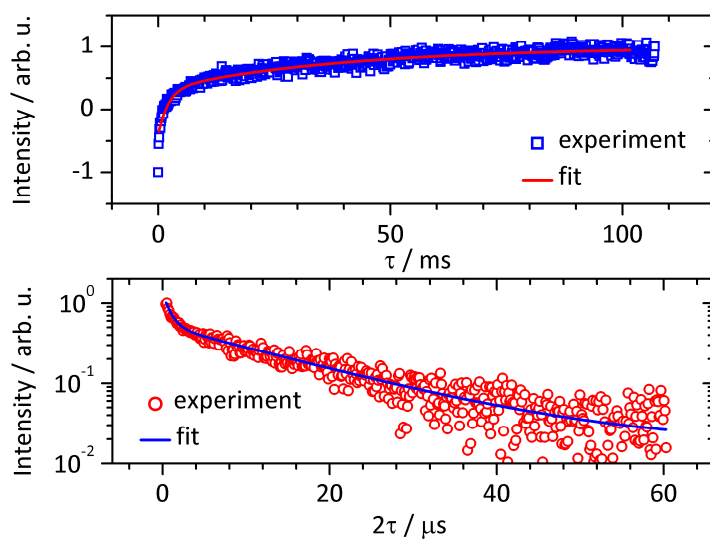
Supplementary Figure 23: ESE-detected EPR spectra of **Cu-Sdto^{P/d}** in 1 mM solution in CD₂Cl₂/CS₂ (1:1) recorded at Q-band (35.000 GHz) and 7 K. Blue, solid line represents experimental data. Red, dotted line indicates simulation. The asterisk marks magnetic field position for spin dynamics measurements.



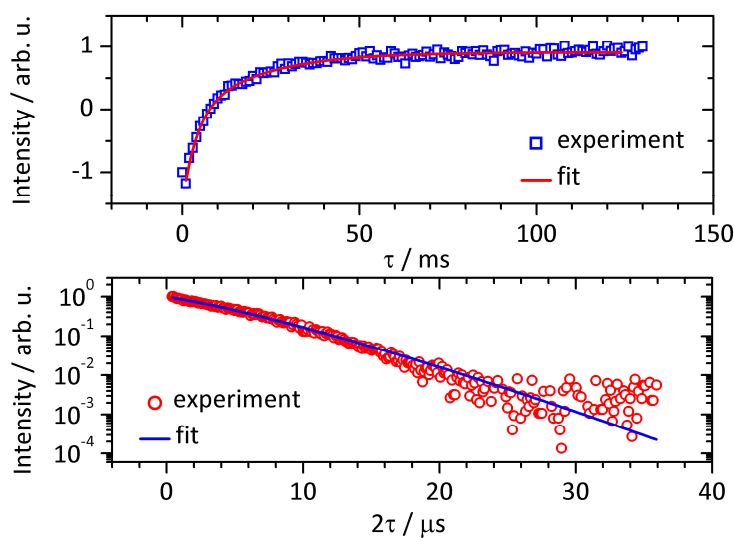
Supplementary Figure 24: ESE-detected EPR spectra of **Cu-Smnt^{P/d}** in 0.01 % doped powder recorded at Q-band (34.994 GHz) and 7 K. Blue, solid line represents experimental data. Red, dotted line indicates simulation. The asterisk marks magnetic field position for spin dynamics measurements.



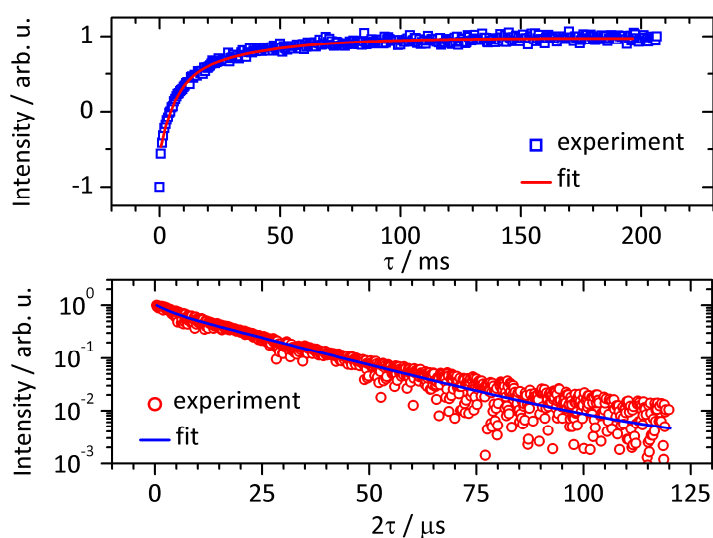
Supplementary Figure 25: ESE-detected EPR spectra of $\text{Cu-Sdto}^{\text{P/d}}$ as 0.01 % doped powder recorded at Q-band (35.000 GHz) and 7 K. Blue, solid line represents experimental data. Red, dotted line indicates simulation. The asterisk marks magnetic field position for spin dynamics measurements.



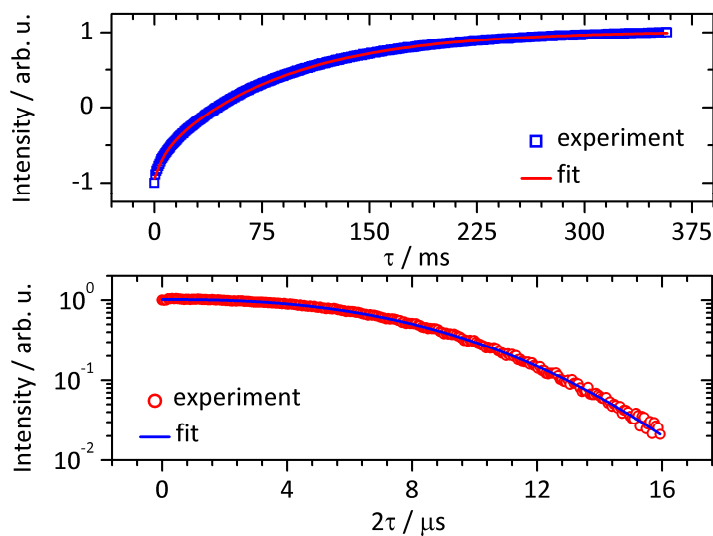
Supplementary Figure 26: Electron spin relaxation measurements and fits of $\text{Cu-Smnt}^{\text{P}}$ in 1 mM solution (1:1 $\text{CD}_2\text{Cl}_2/\text{CS}_2$) measured at Q-band (35.000 GHz in both cases) and 7 K. Top panel: Inversion recovery experiment. Blue, open squares indicate experimental data and red, solid line represents fit function. Bottom panel: Hahn echo experiment. Red, open circles indicate experimental data and blue, solid line represents fit function.



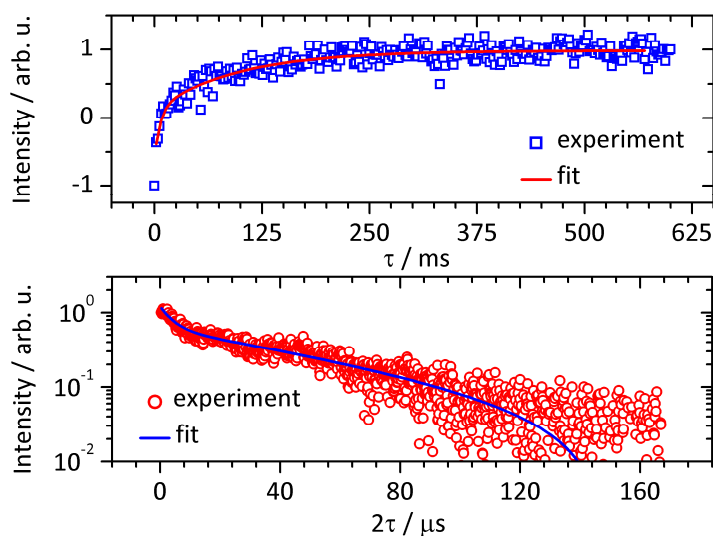
Supplementary Figure 27: Electron spin relaxation measurements and fits of $\text{Cu-Smnt}^{\text{P/d}}$ in 1 mM solution (1:1 $\text{CH}_2\text{Cl}_2/\text{CS}_2$) measured at Q-band (35.000 GHz in both cases) and 7 K. Top panel: Inversion recovery experiment. Blue, open squares indicate experimental data and red, solid line represents fit function. Bottom panel: Hahn echo experiment. Red, open circles indicate experimental data and blue, solid line represents fit function.



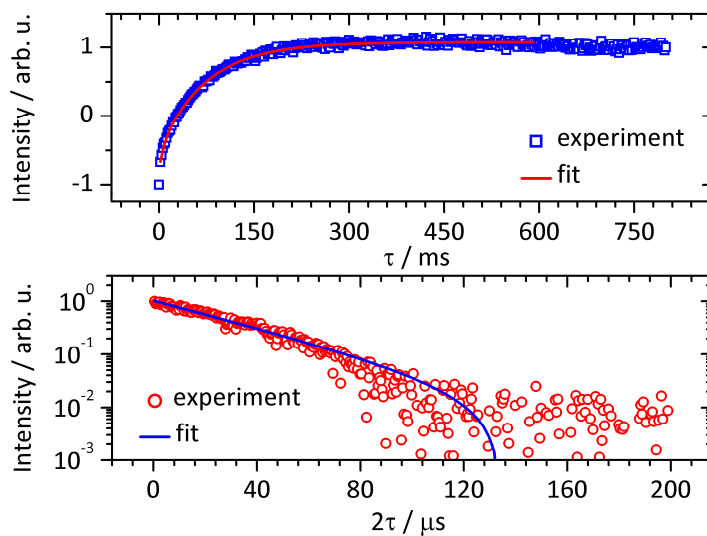
Supplementary Figure 28: Electron spin relaxation measurements and fits of $\text{Cu-Smnt}^{\text{P/d}}$ in 1 mM solution (1:1 $\text{CD}_2\text{Cl}_2/\text{CS}_2$) measured at Q-band (35.000 GHz in both cases) and 7 K. Top panel: Inversion recovery experiment. Blue, open squares indicate experimental data and red, solid line represents fit function. Bottom panel: Hahn echo experiment. Red, open circles indicate experimental data and blue, solid line represents fit function.



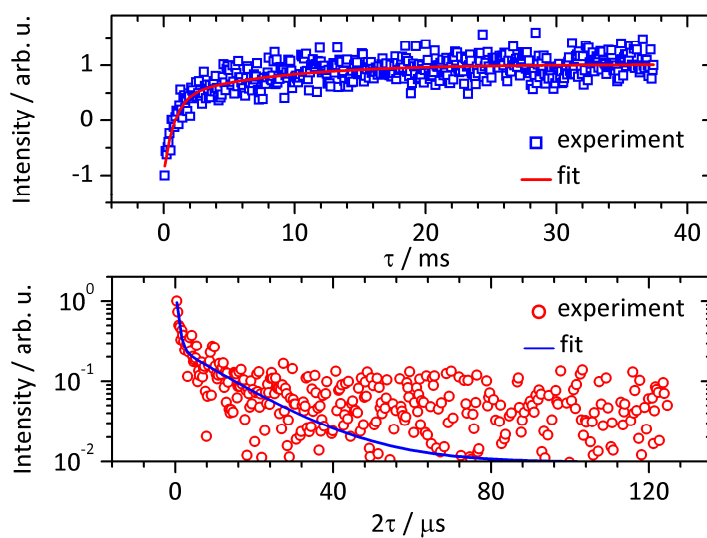
Supplementary Figure 29: Electron spin relaxation measurements and fits of **Cu-Smnt^P** in 0.001 % doped powder measured at Q-band and 7 K. Top panel: Inversion recovery experiment (33.766 GHz). Blue, open squares indicate experimental data and red, solid line represents fit function. Bottom panel: Hahn echo experiment (33.700 GHz). Red, open circles indicate experimental data and blue, solid line represents fit function.



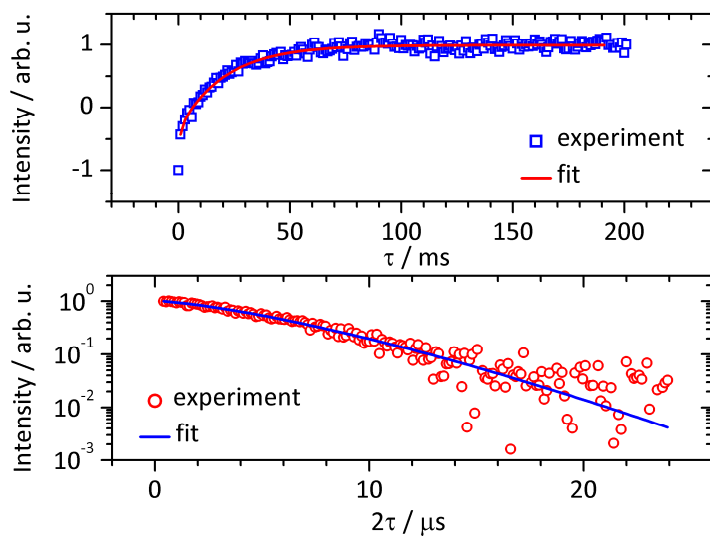
Supplementary Figure 30: Electron spin relaxation measurements and fits of **Cu-Smnt^{P/d}** in 0.01 % doped powder measured at Q-band and 7 K. Top panel: Inversion recovery experiment (35.000 GHz). Blue, open squares indicate experimental data and red, solid line represents fit function. Bottom panel: Hahn echo experiment (34.999 GHz). Red, open circles indicate experimental data and blue, solid line represents fit function.



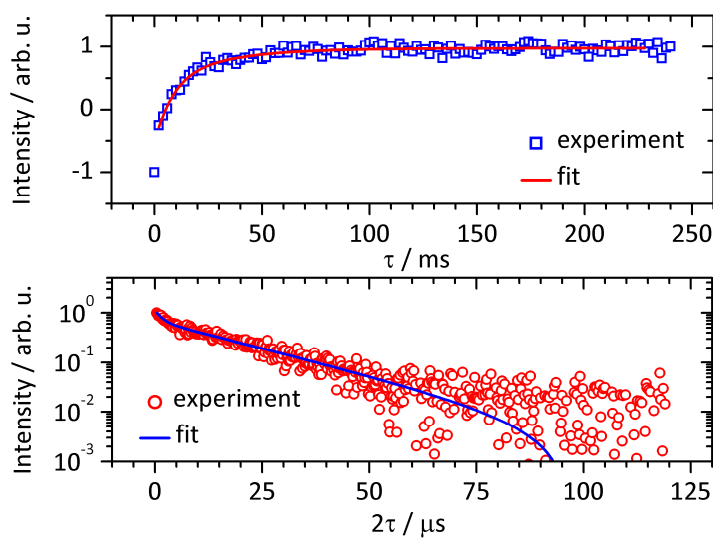
Supplementary Figure 31: Electron spin relaxation measurements and fits of $\text{Cu-Smmt}^{\text{As/d}}$ in 0.01 % doped powder measured at Q-band (35.000 GHz in both cases) and 7 K. Top panel: Inversion recovery experiment. Blue, open squares indicate experimental data and red, solid line represents fit function. Bottom panel: Hahn echo experiment. Red, open circles indicate experimental data and blue, solid line represents fit function.



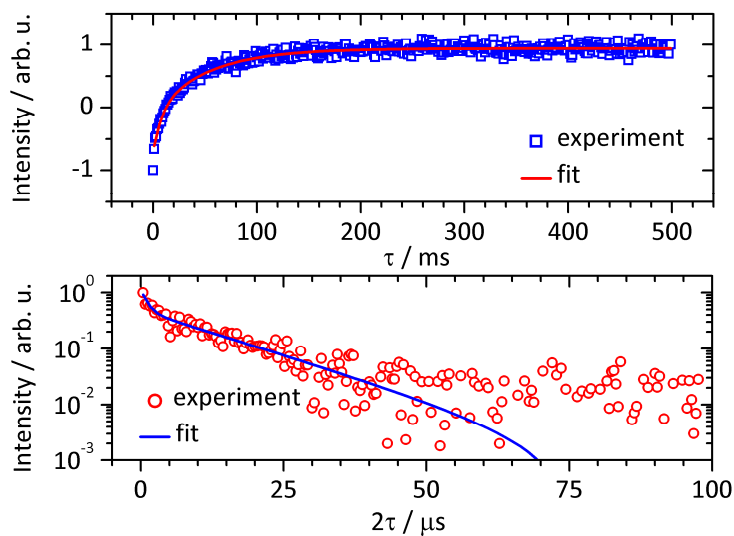
Supplementary Figure 32: Electron spin relaxation measurements and fits of $\text{Cu-Smmt}^{\text{Ns}}$ in 0.01 % doped powder measured at Q-band and 7 K. Top panel: Inversion recovery experiment (35.000 GHz). Blue, open squares indicate experimental data and red, solid line represents fit function. Bottom panel: Hahn echo experiment (34.999 GHz). Red, open circles indicate experimental data and blue, solid line represents fit function.



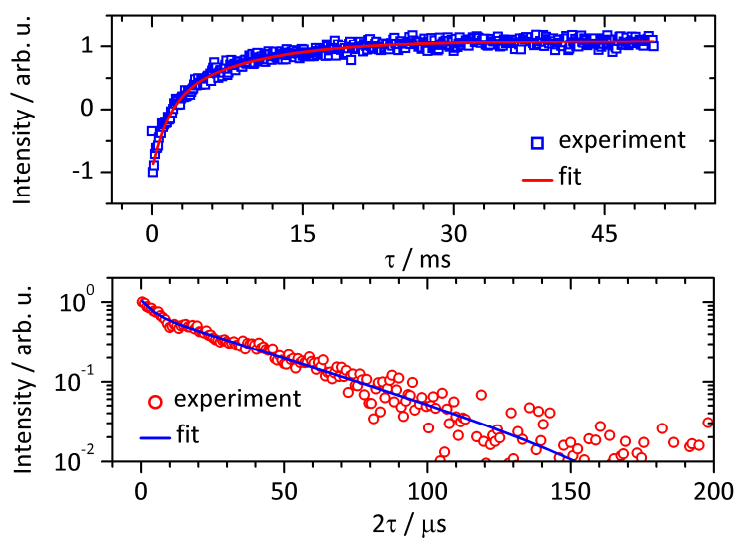
Supplementary Figure 33: Electron spin relaxation measurements and fits of $\text{Cu-Sdto}^{\text{P}}$ in 0.01 % doped powder measured at Q-band (35.000 GHz in both cases) and 7 K. Top panel: Inversion recovery experiment. Blue, open squares indicate experimental data and red, solid line represents fit function. Bottom panel: Hahn echo experiment. Red, open circles indicate experimental data and blue, solid line represents fit function.



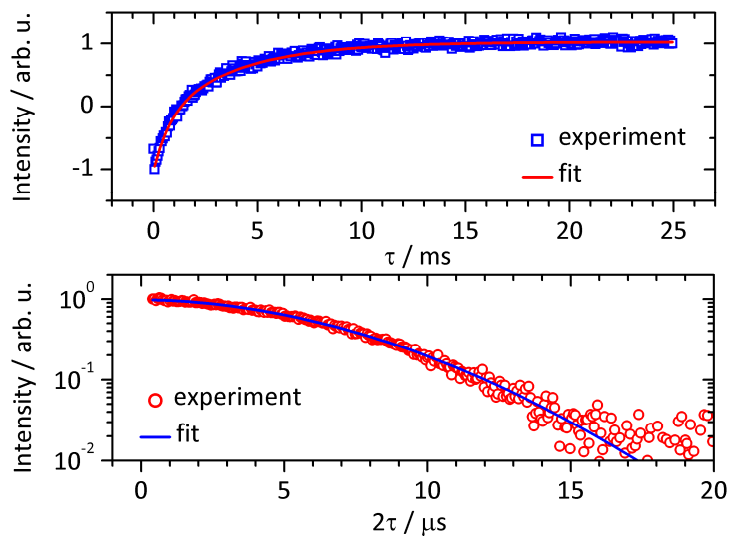
Supplementary Figure 34: Electron spin relaxation measurements and fits of $\text{Cu-Sdto}^{\text{P/d}}$ in 0.01 % doped powder measured at Q-band and 7 K. Top panel: Inversion recovery experiment (35.000 GHz). Blue, open squares indicate experimental data and red, solid line represents fit function. Bottom panel: Hahn echo experiment (34.997 GHz). Red, open circles indicate experimental data and blue, solid line represents fit function.



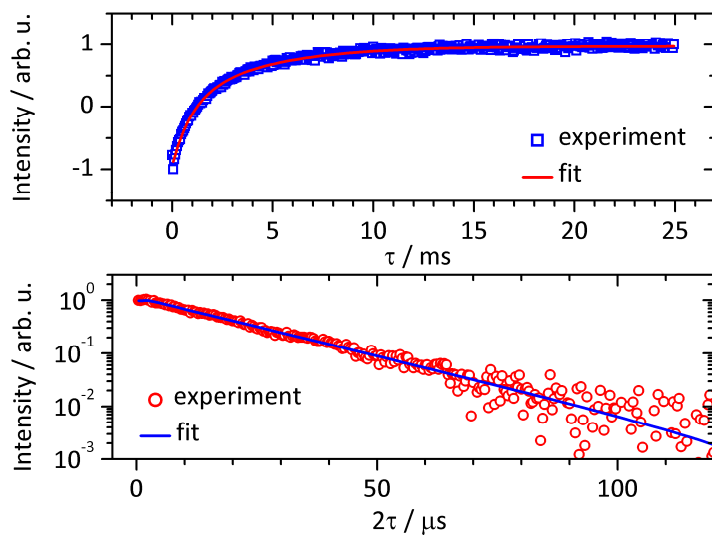
Supplementary Figure 35: Electron spin relaxation measurements and fits of **Cu-Sdto^{As/d}** in 0.01 % doped powder measured at Q-band (35.000 GHz in both cases) and 7 K. Top panel: Inversion recovery experiment. Blue, open squares indicate experimental data and red, solid line represents fit function. Bottom panel: Hahn echo experiment. Red, open circles indicate experimental data and blue, solid line represents fit function.



Supplementary Figure 36: Electron spin relaxation measurements and fits of **Ni-Smnt^{P/d}** in 1 mM solution (1:1 CD₂Cl₂/CS₂) measured at Q-band (35.000 GHz in both cases) and 7 K. Top panel: Inversion recovery experiment. Blue, open squares indicate experimental data and red, solid line represents fit function. Bottom panel: Hahn echo experiment. Red, open circles indicate experimental data and blue, solid line represents fit function.

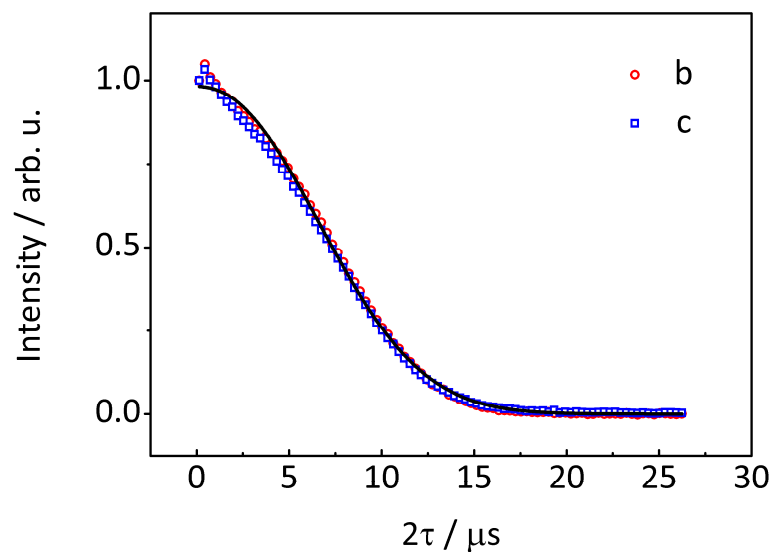


Supplementary Figure 37: Electron spin relaxation measurements and fits of $\text{Ni-Smnt}^{\text{P}}$ in 0.01 % doped powder measured at Q-band (35.000 GHz in both cases) and 7 K. Top panel: Inversion recovery experiment. Blue, open squares indicate experimental data and red, solid line represents fit function. Bottom panel: Hahn echo experiment. Red, open circles indicate experimental data and blue, solid line represents fit function.

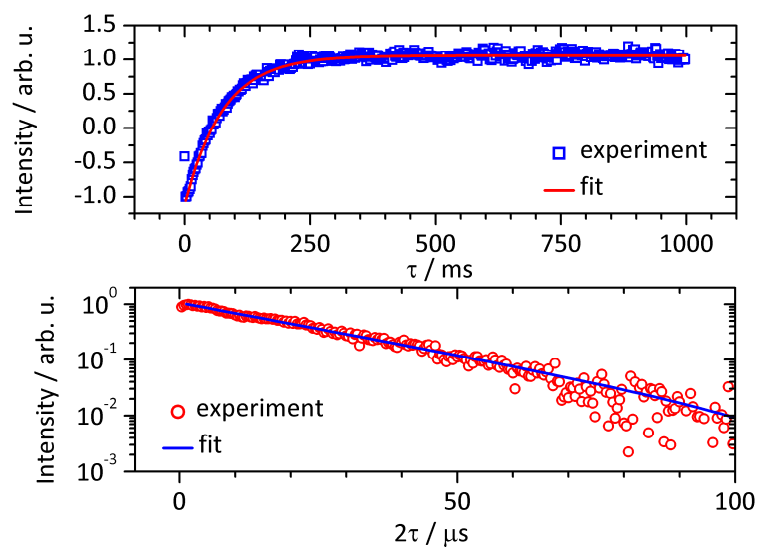


Supplementary Figure 38: Electron spin relaxation measurements and fits of $\text{Ni-Smnt}^{\text{P/d}}$ in 0.01 % doped powder measured at Q-band (35.000 GHz in both cases) and 7 K. Top panel: Inversion recovery experiment. Blue, open squares indicate experimental data and red, solid line represents fit function. Bottom panel: Hahn echo experiment. Red, open circles indicate experimental data and blue, solid line represents fit function.

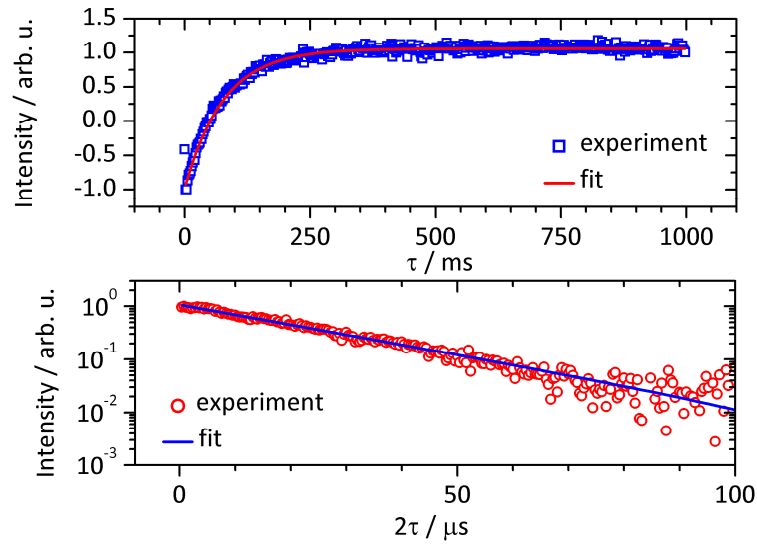
6.4 Supplementary Information to Orientation Dependence of Spin Dynamics



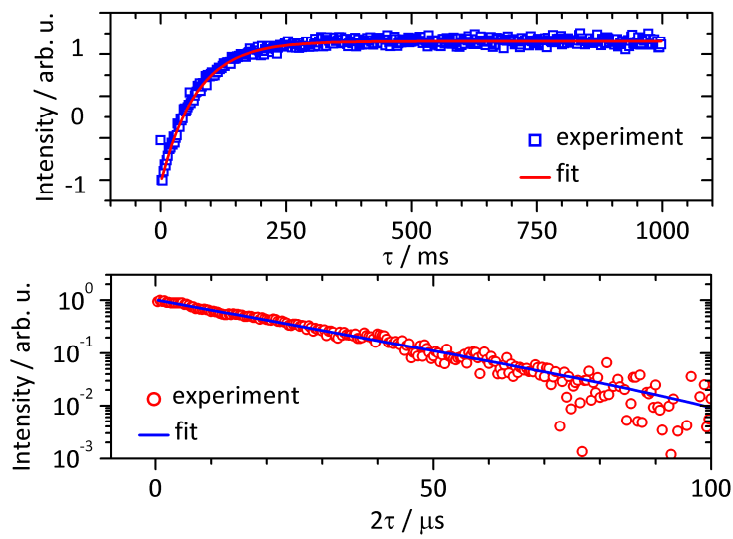
Supplementary Figure 39: Constructed Hahn echo decay curves from surface representation of ESE-detected EPR spectra of $\text{Cu-Smnt}^{\text{P}/0.001\%}$, complementary to Figure 36.



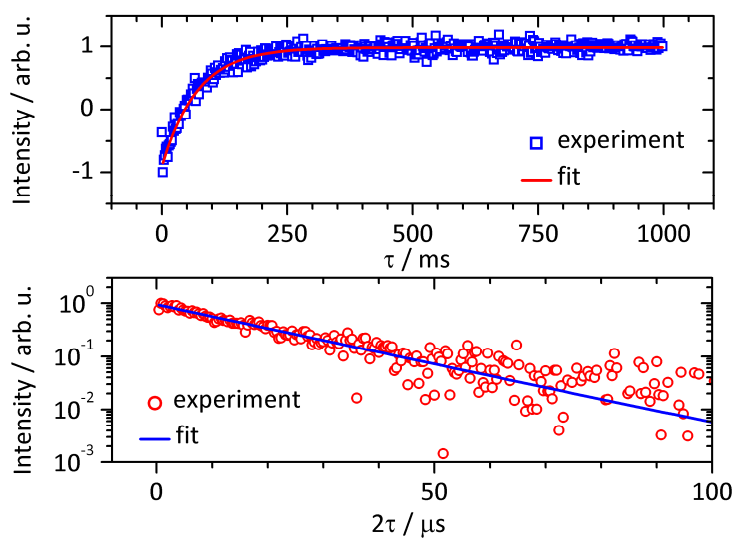
Supplementary Figure 40: Electron spin relaxation measurements and fits of $\text{Cu-Smnt}^{\text{P}/0.01\%}$ measured at Q-band (35.000 GHz in both cases, Stuttgart) and 7 K, magnetic field was 1239.3 mT (resonance line b). Top panel: Inversion recovery experiment. Blue, open squares indicate experimental data and red, solid line represents fit function. Bottom panel: Hahn echo experiment. Red, open circles indicate experimental data and blue, solid line represents fit function.



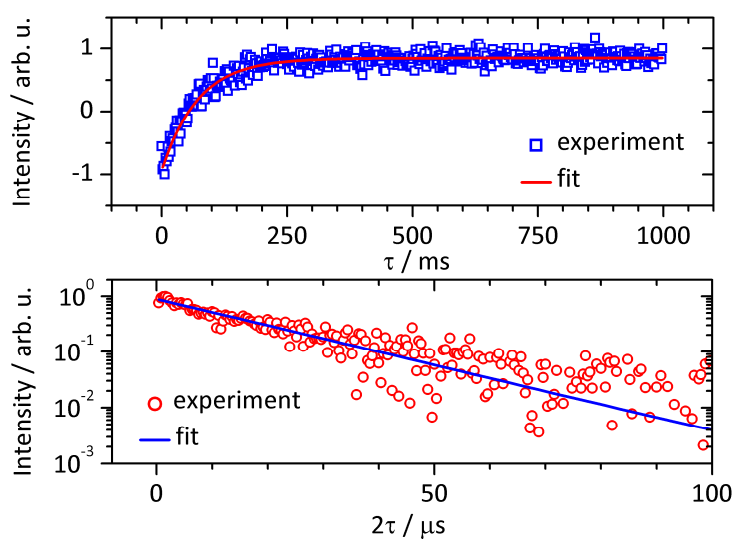
Supplementary Figure 41: Electron spin relaxation measurements and fits of $\text{Cu-Smnt}^{P/d}_{0.01\%}$ measured at Q-band (35.000 GHz in both cases, Stuttgart) and 7 K, magnetic field was 1234.9 mT (resonance line c). Top panel: Inversion recovery experiment. Blue, open squares indicate experimental data and red, solid line represents fit function. Bottom panel: Hahn echo experiment. Red, open circles indicate experimental data and blue, solid line represents fit function.



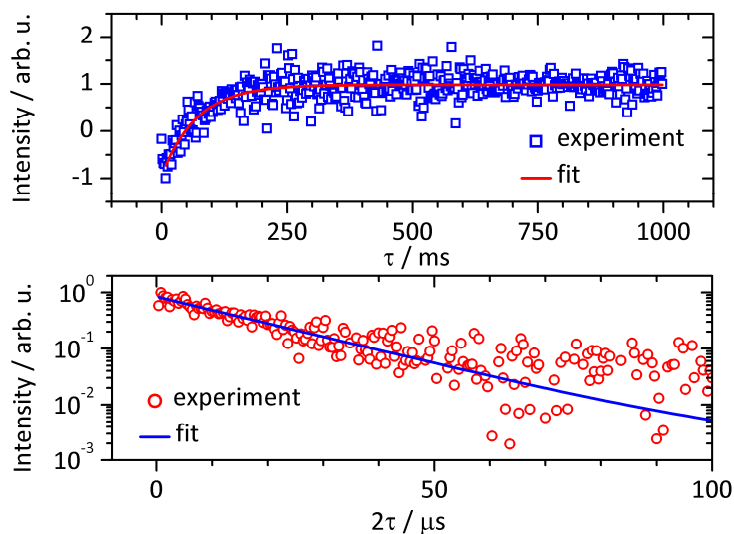
Supplementary Figure 42: Electron spin relaxation measurements and fits of $\text{Cu-Smnt}^{P/d}_{0.01\%}$ measured at Q-band (35.000 GHz in both cases, Stuttgart) and 7 K, magnetic field was 1230.7 mT (resonance line d). Top panel: Inversion recovery experiment. Blue, open squares indicate experimental data and red, solid line represents fit function. Bottom panel: Hahn echo experiment. Red, open circles indicate experimental data and blue, solid line represents fit function.



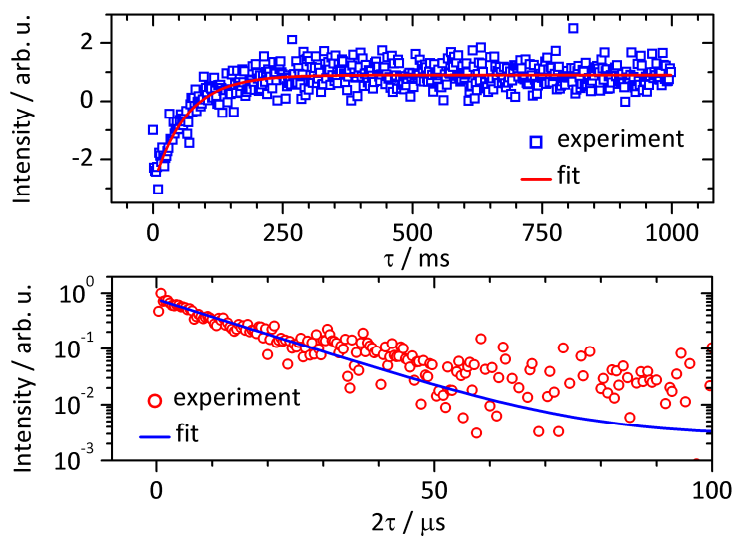
Supplementary Figure 43: Electron spin relaxation measurements and fits of $\text{Cu-Smnt}^{P/d}_{0.01\%}$ measured at Q-band (35.000 GHz in both cases, Stuttgart) and 7 K, magnetic field was 1222.9 mT (resonance line e). Top panel: Inversion recovery experiment. Blue, open squares indicate experimental data and red, solid line represents fit function. Bottom panel: Hahn echo experiment. Red, open circles indicate experimental data and blue, solid line represents fit function.



Supplementary Figure 44: Electron spin relaxation measurements and fits of $\text{Cu-Smnt}^{P/d}_{0.01\%}$ measured at Q-band (35.000 GHz in both cases, Stuttgart) and 7 K, magnetic field was 1205.7 mT (resonance line f). Top panel: Inversion recovery experiment. Blue, open squares indicate experimental data and red, solid line represents fit function. Bottom panel: Hahn echo experiment. Red, open circles indicate experimental data and blue, solid line represents fit function.

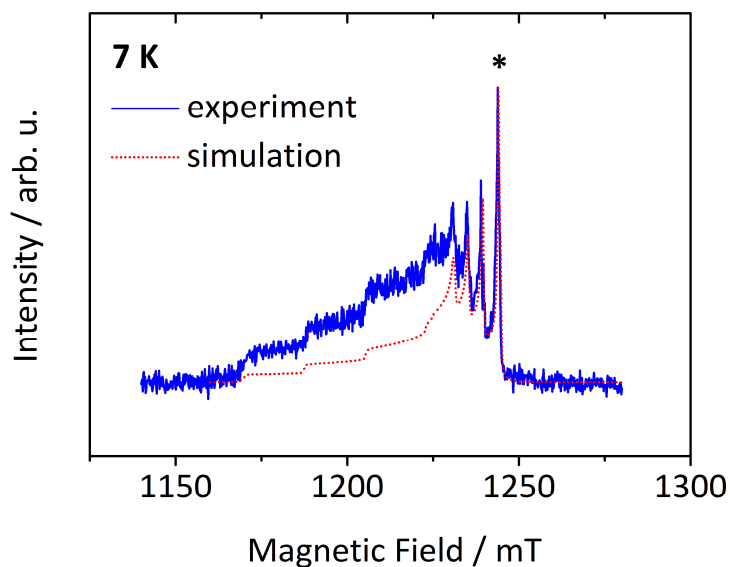


Supplementary Figure 45: Electron spin relaxation measurements and fits of $\text{Cu-Smnt}^{P/d_{0.01\%}}$ measured at Q-band (35.000 GHz in both cases, Stuttgart) and 7 K, magnetic field was 1188.5 mT (resonance line g). Top panel: Inversion recovery experiment. Blue, open squares indicate experimental data and red, solid line represents fit function. Bottom panel: Hahn echo experiment. Red, open circles indicate experimental data and blue, solid line represents fit function.

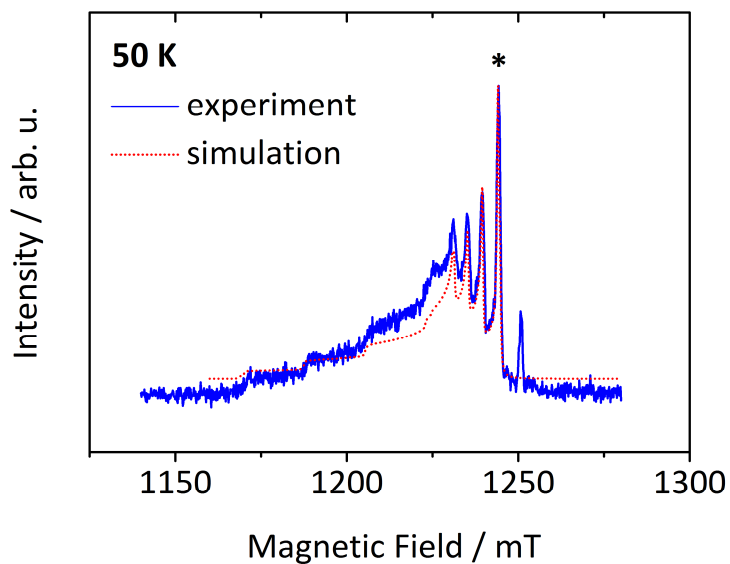


Supplementary Figure 46: Electron spin relaxation measurements and fits of $\text{Cu-Smnt}^{P/d_{0.01\%}}$ measured at Q-band (35.000 GHz in both cases, Stuttgart) and 7 K, magnetic field was 1171.4 mT (resonance line h). Top panel: Inversion recovery experiment. Blue, open squares indicate experimental data and red, solid line represents fit function. Bottom panel: Hahn echo experiment. Red, open circles indicate experimental data and blue, solid line represents fit function.

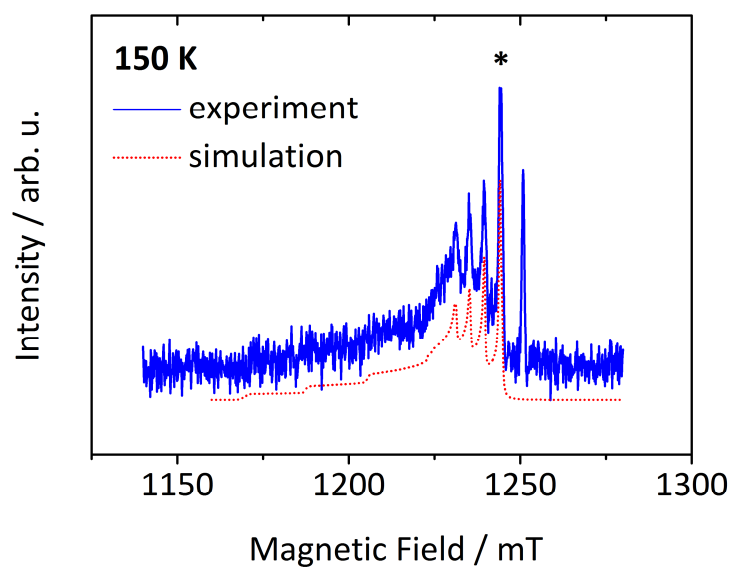
6.5 Supplementary Information to Temperature Dependence of Spin Dynamics



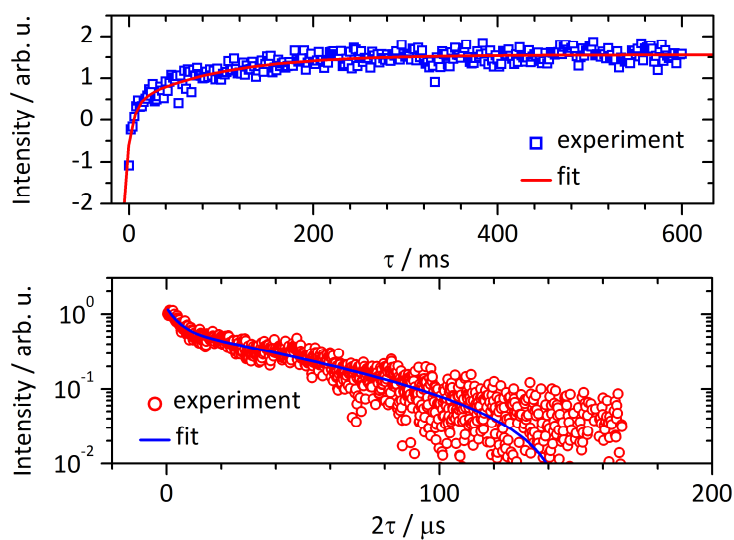
Supplementary Figure 47: ESE-detected EPR spectra of $\text{Cu-Smnt}^{P/d}_{0.01\%}$ at Q-band (34.994 GHz, Stuttgart) and 7 K. Blue, solid line represents experimental data. Red, dotted line indicates simulation. The asterisk marks magnetic field position for spin dynamics measurements.



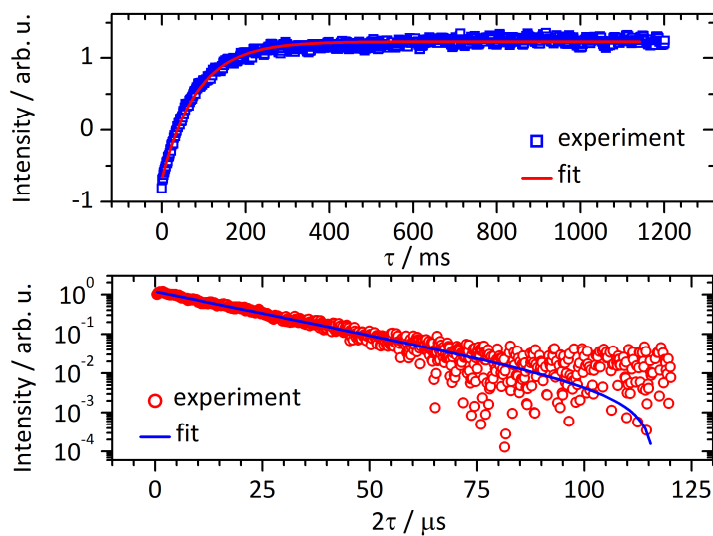
Supplementary Figure 48: ESE-detected EPR spectra of $\text{Cu-Smnt}^{P/d}_{0.01\%}$ at Q-band (35.001 GHz, Stuttgart) and 50 K. Blue, solid line represents experimental data. Red, dotted line indicates simulation. The asterisk marks magnetic field position for spin dynamics measurements.



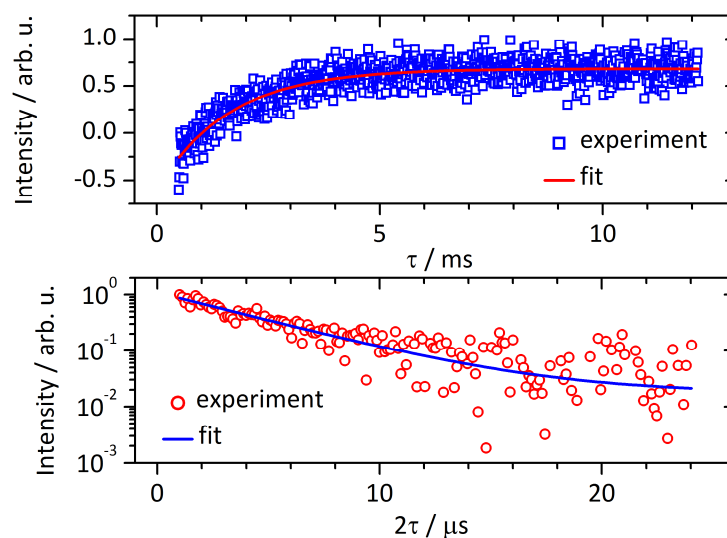
Supplementary Figure 49: ESE-detected EPR spectra of $\text{Cu-Smnt}^{\text{P/d}}_{0.01\%}$ at Q-band (35.001 GHz, Stuttgart) and 150 K. Blue, solid line represents experimental data. Red, dotted line indicates simulation. The asterisk marks magnetic field position for spin dynamics measurements.



Supplementary Figure 50: Electron spin relaxation measurements and fits of $\text{Cu-Smnt}^{\text{P/d}}_{0.01\%}$ at Q-band (35.000 GHz, Stuttgart) and 7 K. Top panel: Inversion recovery experiment. Blue, open squares indicate experimental data and red, solid line represents fit function. Bottom panel: Hahn echo experiment. Red, open circles indicate experimental data and blue, solid line represents fit function.

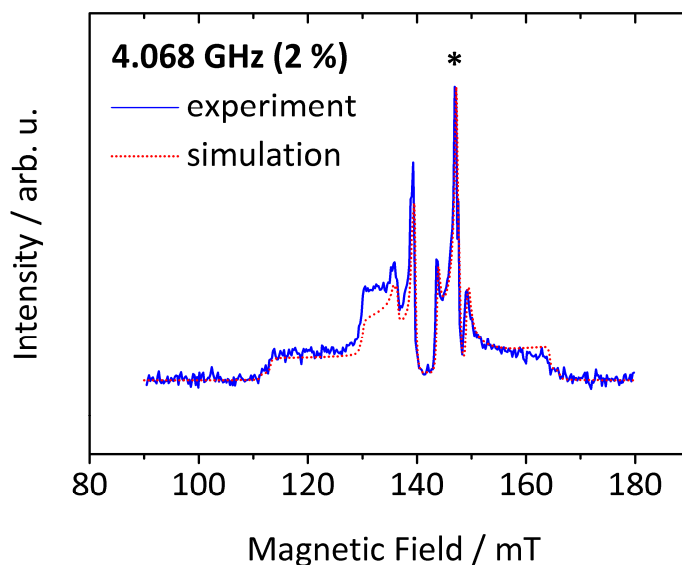


Supplementary Figure 51: Electron spin relaxation measurements and fits of $\text{Cu-Smnt}^{P/d}_{0.01\%}$ at Q-band (35.000 GHz, Stuttgart) and 50 K. Top panel: Inversion recovery experiment. Blue, open squares indicate experimental data and red, solid line represents fit function. Bottom panel: Hahn echo experiment. Red, open circles indicate experimental data and blue, solid line represents fit function.

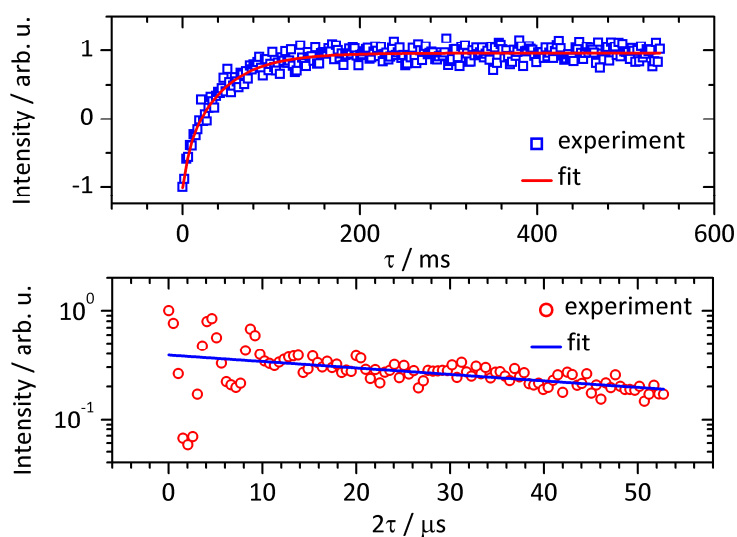


Supplementary Figure 52: Electron spin relaxation measurements and fits of $\text{Cu-Smnt}^{P/d}_{0.01\%}$ at Q-band (35.000 GHz, Stuttgart) and 150 K. Top panel: Inversion recovery experiment. Blue, open squares indicate experimental data and red, solid line represents fit function. Bottom panel: Hahn echo experiment. Red, open circles indicate experimental data and blue, solid line represents fit function.

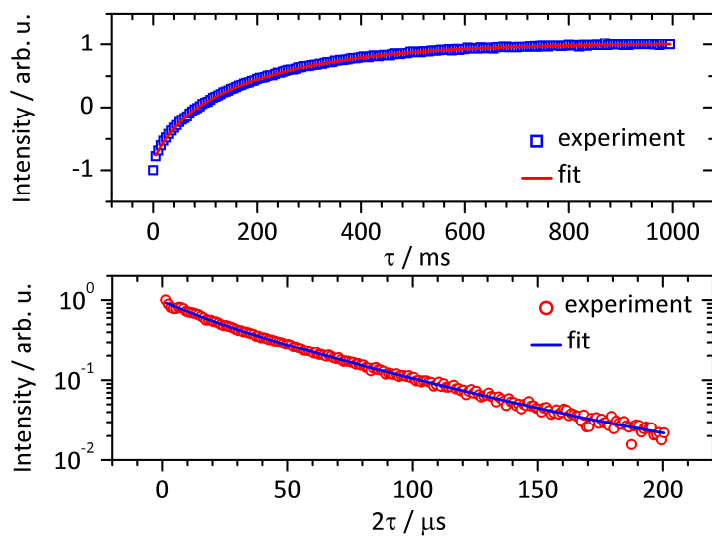
6.6 Supplementary Information to Frequency Dependence of Spin Dynamics



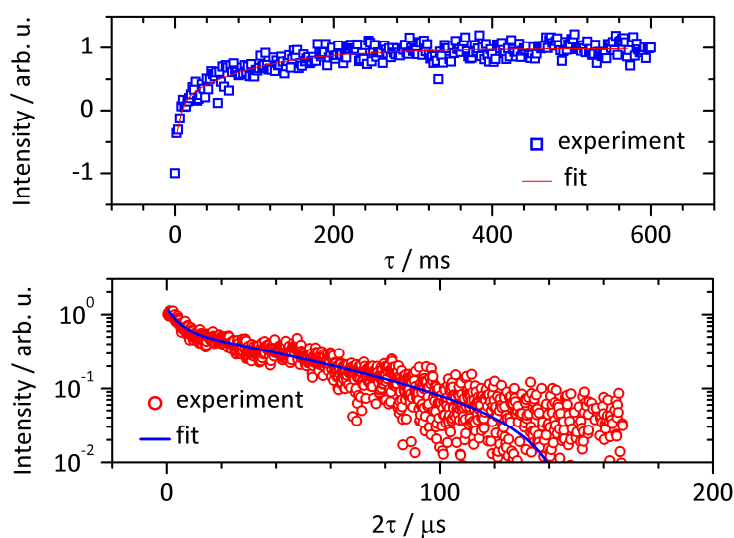
Supplementary Figure 53: ESE-detected EPR spectra of $\text{Cu-Smnt}^{P/d_{2\%}}$ at S-band (4.068 GHz) and 7 K. Blue, solid line represents experimental data. Red, dotted line indicates simulation. The asterisk marks magnetic field position for spin dynamics measurements.



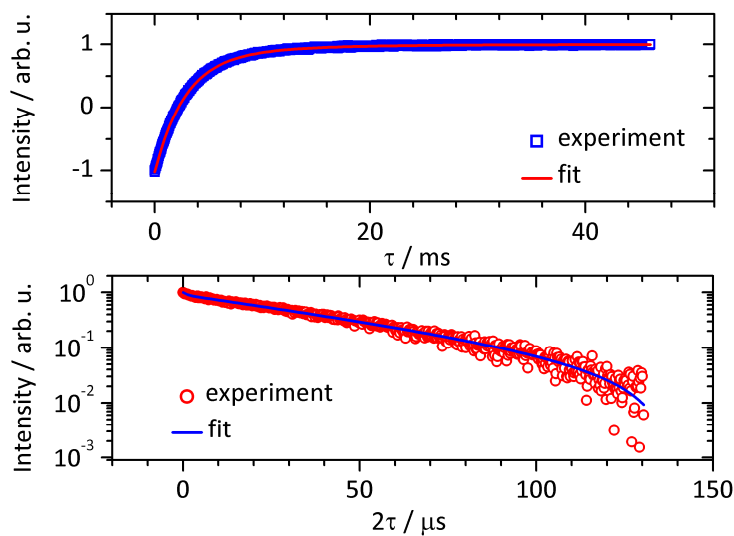
Supplementary Figure 54: Electron spin relaxation measurements and fits of $\text{Cu-Smnt}^{P/d_{0.01\%}}$ at S-band (3.700 GHz) and 7 K. Top panel: Inversion recovery experiment. Blue, open squares indicate experimental data and red, solid line represents fit function. Bottom panel: Hahn echo experiment. Red, open circles indicate experimental data and blue, solid line represents fit function.



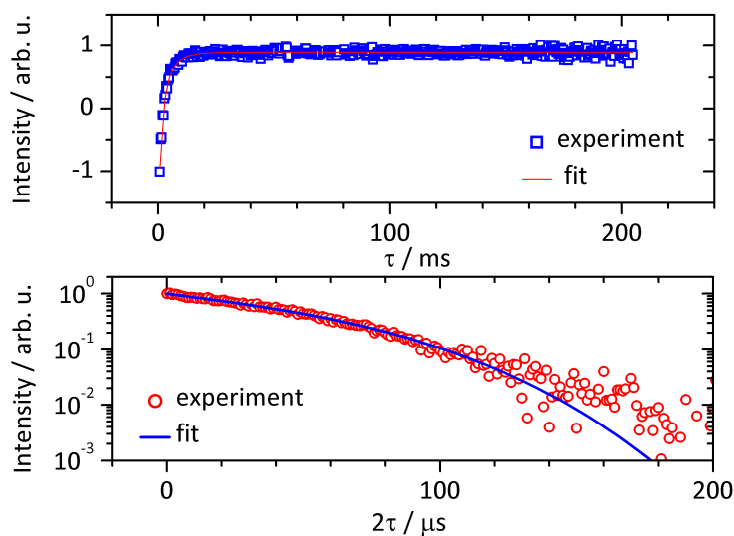
Supplementary Figure 55: Electron spin relaxation measurements and fits of $\text{Cu-Smnt}^{P/4}_{0.01\%}$ at X-band (9.563 GHz) and 7 K. Top panel: Inversion recovery experiment. Blue, open squares indicate experimental data and red, solid line represents fit function. Bottom panel: Hahn echo experiment. Red, open circles indicate experimental data and blue, solid line represents fit function.



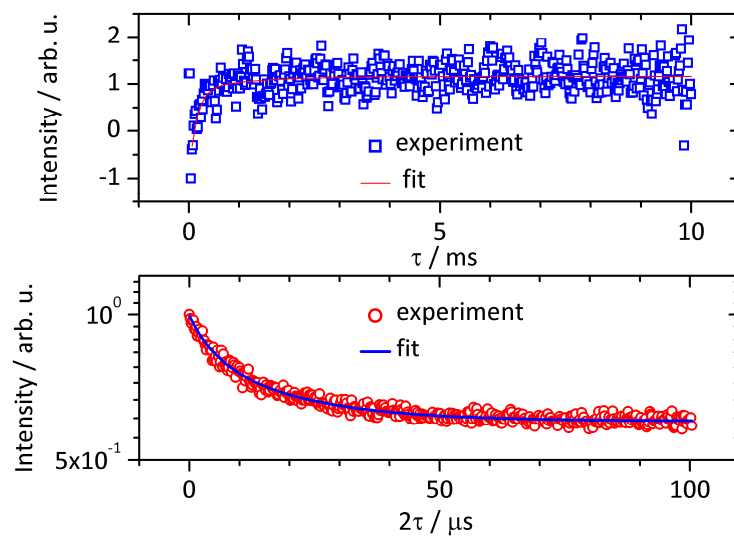
Supplementary Figure 56: Electron spin relaxation measurements and fits of $\text{Cu-Smnt}^{P/4}_{0.01\%}$ at Q-band (35.000 GHz) and 7 K. Top panel: Inversion recovery experiment. Blue, open squares indicate experimental data and red, solid line represents fit function. Bottom panel: Hahn echo experiment. Red, open circles indicate experimental data and blue, solid line represents fit function.



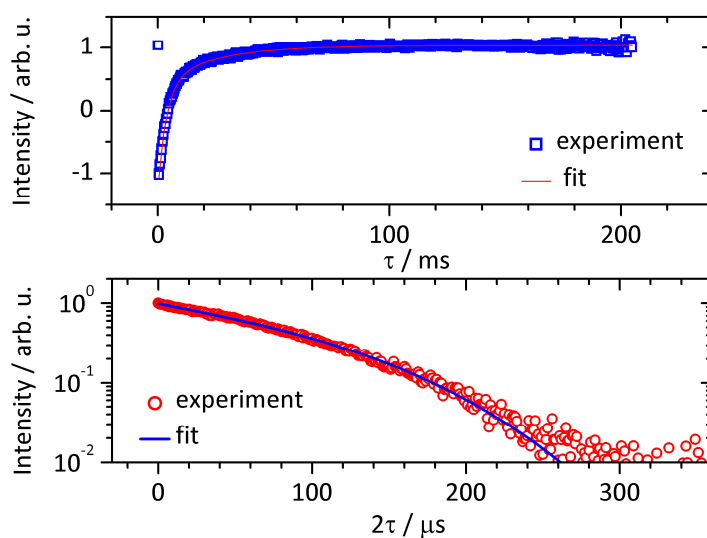
Supplementary Figure 57: Electron spin relaxation measurements and fits of $\text{Cu-Smnt}^{\text{P/d}}_{0.01\%}$ at W-band (94.021 GHz) and 7 K. Top panel: Inversion recovery experiment. Blue, open squares indicate experimental data and red, solid line represents fit function. Bottom panel: Hahn echo experiment. Red, open circles indicate experimental data and blue, solid line represents fit function.



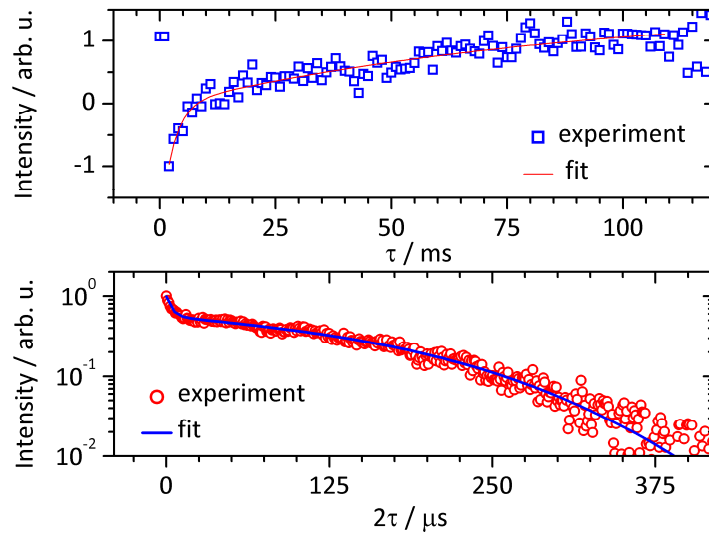
Supplementary Figure 58: Electron spin relaxation measurements and fits of $\text{Cu-Smnt}^{\text{P/d}}_{0.01\%}$ at F-band (120 GHz) and 7 K. Top panel: Inversion recovery experiment. Blue, open squares indicate experimental data and red, solid line represents fit function. Bottom panel: Hahn echo experiment. Red, open circles indicate experimental data and blue, solid line represents fit function.



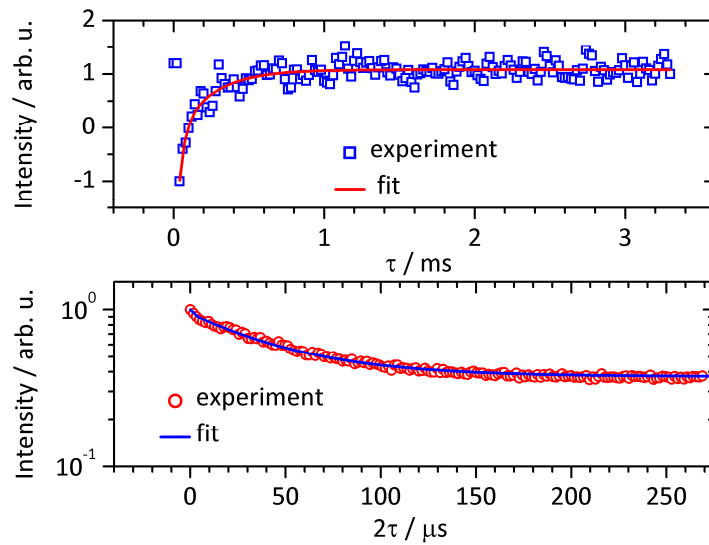
Supplementary Figure 59: Electron spin relaxation measurements and fits of $\text{Cu-Smnt}^{\text{P/4}}_{0.01\%}$ at Y-band (240 GHz) and 7 K. Top panel: Inversion recovery experiment. Blue, open squares indicate experimental data and red, solid line represents fit function. Bottom panel: Hahn echo experiment. Red, open circles indicate experimental data and blue, solid line represents fit function.



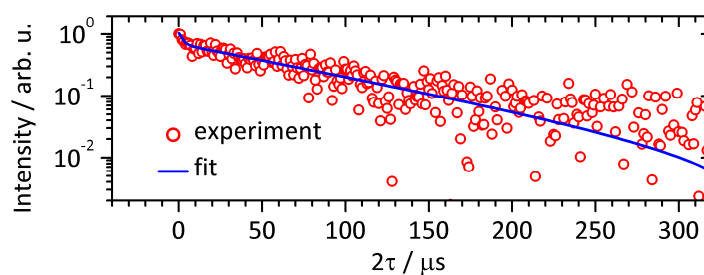
Supplementary Figure 60: Electron spin relaxation measurements and fits of $\text{Cu-Smnt}^{\text{P/4}}_{0.01\%}$ at F-band (120 GHz) and 3 K. Top panel: Inversion recovery experiment. Blue, open squares indicate experimental data and red, solid line represents fit function. Bottom panel: Hahn echo experiment. Red, open circles indicate experimental data and blue, solid line represents fit function.



Supplementary Figure 61: Electron spin relaxation measurements and fits of $\text{Cu-Smnt}^{\text{P}/4}_{0.01\%}$ at F-band (120 GHz) and 1.5 K. Top panel: Inversion recovery experiment. Blue, open squares indicate experimental data and red, solid line represents fit function. Bottom panel: Hahn echo experiment. Red, open circles indicate experimental data and blue, solid line represents fit function.

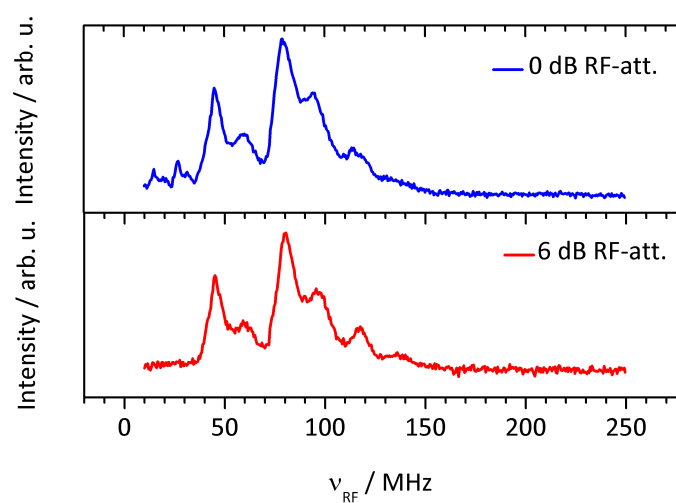


Supplementary Figure 62: Electron spin relaxation measurements and fits of $\text{Cu-Smnt}^{\text{P}/4}_{0.01\%}$ at Y-band (240 GHz) and 3 K. Top panel: Inversion recovery experiment. Blue, open squares indicate experimental data and red, solid line represents fit function. Bottom panel: Hahn echo experiment. Red, open circles indicate experimental data and blue, solid line represents fit function.



Supplementary Figure 63: Electron spin relaxation measurements and fits of $\text{Cu-Smnt}^{\text{P/d}_{0.01\%}}$ at Y-band (240 GHz) and 1.5 K: Hahn echo experiment. Red, open circles indicate experimental data and blue, solid line represents fit function. Due to temperature stabilization problems, the S/N was very low and no useful inversion recovery experiment was recorded.

6.7 Supplementary Information to Couplings to Nuclear Spins



Supplementary Figure 64: Davies-ENDOR for $\text{Cu-Smnt}^{\text{P/d}_{10\%}}$ at Q-band (34.067 GHz), 15 K and 1211.3 mT at two different RF-power levels (0 dB RF-attenuation, top panel: solid, blue line; 6 dB RF-attenuation, bottom panel: solid, red line).

7 References

- [1] G. R. Eaton, S. S. Eaton, *J. Magn. Reson.* **1999**, *136*, 63-68.
- [2] J. M. Zadrozny, J. Niklas, O. G. Poluektov, D. E. Freedman, *ACS Cent. Sci.* **2015**, *1*, 488-492.
- [3] S. S. Eaton, G. R. Eaton, in *Distance Measurements in Biological Systems by EPR*, Ch. 2, Biological Magnetic Resonance, *Vol. 19* (Eds.: L. Berliner, G. Eaton, S. Eaton), Springer US, **2002**.
- [4] J. van Slageren, *Top. Curr. Chem.* **2012**, *321*, 199-234.
- [5] M. Atzori, L. Tesi, E. Morra, M. Chiesa, L. Sorace, R. Sessoli, *J. Am. Chem. Soc.* **2016**, *138*, 2154-2157.
- [6] M. Atzori, E. Morra, L. Tesi, A. Albino, M. Chiesa, L. Sorace, R. Sessoli, *J. Am. Chem. Soc.* **2016**, *138*, 11234-11244.
- [7] A. Ferretti, M. Fanciulli, A. Ponti, A. Schweiger, *Phys. Rev. B* **2005**, *72*, 235201.
- [8] C. Bonizzoni, A. Ghirri, K. Bader, J. van Slageren, M. Perfetti, L. Sorace, Y. Lan, O. Fuhr, M. Ruben, M. Affronte, *Dalton Trans.* **2016**.
- [9] L. Escalera Moreno, N. Suaud, A. Gaita Ariño, *arXiv:1512.05690 [cond-mat.mes-hall]* **2015**.
- [10] M. A. Nielsen, I. L. Chuang, *Quantum Computation and Quantum Information: 10th Anniversary Edition*, Cambridge University Press, **2010**.
- [11] L. Grover, *Pramana - J. Phys.* **2001**, *56*, 333-348.
- [12] P. W. Shor, *SIAM J. Sci. Statist. Comput.* **1997**, *26*.

-
- [13] D. P. DiVincenzo, *Fortschr. Phys.* **2000**, *48*, 771-783.
- [14] J. I. Cirac, P. Zoller, *Phys. Rev. Lett.* **1995**, *74*, 4091-4094.
- [15] J. Clarke, F. K. Wilhelm, *Nature* **2008**, *453*, 1031-1042.
- [16] D. Loss, D. P. DiVincenzo, *Phys. Rev. A* **1998**, *57*, 120-126.
- [17] G. Aromí, D. Aguilà, P. Gamez, F. Luis, O. Roubeau, *Chem. Soc. Rev.* **2012**, *41*, 537-546.
- [18] G. Balasubramanian, P. Neumann, D. Twitchen, M. Markham, R. Kolesov, N. Mizuochi, J. Isoya, J. Achard, J. Beck, J. Tissler, V. Jacques, P. R. Hemmer, F. Jelezko, J. Wrachtrup, *Nat. Mater.* **2009**, *8*, 383-387.
- [19] A. M. Tyryshkin, S. A. Lyon, A. V. Astashkin, A. M. Raitsimring, *Phys. Rev. B* **2003**, *68*, 193207.
- [20] S. Bertaina, S. Gambarelli, A. Tkachuk, I. N. Kurkin, B. Malkin, A. Stepanov, B. Barbara, *Nat. Nano.* **2007**, *2*, 39-42.
- [21] M. Warner, S. Din, I. S. Tupitsyn, G. W. Morley, A. M. Stoneham, J. A. Gardener, Z. Wu, A. J. Fisher, S. Heutz, C. W. M. Kay, G. Aeppli, *Nature* **2013**, *503*, 504-508.
- [22] L. Tesi, E. Lucaccini, I. Cimatti, M. Perfetti, M. Mannini, A. Matteo, E. Morra, M. Chiesa, A. Caneschi, L. Sorace, R. Sessoli, *Chem. Sci.* **2016**, *7*, 2074-2083.
- [23] A. Schweiger, G. Jeschke, *Principles of pulse electron paramagnetic resonance*, Oxford Univ. Press, Oxford, **2005**.
- [24] J.-L. Du, G. R. Eaton, S. S. Eaton, *J. Magn. Reson., Ser. A* **1996**, *119*, 240-246.
- [25] Y. Zhou, B. E. Bowler, G. R. Eaton, S. S. Eaton, *J. Magn. Reson.* **1999**, *139*, 165-174.
- [26] A. J. Fielding, S. Fox, G. L. Millhauser, M. Chattopadhyay, P. M. H. Kroneck, G. Fritz, G. R. Eaton, S. S. Eaton, *J. Magn. Reson.* **2006**, *179*, 92-104.

- [27] J. L. Du, G. R. Eaton, S. S. Eaton, *Appl. Magn. Reson.* **1994**, *6*, 373-378.
- [28] A. Ardavan, O. Rival, J. J. L. Morton, S. J. Blundell, A. M. Tyryshkin, G. A. Timco, R. E. P. Winpenny, *Phys. Rev. Lett.* **2007**, *98*, 057201.
- [29] C. Schlegel, J. van Slageren, M. Manoli, E. K. Brechin, M. Dressel, *Phys. Rev. Lett.* **2008**, *101*, 147203.
- [30] C. J. Wedge, G. A. Timco, E. T. Spielberg, R. E. George, F. Tuna, S. Rigby, E. J. L. McInnes, R. E. P. Winpenny, S. J. Blundell, A. Ardavan, *Phys. Rev. Lett.* **2012**, *108*, 107204.
- [31] R. Husted, J.-L. Du, G. R. Eaton, S. S. Eaton, *Magn. Reson. Chem.* **1995**, *33*, S66-S69.
- [32] K. S. Pedersen, A.-M. Ariciu, S. McAdams, H. Weihe, J. Bendix, F. Tuna, S. Piligkos, *J. Am. Chem. Soc.* **2016**, *138*, 5801-5804.
- [33] J. van Slageren, *Vorlesungsskript zu Physikalische Chemie V: Electron Spin Resonance Spectroscopy*, Universität Stuttgart, **2012**.
- [34] N. M. Atherton, *Principles of Electron Spin Resonance*, Ellis Horwood Limited, Chichester, West Sussex, **1993**.
- [35] M. H. Levitt, *Spin dynamics : basics of nuclear magnetic resonance*, Wiley, Chichester, **2002**.
- [36] L. Kevan, R. N. Schwartz, in *Time domain electron spin resonance*, Wiley, New York, **1979**.
- [37] C. Kittel, *Introduction to solid state physics*, 8. ed., Wiley, New York, **2005**.
- [38] A. Abragam, B. Bleaney, *Electron paramagnetic resonance of transition ions*, Oxford Univ. Press, Oxford, **2012**.

-
- [39] S. K. Misra, *Multifrequency Electron Paramagnetic Resonance*, Wiley-VCH, Weinheim, **2011**.
- [40] E. Samuel, D. Caurant, D. Gourier, C. Elschenbroich, K. Agbaria, *J. Am. Chem. Soc.* **1998**, *120*, 8088-8092.
- [41] H. Dilger, *Skript zum Physikalisch-Chemischen Praktikum PCII*, Institut für Physikalische Chemie, Universität Stuttgart, **2013**.
- [42] A. D. Milov, K. M. Salikhov, Y. D. Tsvetkov, *Zh. Eksp. Teor. Fiz.* **1972**, *63*, 2329-2335.
- [43] W. B. Mims, *Phys. Rev.* **1968**, *168*, 370-389.
- [44] W. B. Mims, K. Nassau, J. D. McGee, *Phys. Rev.* **1961**, *123*, 2059-2069.
- [45] J. R. Klauder, P. W. Anderson, *Phys. Rev.* **1962**, *125*, 912-932.
- [46] P. F. Liao, P. Hu, R. Leigh, S. R. Hartmann, *Phys. Rev. A* **1974**, *9*, 332-340.
- [47] A. D. Milov, K. Salikhov, Y. Tsvetkov, *Fiz. Tverd. Tela (Leningrad)* **1972**, *14*, 2259-2264.
- [48] S. K. Hoffmann, W. Hilczler, J. Goslar, *J. Magn. Reson., Ser. A* **1996**, *122*, 37-41.
- [49] P. T. Manoharan, J. S. Annie, S. Pfenninger, *Proc. Indian Acad. Sci., Chem. Sci.* **1994**, *106*, 1691-1705.
- [50] R. Kirmse, B. V. Solovev, B. G. Tarasov, *Ann. Phys.* **1974**, *486*, 352-360.
- [51] Z. M. Tomilo, *J. Engineering Phys.* **1986**, *51*, 962-964.
- [52] C. Kutter, H. P. Moll, J. van Tol, H. Zuckermann, J. C. Maan, P. Wyder, *Phys. Rev. Lett.* **1995**, *74*, 2925-2928.
- [53] S. Takahashi, R. Hanson, J. van Tol, M. S. Sherwin, D. D. Awschalom, *Phys. Rev. Lett.* **2008**, *101*, 047601.
- [54] R. de Sousa, S. Das Sarma, *Phys. Rev. B* **2003**, *68*, 115322.

- [55] R. Konda, J.-L. Du, S. S. Eaton, G. R. Eaton, *Appl. Magn. Reson.* **1994**, *7*, 185-193.
- [56] M. J. Graham, J. M. Zadrozny, M. Shiddiq, J. S. Anderson, M. S. Fataftah, S. Hill, D. E. Freedman, *J. Am. Chem. Soc.* **2014**, *136*, 7623-7626.
- [57] D. Kaminski, A. L. Webber, C. J. Wedge, J. Liu, G. A. Timco, I. J. Vitorica-Yrezabal, E. J. L. McInnes, R. E. P. Winpenny, A. Ardavan, *Phys. Rev. B* **2014**, *90*, 184419.
- [58] I. Tkach, A. Baldansuren, E. Kalabukhova, S. Lukin, A. Sitnikov, A. Tsvir, M. Ischenko, Y. Rosentzweig, E. Roduner, *Appl. Magn. Reson.* **2008**, *35*, 95-112.
- [59] S. Takahashi, J. van Tol, C. C. Beedle, D. N. Hendrickson, L.-C. Brunel, M. S. Sherwin, *Phys. Rev. Lett.* **2009**, *102*, 087603.
- [60] J. J. L. Morton, A. M. Tyryshkin, R. M. Brown, S. Shankar, B. W. Lovett, A. Ardavan, T. Schenkel, E. E. Haller, J. W. Ager, S. A. Lyon, *Nature* **2008**, *455*, 1085-1088.
- [61] C. M. Lieberman, A. S. Filatov, Z. Wei, A. Y. Rogachev, A. M. Abakumov, E. V. Dikarev, *Chem. Sci.* **2015**, *6*, 2835-2842.
- [62] V. V. Skopenko, V. M. Amirkhanov, T. Y. Sliva, I. S. Vasilchenko, E. L. Anpilova, A. D. Garnovskii, *Russ. Chem. Rev.* **2004**, *73*, 737-752.
- [63] A. W. Maverick, F. R. Fronczek, E. F. Maverick, D. R. Billodeaux, Z. T. Cygan, R. A. Isovitsch, *Inorg. Chem.* **2002**, *41*, 6488-6492.
- [64] I. Adato, I. Eliezer, *J. Chem. Phys.* **1971**, *54*, 1472-1476.
- [65] D. A. Johnson, A. B. Waugh, *Polyhedron* **1983**, *2*, 1323-1328.
- [66] M. L. Morris, R. W. Moshier, R. E. Sievers, *Inorg. Chem.* **1963**, *2*, 411-412.
- [67] A. J. Fielding, D. B. Back, M. Engler, B. Baruah, D. C. Crans, G. R. Eaton, S. S. Eaton, in *Vanadium: The Versatile Metal*, Ch. 26, ACS Symposium Series, Vol. 974, American Chemical Society, **2007**.

-
- [68] A. N. A. Zecevic, G. R. Eaton, S. S. Eaton, M. Lindgren, *Mol. Phys.* **1998**, *95*, 1255-1263.
- [69] K. Bader, D. Dengler, S. Lenz, B. Endeward, S.-D. Jiang, P. Neugebauer, J. van Slageren, *Nat. Commun.* **2014**, *5*, 5304.
- [70] K. Bader, M. Winkler, J. van Slageren, *Chem. Commun.* **2016**, *52*, 3623-3626.
- [71] S. Antosik, N. M. D. Brown, A. A. McConnell, A. L. Porte, *J. Chem. Soc.* **1969**, 545-550.
- [72] M. Conrad, *Eine Untersuchung von Kupfer(II)-acetylacetonat-Komplexen mittels ESR-Spektroskopie*, B.Sc. Thesis, Universität Stuttgart, **2014**.
- [73] M. Tran, *Synthese und Untersuchung von Vanadylacetylacetonatkomplexen*, B.Sc. Thesis, Universität Stuttgart, **2014**.
- [74] S. Lenz, *Influences on Electron Spin Relaxation in Mononuclear Transition Metal β -Diketonate Complexes*, M.Sc. Thesis, Universität Stuttgart, **2015**.
- [75] R. Linn Belford, A. E. Martell, M. Calvin, *J. Inorg. Nuc. Chem.* **1956**, *2*, 11-31.
- [76] S. Okeya, O. Shunichiro, K. Matsumoto, Y. Nakamura, S. Kawaguchi, *Bull. Chem. Soc. Jpn.* **1981**, *54*, 1085-1095.
- [77] B.-Q. Ma, S. Gao, Z.-M. Wang, C.-S. Liao, C.-H. Yan, G.-X. Xu, *J. Chem. Crystallogr.* **1999**, *29*, 793-796.
- [78] E. A. Shugam, L. M. Shkol'nikova, A. N. Knyazeva, *J. Struct. Chem.* **1968**, *9*, 166-170.
- [79] P.-K. Hon, C. E. Pfluger, R. L. Belford, *Inorg. Chem.* **1966**, *5*, 516-521.
- [80] S. Stoll, A. Schweiger, *J. Magn. Reson.* **2006**, *178*, 42-55.
- [81] H. A. Kuska, M. T. Rogers, *J. Chem. Phys.* **1965**, *43*, 1744-1747.
- [82] A. Von Zelewsky, H. Fierz, *Inorg. Chem.* **1971**, *10*, 1556-1557.
- [83] M. Chikira, H. Yokoi, *J. Chem. Soc., Dalton Trans.* **1977**, 2344-2348.

-
- [84] A. v. Zelewsky, H. Fierz, *Inorg. Chem.* **1971**, *10*, 1556–1557.
- [85] K. Kadish, R. Guilard, K. M. Smith, in *The Porphyrin Handbook: Volume 17*, Ch., Academic Press, San Diego, Calif., **2003**.
- [86] K. Kadish, R. Guilard, K. M. Smith, in *The Porphyrin Handbook: Volume 16*, Ch., Academic Press, San Diego, Calif., **2003**.
- [87] K. J. Standley, J. K. Wright, *Proc. Phys. Soc.* **1964**, *83*, 361.
- [88] J. M. Assour, J. Goldmacher, S. E. Harrison, *J. Chem. Phys.* **1965**, *43*, 159-165.
- [89] C. Finazzo, C. Calle, S. Stoll, S. van Doorslaer, A. Schweiger, *Phys. Chem. Chem. Phys.* **2006**, *8*, 1942-1953.
- [90] M. Winkler, *Dekohärenz in Übergangsmetall-Phthalocyaninen*, Universität Stuttgart, B.Sc. Thesis, **2015**.
- [91] H. Miyoshi, H. Ohya-Nishiguchi, Y. Deguchi, *Bull. Chem. Soc. Jpn.* **1973**, *46*, 2724-2728.
- [92] H. Miyoshi, *Bull. Chem. Soc. Jpn.* **1974**, *47*, 561-565.
- [93] M.-S. Liao, S. Scheiner, *J. Chem. Phys.* **2001**, *114*, 9780-9791.
- [94] N. Marom, L. Kronik, *Appl. Phys. A* **2009**, *95*, 165-172.
- [95] Y. Zhang, T. Learmonth, S. Wang, A. Y. Matsuura, J. Downes, L. Plucinski, S. Bernardis, C. O'Donnell, K. E. Smith, *J. Mater. Chem.* **2007**, *17*, 1276-1283.
- [96] E. I. Stiefel, K. D. Karlin, *Dithiolene Chemistry (Progress in Inorganic Chemistry)*, John Wiley & Sons, Inc., **2004**.
- [97] N. Robertson, L. Cronin, *Coord. Chem. Rev.* **2002**, *227*, 93-127.
- [98] K. Wang, in *Dithiolene Chemistry*, Ch. 5, Progress in Inorganic Chemistry, Vol. 52 (Ed.: E. I. Stiefel), John Wiley & Sons, Inc., New Jersey, **2004**.

-
- [99] M. L. Kirk, R. L. McNaughton, M. E. Helton, in *Dithiolene Chemistry*, John Wiley & Sons, Inc., **2004**.
- [100] M. L. Kirk, R. L. McNaughton, M. E. Helton, in *Dithiolene Chemistry: Synthesis, Properties, and Applications*, Ch. 52 (Ed.: E. I. Stiefel), John Wiley & Sons, Inc., Hoboken, New Jersey, **2004**.
- [101] J. E. Huyett, S. B. Choudhury, D. M. Eichhorn, P. A. Bryngelson, M. J. Maroney, B. M. Hoffman, *Inorg. Chem.* **1998**, *37*, 1361-1367.
- [102] M. Stein, *Chem. Eur. J.* **2011**, *17*, 15046-15048.
- [103] N. Robertson, L. Cronin, *Coord. Chem. Rev.* **2002**, *227*, 93-127.
- [104] G. R. Lewis, I. Dance, *J. Chem. Soc., Dalton Trans.* **2000**, *18*, 3176-3185.
- [105] L. Horner, G. Mumenthey, H. Moser, P. Beck, *Chem. Ber.* **1966**, *99*, 2782-2788.
- [106] J. Chatt, F. G. Mann, *J. Chem. Soc.* **1940**, 1192-1196.
- [107] W.-H. Ning, L. Zhai, J.-L. Liu, X.-M. Ren, K. Ichihashi, S. Nishihara, K. Inoue, *J. Mater. Chem. C* **2015**, *3*, 7906-7915.
- [108] R. G. Pearson, D. A. Sweigart, *Inorg. Chem.* **1970**, *9*, 1167-1175.
- [109] B. Wenzel, B. Wehse, U. Schilde, P. Strauch, *Z. Anorg. Allg. Chem.* **2004**, *630*, 1469-1476.
- [110] T. Imamura, M. Ryan, G. G. Gordon, D. Coucouvanis, *J. Am. Chem. Soc.* **1984**, *106*, 984-990.
- [111] S. Lenz, *Quantenköhärenz in einkernigen Kupfer-Komplexen*, B.Sc. Thesis, Universität Stuttgart, **2013**.
- [112] R. Kirmse, J. Stach, W. Dietzsch, G. Steimecke, E. Hoyer, *Inorg. Chem.* **1980**, *19*, 2679-2685.

- [113] S. H. Schlindwein, K. Bader, C. Sibold, W. Frey, P. Neugebauer, M. Orlita, J. van Slageren, D. Gudat, *Inorg. Chem.* **2016**, *55*, 6186-6194.
- [114] R. Kirmse, W. Dietzsch, E. Hoyer, *Z. Anorg. Allg. Chem.* **1973**, *397*, 198-208.
- [115] P. F. Taylor, R. A. Vaughan, *J. Phys. C: Solid. St. Phys.* **1970**, *3*, 579.
- [116] S. K. Hoffmann, J. Goslar, S. Lijewski, A. Zalewska, *J. Magn. Reson.* **2013**, *236*, 7-14.
- [117] L. K. White, R. L. Belford, *J. Am. Chem. Soc.* **1976**, *98*, 4428-4438.
- [118] J. Peisach, W. E. Blumberg, *Arch. Biochem. Biophys.* **1974**, *165*, 691-708.
- [119] A. L. P. Román, J. M. Gutiérrez-Zorrilla, J. I. Beitia, M. Martínez-Ripoll, in *Z. Kristallogr., Vol. 198*, **1992**, p. 213.
- [120] M. K. Johnson, in *Dithiolene Chemistry: Synthesis, Properties, and Applications*, Ch. Progress in Inorganic Chemistry, *Vol. 52* (Ed.: E. I. Stiefel), John Wiley & Sons, Inc., Hoboken, New Jersey, **2004**.
- [121] R. Owenius, G. E. Terry, M. J. Williams, S. S. Eaton, G. R. Eaton, *J. Phys. Chem. B* **2004**, *108*, 9475-9481.
- [122] P. T. Manoharan, *Proc. Indian Natl. Sci. Acad., Part A* **1986**, *52*, 715-735.
- [123] G. R. Lewis, I. Dance, *Dalton Trans.* **2000**, 3176-3185.
- [124] L. Golic, W. Dietzsch, R. Kirmse, *Vestn. Slov. Kem. Drus.* **1987**, *34*, 401-410.
- [125] P. I. Clemenson, A. E. Underhill, M. B. Hursthouse, R. L. Short, *Dalton Trans.* **1988**, 1689-1691.
- [126] P. I. Clemenson, A. Underhill, A. Kobayashi, H. Kobayashi, *Polyhedron* **1990**, *9*, 2053-2059.

-
- [127] M. B. Hursthouse, R. L. Short, P. I. Clemenson, A. E. Underhill, *Dalton Trans.* **1989**, 67-71.
- [128] A. E. Underhill, P. I. Clemenson, *Phys. B+C* **1986**, *143*, 316-320.
- [129] A. E. Underhill, P. I. Clemenson, M. B. Hursthouse, R. L. Short, G. J. Ashwell, I. M. Sandy, K. Carneiro, *Synth. Met.* **1987**, *19*, 953-958.
- [130] A. Chapman, R. Cammack, C. E. Hatchikian, J. McCracken, J. Peisach, *FEBS Lett.* **1988**, *242*, 134-138.
- [131] B. Guigliarelli, C. More, A. Fournel, M. Asso, E. C. Hatchikian, R. Williams, R. Cammack, P. Bertrand, *Biochemistry* **1995**, *34*, 4781-4790.
- [132] M. Saggiu, C. Teutloff, M. Ludwig, M. Brecht, M.-E. Pandelia, O. Lenz, B. Friedrich, W. Lubitz, P. Hildebrandt, F. Lenzian, R. Bittl, *Phys. Chem. Chem. Phys.* **2010**, *12*, 2139-2148.
- [133] A. H. Maki, N. Edelstein, A. Davison, R. H. Holm, *J. Am. Chem. Soc.* **1964**, *86*, 4580-4587.
- [134] N. V. Vugman, M. B. de Araújo, N. M. Pinhal, C. J. Magon, A. J. d. C. Filho, *J. Magn. Reson.* **2004**, *168*, 132-136.
- [135] E. Billig, R. Williams, I. Bernal, J. H. Waters, H. B. Gray, *Inorg. Chem.* **1964**, *3*, 663-666.
- [136] R. Kirmse, W. Dietzsch, J. Stach, R. M. Olk, E. Hoyer, *Z. Anorg. Allg. Chem.* **1987**, *548*, 133-140.
- [137] R. Kirmse, P. Strauch, *Z. Anorg. Allg. Chem.* **1991**, *600*, 61-66.
- [138] R. Kirmse, J. Stach, U. Abram, W. Dietzsch, R. Boettcher, M. C. M. Gribnau, C. P. Keijzers, *Inorg. Chem.* **1984**, *23*, 3333-3338.
- [139] R. Kirmse, J. Stach, W. Dietzsch, E. Hoyer, *Inorg. Chim. Acta* **1978**, *26*, L53-L55.

- [140] J. Stach, R. Böttcher, R. Kirmse, *Z. Chem.* **1985**, *25*, 1-13.
- [141] S. K. Hoffmann, J. Goslar, *Appl. Magn. Reson.* **1998**, *14*, 293-303.
- [142] K. J. Standley, P. F. Taylor, *J. Phys. C: Solid. St. Phys.* **1968**, *1*, 551.
- [143] P. Kuppusamy, P. T. Manoharan, *Inorg. Chem.* **1985**, *24*, 3053-3057.
- [144] S. S. Eaton, J. Harbridge, G. A. Rinard, G. R. Eaton, R. T. Weber, *Appl. Magn. Reson.* **2001**, *20*, 151-157.
- [145] A. Schweiger, G. Jeschke, *Principles of pulse electron paramagnetic resonance*, Oxford University Press, Oxford, UK; New York, **2001**.
- [146] I. Gromov, J. Shane, J. Forrer, R. Rakhmatoullin, Y. Rozentzwaig, A. Schweiger, *J. Magn. Reson.* **2001**, *149*, 196-203.
- [147] K. D. Jahnke, B. Naydenov, T. Teraji, S. Koizumi, T. Umeda, J. Isoya, F. Jelezko, *Appl. Phys. Lett.* **2012**, *101*, 012405.
- [148] J. J. L. Morton, A. M. Tyryshkin, A. Ardavan, K. Porfyraakis, S. A. Lyon, G. Andrew D. Briggs, *J. Chem. Phys.* **2006**, *124*, 014508.
- [149] D. Dengler, *ESR-Untersuchungen an molekularen Ein- und Zwei-Quantenbit-Systemen*, University of Stuttgart, Ph.D. Thesis, **2016**.
- [150] M. Willer, J. Forrer, J. Keller, S. van Doorslaer, A. Schweiger, R. Schuhmann, T. Weiland, *Rev. Sci. Instrum.* **2000**, *71*, 2807-2817.
- [151] J. van Tol, L.-C. Brunel, R. J. Wylde, *Rev. Sci. Instrum.* **2005**, *76*, 074101.

8 Acknowledgements

First of all, I would like to thank my supervisor Prof. Dr. Joris van Slageren for providing me such a thrilling and diverse project. I'm very thankful for all the support over the last years, especially with respect to the individual mentoring and the various possibilities to travel in order to learn new methods and discuss science with interesting people. Also I want to thank the whole workgroup for the great time in- and outside the lab and office. Special thanks here to Dr. Dominik Dengler and Samuel Lenz for countless and invaluable hours with the EPR spectrometers. Thanks to my former B.Sc.- and M.Sc.-students for their contributions to my work: Samuel Lenz, Mario Winkler, Maurice Conrad and Michael Tran. I wish you all the best for your further careers and enjoyed working with you.

This thesis wouldn't have been possible without the support of a range of collaborators. I want to thank Prof. Dr. Thomas Prisner for the opportunity to use his X- and Q-band EPR spectrometer and acknowledge the Centre for Biomolecular Magnetic Resonance at the Goethe University Frankfurt for their kind provision of liquid helium for the EPR-measurements there. Thanks to Dr. Burkhard Endeward for all his experience, patience and enthusiasm during our collaborations, through which every stay proved to be scientifically successful. Furthermore I want to acknowledge the National EPR Facility and Service at the University of Manchester for the possibility to perform X- and Q-band EPR measurements. Thanks to Dr. Amgalanbaatar Baldansuren and Dr. Alistair Fielding for the help with the experiments and thanks to Dr. Floriana Tuna and Prof. Dr. Eric McInnes for the fruitful discussions. I would like to acknowledge the CAESR ESR Facility at the University of Oxford for the opportunity to perform pulsed Q-band measurements. Many thanks here to Dr. William Myers and Dr. Alice Bowen for the long nights in front of the spectrometer, for their creativity and expertise which helped me and my project. At this point I want to thank Prof. Dr. Arzhang Ardavan for the input, discussions and support during my visit in Oxford and beyond. I kindly acknowledge the Center for Interdisciplinary Magnetic Resonance at the National High Magnetic Field Laboratory in Tallahassee and Dr. Johan van Tol for the opportunity to perform EPR measurements at 120 and

240 GHz. Thanks Hans for the support and expertise with very high frequency- and very low temperature measurements, I've learned a lot during my stay in the States. Moreover, I want to thank Prof. Dr. Etienne Goovaerts and Prof. Dr. Sabine van Doorslaer at the University of Antwerp for the possibility to perform W-band EPR measurements. Thanks for the great measurements and the kind reception during my visit! Last but not least thanks to Prof. Dr. Gunnar Jeschke for the opportunity to use his S-band EPR-spectrometer and many thanks to Renée Tschaggelar, who kindly introduced me to this device and made the long measurement days feel short.

Not only around the world, but also at the University of Stuttgart there are a lot of people to which I want to express my gratitude: Simon Schlindwein at the Institute for Inorganic Chemistry, for synthesizing d_{20} -AsPh₄Br. Barbara Förtsch at the Institute of Inorganic Chemistry for the performance of elemental analyses. Uta Twiehaus-Heynhold and Sascha Wegner at the Institute for Organic Chemistry for the measurement of NMR-spectra. Dr. Wolfgang Frey at the Institute for Organic Chemistry for the measurement of X-ray crystal structures and also for always having a smile on his face!

Finally, I want to thank my family, my friends and my partner Max with all my heart for their constant love and support through the ups and downs of my life as a Ph.-D.-student. I don't know how I should have survived this without good conversations, relaxing time in nature and all the "adventouring" in and around crags and mountains or simply at home.